Investigation of Bandwidth Utilisation Methods to Optimise Performance in Passive Bistatic Radar

Karl Erik Olsen

A dissertation submitted in partial fulfillment
of the requirements for the degree of
Doctor of Philosophy
of the
University of London.

Department of Electronic and Electrical Engineering
University College London

2011

I, Karl Erik Olsen, confirm that the work presented in this thesis is my own. Where information has been derived from other sources, I confirm that this has been indicated in the thesis.

Abstract

This thesis reports on research into the field of multiband Passive Bistatic Radar (PBR). The work is based on the premise that it is possible to improve on the PBR range resolution by exploiting the full broadcasted bandwidth from transmitters of opportunity. This work comprises both Frequency Modulated (FM) radio and Digital Video Broadcast - Terrestrial (DVB-T) waveforms. The work shows how the exploitation of the available frequency scattered bandwidth broadcasted from single broadcast towers can be achieved by coherently by combining each of the individual channels/bands, and that the range resolution is improved accordingly.

The major contributions of this thesis may be divided into the following parts: Hardware (HW) design and development, algorithm development, simulations, real target data analysis, and finally non-cooperative target recognition and High Range Resolution (HRR) considerations.

The work comprises simple PBR performance predictions for various strong transmitters of opportunity in the southeastern parts of Norway. Hardware for data recording was designed, produced and made working.

The mathematics for coherently combining non-adjacent single channels/bands in the range correlation was developed. The range resolution performance of the algorithm was supported by theoretical simulations using pseudo random generated signals, as well as simulations using real recorded FM radio and DVB-T signals from nearby strong transmitters.

For FM radio and DVB-T airliners and for DVB-T also a propeller aircraft were analyzed. The theoretical claims were supported by the real life target analysis, as the range resolution was improved as predicted for all targets. For the DVB-T waveform, an analysis of the HRR profiles showed that two targets of different type was manually classified as targets of different type.

This work has fully closed the circle from idea, HW design, development and testing, theoretical algorithm development and simulations, and finally real world performance analysis as well as target analysis.

Acknowledgements

The work contained in this thesis would not have been possible without the support of several people, and I would like to take the opportunity to thank them all.

I wish to acknowledge and sincerely thank my supervisors at UCL, Dr. Karl Woodbridge, Prof. Hugh Griffiths and Prof. Chris Baker for their support and guidance during my PhD. I would also like to thank the UCL Radar Group, past and present, while being non-resident in London I did not spend as much time with you as I would have liked. But I always felt very welcome and my research was discussed with insight each time.

I would like to thank FFI for funding this PhD research, and in particular Hans Øhra for offering this opportunity to me. I am deeply grateful for the support from Steinar Johnsrud and Per Sørnes on data recording equipment design and assembly, as well as the assistance from Jonas M. Christiansen on keeping the system running. I would also like to acknowledge Prof. Øystein Lie-Svendsen for proofreading the mathematics of the thesis, and finally I would like to express my gratitude to my colleagues in the FFI Air Surveillance Program, for covering for me when things did not go according to plan.

To close, I want to acknowledge the immense support I have received from my wife, children and parents. I dedicate the work presented here to them.

Publications

Journal papers

K. E. Olsen, K. Woodbridge, ”Performance of a Multiband Passive Bistatic Radar Processing Scheme - Part I”, *IEEE AES System Magazine (AESSM) Special Issue on Passive Coherent Location*, invited paper submitted 31. August 2011, [1].

K. E. Olsen, K. Woodbridge, ”Performance of a Multiband Passive Bistatic Radar Processing Scheme - Part II”, *IEEE AES System Magazine (AESSM) Special Issue on Passive Coherent Location*, invited paper submitted 31. August 2011, [2].

Invited conference papers

K. E. Olsen and C. J. Baker, ”FM-based Passive Bistatic Radar as a function of available bandwidth”, *Proc. of IEEE Radar Conference*, May, 2008, [3].

K. E. Olsen and K. Woodbridge, ”FM Based Passive Bistatic Radar Target Range Improvement”, *Proc. International Radar Symposium*, September, 2009, [4].

K. E. Olsen, K. Woodbridge and I. A. Andersen, ”FM Based Passive Bistatic Radar Target Range Improvement - Part II”, *Proc. International Radar Symposium*, June, 2010, [5].

K. E. Olsen and K. Woodbridge, ”FM Based Passive Bistatic Radar Range Resolution Improvement”, *Proc. International Radar Symposium*, September, 2011, [6].

Regular conference papers

K. E. Olsen and K. Woodbridge, ”Analysis of the Performance of a Multiband Passive Bistatic Radar Processing Scheme”, *IEEE Waveform Diversity & Design Conference*, August, 2010, [7].

Presentations without papers

K. E. Olsen, ”Any PCL Aspect in Norway?”, *PCL Focus Day*, Fraunhofer FHR, Germany, November 2009, [8].

K. E. Olsen and K. Woodbridge, ”Analysis of the Performance of a Multiband Passive Bistatic Radar Processing Scheme”, *PCL Focus Day*, Fraunhofer FHR, Germany, May 2011, [9].

Contents

List of Figures

List of Tables

Glossary of Terms

A/D	Analog to Digital
ADS-B	Automatic Dependent Surveillance - Broadcast
AM	Amplitude Modulated
BSAR	Bistatic SAR
CFAR	Constant False Alarm Rate
COFDM	Coded OFDM
CPI	Coherent Processing Interval
CW	Continuous Wave
DAB	Digital Audio Broadcast
DFT	Discrete Fourier Transform
DiMuRa	Digital Multistatic Radar
DRM	Digital Radio Mondiale
DQD2	Dual Quad DVB-T Demodulator
DSI	Direct Signal Interference
DTV	Digital TV
DVB-T	Digital Video Broadcast - Terrestrial
ERP	Effective Radiated Power
ETSI	European Telecommunications Standards Institute
FFI	Forsvarets forskningsinstitutt, i.e. Norwegian Defence Research Establishment
FFT	Fast Fourier Transform
FM	Frequency Modulated
GDOP	Geometric Dilution of Precision
GPS	Global Positioning System
GSM	Global System for Mobile communications
HA100	Home Alerter 100 (Thales' PCL sensor)
HF	High Frequency, $3MHz - 30MHz$, IEEE Radar Designations
HRR	High Range Resolution
HW	Hardware
IDFT	Inverse Discrete Fourier Transform
IEEE	Institute of Electrical and Electronics Engineers, Inc.

IET	The Institution of Engineering and Technology
IF	Intermediate Frequency
IFFT	Inverse FFT
IQ	In- and Quadrature-phase
ISAR	Inverse SAR
ISLR	Integrated Sidelobe Ratio
ITU	International Telecommunication Union
LO	Local Oscillator
MPEG	Moving Picture Experts Group
MSRS	Multi Site Radar Systems
NATO	North Atlantic Treaty Organization
NBFM	Narrow Band Frequency Modulated
NC3A	NATO C3 (Consultation, Command and Control) Agency
NCTR	Non Cooperative Target Recognition
NECTAR	Thales DVB-T PBR demonstrator
OFDM	Orthogonal Frequency Division Multiplex
OTH	Over-The-Horizon
PARADE	PAssive RAdar DEmonstrator, EADS Cassidian FM and DAB PBR demonstrator
PaRaDe	Passive Radar Demonstrator, Warsaw University of Technology FM PBR demonstrator
PBR	Passive Bistatic Radar
PCL	Passive Coherent Location
PCR	Passive Covert Radar
PRF	Pulse Repetition Frequency
PRBS	Pseudo Random Binary Sequence
PSLR	Peak to Sidelobe Ratio
RADAR	Radio Detection And Ranging
QAM	Quadrature Amplitude Modulation
RCS	Radar Cross Section
RDS	Radio Data System
RF	Radio Frequency
SAR	Synthetic Aperture Radar
SDR	Signal to Direct signal Ratio
SFN	Single Frequency Network
SNR	Signal to Noise Ratio
SS3	Silent Sentry® 3 (Lockheed Martin's PCL sensor)
SW	Software
TDOA	Time Difference Of Arrival
TPS	Transport Parameter Signaling

TV	Television
TX	Transmitter
UCL	University College London
UHF	Ultra High Frequency, $300MHz - 1000MHz$, IEEE Radar Designations
VHF	Very High Frequency, $30MHz - 300MHz$, IEEE Radar Designations
WBFM	Wideband Frequency Modulated

List of Symbols

All symbols are defined in the main body of the text, while the general ones are also listed here.

Symbol	Meaning
a, A	A is the total number of Doppler cells applied in the processing, while a is index of the Doppler cell number a
a_r	Radial component of target acceleration
B	Bandwidth
B_n	Receiver predetection filter
c	Speed of propagation
C_i	Windowing filter in the range dimension, $i = 0, 1, 2, \ldots, N-1$
$C^{p,q}(i, s)$	Defined in equation (5.16)
$C^{p,p}_{\max}(s)$	Defined in equation (5.17)
D_s	Windowing filter in the Doppler dimension, $s = 0, 1, 2, \ldots, A-1$
e	Eccentricity
f_B	Bistatic Doppler shift, frequency
f_c, f_c^p	Carrier/center frequency of the pth broadcasted signal/channel
f_d	Doppler frequency
$f_D^m, f_D^{p,m}$	Constant Doppler shift of the mth target for the pth channel
f_i	Carrier frequency for the ith channel, $i = 0, 1, 2, \ldots, N-1$
f_p	$f_p = f_{ref} - f_{sur}$
f_s	Sampling frequency
f_L, f_0, f_H	Low, center, and high frequency of the bandwidth peak in frequency domain
f_{ref}^{q0}	Initial frequency offset in the pth channel's demodulation
f_{ref}, f_{ref}^p	Receiver reference channel frequency down conversion for the pth channel
f_R	Receiver antenna propagation factor, i.e. antenna diagram
f_{sur}^{p0}	Initial frequency offset in the pth channel's demodulation

f_{sur}, f_{sur}^{p}	Receiver surveillance channel frequency down conversion for the pth channel
f_T	(1) Carrier frequency of transmitter (2) Transmit antenna propagation factor, i.e. antenna diagram
$f(M, T)$	Maximum number of ghosts in the 2D situation, generated by T targets and M bistatic transmit-receive pairs
F, F_n	Receiver noise factor
F_D	Pattern propagation factor for transmitter-to-receiver path
F_R	Pattern propagation factor for target-to-receiver path
$F_{R,X}$	Pattern propagation factor for receiver-to-target path, where X may be T-target or C-clutter
F_R'	Receiver to target propagation factor
F_T	Pattern propagation factor for transmitter-to-target path
$F_{T,X}$	Pattern propagation factor for transmitter-to-target path, where X may be T-target or C-clutter
F_T'	Transmitter to target propagation factor
G_p	Processing gain
G_R	Receiving antenna power gain
$G_{R,X}$	Receiving antenna power gain, where X may be T-target, C-clutter, and D-direct signal
G_T	Transmitting antenna power gain
$G_{T,X}$	Transmitting antenna power gain, where X may be T-target, C-clutter, and D-direct signal
j	The imaginary unit, $j = \sqrt{-1}$
k	Boltzmann's constant [$1.38 \times 10^{-23} W/(Hz\, K)$]
L	Bistatic baseline length
L_r	RF component loss
L_R	Receiving system loss (> 1) not included in other parameters
$L_{R,X}$	Receiving system losses (> 1) not included in other parameters, where X may be T-target, C-clutter, and D-direct signal
L_{sp}	Signal processing loss
L_T	Transmitting system losses (> 1) not included in other parameters
$L_{T,X}$	Transmitting system losses (> 1) not included in other parameters, where X may be T-target, C-clutter, and D-direct signal
m, M	M is the total number of reflectors considered in the processing, while m is the index of reflector number m
n, N	(1) N is the total number of *samples* in the range processing, while n is the index of range sample number n

	(2) $N = P$ is the number of coherently combined channels, see also P
N_0	Noise spectral density
p, P	P is the number of carrier frequencies used, while p is the index of carrier frequency number p
P_n	Receiver noise
P_T	Transmitter power output
R_M	Equivalent monostatic range, or benchmark range
R_R	Range between receiver and target
$R_{R,X}$	Range between receiver and target, where X may be T-target, C-clutter, and D-direct signal
R_T	Range between transmitter and target
$R_{T,X}$	Range between transmitter and target, where X may be T-target, C-clutter, and D-direct signal
R_u	$R_u = nc/\Delta f$, n is number of stepped frequencies
S/D	Signal-to-Clutter signal ratio
S/D	Signal-to-Direct signal ratio
$(S/N)_{\min}$	Minimum signal-to-noise power ratio required for detection
t_c	Coherent integration time
t_i	$t_i = i/f_s$, for $i = 0, 1, 2, \ldots, S-1$
t_L	$t_L = L/c$
t_R	$t_R = R_R/c$
t_T	$t_T = R_T/c$
T	Coherent processing interval
T_0	$290K$
T_a	Antenna contribution to noise temperature
T_e	Receiver contribution to noise temperature
T_i	Receiving system noise temperature
T_m	Temperature of the man-made noise interference
T_r	RF contribution to noise temperature
T_S	Temperature of sky noise interference
$u_{ref}(t_i), u_{ref}^{p}(t_i)$	Reference information signal for the pth channel
$u_{sur}^{m}(t_i - \nu_m), u_{sur}^{p,m}(t_i - \nu_m)$	Surveillance information signal reflected off scatterer m at bistatic range ν_m for the pth channel
$U_{ref}(t_i), U_{sur}(t_i)$	The transmitted, reflected, down converted, filtered and IQ sampled reference/surveillance signal, where t_i is sampled time
v, V	Target velocity
$z_{ref}(i, s), z_{sur}(i, s)$	The two dimensional rearranging of $U_{ref}(t_i), U_{sur}(t_i)$ in order to perform the efficient range-Doppler processing
α_{ref}	$\alpha_{ref} = \xi_{ref} \exp\left(j2\pi\phi_c\right)$

α_{ref}^{p}	$\alpha_{ref}^{p} = \xi_{ref}^{p} \exp\left(j2\pi\phi_c^p\right)$
$\alpha_{ref}(t_{i+sN})$	$\alpha_{ref}(t_{i+sN}) = \xi_{ref}(t_{i+sN}) \exp\left(j2\pi\phi_c\right)$
$\alpha_{ref}^{p}(t_{i+sN})$	$\alpha_{ref}^{p}(t_{i+sN}) = \xi_{ref}^{p}(t_{i+sN}) \exp\left(j2\pi\phi_c^p\right)$
α_{sur}^{k}	$\alpha_{sur}^{k} = \xi_{sur}^{k} \exp j2\pi(-f_c\nu_k - (t_R - t_L)f_D^k + \phi_c)$
$\alpha_{sur}^{p,k}$	$\alpha_{sur}^{p,k} = \xi_{sur}^{p,k} \exp\left(j2\pi\left(-f_c^p\nu_k - (t_R - t_L)f_D^{p,k} + \phi_c^p\right)\right)$
$\alpha_{sur}^{m}(t_{i+sN} - \nu_m)$	$\alpha_{sur}^{m}(t_{i+sN} - \nu_m) = \xi_{sur}^{m}(t_{i+sN} - \nu_m) \exp\left(j2\pi(-f_c\nu_m - (t_R - t_L)f_D^m + \phi_c)\right)$
$\alpha_{sur}^{p,m}(t_{i+sN} - \nu_m)$	$\alpha_{sur}^{p,m}(t_{i+sN} - \nu_m) = \xi_{sur}^{p,m}(t_{i+sN} - \nu_m) \exp\left(j2\pi\left(-f_c^p\nu_m - (t_R - t_L)f_D^{p,m} + \phi_c^p\right)\right)$
β	Bistatic angle
δ	Target velocity angle with respect to bistatic bisector
$\delta_D^{p,k}$	Small Doppler shift on top of the regular translational Doppler shift $f_D^{p,k}$ for target number k for channel number p
Δf	(1) Step frequency for frequency band separation, equation (5.22) and (5.23) (2) Step frequency for high range resolution stepped frequency radar, $\Delta f = 1/T$, where T is frequency constant time (3) Frequency deviation, appendix B
$(\Delta f_d)_{bistatic}$	Bistatic Doppler spreading
$(\Delta f_d)_{mono}$	Monostatic Doppler spreading
ΔR	Range resolution
ΔR_B	Bistatic range resolution
ΔR_M	Monostatic range resolution
$(\Delta R_\theta)_u$, $(\Delta R_\theta)_e$	Physical separation of two targets for unequal/equal (u/e) cross-range dimensions of transmit and receive beams
ΔT_i	Coherent integration time T_i for the ith channel out of the N channels, $i = 0, 1, 2, \ldots, N-1$
$\Delta v, \Delta V$	Velocity resolution
$\Delta\theta_R$	Receiving antenna's $3dB$ beamwidth
$\Delta\theta_T$	Transmitting antenna's $3dB$ beamwidth
θ_R	The angle defined by the north direction and the line Rx to target
θ_T	The angle defined by the north direction and the line Tx to target
λ	Wavelength
ν	Doppler shift
ν_m	$\nu_m = (t_T + t_R - t_L) = (R_T + R_R - L)/c$, bistatic target delay, i.e. bistatic TDOA
ξ_{ref}, ξ_{ref}^{p}	Real positive constant, pth channel

$\xi_{ref}(t_i), \xi_{ref}^{p}(t_i)$	Complex time varying function accounting for the potentially time varying target reflectivity in amplitude as well as phase, and for clear air effects like multipath, gaseous absorption, diffraction, and refraction, and non-clear air effects like precipitation and clouds for the pth channel transmitter-receiver path
$\xi_{sur}^{m}, \xi_{sur}^{p,m}$	Real positive constant for the mth scatterer and pth channel
$\xi_{sur}^{m}(t_i), \xi_{sur}^{p,m}(t_i)$	Complex time varying function accounting for the potentially time varying target reflectivity in amplitude as well as phase, and for clear air effects like multipath, gaseous absorption, diffraction, and refraction, and non-clear air effects like precipitation and clouds for the pth transmitter-target-receiver path for the mth scatterer
ρ	Power utilization factor, $\rho \leq 1$
σ_B	Bistatic radar target cross section
σ_B^0	Bistatic scatter coefficient in the bistatic scattering region
σ_M	Monostatic radar target cross section
τ	(1) Compressed pulse width (2) Time delay
ϕ_c, ϕ_c^p	Initial phase of the broadcasted carrier/center frequency of the pth channel
ψ	Aspect angle with respect to the bistatic bisector
$\psi(T_R, f_d)$	Monostatic ambiguity function at the delay range T_R and Doppler f_d
$\psi(R_{RH}, R_{Ra}, V_H, V_a, \theta_R, L)$	Bistatic ambiguity function where R_{RH} and R_{Ra} are the hypothesized and actual ranges (delays) from the receiver to the target, V_H and V_a are the hypothesized and actual radial velocities of the target with respect to the receiver

Chapter 1

Introduction

1.1 Overview

Passive Coherent Location (PCL), Passive Covert Radar (PCR), Passive Bistatic Radar (PBR), passive radar or parasitic radar[1] are all common names for passive radar system exploiting cooperative, noncooperative transmitters, or transmitters of opportunity, [22, pp. 3]. Recent review of the various names resulted in the compromise PBR, [23, pp. 248], and this work will try to be faithful to that. It should be noted that the PCL name is still being used for full systems like Lockheed Martin's - Silent Sentry® [24, 25], and Thales' - Home Alerter 100 [26], and they may be considered as a system of PBR systems.

Figure 1.1 shows a generic PBR system consisting of two transmitters, and one receiver. The distances between the transmitters and the receiver are known, and hence, the Time Difference Of Arrival (TDOA) between the direct signal and the target reflected signals can be extracted by the receiver. This generates two constant range ellipses as seen in figure 1.1 (the equivalent for monostatic radars being constant range circles). By using two transmitters, giving two TDOAs, the intersections between the resulting ellipses can be calculated, and subsequently, the correct target position extracted through a deghosting process. The deghosting process sorts out the false target crossings such as the one just below the receiver in figure 1.1. The correct target crossing is indicated by the aircraft. Two transmitter-receiver pairs gives the 2D-position, while the 3D positioning can be calculated using three transmitter-receiver pairs.

PBR systems have received much interest in the academic as well as military communities. Since the end of World War II the interest for bistatic radars has been going in cycles with a periodicity of 15 to 20 years [22, Preface], and the most successful bistatic radar application since the mid 40's is the semi-active homing missiles. The interest for PBR is at the moment at a wide peak, mainly due to the rapidly emerging PBR technology, which has matured enough for the military to see PBR as a potential sensor for air surveillance. In addition to this, the computing power/data recording hardware is finally at a cost/performance level where it is possible for universities and institutes to collect data at a cost effective rate.

---

[1] Radio Detection and Ranging

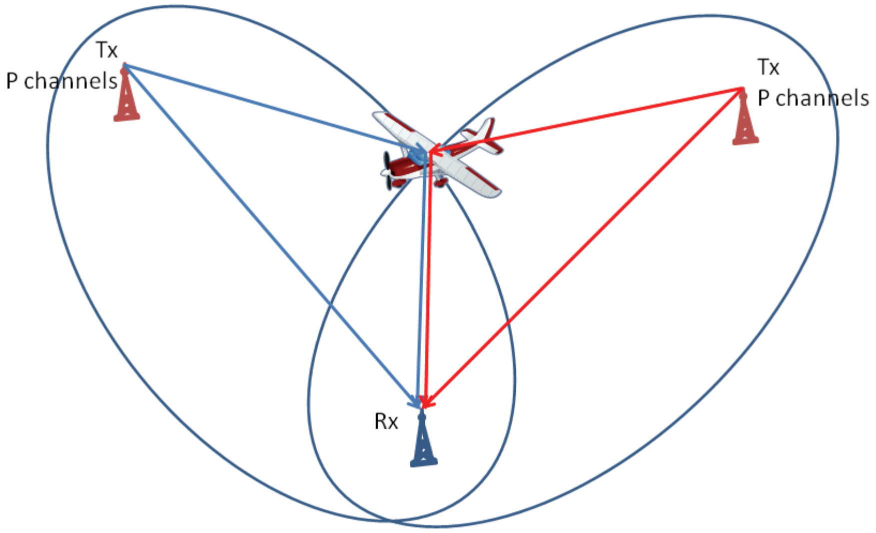

Figure 1.1: The figure shows the target location principle of a generic multilateration PBR system. Two transmitters (Tx) and one receiver (Rx) are positioning in 2D a target by TDOA ellipse intersections. False target crossings are separated from real target crossing in the signal processing.

The claimed military benefits from operating a passive sensor in the FM (Frequency Modulated) and/or Digital Video Broadcast - Terrestrial (DVB-T) frequency range are a major drive for the interest: covert operations, radar operations without radiation hazards or the need to acquire frequency allocation, multistatic geometry which is claimed to be effective against modern shaped targets and (modern) jamming techniques, the low frequency band (Very High Frequency (VHF)/Ultra High Frequency (UHF)) is claimed to be attractive with respect to detection and tracking of modern targets, as well as the potential for low level coverage. All this for a potentially low price compared to traditional active radar systems, although this has yet to be proved for operational systems by the industry. The two competing PBR systems from Lockheed Martin - Silent Sentry® [24,25], and Thales - Home Alerter 100 [26], are participating in various trials arranged with potential customers, and through official channels high level results and performances are reported.

The three types of terrestrial broadcasters which is found to be suitable transmitters for domestic Norwegian long range PBR applications are FM radio, Digital Audio Broadcast (DAB) and DVB-T. The DAB radio has not been a success in Norway for several reasons, one of them being the relatively poor coverage compared to the FM radio system which covers all of Norway. The DAB system has only been serving the largest cities and the major roads between them. Although a recent expansion of the system resulted in better coverage, the number of transmitters is still low compared to the FM and DVB-T. Figure 1.2 shows the Norwegian FM and DVB-T transmitters as a function of Effective Radiated Power (ERP) in February 2007. The color coding is: blue means ERP$\leq 20dBW$, yellow $20dBW <$ERP$\leq 30dBW$, and red ERP$> 30dBW$. In the case of several transmitting channels on the same tower, the strongest is shown. The following research will thus

Table 1.1: Examples of broadcasted carrier frequencies for Norwegian transmitters (TX) where the $ERP > 30dBW$.

System	TX name	Carrier frequency [MHz]			
FM radio	Tryvann	88.7	93.5	100.0	103.9
	Holtberget	89.8	93.9	96.1	
	Hoeyaas	89.1	94.8	101.5	106.1
DVB-T	Tryvasshoegda	722.0	770.0	794.0	
	Kongsvinger	498.0	690.0	746.0	
	Halden	610.0	642.0	802.0	

focus on FM radio and DVB-T.

The FM radio, Norwegian license $88 - 108MHz$, and the DVB-T, Norwegian license $470 - 790MHz$ are broadcasting multiple radio/TV channels in different ways. The FM radio is broadcasting each radio channel at a different frequency, the frequencies being separated by at least $200kHz$, while the DVB-T is broadcasting multiple TV channels in $8MHz$ wide Coded OFDM (COFDM) bands, and until fall 2010 each DVB-T transmitter was broadcasting three bands each at different frequencies, and after fall 2010 five bands were broadcasted. (I.e. one of the Norwegian regions was using channel 24, 48 and 55, which meant that the three $8MHz$ band's center frequency were $498MHz$, $690MHz$, and $746MHz$ respectively). The frequency reuse policy is also different. FM radio transmissions try to serve one area for one frequency only, while DVB-T is a Single Frequency Network (SFN), which means that multiple transmitters at the same frequency is serving the same area. The DVB-T system consists of multiple SFN networks, each serving a single region.

Figures 1.3 and 1.4 gives examples of the available FM radio and DVB-T bandwidth each from one transmitter in the Oslo region of Norway. Table 1.1 lists the broadcasted channels from a few of the strong broadcasters of the southeastern parts of Norway ($ERP > 30dBW$). The main focus of this work will be on how to take advantage of the available broadcasted energy with respect to both time and bandwidth.

The unclassified/open PBR research is ongoing at universities and research facilities around the world. The majority of this research has been focused on the signal and waveform availability [27–34], the detection performance of PBR systems [22,23,26,35–42], and finally multifrequency fusing of data from similar as well as different PBR systems relying on FM radio, DAB and DVB-T transmitters of opportunity in order to improve target detection [26,33,38–41].

Current versions of Silent Sentry® and Home Alerter 100 both rely on target detection in multiple transmitter-target-receiver geometries in order to position targets spatially, and in some areas this might be a challenge to achieve due to the potential lack of enough geographically separated high power transmitters. Recent work, [43], claims that target tracking down to a single transmitter-target-receiver geometry might be achievable also for FM radio based PBR systems, and this would drastically increase the target tracking per-

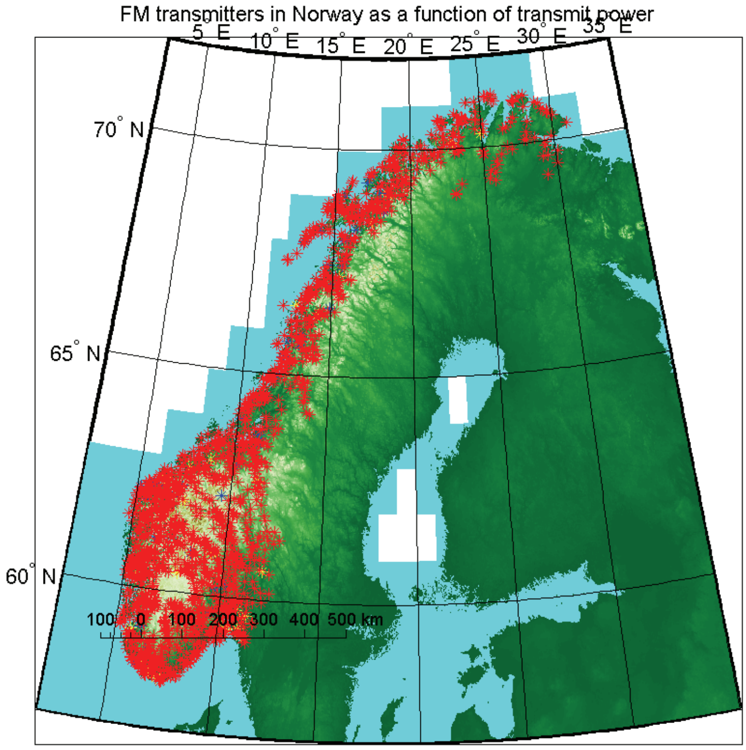
FM transmitters in Norway as a function of transmit power

(a) FM radio.

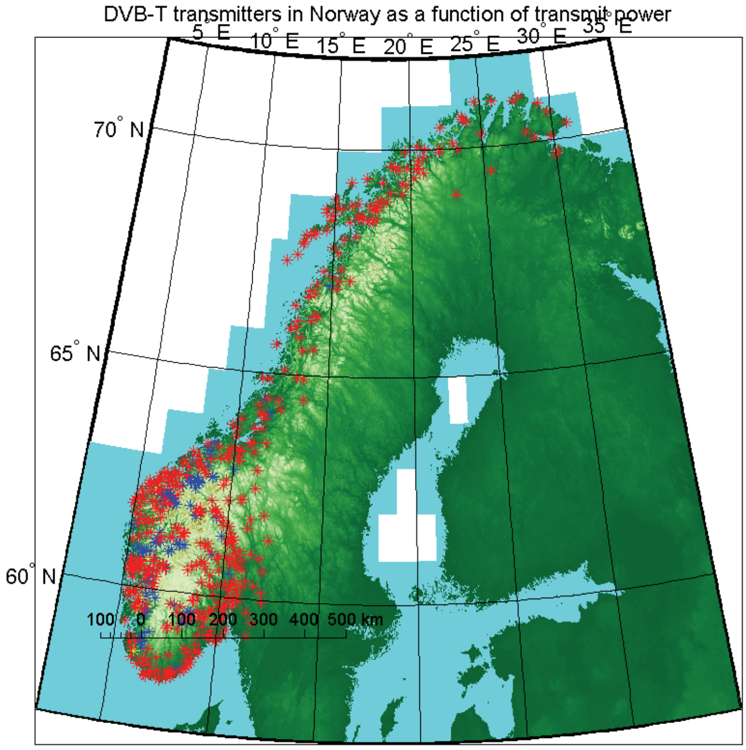
DVB-T transmitters in Norway as a function of transmit power

(b) DVB-T.

Figure 1.2: The Norwegian FM and DVB-T transmitters as a function of ERP in February 2008. The transmit power is asterisk color coded, blue ERP$\leq$ $20dBW$, yellow $20dBW$ $<$ERP$\leq$ $30dBW$, and red ERP$>$ $30dBW$. In the case of several transmitting channels on the same tower, the strongest is shown.

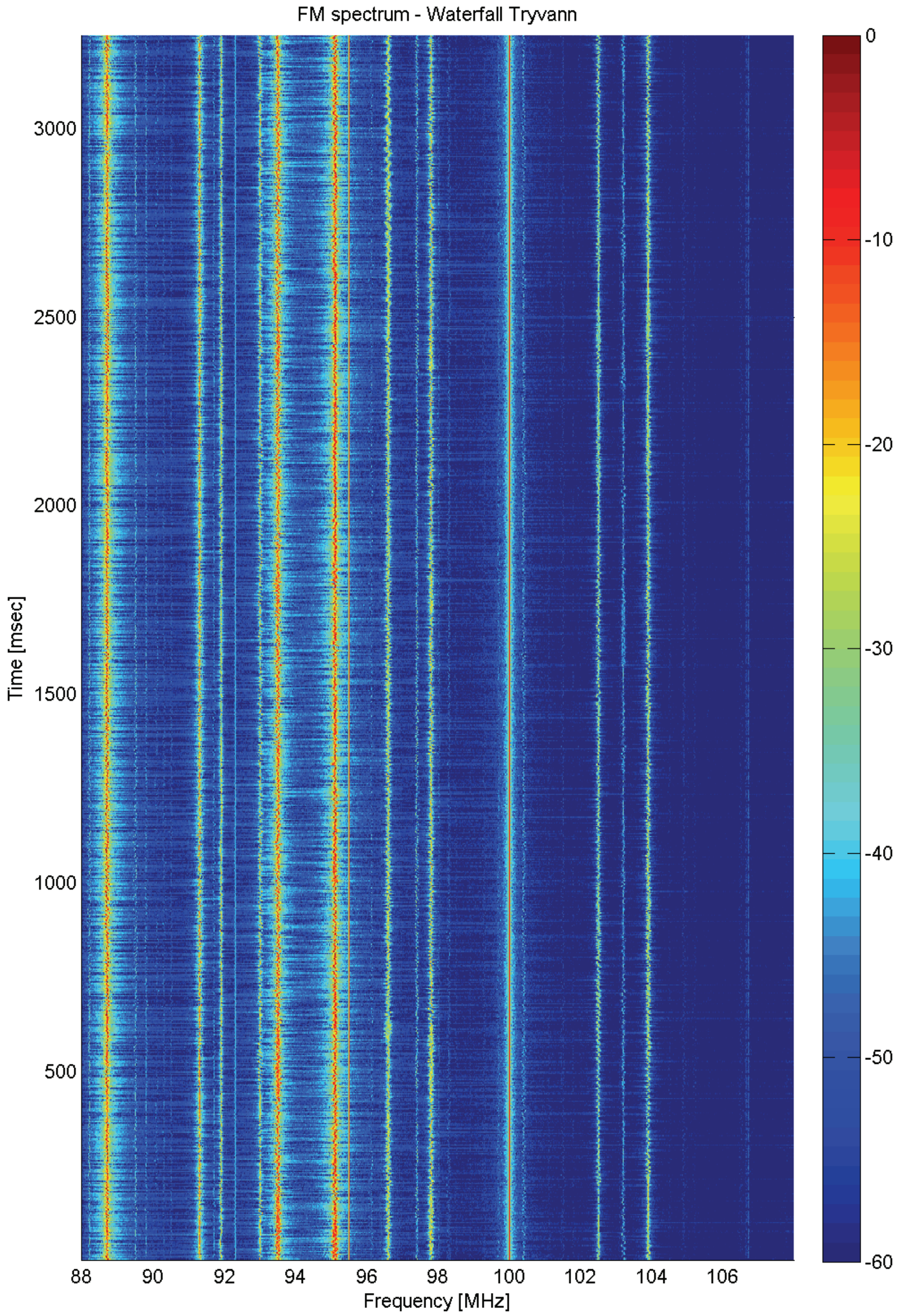

Figure 1.3: The entire FM radio band as a function of frequency and time. The color coding is in relative dB as shown in the colorbar to the right of the plot.

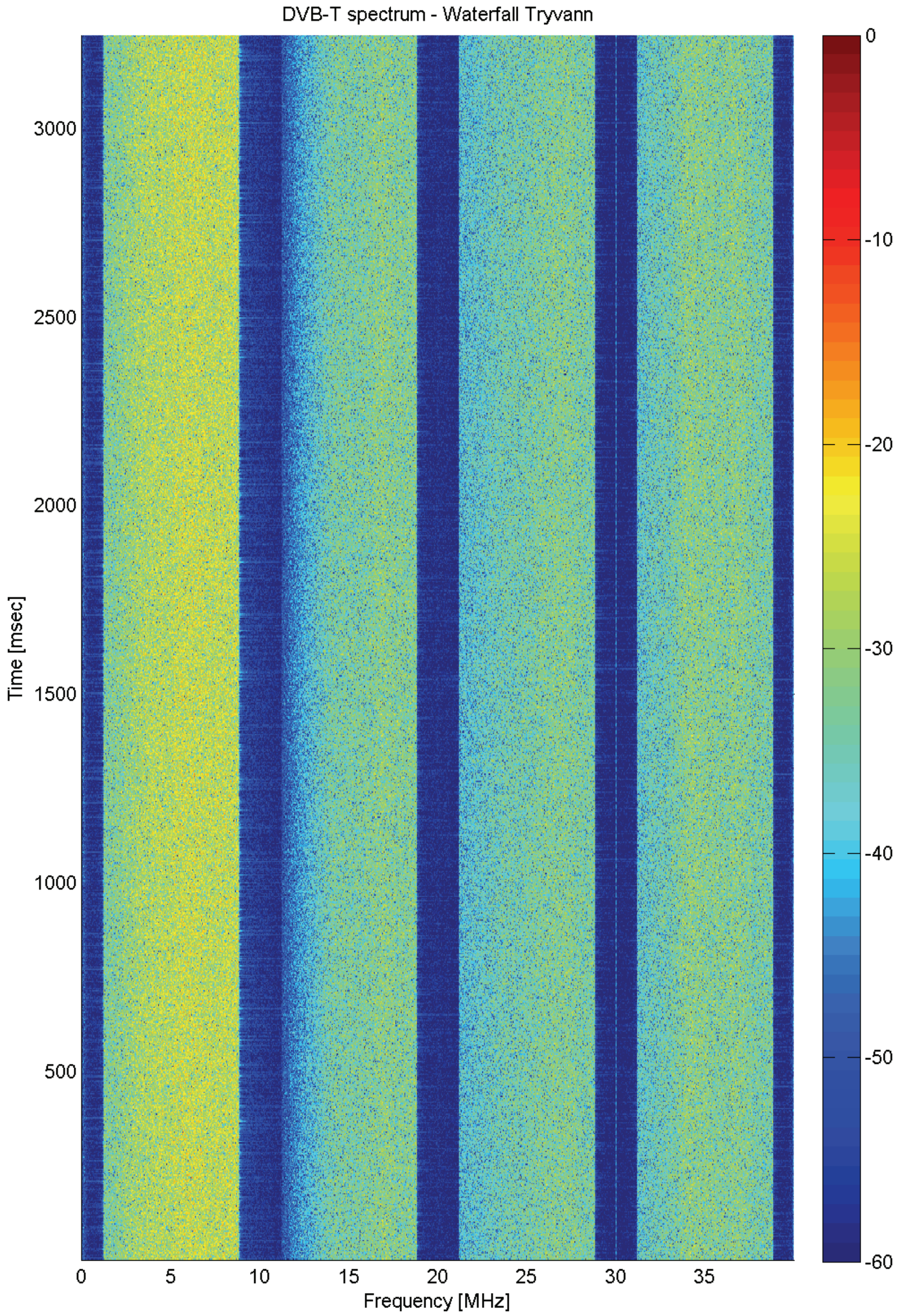

Figure 1.4: Four DVB-T channels down modulated to adjacent bands as a function of frequency and time. The color coding is in relative dB as shown in the colorbar to the right of the plot.

formance of such systems, since the FM radio system seems to have at least one powerful multichannel transmitter in all regions[2]. Single transmitter tracking is probably achievable also for the DVB-T case, as indirectly supported by [26], where angular azimuthal accuracies for target detections based on one bistatic geometry are presented. For the FM radio system (Home Alerter 100) an azimuthal accuracy of 3.7 degrees is claimed, while it is claimed an azimuthal accuracy of 2.9 degrees for the DVB-T system with a planar array with four elements. The higher frequency of DVB-T (in Norway 470-790MHz) compared to FM radio (88-108MHz) also suggests that a (manageable) higher gain antenna might be applied.

In addition to this, [38, 39] showed that the detection performance is improved by using several FM radio channels for detection, as frequency diversity is achieved as well as a robustness against the bandwidth fluctuations arising from the combination of the FM radio modulation technique and the time varying program content. The Norwegian high power FM transmitters seem to broadcast at least three high power FM radio channels, as is the case for the DVB-T system, where each DVB-T transmitter is broadcasting at least three channels as seen in table 1.1.

1.2 Aims of this work

This work is aiming at adding another capability to the single transmitter PBR work on detection and tracking, namely improved target range estimation. For FM radio, the bistatic range resolution is reported to be in the order of $3 - 30km$, while the corresponding number for the DVB-T is $40m$, [26]. This work is focusing on how to improve the range resolution in the range correlation of the matched filter processing by exploiting multiple broadcasted channels from a single transmitter. The latter requirement is important in order to achieve the same geometry for all channels for the same target, i.e. same time-delayed processing. One of the goals of the work is to achieve the improved range resolution, while maintaining the high Doppler resolution from the relatively long integration time. It is believed that this work will fit nicely in a future system design alongside the improved detection performance of [38,39], and the single transmitter target tracking of [43].

There are two special properties in the PBR systems relying on FM radio and DVB-T broadcast transmitters that should be exploited: 1) The broadcast transmitters are transmitting continuously, with a duty cycle of 100%, and the receiver of the FM and DVB-T based PBR systems are using antennas with stationary beams covering the surveillance area/volume 100% of the time. (Although not all systems are capable of processing continuously in real time due to the huge processing power needed). This means that the radar potentially is 100% time on target. 2) The FM radio and DVB-T based PBRs are using

---

[2] It should be noted that earlier demonstrators of PBR performance, Silent Sentry® and the NATO C3 (Consultation, Command and Control) Agency (NC3A) sensor [44], used a linear array receiver antenna to measure the angle from receiver to target with respect to a reference accurately enough in order to achieve high quality spatially detection data and thus obtain single transmitter target tracking. However, none of the current FM radio PBR systems seem to have kept this solution, probably due to customer demands of full 360 degrees azimuthal surveillance at an affordable price.

relatively long integration times (compared to the classical monostatic radars in similar roles), which yields very good Doppler resolution, and thus a potential for accurately separating targets, even though they are not separated in range. However, it is underlined that the research of this thesis is not trying to investigate the potentials of Doppler tracking.

The work will not include tracking as a mean to improve resolution and/or accuracy, since one of the research goals is to improve the localization of especially challenging targets, like maneuvering targets, and targets which are observed only for short periods, as well as low signal to noise ratio targets, all factors which make the tracking process hard. In general the tracking procedure requires at least a few updates in order to provide improved estimates on target position. Some of the mentioned targets might not allow this, and instant high resolution and accuracy is required. In this context is the tracking of big targets in straight flight of less interest.

The work will not include multiband processing techniques like interpolation and/or extrapolation. The actual information available in the different bands is pinpointed without interpolating and/or extrapolating, mainly due to the fact that the signal processing should be applicable within the processing framework already in place today. The proposed algorithm is capable of that. But maybe most important is the fact that the bands are independent in terms of coding and content, as well as highly time varying bandwidth (FM radio). The works on interpolation and/or extrapolation are considering known waveforms behaving predictably across bands [45], which definitely is not the case for PBR systems relying on broadcasters of opportunity. However, it will not be impossible to obtain, but that would call for an extremely complex processing.

By introducing improved range resolution, a radar sensor with high range and Doppler resolution is achieved, as well as 100% time on target. This will be a good starting point for creating bistatic High Range Resolution (HRR) profiles, and for creating bistatic Inverse Synthetic Aperture Radar (ISAR) images, using both narrow angle imaging (high bandwidth and small aperture angle (short time)), and wide angle (low/high bandwidth and large angle (long time)) imaging. For the time being the imaging aspects are considered to be outside the main scope of this work, however some essentials of the gound work will be achieved, i.e. combining non-adjacent broadcasted signals of opportunity coherently in order to improve range resolution while maintaining the good Doppler resolutioin.

In order to reach these goals, the work comprises the design, development, and testing of the data recording equipment described in chapter 4. The driving motivation behind the data recording equipment were to be able to record both FM radio and DVB-T PBR target datasets of such a quality that analysis of longer periods, i.e. tens of minutes could be analyzed continuously. In addition to this, the whole FM band, as well as up to four non-adjacent DVB-T channels of choice, each of maximum $8MHz$ bandwidth, for both reference and surveillance channel should be recorded. All this requirements were met by the equipment, as will be seen in chapters 6 and 7.

Obviously, the development of the algorithm is the central part of this study. The work has been inspired by the work being performed on high resolution radar, where multiple stepped frequency waveforms are synthesized together in order to achieve higher range resolution [46]. The following differences from high resolution radar to PBR are noted:

1. In the PBR case, no control of the transmitted waveforms can be assumed, nor their carrier frequencies. As seen in table 1.1, the spacing of the carrier frequencies of a few powerful Norwegian FM radio and DVB-T transmitters are not regular.

2. In addition to this, the main high range resolution work is not considering coded waveforms for stepped frequency applications, and are transmitting non-modulated continuous waveforms processed in sequence. This work is considering independently broadcasted signals, consisting of an information carrying signal modulated to a carrier frequency. All channels are broadcasted simultaneously, and are processed simultaneously. This means an understanding of the importance of in-channel cross-correlation between the reference and surveillance channels as well as the out-of-channel cross-correlation between reference and surveillance channels, is needed.

3. Finally, by using different broadcasted channels in the correlation process, each of the channels will result in different Doppler shifts from the same target, as each of the channels are using different carrier frequencies. A PBR strategy in order to cope with this is to keep the coherent integration time low, and thus reducing the Doppler resolution, making all shifts end up in the same Doppler cell, [4, 38]. Through the work it will be shown why this to some extent will work. However, [46] suggests a phase correction term for each frequency (band), and it will be shown how this can be extended to the PBR case relying on waveforms of opportunity.

In chapter 5 these issues will be addressed, as well as other details which require attention in order to make the proposed algorithm work. The algorithm's performance and behavior are illustrated by theoretical simulations in order to verify the claims. However, realizing the danger of concluding based on theoretical studies alone, an effort is made on collecting real life target data and analyzing these in order to check the algorithm's consistency with the real world.

The algorithm is also tested systematically on real recorded signals from nearby FM radio and DVB-T broadcasters providing high signal quality. Artificial targets were synthesized, and the algorithm's resolution performance for both waveforms was systematically mapped. Following this, the algorithm's performance in real life by recording and analyzing FM/DVB-T PBR targets of opportunity in order to improve the range resolution, yielding better target positioning, was also mapped. In the DVB-T case, simple HRR analysis of two different targets of opportunity, one airliner and one propeller aircraft is presented.

1.3 Contributions of this study

The work is based on the claim that exploitation of the available (frequency scattered) bandwidth broadcasted from single FM radio and DVB-T transmitter towers may be achieved by coherently combining each of the individual channels/bands, in order to improve on the range resolution. This thesis supports that claim, and it will be shown that higher target range resolution is achieved for both FM radio and DVB-T waveforms of opportunity. In addition to this, for the DVB-T waveform, novel examples of PBR HRR will be presented. One of the goals of this research has been to develop the foundations for an PBR operator zoom function in order to make her/him able to decide whether there are one, two or more targets present in the scene (FM radio and DVB-T), or classify targets (DVB-T).

The major contributions of this thesis may be divided into the following parts: Hardware design and development, algorithm development, simulations, real target data analysis, and finally Non Cooperative Target Recognition (NCTR) and HRR considerations. Each of them are summarized below.

The work started with simple performance predictions for various strong transmitters of opportunity in the southeastern parts of Norway, in particular around Oslo. It was shown that target detections and real life data recording should be possible for ranges of interest to the research. Data recording equipment was designed, produced and made working. It was used to record the full FM radio band, as well as up to four non-adjacent DVB-T channels of choice for both reference and surveillance channel. Normally 10-20 minutes recording time was used, and all datasets were analyzed.

In parallel, the mathematics and implementation of an algorithm for coherently combining the non-adjacent single channels/bands were developed. The performance of the algorithm was supported by theoretical simulations using pseudo random generated signals, as well as simulations using real recorded FM radio and DVB-T signals from nearby strong transmitters. The ability to resolve nearby targets for both waveforms with respect to the single channel case was demonstrated.

Finally, the algorithm's performance was also supported by real data analysis of targets of opportunity for both FM radio and DVB-T PBR. It was shown that the range resolution is improved by using the algorithm to combine the available bandwidth. In the DVB-T case, the research also includes novel analysis of HRR profiles for two different targets of opportunity: An airliner and a propeller aircraft, which is claimed to behave differently enough for an operator to classify them as targets of different type.

1.4 Thesis outline

Chapter 1 has provided an introduction to the thesis, aims of the work as well as contributions of the study.

Chapter 2 is the literature critique which focuses on the publications that are of direct interest to the work of this thesis, i.e. PBR resolution, multi frequency PBR, PBR waveforms, and PBR signal processing.

Chapter 3 presents the basic theory of bistatic radar with respect to the PBR application, and especially be focusing on the theoretical work on bistatic resolution. But also the theory for performance assessments of FM radio and DVB-T based PBR systems are presented. Finally, the most common ways of processing PBR signals is presented.

Chapter 4 starts out by presenting the expected performance for the data recording equipment as well as concluding on potential FMR and DVB-T geometries that should be applicable for the research. Further, the data recording equipment is presented alongside a mapping of noise and interference in the system, as well as recommendations for use.

Chapter 5 derives in detail the proposed signal processing algorithm to be used later on real life signal and target data analysis. In this chapter the discussion is limited to theoretical simulations of the algorithm's performance, while real life target analysis, results, and performances are presented in the next chapters.

Chapter 6 presents the performance analysis of the FM radio waveform in the developed algorithm presented in chapter 5. It shall be seen that the proposed algorithm offers better range resolution capabilities supported by simulations, as well as real life target analysis. All datasets in this chapter have been collected with the hardware described in chapter 4.

Chapter 7 presents the performance analysis of the DVB-T waveform in the developed algorithm presented in chapter 5. Again, the proposed algorithm offers better range resolution capabilities supported by simulations, as well as real life target analysis. All datasets in this chapter have been collected with the hardware described in chapter 4. Finally, novel PBR HRR results from two different targets of opportunity are presented.

Chapter 8 closes the thesis by summing up all the previous chapters that include novel research. This chapter will draw definite conclusions based on these summaries, as well as areas for future work in which future research may be considered.

Chapter 2

Literature Critique

The literature critique will focus on the publications that are of direct interest to the work of this thesis. The books which are included are regarded as the key sources of PBR information, where some of them are relatively new and can be regarded as the results of the last decades open PBR research, with some examples of older declassified work.

The literature critique will focus on the PBR range and Doppler resolution, with an emphasis on range resolution improvement work/techniques. The idea is to exploit higher signal bandwidth in the range correlation processes from multiple bands, meaning any publication on multiband and multiple frequency PBR have been considered. In order to achieve this, any publications on PBR waveform analysis with respect to radar applications, and any work on target long time behavior in the signal processing stage up to and including the range-Doppler surface processing will be considered.

Work on target tracking will be disregarded, as the focus on this research is on improving the resolution prior to the tracking process. The interested reader might have a look at the publications on PBR tracking accuracy by Malanowski and Kulpa [47, 48] as well as [44, 49–59]. These are believed to be among the most substantial published PBR tracking work in the on the subject of PBR tracking on various waveforms.

The work will not include multiband processing techniques like interpolation and/or extrapolation. The actual information available in the different bands is pinpointed without interpolating and/or extrapolating, mainly due to the fact that the signal processing should be applicable within the processing framework already in place today. The proposed algorithm is capable of that. But maybe most important is the fact that the bands are independent in terms of coding and content, as well as highly time varying bandwidth (FM radio). The works on interpolation and/or extrapolation are considering known waveforms behaving predictably across bands [45], which definitely is not the case for PBR systems relying on broadcasters of opportunity.

[23, pp. 250] and [29], reviews the available work with respect to PBR, and claims *"...that there have been few publications describing detailed aspects of system performance such as waveform properties and real geometrical factors and almost nothing on the impact these features may have on the overall system capability."*

This thesis has resulted in a number of publications which are listed in section "Publications". These works will be reported on in depth in this thesis, and thus are not directly treated in the literature critique.

2.1 PBR resolution

N. Willis's [11] book "Bistatic radar" is the renowned known book on the bistatic topic, and the natural source of information for the well established theory regarding bi- and multistatic radar. All aspects of these systems are covered at large in the book. Target resolution is allocated a whole chapter, covering range, Doppler, and azimuth resolution as well as synthetic aperture radar isorange resolution, where the latter is out of the scope for this thesis' research. The former is interesting, and will be treated in more detail in section 3.2, while the focus of Willis is to explain the basic formulas for range resolution for a bistatic system. I.e.

$$\Delta R \approx \frac{c\tau}{2\cos\left(\beta/2\right)\cos\psi}, \tag{2.1}$$

where τ is the radar's (compressed) pulse width, c is the speed of propagation, β is the bistatic angle, and ψ is the aspect angle with respect to the bistatic bisector, [11, pp. 132, figure 7.1]. The discussion on Doppler and angular resolution is on the same level, i.e. basic theory. This book has been the major source of information for several years for anyone working on bistatic radars. However, this thesis research is outside the scope of [11], but for the background theory, [11] will be the major contributor.

M. Skollnik [60] edited the "Radar handbook" which contains a chapter on bistatic radar, written by Willis. The chapter is essentially covered by Willis' own book [11].

H. D. Griffiths and C. J. Baker wrote the paper entitled "Bistatic and Multistatic Radar Sensors for Homeland Security" [28], which was presented at the NATO Advanced Study Institute in 2005. The paper explains the essentials of bistatic radar in terms of the bistatic radar range equation, the problem of direct path signals in PBR systems through the fraction of target reflected signal versus the direct path signal, and an example of the estimated detection range of a PBR system using the Wrotham FM radio transmitter. The monostatic ambiguity function for a FM radio BBC radio 4 transmission is plotted and analysis of this presented, as well as 10 collections of FM radio bandwidth variations of speech waveforms. Further, the bistatic form of the ambiguity function is presented (3.23), and an example of normalized bistatic range resolution to the self ambiguity case as a function of target position for two transmitters and one receiver is presented. In other words, the effect of geometry is illustrated, removing (normalizing) the waveform contribution.

The book edited by N. Willis and H. D. Griffiths entitled "Advances in Bistatic Radar" [22] is a result of the bistatic radar's "third resurgence", which started in the mid 1990s and still is ongoing. The authors of the books aim at updating the declassified bistatic/multistatic radar work/publications that has not previously been published, as well as also reporting on the ongoing research in a few areas, one of those being air surveillance, which is dedicated a whole chapter in the book.

Further, the geometry dependent ambiguity performance is discussed through the ambiguity function for bistatic radar (3.23), as well as in [28]. It is made clear that the ambiguity function for bistatic radar can be divided into two parts: A waveform part, which is most efficiently analyzed through the monostatic ambiguity function (3.22), and a geometrical part, which is accounted for in the bistatic ambiguity function (3.23). A few examples of such, other than the ones shown in [28], are presented.

[22] also discusses the range and geometry components in terms of the maximum range product, $(R_T R_R)_{\max}$ from (3.7), and introduces the bistatic radar benchmark $R_M = \sqrt{R_T R_R}$ as a measure of range performance. However, the geometrical shape of the maximum range contours differ from that of a circle when the baseline is not zero, i.e. the transmitter and receiver are at different locations, and this discussion constitutes the geometrical part of the bistatic range equation.

[22] also highlights another important aspect of the range equation (3.7): the coherent processing time, t_c, which is defined as the inverse of the noise bandwidth of the receiver's predetection filter, B_n. The time available for coherent processing is determined by the target's spread in Doppler, and $\Delta f_d = t_c^{-1} = B_n$. For the monostatic case the Doppler spreading is given as

$$(\Delta f_d)_{mono} = \sqrt{\frac{2a_r}{\lambda}}, \tag{2.2}$$

where a_r is the radial component of target acceleration. This equation also applies to the bistatic case for small bistatic angles β, (3.2). In the case of larger β, e.g. $\beta = 90$ degrees, a rule of thumb is

$$(\Delta f_d)_{bistatic} = \sqrt{\frac{a_r}{\lambda}}, \tag{2.3}$$

and this equation is used to set the coherent processing time t_c and hence the noise bandwidth of the receiver's predetection filter B_n, [22, pp. 126]. In order to process for longer periods than t_c, non-coherent integration of multiple coherent intervals is suggested. Numerical examples show that for small bistatic angles, $1g$ radial acceleration (along the bistatic bisector) and $f = 100MHz$, results in $t_c = 0.39$ sec of coherent integration time (2.2), while the same acceleration for a bistatic system with large bistatic angle might do coherent integration for $t_c = 0.55$ sec, (2.3). Corresponding numbers for the higher frequency $600MHz$, yields $t_c = 0.16$ sec and $t_c = 0.23$ sec, respectively.

Willis and Griffiths present interesting work on multistatic measurement and Geometric Dilution of Precision (GDOP), [22, pp. 152-160]. A simple model for estimating the target location errors of a PBR operating in a multilateration mode with two or more FM broadcast transmitters, where the errors for both bistatic range and bistatic Doppler measurements are developed. The model is perfectly well described, and might be considered an alternative to the traditional range, Doppler and angular resolution presented by Willis [11]. The aim of the model is not to be the most accurate model available, but rather to be a model which provides a good and simple procedure for predicting the relationship of target location errors to system geometry and target trajectory, so that test results (past and future) may be interpreted and extrapolated to other system configurations and targets.

M. Cherniakov's book entitled "Bistatic Radar: Principles and Practice" [42] is also aiming at collecting the research since N. Willis' book "Bistatic Radar" [11]. The book is divided into three parts, where part I is written in a tutorial style, not intended to substitute any other radar book available today. This part highlights the main aspects of monostatic radar and especially the parts which is important with respect to bistatic radar. Part II of the book is dedicated to bistatic radar analysis, mostly covered by Willis, where all the details can be found. The main section of part II discusses the electromagnetic wave analysis claimed not to be presented in a systematic manner before; bistatic wave scattering, radar cross section and signal models. The final part of the book: Part III is on forward scatter radar for air target detection and tracking.

The book does not specifically discuss PBR, the closest it gets is a section on Continuous Wave (CW) radars, which is being divided into unmodulated and modulated waveform radars. The latter restricted to chirped radars and radars using binary phase coded waveforms. In summary, this book is not covering the scope of this thesis' research.

The book by V. S. Chernyak entitled "Fundamentals of Multisite Radar Systems - Multistatic Radars and Multiradar Systems" [61]. Multisite Radar Systems (MSRS) is defined [61, pp. 3] so that it includes both multistatic radars and multiradar/netted radar systems, although it is noted that bistatic radars consisting of spatially separated single transmitter and receiver sites do not belong to the MSRS, due to the lack of fusing information (it is required more than one sensor, and fusing of information from those), several transmitters and one receiver and vice versa fusing measured information would be within the scope of the definition though. The book by V. S. Chernyak is very comprehensive, especially since it covers several parts of MSRS: General characteristics, target Radar Cross Section (RCS), detection and tracking, system coverage and coordinate estimations.

The radar bistatic theory seems to be well covered in the other more specialised books on the topic, [11], [22], [23], [42], and in addition to this V. S. Chernyak has introduced his own notation, which makes the book harder accessible, and thus will not be further referenced.

Three independent recent work report PBR resolution numbers: "Frequency and Waveform Complementarities for Passive Radar Applications" is written by J.M. Ferrier, M. Klein, and S. Allam [26], which states that the bistatic range resolution for the DVB-T system is $40m$. "On the resolution performance of passive radar using DVB-T illuminations" [62] was presented at the International Radar Symposium 2010, and "A Hybrid Multi-Frequency Passive Radar Concept for Medium Range Air Surveillance" [63] was presented at the PCL Focus Day at Fraunhofer May 2011, both written by H. Kuschel, J. Heckenbach, D. O'Hagan, and M. Ummenhofer. The works claim an averaged DVB-T bistatic range resolution of $60m$, and this result is averaged over many geometries for a flight path. The corresponding number for DAB is $158m$. All of the works use the terminology resolution, although they have been tested against single targets in flight trials. Most likely the resolution is the difference between the Global Positioning System (GPS) track and the PBR measured target distance, which would be more a measure of precision rather than resolution. None of the works reports any work on two target separation studies.

2.2 PBR multi frequency

Tasdelen and Köymen published the paper ”Range Resolution Improvement in Passive Coherent Location Radar Systems Using Multiple FM Radio Channels” [64]. The paper is focusing on using multiple FM radio stations to improve the range resolution in FM based PBR systems. Especially discussing 1) the ambiguity function of single and multi channel FM waveforms and 2) the minimum Signal to Noise Ratio (SNR) criterion for detection using one and several radio channels.

The work is based on using adjacent FM radio stations considered to be one band, i.e. in the paper the frequency ranges from $94.7 - 95.6MHz$ and $96.5 - 97.0MHz$ at Bilkent University are considered promising due to the spectral congestion there. Ambiguity functions of single and multi channel FM waveforms are presented, using one, three, and seven channels. The highest bandwidth reported on, is $1.5MHz$, where the channels are not distributed evenly, the distances between them varies from $150kHz$ to $250kHz$. The ambiguity function in the range direction is peaky, with lots of ambiguities, and it is reported that the envelope for multiple radio stations is the cross-correlation function for one radio channel, due to the similarity of each radio station. In the range profile a sinc structure is observed and reported to arise from the periodicity of the correlated signal(s), with the autocorrelation peaks being narrower since the bandwidth of the signal is higher when multiple channels are applied. The sinc structure is deteriorating when the distance between the applied channels are not equidistant, and the sinc sidelobes are increasing.

The paper continues to discuss the minimum required SNR for the ambiguity function to be preserved in the presence of Gaussian and white noise. The simulated autocorrelation function for one and seven channels (equal amplitude, spaced $100kHz$ apart) are presented as a function of SNR of the input signal. The paper concludes that the autocorrelation function's shape is preserved down to $-19.2dB$ for one channel, while the corresponding number is $-26.0dB$ for the seven channels case.

Further, the paper shows how the detection can be performed using several channels. The problem is rewritten to a linear estimation problem, where estimators are available. Further work is outlined to be focusing on the linear estimation problem, and the usage of one channel to detect, and several channels for target accurate localization. Neither of the authors seem to have published any further work on the topic as of January 2011.

This paper represents very interesting work on how to improve the target range correlation by using multiple FM radio channels in the range correlation process. This is the only paper found directly related to the range improvement problem, there seems to be no traces of other work in this area. The theory behind the idea of putting multiple frequencies together, synthetic high-range-resolution, can be found in the literature [46], page 148, equation (4.14) and further described in chapter 5.

The work, [64], is focused on improving target resolution in order to improve target positioning and resolving targets. However, the work seems to be focusing on the autocorrelation function, one channel correlated against itself - normally the reference channel. It is believed that there is no recorded surveillance channel, and therefore no real target data involved. The perfect correlation might also suggest that the channels in question are the same channel repeated in frequency. There are no traces of any further work in this area from any of the authors to be found, or any other authors, except from the published work from this thesis.

The classical ambiguity function (3.22) does not take into account the relative positions of the target, transmitter, and receiver and thus can be considered as the monostatic equivalent of the bistatic ambiguity function (3.23). Cherniakov's book "Bistatic Radar - Emerging Technology" [23] gives examples of ambiguity surfaces based on various signal waveforms: FM radio (speech and music), Global System for Mobile communications (GSM), UHF analogue television signals. For the bistatic ambiguity functions, a few examples of the geometrical importance is illustrated by comparing the classical and the bistatic (multistatic) ambiguity function, making the importance of geometry very clear. One immediate conclusion is that it should be possible to mend the resolution reduction by careful inclusion of multiple transmitter-receiver pairs (receiver being at the same position, transmitters at differenct locations), since two such pairs will not suffer from the same range resolution degradation, potentially making the overall resolution better.

Another aspect, which is briefly mentioned in [23], of combining multiple transmitter-receiver pairs is the independent nature of the transmitted waveforms. This will most likely result in different non-coherent and coherent integration times for the same clutter and target(s). If the transmitters are geographically separated, the geometrical situations for each transmitter-target-receiver triples will be different. In addition to this, the bandwidth of the signals may be time varying, and this may affect the total system. The straightforward approach to this would be to process individual transmitter-receiver pairs, and then add the results of these non-coherently, as is suggested by [23].

Another multi frequency approach was published by Bongioanni, Colone, and Lombardo in the work entitled "Performance Analysis of a Multi-Frequency FM Based Passive Bistatic Radar" [38]. The work evaluates the target detection performance of a multi frequency FM based PBR system. The work is motivated by the recognition that target detection performance largely depends on 1) the instantaneous transmitted waveform, and 2) the instantaneous characteristics of the propagation for the considered channel. Two versions of data recording equipment is used: one version with direct sampling, and one version with analog down mixing and sampling at Intermediate Frequency (IF). Of the two systems, the direct sampling system is considered to perform slightly better, although the results roughly are similar. Each system records reference and surveillance channel, direct path cancellation is performed before cross-correlation, and finally Constant False Alarm Rate (CFAR) thresholding is applied. As in [36,37], it is demonstrated that target detection is different for different frequencies.

An interesting aspect which is treated in [38, pp. 473] is the variation of integration times as a function of frequency, in order to achieve the same velocity resolution from each exploited FM radio channel. The requirement for the same velocity resolution arises from the wish to do non-coherent integration of multiple range-Doppler surfaces. The integration time T_i for the ith channel out of the N channels is then

$$\Delta T_i = \frac{c}{\Delta v f_i} \qquad \text{for } i = 1, 2, \ldots, N, \tag{2.4}$$

where c is the speed of propagation in m/s, f_i is the carrier frequency of the ith channel in Hz, and Δv is the required velocity resolution in m/s. The time-bandwidth product, $B\tau$, over the frequency span in question, $89.8MHz$ to $94.3MHz$, for a bandwidth of $B = 100kHz$, and the coherent integration times as a function of frequency resulting from (2.4) yields a $0.2dB$ loss, and consequently can be disregarded. The formula and ideas were in the paper, but the latter analysis was not.

The paper concludes that using multiple frequencies for target detection increases the detection performance. However, how to implement such a solution, in terms of algorithms etc. is not presented. I.e. it is claimed that three frequencies yields the best results, while four frequencies do not improve performance due to the fourth channel having poor waveform characteristics during time of integration. It is then suggested to use only radio channels with good waveform characteristics, not how to, and which criteria that might be used to select the best channels, and the implementation/algorithm issues that will arise from such a solution.

The results are discussed as a function of three range intervals, and four elevation spans, and the performances for all cases are summarized in a table, too comprehensive to go into detail. The detection results are compared in the range-Doppler domain to tracks from live air traffic control, and most targets seem to be detected. The focus of this paper is solely on using multiple frequencies for target detection improvement, and is out of the scope of this thesis. However, the idea of multi frequency target tracking fits nicely with the exploitation of multiple frequencies for improved target localization.

The papers by D. W. O'Hagan, F. Colone, C. J. Baker and H. D. Griffiths entitled "Passive Bistatic Radar (PBR) demonstrator" [37] and D. W. O'Hagan and C. J. Baker entitled "Passive Bistatic Radar (PBR) using FM radio illuminators of opportunity" [36] analyse the merits of FM radio broadcast transmissions for use as radar signals. Both papers demonstrate the effect of using multiple frequencies in a PBR based FM radio system, giving examples of detections of large passenger aircrafts over central/greater London for two different geometries, each for two different simultaneous recorded frequencies (actually the whole FM radio band is recorded). The former paper shows only range-Doppler surfaces of the targets, while the latter specifically shows the difference of detection of the same target for the two frequencies at a processing instant.

The focus of this work is on verifying (missing) target detections in an experimental PBR system. However, no further analyzing of detections as a function of (multiple) frequencies are to be found. There are no traces of any work on trying to combine multiple bands in order to improve the detection performance.

The paper written by P. Lombardo, F. Colone, C. Bongioanni, A. Lauri, and T. Bucciarelli entitled "PBR activity at INFOCOM: adaptive processing techniques and experimental results" [39] is a parallel paper to [38]. It deals with the direct path cancellation algorithm to be used with PBR multiple frequency target detection. However, most of the information contained in this paper on the multiple frequency target detection, is available in [38], however the range-Doppler target detection plots of this paper seems to be slightly more in accordance with the ground truth data from the live air traffic control.

Baker and Griffiths [28] analyze the case where a number of nodes are spatially distributed, M receivers receiving all the target scattered signal from the N transmitters, and thus making this a bistatic netted radar, each receiver coherently processing the received signals, and joining them incoherently in a central processing unit. Examples of range and Doppler resolution are shown for rectangular transmitted pulses, how the resolution might be degraded and how to cope with it by using/adding transmitters in different locations. The special case of PBR, one receiver and multiple transmitters is mentioned explicitly since the authors believe that for this system it will not be possible to process multiple transmitters coherently. However, the geometrical and frequency diversity is considered to be of high interest since it might be exploited to advance. The paper does not go into detail about PBR systems or the processing of such signals, other than pointing out the potential of multiple perspective looks on targets, especially for target classification.

The entitled paper "FM and DAB Experimental Passive Radar System: Concept and Measurement Results" is written by M. Edrich, F. Wolschendorf, A. Schröder [41] is aiming at presenting an experimental PAssive RAdar DEmonstrator (PARADE)[1] exploiting both FM radio and DAB transmitters of opportunity, as well as showing results from measurement campaigns with cooperative and non-cooperative targets.

PARADE might be considered as two subsystems, one FM and one DAB based PBR system. Each of the subsystems is equipped with an antenna consisting of 8 ground plane antennas, arranged in two elevation levels of 4 antennas each. This allows for azimuth as well as elevation bearing detection.

For the trials, the FM sensor exploited one transmitter WDR3 in Bonn, at $93.1MHz$, and the target (reported as medium aircraft) was in the FM sensor detected reliably out to $40km$, with a range accuracy of $400m$, and Doppler accuracy of $3Hz$. The DAB sensor exploited 9 illuminators of the DAB single frequency network at $229.072MHz$ in the Cologne area. In the DAB system, the same target is reported to be regularly detected within a $30km$ bistatic range area, although no resolution accuracies are reported.

In the paper, a bistatic two way propagation model is used to investigate the received signal level at the receiver as a function of geometry. In addition to the traditional transmitter-target-receiver path, two additional paths are added: transmitter-ground-target, and target-ground-receiver. Analyzing the received signal level for these, the reported FM based PBR system's systematic misdetections during the trials are believed to be explained.

The FM based results from the trials are reported in time plots versus range, and time versus level (dB), and time versus azimuth. The DAB results are shown overlaid on a map with an indication on whether the detections are based on more than three illuminators

---

[1] Not to be confused with the Polish PaRaDe - Passive Radar Demonstrator, developed at Warsaw University of Technology by K. Kulpa and M. Malanowski

or less than three illuminators, or no detections at all. This makes it impossible to extract anything on the potential of using multiple bands, and the authors are not reporting any work on fusing data from the different bands, or utilising the multiple bands in any way other than indicating that the motivation is to improve the overall target detection.

Poullin published the paper entitled "Passive detection using digital broadcasters (DAB, DVB) with COFDM modulation" [65] where he presents the Orthogonal Frequency Division Multiplex (OFDM) modulation used in DAB and DVB-T transmissions, before he moves on to the adaptive filter analysis, and finally demonstrates target detection after adaptive filtering for DAB. The paper mainly focuses on the performance of an adaptive filter for the class of OFDM signals, here DAB and DVB-T, but makes no efforts in combining these two types of signals, or in any other way using multiple frequencies. This work will not be studying the adaptive filtering problem. However, for the interested reader a good starting point for the Direct Signal Interference (DSI) algorithm, which exist in many versions, is [35].

Gould, Pollard, Sarno, and Tittensor presented "Developments to a Multiband Passive Radar Demonstrator System" [40] where a multiband PBR demonstrator, exploiting DAB and DVB-T signals is described, and range-Doppler plots from the cross ambiguity function simulated performance relying on DVB-T ($570 MHz$) is analyzed. The first detection results of the system (from a NATO trial, November 2006 in the Hauge, in the Netherlands, under the NATO SET 108 RTG), is presented (DVB-T at two frequencies: $490 MHz$ and $570 MHz$) in physically separated plots. It is mentioned that the analyses is ongoing, and no results of these are presented.

The focus of this work seems to be on improving the target detection by using multiple bands also from different transmitter systems, in this case the DAB and DVB-T, although there is no traces of reported DAB data in the paper, even though the system is claimed to have been exploiting DAB signals at $227.36 MHz$, in addition to the two DVB-T frequencies. There are no traces of effort put into fusing the two reported DVB-T bands in any way.

"Frequency and Waveform Complementarities for Passive Radar Applications" is written by J.M. Ferrier, M. Klein, and S. Allam [26]. The paper is aiming at demonstrating improved passive radar detection through simultaneous use of ... *heterogeneous transmitters of opportunity*. In the paper that means FM radio in the $88 - 108 MHz$ band, and the DVB-T in the $470 - 860 MHz$ band.

The paper describes the two systems in question, Thales Home Alerter 100 (HA100), and the Thales sensor NECTAR, both systems developed with support from ONERA. The HA100 are using up to 8 FM transmitters for detection and tracking, while the NECTAR system is using only one DVB-T channel. The HA100 antenna is a circular array of 8 dipoles resulting in an azimuthal coverage of 360 degrees, while the NECTAR system antenna is a linear array of 4 dipoles resulting in an azimuthal coverage of 120 degrees. The HA100 is providing the air picture live - in real time, while the signal and data processing of NECTAR is performed off line.

Thales is providing some of the characteristics of the two systems. Among other parameters, the bistatic range resolution of HA100 is claimed to be $3-30km$, depending on the signal bandwidth, which is varying between $100kHz-10kHz$, respectively. In contrast, the NECTAR system's corresponding values are stationary, due to the random and noisy behaving DVB-T signal (Pseudo Random Binary Sequence (PRBS) coded OFDM of constant bandwidth), providing the bistatic range resolution of $40m$, for a signal bandwidth of $7.6MHz$. It is also interesting to note that the bistatic Doppler resolutions for both the systems are reported to be $5m/s$.

The paper is reporting on results from a dedicated trial that was conducted at the Thales site at Limours, 30km outside of Paris. The Eiffel tower, which is broadcasting FM radio at $105.9MHz$, and DVB-T at $498MHz$ was used for the tests in order to get the same geometry, which would simplify the comparison of performance for the HA100 and NECTAR. The baseline in the experiment was $30km$. The bistatic detections from both systems are compared to the ground truth data from the cooperative target, and the overall results show that the HA100 detected the target for 51% of the time, while NECTAR's performance was 47%. The bistatic range accuracy was for HA100 $275m$, compared to the $17m$ for the DVB-T system. However, the bistatic velocity accuracy for the FM system is better than for the DVB-T system, $1.2m/s$ compared to $2.5m/s$, while the corresponding azimuthal accuracies are 3.7 degrees and 2.9 degrees, respectively.

Although the detection performance for both systems are around 50%, combining them, by using a basic logical OR-functionality, yields a target detection figure of roughly 75%, due to the fact that the systems are not detecting the target at the same times. The performance as a function of time shows that the detections are distributed differently in time for the two systems, resulting in the high detection improvement for the common (logically OR) system. The authors point at two main reasons for the difference in detections, keeping in mind that the geometry is close to identical for the two systems: First, it is claimed that the frequency diversity yields differences in multipath, and second the target's RCS will also be varying with frequency, especially since the two frequencies exploited in this trial are (very) different, $105.9MHz$ and $498MHz$.

Another gain in using these two systems together is the localization issue. The authors claim that the DVB-T waveform improves the FM accuracy, while the FM detections help solve the DVB-T single frequency ghosting problem. However, it should be noted, in order to do this efficiently, both systems should see the target simultaneously.

The paper gives interesting results from fusing multiple bands in order to gain detection performances, and it is indicated, though not demonstrated that the DVB-T system is improving the target localization process, and the FM radio system is helping resolving target ghosting problems in the single frequency networks of DVB-T. However there are no traces of work focusing on using multiple frequencies within the different bands to aid such a process.

"A Hybrid Multi-Frequency Passive Radar Concept for Medium Range Air Surveillance" [63] written by H. Kuschel, J. Heckenbach, D. O'Hagan, and M. Ummenhofer was presented at the PCL Focus Day at Fraunhofer May 2011. The work reports on efforts on combining the long range detection and high level tracking of FM based PBR, while the medium and short range detection and tracking as well as accuracy is taken care of by the DAB/DVB-T systems. No work on coherently combining the bands were reported, however some thoughts on how to scale the frequencies of the different bands were presented.

”High range resolution DVB-T Passive Radar” [66] was presented at the 2010 European Radar Conference, while ”High Resolution and Artifact Cancellation in Wideband DVB-T Passive Radar” [67] was presented at the PCL Focus Day at Fraunhofer in May 2011. Both works are written by M. Conti, D. Petri, A. Capria, F. Berizzi, and M. Martorella from University of Pisa. The presented works are partly supported by the work in this thesis, as Norwegian Defence Research Establishment (FFI) and the undersigned have provided real life data for parts of the studies at University of Pisa. The work is in its starting phase, and for the moment been focusing on the combining of adjacent channels as well as artifact cancellation.

2.3 PBR waveforms

Cherniakov's book entitled ”Bistatic Radar: Emerging Technology” [23] is the logical continuation of ”Bistatic Radar: Principles and Practice” [42]. The book is an attempt to gather the current intense and ongoing research concerning bistatic radar. There are two main areas which are discussed: Bistatic SAR (BSAR) and PBR System. In the PBR System section there are especially two chapters which is of interest to this research, entitled ”Passive Bistatic Radar Systems”, written by Howland, Griffiths, and Baker, and ”Ambiguity Function Correction in Passive Radar: DVB-T Signal”, written by Cherniakov himself.

The sensitivity and coverage analysis for PBR systems provide a thorough walk through of all the aspects of PBR one needs to take into account[2] when designing such a system, accompanied with numerical examples taken from FM radio, cell phone base stations and DAB radio. The work is descriptive in nature, and it would have been nice to see some sort of PBR version of the Blake chart, especially since all the ground work seems to be in there. Important observations such as the relatively high noise figure (up to $25dB$ is reported!), the integration gain as a function of coherent integration time and effective bandwidth is treated, and finally sensitivity analyses for the estimation of the probable target range detection is highlighted with what is believed to be realistic figures, i.e. one second coherent integration time, target RCS of $1m^2$, and omni-directional antennas. Under these assumptions detection ranges up to a few tens of kms are reported.

Chapter 8 of [23] is a supplementary version of the paper entitled ”DTV signal ambiguity function analysis for radar application”, written by Saini and Cherniakov [32]. However, no new essential information is made available in [32], and the following discussion applies to both.

The DVB-T signal structure is briefly presented and the COFDM signal's ambiguity

---

[2] I.e. the bistatic radar equation, the bistatic RCS, the receiver noise figure, the effective bandwidth and integration gain, and DSI. The list is not exhaustive.

function behavior, which is cluttered with ambiguities, is discussed. The range ambiguity resulting from the guard interval, which is generated by inserting the end of the transmitted symbol ahead of the same symbol, is removed by blanking the guard interval in the reference signal channel before the range correlation process. However, this results in new ambiguity sidelobes at Doppler frequencies of $4kHz$, which is dealt with by processing the ambiguity function in two stages based on the range of interest: intrasymbol (within the symbol range T_S, for $t < T_S$) and intersymbol (outside symbol range for $t > T_S$) ambiguities.

The DVB-T COFDM signal comprises 5 different types of carriers: Inactive, payload, continual pilots, scattered pilots and Transport Parameter Signaling (TPS) carriers. The inactive carriers are set to zero amplitude, i.e. the carriers at the top and bottom of the channel edge. The payload carriers generates no ambiguities due to their random behavior (Moving Picture Experts Group (MPEG) and PRBS) coding, while the TPS carriers can be shown to generate no ambiguities [23, pp. 322]. The continual and scattered pilots are transmitted at boosted power levels, resulting in intrasymbol ambiguities, which are removed by an equalization procedure where the continual and scattered pilots are filtered by a factor 3/4. The intersymbol peaks arise from the repetition of pilot carriers, and they are removed by a filtering process which removes all the pilot carriers. These two processes are contradictory, and have effects on different parts of the ambiguity function, and thus are used to generate different parts of the ambiguity surface through a parallel process as described in both [23] and [32].

The two references [23, 32] are the only two references found really considering and analyzing the DVB-T waveform and its implications on the ambiguity function. This might be due to the completeness of the work, which explains why the ambiguities appear, and how to cope with them.

[22, 31] discusses radio frequency interference, especially in the FM radio band, where the interference is high. This is mainly caused by the density of radio stations, and the fact that a typical FM radio signal $-3dB$ peak width may be around $50kHz$, but around $45dB$ lower, the same signal may span $200 - 300kHz$, which causes severe interference in adjacent channels, and thus effectively is limiting the passive radar performance in this (those) channel(s). It is reported [22, pp. 119], through private communication, that direct signal interference cancellation schemes could be made effective to levels $20 - 30dB$ above the receiver thermal noise level.

[22] is investigating a variety of waveforms and their interferences by looking at the monostatic ambiguity function of off-air FM radio, analogue TV, GSM mobile phone, DAB radio, Digital Radio Mondiale (DRM), and DVB-T signals. It is further concluded that analogue waveforms are transmitted at higher power (FM radio - $P_tG_t \approx 250kW$, and analogue TV - $P_tG_t \approx 1MW$,), than the digital waveforms (DAB - $P_tG_t \approx 10kW$, digital TV (UK) - $P_tG_t \approx 8kW$, cell phone base stations - $P_tG_t \approx 100W$). The exception is the High Frequency (HF) DRM, which has a typical $P_tG_t \approx 50MW$! This favors the analogue waveforms in terms of air surveillance applications. However, their waveforms are not as suitable for high resolution radar applications as the digital waveforms are (DAB, DVB-T,

mobile phones). The digital waveform's ambiguity function is more stable with time, in addition to the peak of the being narrower, and the side lobes are lower.

Baker, Griffiths and Papoutsis published the paper entitled "Passive coherent location radar systems. Part 2: Waveform properties" [30]. This paper focuses on the autocorrelation or self-ambiguity function for FM radio, GSM 1800 mobile phone, and UHF analogue television signals. Both the monostatic (3.22) and the bistatic ambiguity function (3.23) are considered, and it is shown how the waveform and its bandwidth is affecting the target peak in the monostatic ambiguity function. Further, the importance of geometry is illustrated through examples of the ambiguity function for three target positions with respect to the stationary transmitter and receiver. Normalized plots of range and Doppler resolution is shown, where it is demonstrated that the problems of poor resolution in range and Doppler due to geometry might be mitigated through careful consideration of adding more transmitter-receiver pairs.

The problem with the time varying bandwidth, and thus system performance as well, is suggested solved by using multiple transmitters, which in turn might mean multiple frequency bands. However, no work in this direction is in the paper.

Lauri, Colone, Cardinali, Bongioanni, and Lombardo wrote the paper entitled "Analysis and Emulation of FM Radio Signals for Passive Radar", [33]. This paper is the only paper found which takes a closer look at the FM radio modulation, and the importance of the modulating signal. A simple model for the FM radio modulation has been developed, and controlled inputs are being frequency modulated in order to generate FM radio waveforms of choice. Especially the behavior of the range resolution, the self ambiguity surface, as a function of the amplitude statistics is studied. A simple two path propagation model is applied to simulate a propagation channel in order to link the simulations to real datasets, and this seems to be successful, although it is commented that not all effects can be simulated considering a channel with only two rays. Finally, the paper wraps it up by very briefly explaining an algorithm for automatic silence detection.

The FM radio emulator is programmed in accordance with the International Telecommunication Union (ITU) transmission standards [16], and will not be further explained here. In order to measure the self ambiguity, three measures are provided. 1) The range resolution is defined as the $-3dB$ width of the main lobe of the self ambiguity function in the plane at zero Doppler shift, and 2) the Peak to SideLobe Ratio (PSLR) is defined as

$$PSLR \overset{\text{def}}{=} \frac{1}{A_0^2} \max\{A_n^2\} \qquad \text{for all } n \neq 0, \tag{2.5}$$

where A_0 is the main peak in the ambiguity function, and A_n is the amplitude of the nth sidelobe, and finally, 3) the Integrated SideLobe Ratio (ISLR) is defined as

$$ISLR \overset{\text{def}}{=} \frac{1}{A_0^2} \sum_{n=1}^{N} A_n^2. \tag{2.6}$$

First, the range resolution is compared to the standard deviation of the modulated signal's amplitude, and for the emulated datasets, the performance match the expected values.

However for the real datasets, the behavior is slightly different, but there is a relatively high match, over 50%. The measures PSLR and ISLR are then matched against the modulating signal's content, music or voice, but no significant difference between program content and range performance is found. Music and voice might yield good range resolution or they might not yield good range resolution, no conclusion is drawn there. However, it is concluded that silence leads to very bad range resolution, due to the low bandwidth. Therefore, an automatic silence detection algorithm is presented. Silence is defined as the absence of audio signal or the absence of transmissions at all. In order to detect these situations, a fixed parameter threshold is applied with respect to the modulating signal's standard deviation. For the cases studied, a threshold of $-23dB$ is considered as the border between silence $> -23dB$, and non-silence $< -23dB$, and this seems to work well for the situations that were studied.

In summary, it is concluded that the range resolution can be predicted by means of especially the standard deviation of the modulated signal, and that a simple two ray model can be applied to explain the difference between emulated data and real data, however it is not completely clear from the paper how this is proved. In order to detect silence or absence of audio, a simple threshold applied to the modulating signal's standard deviation is applied.

2.4 PBR signal processing

Howland, Griffiths, and Baker are in the book ”Bistatic Radar: Emerging Technology” [23] discussing various ways of processing PBR signals. The narrowband [23, pp. 260-268] and wideband [23, pp. 268-273] processing is presented. Narrowband processing is defined as the process of locating the target from measurements of Doppler and bearing, reflecting the situation of a signal transmitter of low bandwidth, or the case where only parts of the transmitted signal is usable for target location. E.g. the amplitude modulated carrier of analogue television. Wideband processing uses the full bandwidth of the transmitted signal and applies a conventional matched filter approach to the detection problem, measuring bistatic range (bistatic time delay) and bistatic Doppler of the target returns. Both of the processing methods are presented in a descriptive manner, and not mathematically treated.

Howland, Maksimiuk and Reitsma's [44] paper ”FM radio based bistatic radar” presents an experimental bistatic radar system developed at NC3A in The Netherlands. The system is exploiting one FM radio transmitter (in the paper 96.8MHz is used), positioned in an over-the-shoulder geometry, which means that the transmitter is illuminating the surveillance area from behind the (directional) receiver antenna's surveillance sector. (The NC3A system surveys a sector approximately 120° in azimuth). The receiver antenna consists of two vertically polarized half-wave dipoles over a wire-mesh backplane of 1.5 wavelengths by 1.5 wavelengths. The system concept and limitations on performance are described, followed by details on the processing used to implement the system. The processing consists of DSI suppression and range-Doppler estimation algorithms, a CFAR process, a bearing process, and finally tracking. Two ways of computing the range-Doppler surface is described, one brute force, and one efficient algorithm, which will elaborated on in section 3.5.

The paper contains interesting performance predictions, which are verified by a working PBR system. In a future extension of the system multiple transmitters and frequencies will be incorporated, but status in 2005, says a single frequency system. No further extension of this work has been reported on in the open literature.

Wehner's book "High-Resolution Radar" [46] seems to be the major source of information on high resolution radar, as well as the recent book by Jankiraman "Design of Multi-Frequency CW Radars" [68]. These books are not mentioning anything of bistatic radar, nor PBR. But the books contain the theory for high-range-resolution techniques, and especially synthetic HRR radar, which are techniques this work will try to apply to the PBR. This is very well explained in the books, and there is no reason for elaborating on this here. However, a few differences from the PBR point of view should be noted. This research should be considered an extension of the work on continuous discrete frequency coding techniques [46, pp. 142-149], and [46, pp. 197-220], in order to make it applicable for PBR systems. Jankiraman, [68, pp. 187] presents the theory of multi frequency radar in terms of linear frequency modulated waveforms, and claims that the theory can be readily applied to stepped frequency waveforms also. However, the latter is not performed, and thus the following differences apply:

In the PBR case, no control of the transmitted waveforms can be expected, nor the spacing of different frequency channels, nor the carrier frequency of those. As seen in table 1.1, the spacing of the carrier frequencies of a few powerful Norwegian FM radio and DVB-T transmitters are not regular.

In addition to this, the work in [46,68] is not considering coded waveforms for stepped frequency applications in order to keep the receiver bandwidth low, and are thus transmitting non-modulated continuous waveforms processed in sequence. In this thesis, independently broadcasted signals, consisting of an information carrying signal modulated to a carrier frequency, are considered. All channels are broadcasted simultaneously, and are processed simultaneously. This means an understanding of the importance of in-channel cross-correlation between the reference and surveillance channels as well as the out-of-channel cross-correlation between reference and surveillance channels, is needed.

Finally, by using different broadcasted channels in the correlation process, each of the channels will result in different Doppler shifts from the same targets, as each of the channels are using different carrier frequencies, and examples of this is seen in table 5.1. A common strategy in order to cope with this is to keep the coherent integration time low, and thus reducing the Doppler resolution, making all shifts end up in the same Doppler cell, [4,38]. However, [46] suggests a phase correction term for each frequency (band), and it will be shown how this can be extended to the PBR case where waveforms of opportunity are exploited.

One of the fundamental problems of PBR imaging as of today is the relatively poor range resolution, FM radio PBR $3 - 30km$ and DVB-T PBR systems around $40m$ [26].

This might be mitigated by using multiple bands and/or frequencies in order to improve the bandwidth of the range correlation in the signal processing. The Doppler resolution (FM PBR $1 - 2Hz$, DVB-T PBR $5 - 10Hz$) seems to be available, and improving on the processing time will further improve the resolution. For the DVB-T system improving the range resolution and increasing the coherent integration time might make target run through resolution cells during integration.

Bistatic imaging radar has been widely reported on, e.g. [69–72], while PBR imaging has only been mentioned in a few of the major PBR publications, [23, pp. 287], [30]. The nature of PBR systems, with many transmitter-receiver pairs, makes this a geometrical interesting approach. [23] suggests ISAR imaging using multiple images from multiple geometries. For example, a PBR system consisting of two orthogonal baselines imaging a target making trajectories of 45° to the baselines would enable two close to orthogonal image projection planes to be generated and hence high-resolution two-dimensional imagery could be produced.

Recent work, 2010 [73], claims to have imaged a target using six adjacent digital TV channels of opportunity, resulting in a bandwidth of $36MHz$, giving a range resolution of $5m$ at a bistatic angle of 68 degrees. The data is range migration compensated, and an image is formed by integrating five seconds of data. It is concluded that "...moderate resolution ISAR imaging is feasible ...". However, in the resulting image it is hard to interpret individual scatterers. This work is supported by recent results, 2010/11, reported from University of Pisa in [66, 67], which claim that PBR ISAR imaging is possible, although high range as well as long integration times are to be applied. The work of Pisa University has been supported by the research under this thesis by providing DVB-T data from for targets.

The most comprehensive PBR target imaging work found to date seems to be "Wide-angle radar imaging using time-frequency distributions" of Lanterman, Munson, and Wu [74] on back-propagation techniques using different look angles to generate high-resolution imagery. This work is considering the wide-angle formulation of ISAR imaging using simulations, and show impressive results supported by other work, [75–78]. The work in this thesis will not consider wide angle imaging, however since the simplest form of ISAR imaging can be achieved by Doppler processing of high range resolution profiles, the research of this thesis has briefly mapped the potential.

No publications other than [73] reports of real target data PBR imaging. Some work is found on ship imaging using terrestrial transmitters as well as satellite transmitters of opportunity, [79], and a work on RCS calculations in support of passive bistatic ISAR [80].

No work reporting on PBR HRR was found, but under the umbrella of PBR NCTR theoretical work on automatic target classifiers was found [50, 81].

However, at the start of this work, none of the above publications had considered the potential of improved range resolution in order to make PBR HRR, nor PBR imaging based on HRR profiles. When finishing this thesis, work which are in line with the results of this thesis started to emerge [66, 67, 73]. While these publications are limited to adjacent channels of digital TV transmissions of opportunity, they all support the findings of this thesis.

2.5 Summary

This survey has shown that there have been major book and paper publications within the field of bistatic radar, and in particular that they have treated PBR in such a comprehensive way. The research has made great progress since the release of N. Willis' "Bistaic Radar" [11].

The work described in this thesis will consider in greater detail how to utilize multiple frequencies from the same geographical located transmitter. The FM radio system separates individual radio stations from each other in frequency, and this applies to broadcasted radio stations from the same transmitter as well as for broadcasted radio stations in the same geographical region (multiple transmitters). In order to avoid interference, there is no reuse of a frequency within an area, since the FM radio relies on single transmitter reception, and multiple transmitter reception will cause problems for the receiver. A DVB-T signal channel, in Norway a channel ranging from $21-60$, i.e. $470-790MHz$, contains multiple TV channels, and each transmitter normally broadcasts several of these signal channels separated in frequency, which makes the situation for both systems comparable. The work in this thesis is considering one transmitter which is broadcasting multiple FM radio stations/signal channels in frequency, and thus the same transmitter-target-receiver geometry for each radio/signal channel is obtained. It will also be the same waveform, since fusion of FM radio and DVB-T signals, is not considered. However, since the signals of interest are separated in frequency, they will have different target Doppler shifts for the same target(s). This calls for information on PBR range resolution, multi frequency, waveforms, and signal processing. During the literature search, no work really considering this in depth was found, except one paper on the topic using multiple bands for the FM radio case [64].

The focus of this literature critique has been on PBRs exploiting FM radio and DVB-T broadcast transmitters, and much work has been put into analyzing the ambiguity function of these (and other) signals. However, very little publications on the two waveform's properties with respect to radar applications beyond the ambiguity function, was found. Only one paper [33], which made an effort to gain deeper insight into the FM radio waveform, was found. However, there still are uncertainties regarding the FM radio waveform and its impact on passive radar. For the DVB-T waveform the situation is more understandable, since the DVB-T signal is well described in the DVB-T specifications [12], as well as the fact that the signal is constructed to be deterministic in its behavior, meaning not directly dependent on the transmitted program content. The work presented in [23, 32] on the removal of DVB-T ambiguities in the ambiguity function is very complete, and thus there is no real need for deeper research into that area.

Several of the papers considered the ambiguity functions, both the monostatic and the bistatic version, the latter which takes into account the geometry of the PBR in addition to the waveform's properties. The framework for understanding the waveform's impact on the monostatic ambiguity function is well understood, and the recent work on the importance of geometry in PBR is well treated by the bistatic ambiguity function, and the formalism introduced in the work considered here.

Much work and several experimental systems are emerging on the combination of FM radio and DAB/DVB-T. A few of the considered papers were on utilising multiple bands within FM radio and DAB/DVB-T in order to improve detection, but only one that really had performed a complete work [38]. Only one paper dealing with the combination of multiple FM radio stations in order to achieve better range resolution was found [64]. However this work was not conclusive and lacked the combination of reference and surveillance channels and no further work has been found anywhere. No work on combining multiple non-adjacent DVB-T bands in order to gain higher range resolution has been found.

HRR is not mentioned in any of the considered PBR publications, however the theory of HRR radar is readily understood form an active radar system's point of view, but not from the PBR perspective. A few papers were found on PBR NCTR, while considerable simulation work has been performed on theoretical wide angle PBR ISAR.

By finishing this thesis, one publication [73] from 2010 showed real target results of high range compensated HRR PBR ISAR by using adjacent digital TV channels in the range correlation as well as long integration times. Recent work, 2010/11 [66, 67], supported those results on adjacent channels PBR ISAR imaging, while all publications [66, 67, 73] supports the findings of this thesis.

In summary, no comprehensive and conclusive work has been found on range resolution improvement using wider correlation bandwidths by combining multiple non-adjacent broadcasted bands coherently while maintaining the Doppler resolution of the relatively long integration time. And very little work has been focusing on characterizing the FM/DAB/DVB-T radio's waveform behavior in radar applications beyond their ambiguity functions. While writing up, interesting results supporting the findings of this thesis were published [66, 67, 73].

Chapter 3

PBR Fundamentals

This chapter will present the basic theory of bistatic radar with respect to the PBR application, and especially be focusing on the theoretical work on bistatic resolution, but also the basics for performance assessments of PBR systems for FM radio and DVB-T. Finally, the chapter will present common ways of processing PBR signals.

The theory will mainly be based on the contents of Willis book ”Bistatic Radar” [11], and the recent publication by Willis and Griffiths ”Advances in Bistatic Radar” [22], which can be considered an update of [11].

3.1 Basics

The basic definitions of radar, bistatic radar, geometry, and bandwidth are presented in the following section.

3.1.1 Definitions

In this work, unless otherwise is stated, a radar is defined according to the IEEE definition [82]:

Definition 3.1 (Radar)**.** *An electromagnetic system for the detection and location of objects that operates by transmitting electromagnetic signals, receiving echoes from objects (targets), within its volume of coverage, and extracting location and other information from the echo signal.*

There are two notes to this definition: 1) Radar is an acronym for radio detection and ranging, and 2) Radar equipment can be operated with the transmitter turned off, as a passive direction finder on sources radiating within the band of the receiving system [82].

In 1990 Willis wrote the Bistatic Radar chapter in Skolnik's Radar Handbook [60]. Willis defined a bistatic radar to be a radar that employs two sites, transmit and receive, which are separated by a considerable distance, a statement he never clarified, even though he mentioned two examples to clarify it: 1) A radar using different transmit and receive antennas at a single site should be considered monostatic. 2) An over-the-horizon (OTH) radar's transmitter and receiver could be separated by 100 km or more, and still be considered monostatic when the target location is thousands of kilometers.

In Bistatic Radar [11] Willis uses the IEEE bistatic radar definition: Bistatic radar is defined as a radar that uses antennas at different locations for transmission and reception. Willis points out that the IEEE definition does not specify how far the transmitting and receiving sites must be separated. Attempts to quantify this separation has been made, both by Skolnik [60] and Blake [83, 84].

Willis writes that Skolnik (1990) [60] defined the separation as ”a considerable distance”, while he earlier [85] considered considerable distance as ”comparable with the target distance,” a definition which principally applies to forward-scatter fences. Willis also claims that Skolnik in the same paper defined the separation such that ”. . . the echo signal does not travel over the same [total] path as the transmitted signal”.

Blake [83, 84] defines two conditions for separation of transmitter and receiver by demanding *either*

> the *directions* of the transmitter and receiver [from the target] differ by an angle that is comparable to or greater than either beamwidth

or

> . . . the *distances* from the target to the transmitter [R_T] and receiver [R_R] differ by an amount that is a significant fraction of either distance.

These definitions apply to all bistatic configurations, including forward-scatter fences, but they do not provide a measurable quantity, due to the terms ”comparable” and ”significant fraction”. The Radar Technology Encyclopedia [86] by Barton and Leonov uses the definition of Willis:

> A bistatic radar, by definition, is one in which the transmitter and receiver sites are separated by a significant distance.

This work defines bistatic radar according to the IEEE [82]:

Definition 3.2 (Bistatic radar)**.** *A radar using antennas for transmission and reception at sufficiently different locations that the angles or ranges from those locations to the target are significantly different.*

Willis [11] defines a radar multistatic when ”. . . two or more receiving sites with common (or overlapping) spatial coverage are employed, and data from targets in the common coverage area are combined at a central location”. The Radar Technology Encyclopedia [86] defines multistatic radar as a radar in which information on a target is obtained by means of simultaneous processing of signals of several spatially separated transmitting, receiving or transceiving positions. In this work, unless otherwise stated, a multistatic radar is defined according to IEEE [82]:

Definition 3.3 (Multistatic radar)**.** *A radar system having two or more transmitting or receiving antennas with all antennas separated by large distances when compared to the antenna sizes.*

And finally, the Radar Technology Encyclopedia [86] defines the radar resolution as

Definition 3.4 (Radar resolution)**.** *In radar, resolution is the ability to separate the signals from adjacent sources. The ability to distinguish one target from another is defined by a four-coordinate radar response, so angular, range, and Doppler resolutions typically are distinguished. The common measure to consider two targets to be resolved in a particular dimension is when they are separated by a distance equal or more than half-power width of the radar response in this dimension: angle, range (time), or velocity (Doppler frequency).*

Many definitions on signal bandwidth are available, it might seem as if every application has its own definition of signal and/or system bandwidth. Unless otherwise stated this work will use the $-3dB$ bandwidth, which is well known within the radar communities, and it is illustrated in figure 3.1 [10]. Normally, but this is modulation dependent, $f_H - f_0 \approx f_0 - f_L$, may be considered, and thus

$$B \approx 2(f_H - f_0) \approx 2(f_0 - f_L) \approx f_H - f_L. \tag{3.1}$$

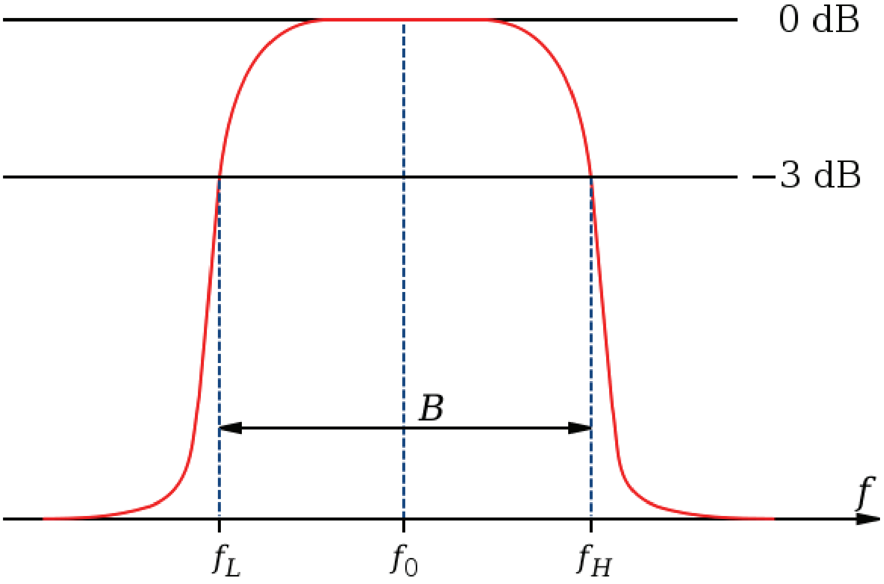

Figure 3.1: The figure illustrates the $-3dB$-bandwidth. The figure is from [10].

3.1.2 Geometry

The bistatic geometry [11], as used by Jackson [87], is shown in figure 3.2, where Tx is the transmitter, Rx is the receiver and the distance between them, the baseline is called L. The target is at a distance R_T from the transmitter and at a distance R_R from the receiver. The triangle formed by the three points Tx, Rx and the target lies in the bistatic plane, and is often called the bistatic triangle. The angle defined by the triplet Tx-Target-Rx is called the bistatic angle β, and it can be shown that [11]

$$\beta = \theta_T - \theta_R \tag{3.2}$$

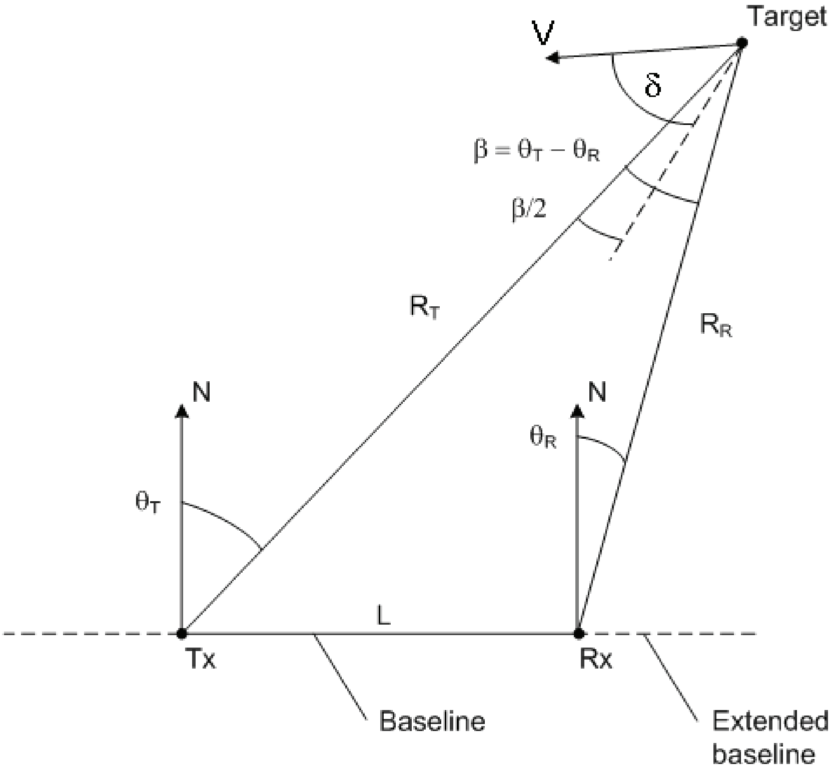

Figure 3.2: The bistatic geometry - North referenced, adapted from [11], figure 3.1.

where θ_T is the angle defined by the north direction and the line Tx to target, while θ_R is the angle defined by the north direction and the line Rx to target, both angles are taken as positive when going clockwise from North. The bisector of the bistatic angle, $\beta/2$ is a commonly used parameter and is also indicated in figure 3.2 [11].

A bistatic radar measures target range as the range sum, $R_T + R_R$. In 2D this constitutes an ellipse, while in 3D an ellipsoid. This chapter will in the following be restricted to the 2D bistatic plane, and subsequently the term ellipse will be used. This can be done without loss of generality for the theory to be presented. Without further restrictions, one range sum defines an ellipse, and this ellipse is called an isorange contour, or contour of constant range sum. Each target echo in a bistatic radar system will generate one constant range sum ellipse in 2D, or a part of an ellipse depending on the way the radar system operates. Consider a transmitter with an omni-directional antenna transmitting a signal with a bandwidth of $B = 100kHz^1$, giving a range resolution of $\Delta R = c/(2B) = 1500m$. Assume there is a receiving station positioned $40km$ east of the transmitter, with an omni-directional antenna. The bistatic radar resolution for this system is shown in figure 3.3, where the isorange contours are plotted. The distance between the isorange contours are given by the signal bandwidth.

The bisector, the dotted line in figure 3.2 that halves the bistatic angle, of the bistatic

---

[1] According to [27] this bandwidth is a bit high, but close to what is achievable/expectable in a FM radio transmitter of opportunity that exists today.

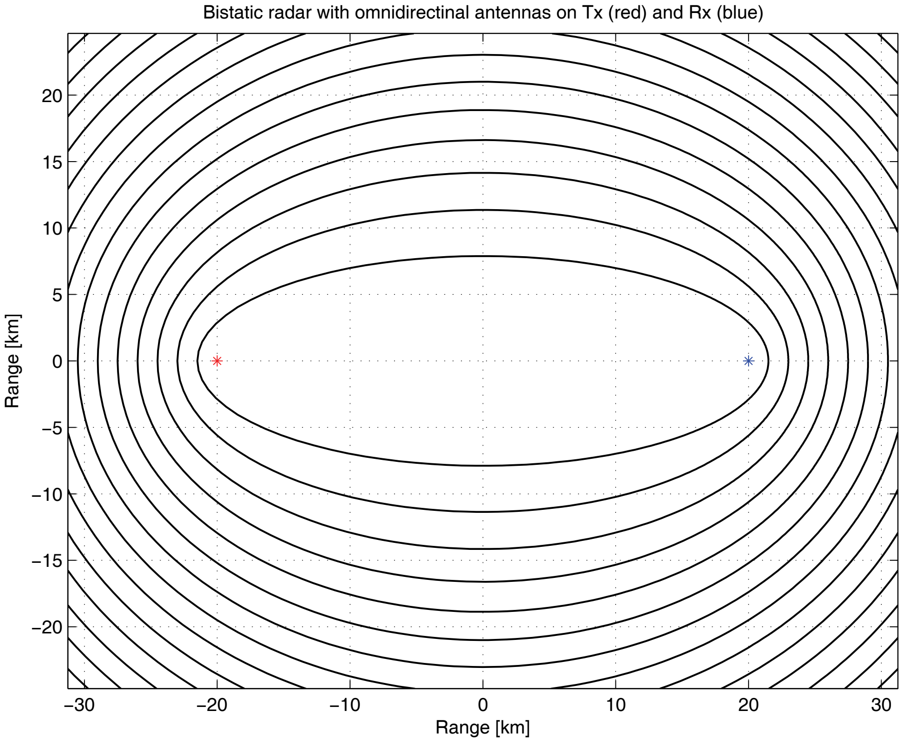

Figure 3.3: The bistatic range resolution, i.e. isorange contours, where the distance between the contours are given by the signal bandwidth.

angle is orthogonal to the tangent of the isorange contour at any point on the bistatic isorange contour. This is an important observation since the tangent is often a reasonable approximation to an isorange contour within the bistatic footprint [11].

The eccentricity, e, of the isorange contour or ellipse is [11]

$$e \overset{\text{def}}{=} \frac{L}{R_T + R_R}, \tag{3.3}$$

where it can be seen that $0 \leq e \leq 1$. For the monostatic case, $R_T = R_R$, $L = 0$ resulting in $e = 0$. For the forward scatter case, when the target is on the baseline between the transmitter and the receiver, that is $L = R_T + R_R$, the eccentricity is $e = 1$. In this case there is no range or Doppler information available in the received signal. The eccentricity can be regarded as a measure of how bistatic the transmitter-target-receiver geometry is, $e = 0$ being monostatic, and $e = 1$ meaning the transmitter, target and receiver being on a line with the transmitter facing the receiver. Willis [11, pp. 63] writes that "... either large values of β or large values of e should raise an "error flag" whenever they are encountered."

Figure 3.4 shows an illustration of a multistatic radar system. In the scene, three transmitters and one receiver, all with omni directional antennas, are assumed to see the target simultaneously. For each transmitter-receiver pair the target's constant range profile is drawn. From the illustration it is clear that the target is located at the intersection of the three ellipses. The rest of the intersections not corresponding to real targets are called ghosts and should be recognized as such in the signal processing. They can easily be found in figure 3.4, since this is an oversimplified situation used to illustrate the concept. In real life the number of transmitters can be more than three, it is ellipsoids and not ellipses, and the number of targets is usually higher than one. An example of such situation from a real system is shown by Howland in [22, pp. 168, figure 6-42].

[22] has developed a general expression for the maximum number of ghosts in the 2D situation, $f(M,T)$, generated by T targets and M transmit-receive pairs

$$f\left(M,T\right)=\left(2T^2-T\right)\left(M^2-M\right)/2, \tag{3.4}$$

and table 3.1 shows the maximum intersections as a function of bistatic transmitter-receiver pairs M and targets T present in the scene. It is seen that the number of ghosts increases rapidly as new transmitters and/or targets are added to the scene. For $M = 8$ (i.e. the PBR systems Thales' HA100 and Lockheed Martin's Silent Sentry$^{\circledR}$ 3 (SS3)) transmitter-receiver pairs, and $T = 1$ the maximum number of ghosts is $f(8,1) = 28$. The corresponding numbers for $T = 5$, and $T = 10$ are $f(8,5) = 1260$, and $f(8,10) = 5320$, respectively. In order to reduce the number of ghosts an indication of target direction might be very efficient. If the receiver is able to determine in which quadrant the target is, the maximum number of intersections is drastically reduced. This spatial discrimination will also reduce the number of targets generating constant range ellipses, and thus also the number of ghosts. This is exemplified with two red lines in figure 3.4, where the number of candidates are reduced from four to two. This rough direction/quadrant estimate is normally achieved by the receiver antenna beamforming.

Willis [11, table 3.1] summarizes several useful relationships on the bistatic plane together with their parameters. For bistatic radar systems where the positions of the transmitter and receiver is known (or possible to estimate), and the target azimuth angle θ_T or θ_R from transmitter and/or receiver is known (or possible to estimate), measuring the range sum $R_T + R_R$ enables the radar system to calculate the target location through the now known parameters, L, θ_T (or θ_R) and $R_R + R_R$

$$R_T = \frac{\left(R_T + R_R\right)^2 - L^2}{2\left(R_T + R_R - L\sin\theta_T\right)}, \tag{3.5}$$

and

$$R_R = \frac{\left(R_T + R_R\right)^2 - L^2}{2\left(R_T + R_R + L\sin\theta_R\right)}, \tag{3.6}$$

as seen in [11].

3.1.3 Bistatic Radar Equation

The bistatic radar equation is derived in a similar manner to the monostatic radar equation, and can be written [22, pp. 125]

$$\left(R_T R_R\right)_{\max} = \sqrt{\frac{P_T \rho G_T G_R t_c \lambda^2 \sigma_B F_T^2 F_R^2}{\left(4\pi\right)^3 k T_i (S/N)_{\min} L_T L_R L_{sp}}}, \tag{3.7}$$

$M\backslash T$	1	2	3	4	5	6	7	8	9	10
2	1	6	15	28	45	66	91	120	153	190
3	3	18	45	84	135	198	273	360	459	570
4	6	36	90	168	270	396	546	720	918	1140
5	10	60	150	280	450	660	910	1200	1530	1900
6	15	90	225	420	675	990	1365	1800	2295	2850
7	21	126	315	588	945	1386	1911	2520	3213	3990
8	28	168	420	784	1260	1848	2548	3360	4284	5320

Table 3.1: Maximum number of ghosts generated by T targets for M transmit-receive pairs [22].

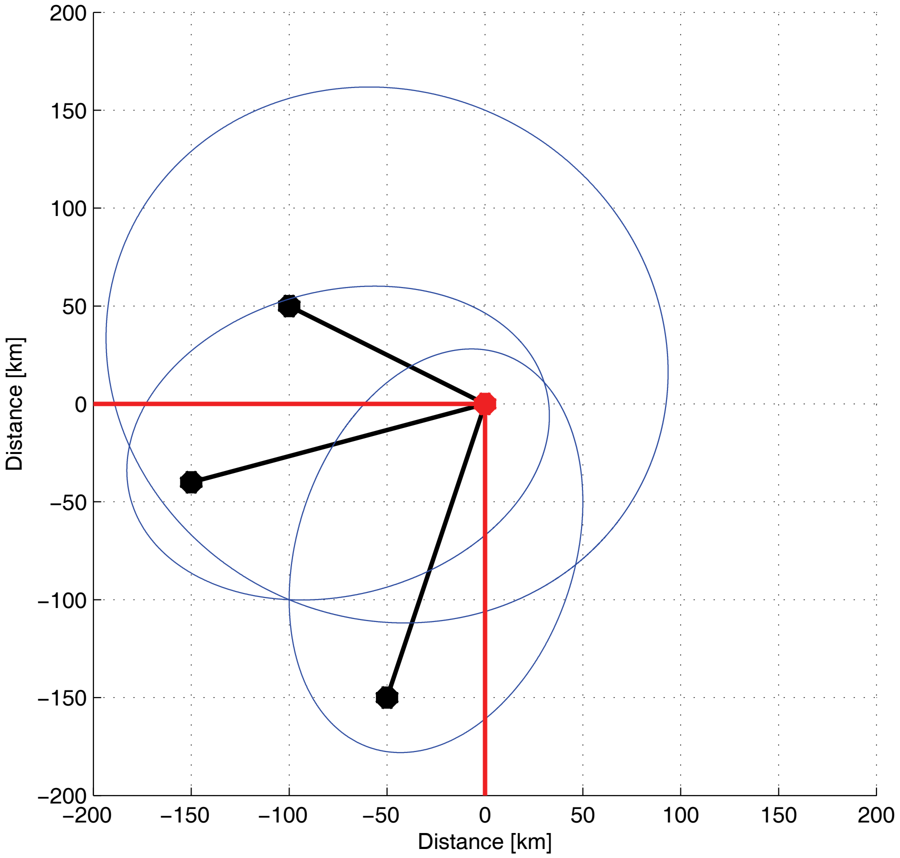

Figure 3.4: The figure shows a multistatic radar system with three transmitters (black circles) and one receiver (red circle). In the scene there is one target present at position $(-100km, -100km)$. The target's constant range profile is drawn for each of the three transmitter-receiver pairs (black lines), also showing three ghosts. The red lines indicate a quadrant with respect to the receiver, mimicking a coarse receiver antenna beamforming.

where

R_T = transmitter-to-target range [m],
R_R = receiver-to-target range [m],
P_T = transmitter power output [W],
t_c = coherent processing time/interval, $t_c = 1/B_n$,
where B_n is the receiver predetection filter,
ρ = power utilization factor, $\rho \leq 1$,
G_T = transmitting antenna power gain,
G_R = receiving antenna power gain,
λ = wavelength [m],
σ_B = bistatic radar target cross section [m^2],
F_T = pattern propagation factor for transmitter-to-target path,
F_R = pattern propagation factor for target-to-receiver path,
k = Boltzmann's constant [$1.38 \times 10^{-23} W/(Hz\, K)$],
T_i = receiving system noise temperature [K],
$(S/N)_{\min}$ = minimum signal-to-noise power ratio required for detection,
L_T = transmitting system losses (> 1) not included in other parameters,
L_R = receiving system loss (> 1) not included in other parameters,
L_{sp} = signal processing loss.

Equation 3.7 is related to the corresponding monostatic radar equation by the following: $\sigma_M = \sigma_B$, $L_M = L_T L_R$, and $R_M = R_T = R_R$. R_M is sometimes called the equivalent monostatic range for $R_M = \sqrt{R_T R_R}$ when the baseline $L = 0$ [11, pp. 68], and [22, pp. 125]. This is an artificial measure, since all practical applications of bistatic radar requires separation of transmitter and receiver, physically and/or electronically, as is discussed in detail in [22, pp. 125].

The bistatic range equation (3.7) applies for all types of waveforms, CW, Amplitude Modulated (AM), FM, or pulsed [11]. The power utilization factor ρ is a quantity that specifies the fraction of the total transmitter power utilized by the PBR receiver [22]. It is usually accomplished by band limiting the PBR receiver, and becomes significant when narrowband Doppler operation is used, i.e. exploiting analogue TV transmissions, where $\rho \in [0.1, 0.5]$.

The coherent processing time, t_c, the Coherent Processing Interval (CPI), is defined as the inverse of the noise bandwidth of receiver's predetection filter B_n [22]. However, when a smaller portion, not necessarily narrowband processing, of the receiver bandwidth is utilized

$$\rho = \frac{B}{B_n}, \tag{3.8}$$

where ρ is the power utilization factor 3.7, and $B \leq B_n$ is the applicable Radio Frequency (RF) signal input bandwidth. This allow the expression from the time-bandwidth product to be used, or processing gain $G_p = t_c B$. From equation (3.7)

$$\rho t_c = \frac{t_c B}{B_n} = \frac{G_p}{B_n}. \tag{3.9}$$

The latter formulation is more applicable to PBR operations, where often $B \leq B_n$, and the coherent processing interval can be quite long, i.e. for FM radio PBR systems $0.5sec$, and for DVB-T $0.1sec$ yielding a processing gain of $G_p = 47dB$ and $G_p = 59dB$ respectively [26].

The time available for coherent processing is typically set by the amount of Doppler spreading or velocity walk, Δf_d generated by the target. Specifically, $\Delta f_d = 1/t = B_n$. In the monostatic case and for small bistatic angles β Doppler spreading is given as [22, pp. 126]

$$(\Delta f_d)_{mono} = \sqrt{\frac{2a_r}{\lambda}}, \tag{3.10}$$

and for the bistatic case for larger bistatic angles β, e.g. $\beta = 90$ degrees

$$(\Delta f_d)_{bist} = \sqrt{\frac{a_r}{\lambda}}, \tag{3.11}$$

where a_r is the radial component of target acceleration.

The RF interference comprises two parts [22, pp. 118]: the sky noise and man-made noise, the former being sun, galactic, and atmospheric noise. The latter consists of signals from communications, broadcast, surveillance, and navigation transmitters, and impulsive noise from older automobile ignitions, power tools fluorescent lights, cooling fans, etc. [22, pp. 118], combines all interference components into a single source at the antenna output terminal, represented by an input termination resistor with a temperature T_i, which makes available to the receiver a noise with the spectral density W/Hz

$$N_0 = kT_i \tag{3.12}$$

where T_i can be further divided into

$$T_i = T_a + T_r + L_r T_e. \tag{3.13}$$

T_a is the antenna contribution $= T_s + T_m$, T_r is the RF component contribution $\cong T_0(L_r - 1)$, and T_e is the receiver contribution $= T_0(F_n - 1)$. T_S is the temperature of the sky-noise interference, T_m is the temperature of the man-made interference, L_r is the RF component loss, F_n is the receiver's noise factor, and $T_0 = 290K$. As an example, it is calculated that a well designed receiver is expected to have $T_r + L_r T_e = 865K$. To this must be added the contributions from interference, $T_a = T_s + T_m$, which is sky noise, T_s, and man-made noise, T_m. [22, pp. 118] deduces that of these two are the man-made interference much more severe.

Figure 3.5a shows the receiver's reference channel frequency response for the FM radio channel's internal noise (open input), and figure b the frequency spectrum with an antenna

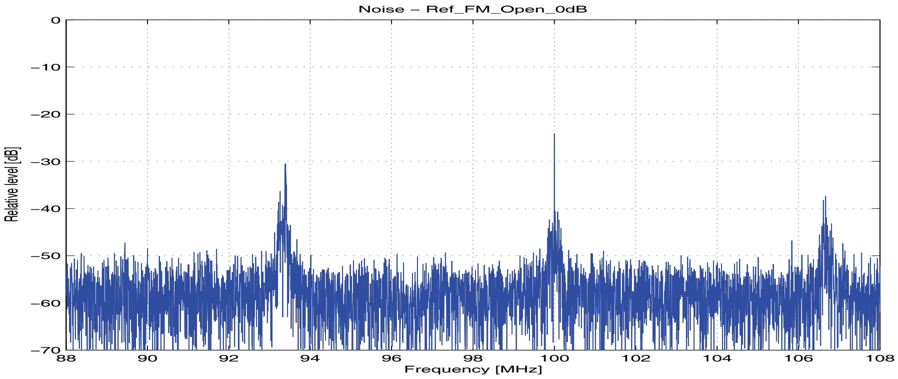

(a) FM radio, no input signal, $0dB$ attenuation.

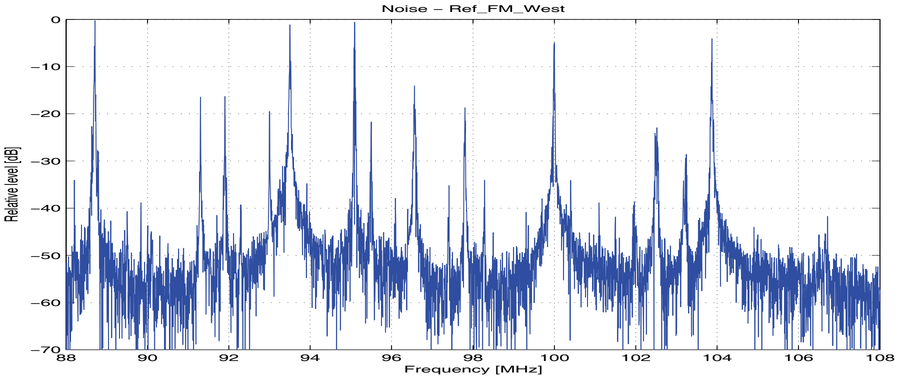

(b) FM radio, reference antenna at strong transmitter, $0dB$ attenuation.

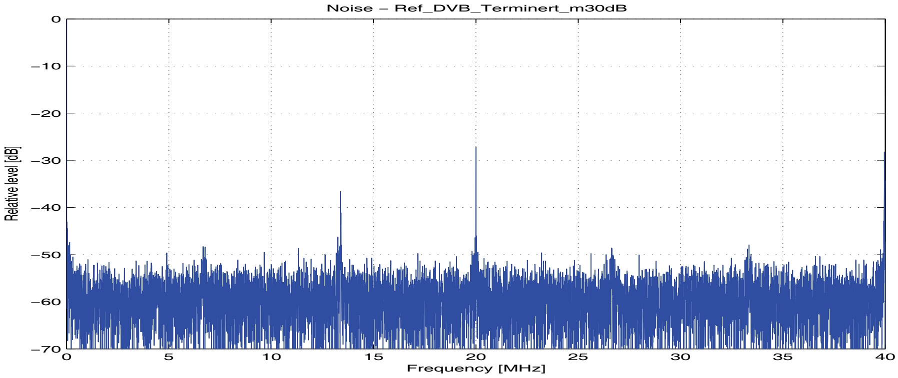

(c) DVB-T, terminated input, $30dB$ attenuation.

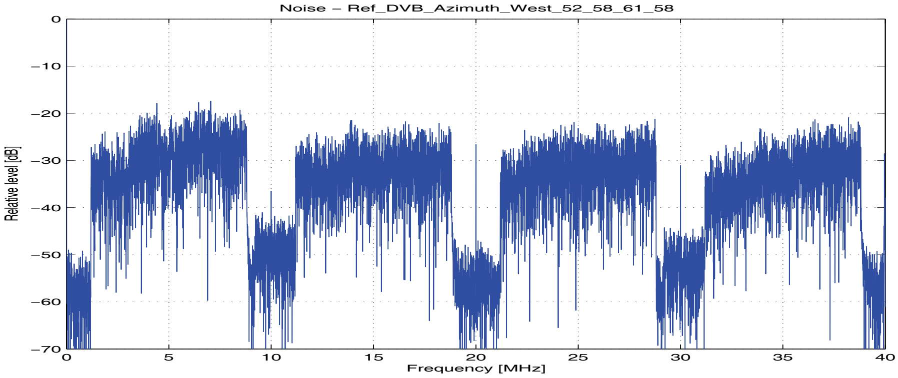

(d) DVB-T, reference antenna at strong transmitter, $30dB$ attenuation.

Figure 3.5: The figure shows the noise floors in the receiver for the FM radio and the DVB-T channels, and the corresponding channels with signal input.

connected and directed at a nearby strong FM transmitter, data recorded with the data recording equipment to be explained in chapter 4. Similarly, figure c shows the wideband channel's internal noise (terminated input), while figure d shows the frequency spectrum when an antenna is connected, and directed at a nearby strong DVB-T transmitter.

For the FM radio case, in figure b, several strong frequencies, $88.7MHz$, $93.5MHz$, $95.1MHz$, $100.0MHz$, and $103.9MHz$ is seen. Narrow as their peaks may be, $40dB$ down they are occupying a band ranging from $0.5MHz$ to $0.7MHz$ in width. Additional $10dB$ down, their widths are ranging from $1.4MHz$ to $2.4MHz$. This widening, or roll-off, will cause problems for DSI suppression algorithms [22, pp. 119], since the signal in question is leaking into adjacent radio channels, which is not a problem for the FM radio listeners, but for a radar system, working several tens of dBs further down in signal levels, this causes problems. The DSI algorithms are reported to be effective down to $20 - 30dB$ above the receiver thermal noise channel due to this roll-off effect, [22, pp. 119].

Similarly, for the DVB-T case, figure 3.5c and d show that the DVB-T signals are extending up to $30dB$ above the receiver noise floor, with the signal shoulders varying from $0 - 10dB$ above the noise floor. In the theoretical signal spectrum for $8MHz$ channels, [12] the shoulders start $4MHz$ to each side from the center frequency, $40dB$ below the normalized signal power ($0dB$). $5MHz$ from center frequency, the signal is down to $-47dB$, while $8MHz$ to each side from the signal's centre frequency (this is the centre frequency of the two adjacent channels), the signal is down to $-53dB$. In order to avoid interference, especially with the analogue TV transmissions, a spectrum mask might be applied, typical values are given in figure 3.6, from which it is seen that the DVB-T output signal may be attenuated additional $20dB$ or more at the signal shoulders, i.e more than $4MHz$ from the signal center frequency.

[22, pp. 118] estimates the receiver noise to be $P_n = kT_0BF$, where $k = 1.38 \times 10^{-23} Ws/K$ is Boltzman's constant, $T_0 = 290K$, $B = 50kHz$, and the receiver noise figure $F = 5dB$, which results in $P_n = -122dBm$. The receiver noise is found to be way below the received FM radio broadcasted signals in this case presented for $95 - 100MHz$, where the lowest FM signal level is $30dB$ above receiver noise floor [22, pp. 119], and thus has to be dealt with, see further details for DSI cancellation in section 3.3. Comparing to the data recording equipment's receiver noise figure, all parameters are kept constant, except for the receiver noise bandwidth, which is $B = 20MHz$, yields $P_n = -96dBm$. Similar argument can be made for the DVB-T channel, resulting in the receiver thermal noise to be $P_n = -93dBm$, for $B = 40MHz$. This example shows that the main problem of PBR relying on broadcast transmitters operating continuously is the interference from DSI, and not necessarily the equipment internal noise figure, as well as interference from adjacent non-exploited channels, figure 3.5. Further and more dedicated analysis of the receiver will be made in chapter 4.

The transmitting and receiving pattern propagation factors, F_T and F_R of (3.7) are defined as $F_T = F'_T f_T$ and $F_R = F'_R f_R$, where F'_T and F'_R are the propagation factors and f_T and f_R are the antenna pattern factors [11]. These factors are applied whenever the target is not at the peak of the transmitting and receiving beams. The propagation

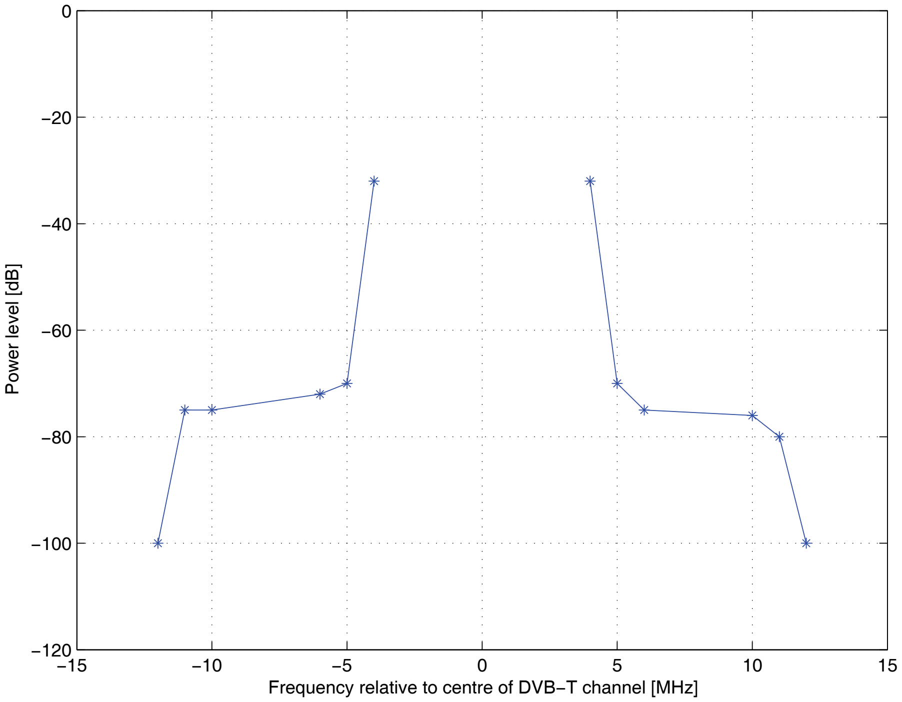

Figure 3.6: Roughly averaged spectrum mask for a digital television operating on a lower or higher adjacent channel to a co-sited analogue television transmitter. The figure is adapted from [12].

factors F_T' and F_R' customarily include the effects of multipath, diffraction, and refraction, with atmospheric absorption effects included in the loss terms, L_T and L_R.

The Ovals of Cassini [11] are contours where the SNR and the range product $R_T R_R$, equation (3.7) are held constant. The SNR is highest around the transmitter and receiver sites, dropping off as one gets further and further away from these. At one point, on the middle of the baseline $L/2$ from the transmitter and receiver sites, the ovals break into two non-connected ovals, one around the transmitter and the other around the receiver. The point on the baseline [11] where this happens, is called the *cusp*, and the curve is called a *lemniscate* (of two parts), and it looks like the infinity sign ∞. The Ovals of Cassini are shown in figure 3.7 for a bistatic radar system where the baseline is $40km$. The lemniscate is not shown, but the cusp is at origin, and the behavior of the ovals are apparent. If the baseline is increased, the ovals will shrink towards a lemniscate, and finally collapse in a circle, one around the transmitter and one around the receiver [11].

For the monostatic radar, the Ovals of Cassini collapses to circles of constant SNR with the radar in the center, and the constant range contours (circles) coincide with the constant SNR cotours. For the bistatic case this is not true. Figure 3.8 shows the Ovals of Cassini overlaid the isorange contours, the constant range ellipses, for a bistatic radar system. It is obvious from the figure, that two targets (assumed to be equal) at different range profiles can result in the same SNR, or vice versa, that two equal targets at the same isorange contour can result in different SNR in the radar. Willis [11] has estimated the instantaneous SNR dynamic range for an isorange contour in a bistatic radar system

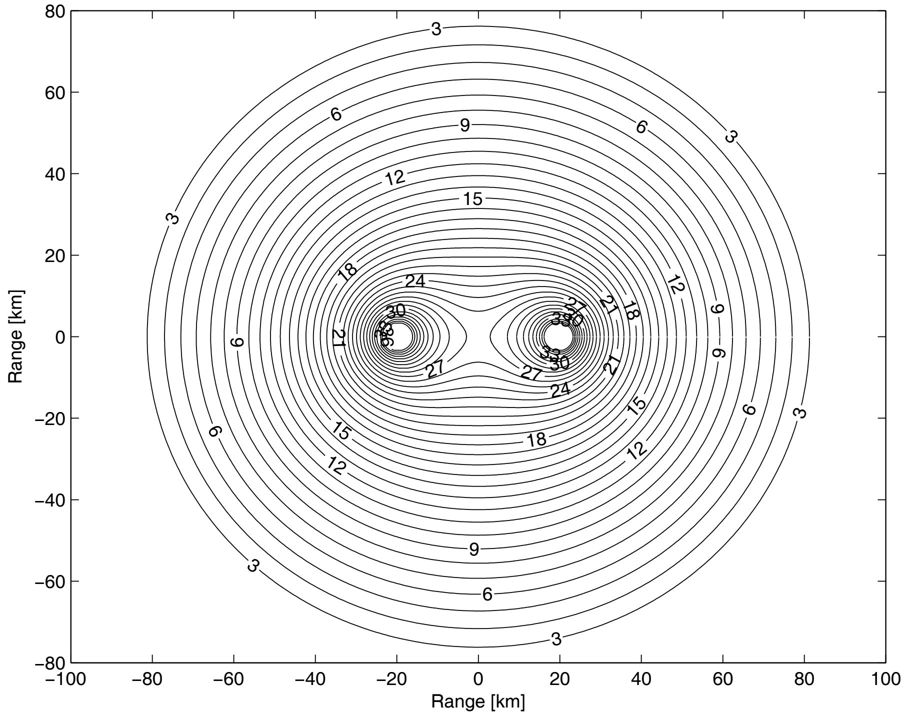

Figure 3.7: The Ovals of Cassini - the contours of constant SNR.

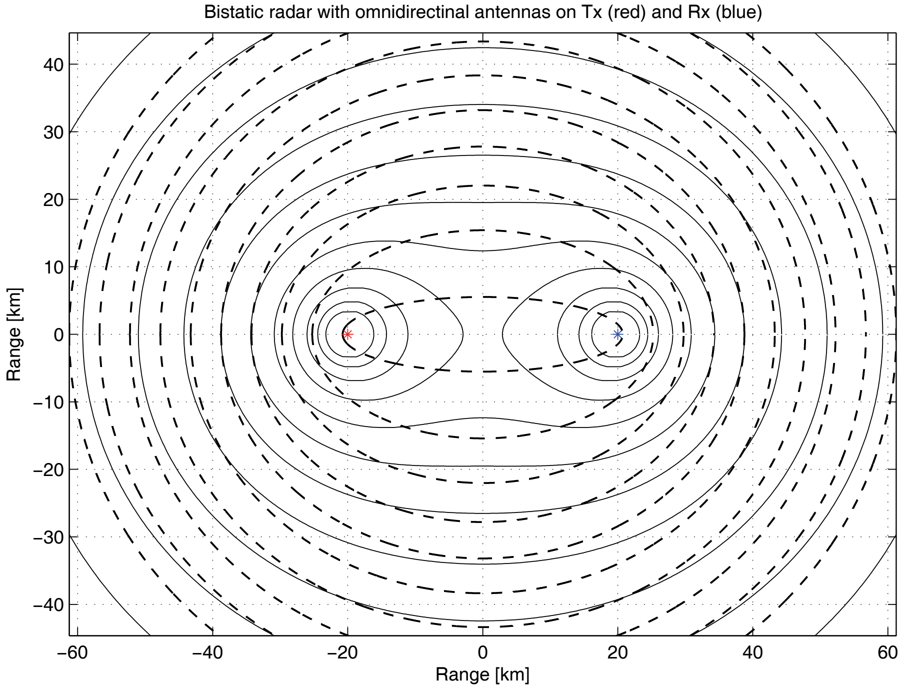

Figure 3.8: The Ovals of Cassini (solid line), and the isorange contours (dotted lines).

as a function of the eccentricity e

$$\Delta \frac{S}{N} = \frac{4}{\left(1+\cos(2\sin^{-1} e)\right)^2}, \tag{3.14}$$

and this is plotted in figure 3.9 where the ratio of maximum to minimum target SNR on an isorange contour, defined as an ellipse of eccentricity, e. From this figure it is clear that it is especially in the forward scatter applications that the instantaneous dynamic range can be large, that is, eccentricity, $e \to 1$. For the monostatic case, eccentricity $e = 0$, and the dynamic range difference is as expected, zero.

This means that as the target gets further and further away from the transmitter/receiver pair, the Ovals of Cassini will approach circles, and as expected targets are approaching the monostatic situation. However, going the other way, approaching the baseline, the effects of this might get quite severe, as seen from figure 3.9.

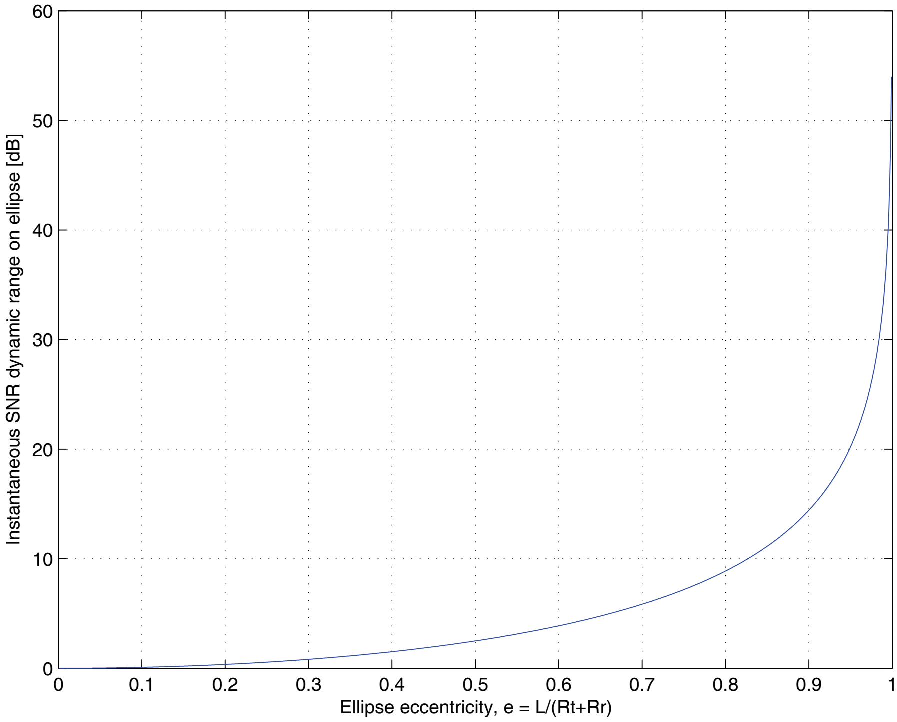

Figure 3.9: Ratio of maximum to minimum target SNR on an isorange contour, defined as an ellipse of eccentricity, e, as in [11], figure 4.9.

3.1.4 Waveforms

PBR can in principle rely on any waveform of opportunity, however once an application is set, the limiting factors of the waveform in question becomes evident. Some waveforms and their distribution are more applicable than others, i.e. modulation, transmitted power, antenna diagram (azimuth and elevation), total coverage, signal bandwidth, signal availability to mention some aspects to be considered by the radar designer. Section 2.3 in the literature critique focused on the FM radio and DVB-T published PBR research, while other waveforms may also be used successfully for PBR purposes.

The research and publication on the availability of waveforms and their performance with respect to various applications, has been extensive [27–34], however, it is fair to claim that the majority of these has been focused on air surveillance.

Howland exploited a narrowband PBR relying on Doppler tracking of targets using analogue TV signals [57], while many systems emerged on FM radio: Lockheed Martin's Silent Sentry® [24, 25], Thales' Home Alerter 100 [26], the NC3A sensor [44], as well as the EADS sensor [88]. DAB PBR is extensively reported on in [62, 63, 88, 89]. Recent work on using the GSM mobile phone base stations as transmitters of opportunity has been published [90–92], as well as work on exploiting the computer wireless network transmitters (WiFi) of opportunity [93,94], and even attempts on using digital HF signals [95]. This list is even not exhaustive, and [22, tables 6-1,6-2,6-7] provides a more complete overview of various PBR projects as well as transmitters and waveforms of opportunity where research has been conducted in past and present.

The research of this thesis will focus on exploiting the FM radio and DVB-T broadcasters of opportunity. The DVB-T waveform is well explained in the ETSI standard [12] and recent research on the DVB-T waveform for PBR purposes published [23,32,96]. The Norwegian DVB-T waveform is broadcasted in $8MHz$ bands using $8k$-carriers modulated with 64 Quadrature Amplitude Modulation (64QAM) [97], and this information relates to the ETSI standard [12].

The basics of the FM radio waveform is presented in appendix B, in particular the FM modulation in section B.1. A short survey is presented in section B.2 of the various bandwidth considerations coming from the communication research. It is shown that these considerations are not suitable for radar purposes, as they are focusing on providing sufficient bandwidth for proper channel quality and stability, while efficiently exploiting the limited frequency available. Finally, section B.3 provides a mathematically formulated version (in the nomenclature of this thesis, section B.1), of a FM SW radio demodulation algorithm [98]. With respect to the nomenclature of appendix B, the Norwegian FM radio broadcast system is using modulation index $\beta = 5$, and frequency deviation $\Delta f = 75kHz$.

3.2 Bistatic Radar Resolution

Figure 3.10 shows the bistatic radar resolution for a bistatic radar with an omni-directional transmitter antenna and a directional receiver antenna with beamwidth $\Delta\theta_R = 10^\circ$, and the signal bandwidth is $B = 100kHz$. This figure also illustrates the impact on antenna resolution with reference to equations (3.5) and (3.6), and further detailed in section 3.2.3. From the figure it is clear that the bistatic radar resolution is much more complex than the monostatic radar range resolution, where the resolution cells are determined only by the radar's range resolution (transmitted signal's bandwidth) and the transmit/receiver antenna's beamwidths. For bistatic radar, the bistatic geometry, defined by the target, transmitter and receiver's positions determines the radar's range resolution in addition to the transmitted signal's bandwidth. The angular resolution is defined by the intersection

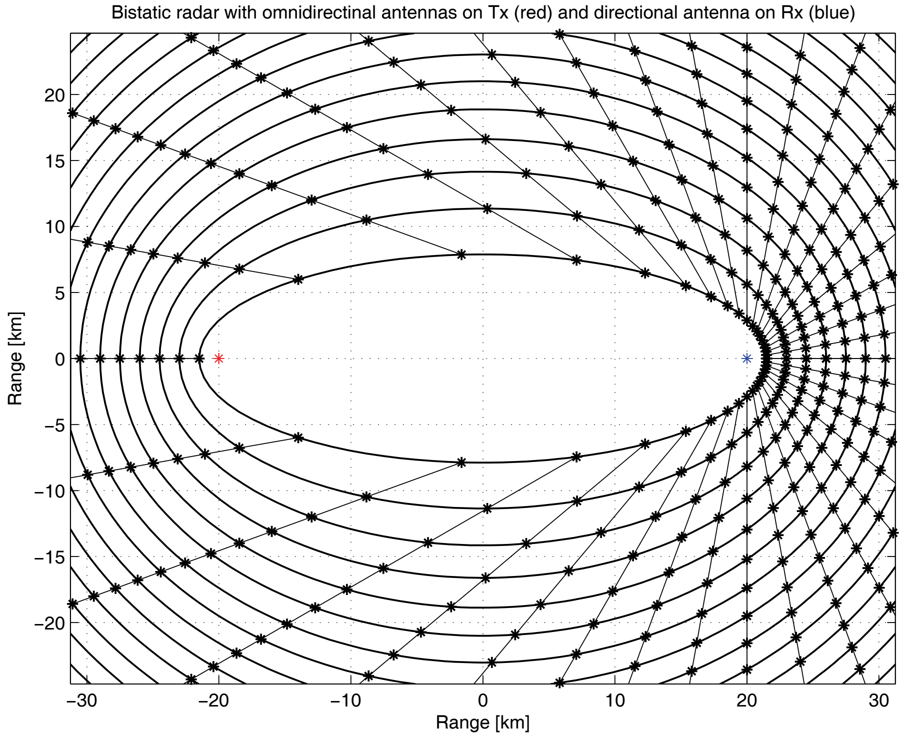

Figure 3.10: The bistatic radar range resolution cells as a function of receiver antenna beam width $\Delta\theta_R = 10^\circ$ and transmitted signal bandwidth $B = 100kHz$.

of the transmitter's and receiver's beams, and is influenced by the geometry, as fll as the bistatic Doppler shift, which is affected by the bistatic geometry with respect to the monostatic case. Willis, [11], provides a well worked through description of the bistatic resolutions; range, Doppler and angle. The main results will be briefly presented, and it is underlined that sections 3.2.1-3.2.3 are an adaptation from [11].

3.2.1 Range resolution

The monostatic range resolution is given as

$$\Delta R_M = \frac{c\tau}{2}, \tag{3.15}$$

where c is the speed of propagation, and τ is the radar's (compressed) pulsewidth, [11] and [99]. Figure 3.11 shows the bistatic radar range resolution geometry. In order to separate two targets, the two targets must lie on different isorange contours, having separation ΔR_B, and that is approximately given as [11]

$$\Delta R_B \approx \frac{c\tau}{2\cos(\beta/2)}. \tag{3.16}$$

When the straight line joining the two targets is not co-linear with the bistatic bisector, their physical separation ΔR_ψ is approximately [11]

$$\Delta R_\psi \approx \frac{c\tau}{2\cos(\beta/2)\cos\psi}, \tag{3.17}$$

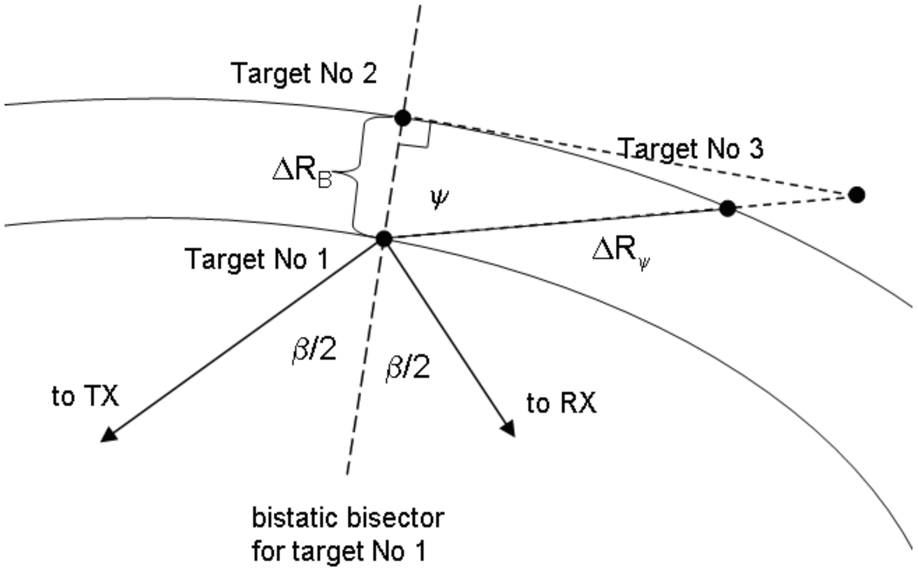

Figure 3.11: Geometry for bistatic range resolution, adapted from [11], figure 7.1.

as defined in figure 3.11. Three approximations have been made in order to develop (3.17) [11],

- $\Delta R_B \leq c\tau/(2\cos(\beta/2))$ for all values of β,
- the ΔR_ψ approximation assumes that the outer isorange contour (ellipse) of figure 3.11 is a straight line, and
- the bisector at target 1 on the inner ellipse is also the bistatic bisector at target 2 on the outer ellipse, and thus perpendicular to the ellipse's tangent at target 2.

All the details are available in Willis book, [11] section 7.1. Willis claims that the estimates can be shown to be conservative, and are in most cases tight upper bounds provided that the ellipses are not too eccentric (3.3) (high values of ϵ), nor that $\Delta R_M = c\tau/2$ becomes a significant fraction of the baseline ($\Delta R_M > 0.1L$). And of course, all the estimates break down for large values of β. As a rule of thumb, one can say that as long as the three assumptions are not seriously violated, the approximations can be regarded as tight upper bound estimates [11].

3.2.2 Doppler shift and Doppler resolution

The bistatic Doppler geometry [11] is shown in figure 3.2, and the bistatic Doppler shift of a target is given by f_B, where

$$f_B = \frac{2V}{c} f_T \cos(\delta) \cos\left(\frac{\beta}{2}\right), \tag{3.18}$$

for δ and β calculated based on the instantaneous bistatic geometry as given in figure 3.2 [11]. Target velocity is V, and the carrier frequency is f_T. This work is only

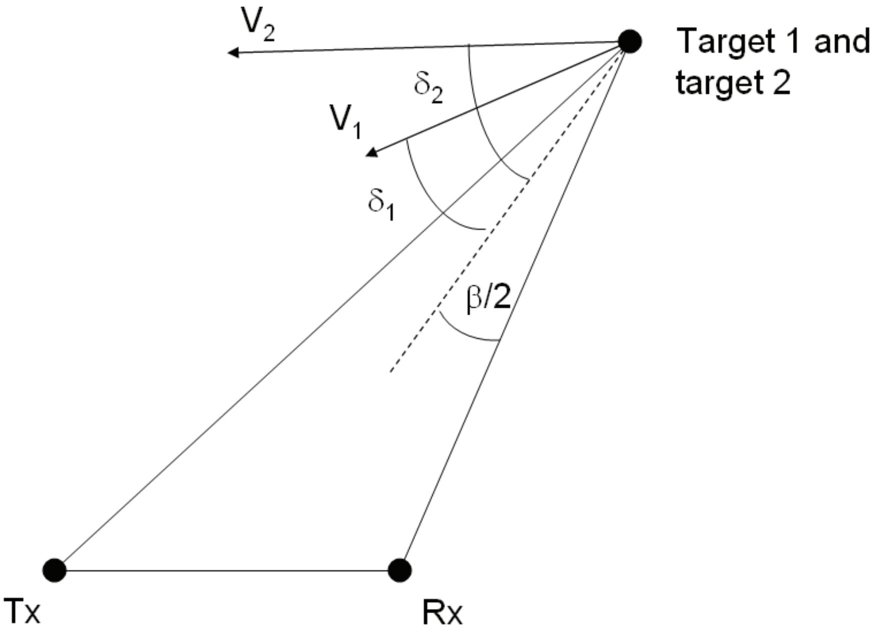

Figure 3.12: Geometry for bistatic Doppler resolution, adapted from [11], figure 7.2.

considering stationary transmitters and receivers, and thus the situation is simplified with respect to the general case, where all units may be moving. The more general case of moving transmitters and receivers is treated in [11].

The monostatic and bistatic radar Doppler resolution is generally considered to be the inverse, $1/T$, of the receiver's coherent processing interval, T, [99] and [11]. For two collocated targets, assumed to share a common bistatic bisector, figure 3.12 the required difference between the two target velocity vectors, projected onto the bistatic bisector, ΔV, is [11]

$$\Delta V = (V_1 \cos(\delta_1) - V_2 \cos(\delta_2)) = \frac{\lambda}{2T \cos(\beta/2)}. \tag{3.19}$$

The assumption that the two targets share a common bistatic bisector can be relaxed as long as [11]

- their separation is not sufficient to allow resolution in another dimension, i.e. range or angle, and
- the angle between the targets bistatic bisectors is small.

3.2.3 Angle resolution

For a monostatic radar, the angle resolution is normally taken to be the $3dB$ antenna beamwidth, $\Delta\theta_M$, [11], [86] and [100]. Two targets at a distance of R_M from the radar are thus physically (the arclength/cross-range) $\Delta\theta_M R_M$ apart. For the bistatic radar, generally $\Delta\theta_T \neq \Delta\theta_R$, and $R_T \neq R_R$, where $\Delta\theta_T$ and $\Delta\theta_R$ is the transmitting and receiving antenna's $3dB$ beamwidth. This means that the monostatic two-times $3dB$ resolutions (transmit and receive beam from the (shared) antenna) for the monostatic

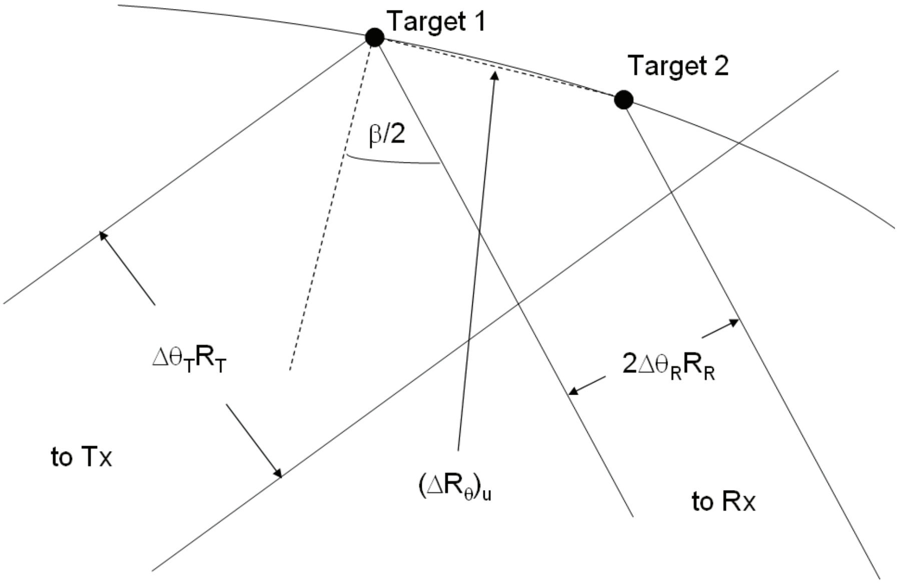

Figure 3.13: Geometry for bistatic angular resolution, adapted from [11], figure 7.3.

radar cannot be applied in the bistatic case. In addition to this, the bistatic geometry further degrades the resolution, for all values of β, except for some special cases [11].

Figure 3.13 shows the geometry for bistatic angular resolution, in the case where $\Delta\theta_T R_T > 2\Delta\theta_R R_R$, which means that the cross-range dimension of the $3dB$ transmitting beam is larger than the receiver's null-to-null beam cross-range dimension [11]. This means that the transmitter's beam is not contributing to the angular resolution, and a conservative estimate of target separation is taken as the null-to-null beam of the receiver, $2\Delta\theta_R$, which in turn means that the required cross-range dimension is $2\Delta\theta_R R_R$. The two targets must thus be physically separated by $(\Delta R_\theta)_u$ [11], where

$$(\Delta R_\theta)_u \approx \frac{2\Delta\theta_R R_R}{\cos(\beta/2)}, \qquad \text{for} \qquad \frac{\Delta\theta_T R_T}{\Delta\theta_R R_R} > 2, \tag{3.20}$$

and the subscript u denotes unequal cross-range dimensions of the transmitting and receiving beams. Similar arguments can be made for the case of $\Delta\theta_T R_T = \Delta\theta_R R_R$ the two targets must be physically separated by $(\Delta R_\theta)_e$, where

$$(\Delta R_\theta)_e \approx \frac{\Delta\theta_T R_T}{\cos(\beta/2)}, \qquad \text{for} \qquad \frac{\Delta\theta_T R_T}{\Delta\theta_R R_R} = 1, \tag{3.21}$$

where the subscript e denotes equal cross-range dimensions of the transmitting and receiving beams [11]. When $1/2 < (\Delta\theta_T R_T)/(\Delta\theta_R R_R) < 2$, a transition region is defined, where the curve approximates the transmitting mainbeam Gaussian roll-off, [11, pp. 138, figure 7.5]. It is underlined that all results in this section also applies to the reciprocal case, receiver ↔ transmitter. In general, a conservative estimate for bistatic angle resolution is (3.20), unless special geometries is considered.

Willis' underlying approximations [11] made to develop equations (3.20), and (3.21) are

- parallel rays for transmitting and receiving beams,
- straight lines for isorange contours,
- a null-to-null beamwidth, $2\Delta\theta_R$ (or $2\Delta\theta_T$), angle separation between two targets required for angle resolution.

Note that this section constitutes the general case of the formulas in equations (3.5) and (3.6), where one of the transmitting and/or receiving beams are contributing to angular resolution.

3.2.4 Mono- and bistatic ambiguity functions

The classical ambiguity function, first suggested by Woodward [101], is written [23, pp. 276]

$$|\psi(T_R, f_d)|^2 = \left| \int_{-\infty}^{\infty} s_t(t) s_t^*(t + T_R) \exp(j2\pi f_d t) dt \right|^2 , \tag{3.22}$$

where $\psi(T_R, f_d)$ is the ambiguity response at the delay range T_R and Doppler f_d, and $s(t)$ is the signal under examination. The bistatic form of the ambiguity function can be written [23, pp. 283], which work is based on [34]

$$\begin{aligned} |\psi(R_{RH}, R_{Ra}, V_H, V_a, \theta_R, L)|^2 = \Big| \textstyle\int_{-\infty}^{\infty} & s_t(t - \tau_a(R_{Ra}, \theta_R, L)) s_t^*(t + \tau_R(R_{RH}, \theta_R, L)) \times \\ & \times \exp\left[j2\pi (f_{DH}(R_{RH}, V_H, \theta_R, L) - 2\pi f_{Da}(R_{Ra}, V_a, \theta_R, L)) t \right] dt \Big|^2 , \end{aligned} \tag{3.23}$$

where R_{RH} and R_{Ra} are the hypothesized and actual ranges (delays) from the receiver to the target, V_H and V_a are the hypothesized and actual radial velocities of the target with respect to the receiver. The f_{DH} and f_{Da} are the hypothesized and actual Doppler frequencies of the target, while θ_R is the angle from the receiver to the target with respect to 'north', and L is the baseline formed by the transmitter and receiver [23, pp. 283].

[22, 28] concludes that the ambiguity function for bistatic radar can be divided into two parts: A waveform part, which is most efficiently analyzed through the monostatic ambiguity function (3.22), and a geometrical part, which is accounted for in the bistatic ambiguity function (3.23). This work stays true to this way of dealing with the waveform analysis, keeping in mind that the best achievable resolution for the bistatic system is the monostatic one, and that is achieved only at the *extended* baseline as shown in figure 3.2, not on the baseline where there is no resolution at all.

However, it is customary for bistatic range-Doppler plots to plot the bistatic range, which should not be confused with the bistatic range resolution. With reference to figure 3.2, the bistatic range is simply the range sum minus the baseline distance, i.e. $R_T + R_R - L$. Monostatic radars can easily estimate the range to target, simply by measuring the round trip time t of the signal, and thus calculating $R = ct/2$. This is not the case for bistatic radars, and thus these systems plot the quantity $R_T + R_R - L$. It should be noted though, that this may be considered the unambiguous range coherent signal processing time interval, which will be treated in full detail in section 3.5. In this way the range-Doppler plots are not linked directly to the transmitter-target-receiver geometry which in principle is unknown. For the target geometry to be known for a single transmitter-target-receiver geometry, the transmitter and/or receiver have to measure accurately the angle to target, and thus the target position can be directly calculated as presented in section 3.2.3, and Willis [11, pp. 65] by equations (3.5) and (3.6).

3.3 Direct signal and clutter

One of the major, if not the major, challenge for PBRs based on broadcast transmitters is the direct signal and its received strength compared to the strength of the target reflected signal. In many applications this signal will be received directly, i.e. the receiver is in line of sight from the transmitter, the signal might be diffracted over terrain, or reflected by surfaces/infrastructures, as illustrated in figure 3.14. Willis and Griffiths [22, pp. 135] tabulates the required direct path cancellation for various PBR transmitters, and for all the systems looking at targets around $100km$, the required direct signal suppression typically lies in the interval $70 - 90dB$. Howland et. al. [44, pp. 108], illustrates the challenge of DSI by an example from the NC3A system, where a target echo from a target at a range of $150km$, RCS of $\sigma_B = 10dBSm$, would be $S_D/S_T = -90dB$ below the received direct signal if no signal interference rejection was applied.

Figure 3.14 shows the generic geometry for target reflected signal and direct signal and clutter interference. The clutter interference may be divided into two categories; terrain/landscape clutter and infrastructure/man-made clutter, the latter consisting of buildings, cars/trucks, and windmills.

There are many ways of dealing with the DSI, and referring to figure 3.15, the DSI cancellation may be considered to part of the whole signal processing chain of the system: Terrain shielding, applying antenna nulls

Starting ahead of the antennas, terrain shielding is the first and traditional way of coping with the interference, and the most famous system relying on this strategy is the Manastash Ridge radar [102,103]. The Manastash Ridge Radar is a passive bistatic radar which relies on commercial FM radio broadcaster in the $88 - 108MHz$ band to study density irregularities in the ionosphere. There are GPS synchronized receivers located at the University of Washington as well as at Manastash Ridge, while the transmitters are behind the mountain. Exploiting the terrain shielding is also the strategy for this thesis' work.

The next step would be to arrange antenna nulls in the direction of the interfering signal, either by applying beamforming [104] or using an over-the-shoulder geometry [44] by shielding the receiver antenna (array) or adjusting to the DSI drops. This work is using Yagi antennas, and thus the DSI cancellation achieved comes from the antenna diagram.

Considerable work has been reported on beamforming for PBR systems in order to reduce the DSI [89,105–107], an approach which requires an antenna array of more than one element. Also successful work on exploiting the polarization has been reported [96,

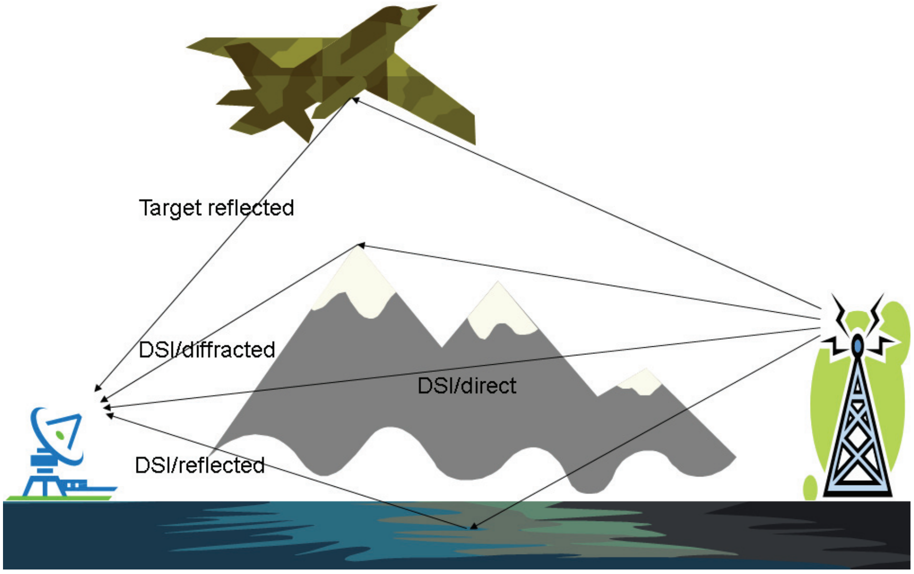

Figure 3.14: Generic geometry for target reflected signal and direct signal and clutter interference.

104, 108].

The signal conditioning, figure 3.15, may also be part of the DSI cancellation, as this step normally includes processing in order to improve the reference signal's quality, and thus better adaptive filtering and/or cross-correlation is achieved. Some work is reported on high quality reconstruction of the reference signal in order to avoid the adaptive filtering, and only be relying on the cross-correlation [63, 109]. This is an approach best suited for the digital waveforms comprising error correction coding in which in theory the exact signal may be reconstructed.

Nevertheless, the most common approach is to also apply adaptive filtering, which in principle consists of estimating the interfering signal, and then removing it from the surveillance channel. This can be done in HW [110], and the advantage of this is the reduced dynamic range requirement of the A/D converters of the system. However, the most common adaptive filtering is made in SW, and numerous publications are available on the topic [35, 107, 111–115]. [115] summarizes the common SW algorithms and their performance in the PBR case for FM radio signals: Least Mean Square, Normalized Least Mean Square, Recursive Least Square, are compared to the Extensive Cancellation Algorithm, and Sequential Cancellation Algorithm. It is concluded that in general one can trade performance for computation load and vice versa. It is worth noting that [111] takes the DSI issue one step further, by considering strong targets also to be sources of DSI which can mask weak targets. In early PBR days, this was a matter of concern due to the potential enormous dynamic range of targets passing close to either the transmitter or receiver compared to targets further away from each.

And finally, the cross correlation step, figure 3.15 including Doppler processing, where the DSI, which is assumed to be stationary, is filtered out.

No dedicated DSI-algorithm is implemented or applied in the equipment used for data recording for the research reported on in this thesis. The focus of this work will be on the achievable performance of PBR with respect to the multiple signal band exploitation. However, a brief survey on the influence of the DSI on this work will be presented in theory here, and in performance estimates in section 4.1. It will be shown that the terrain shielding offered by the transmitter to receiver paths should be sufficient attenuation for the goals of this thesis.

The received signal reflected from a target is

$$S_{Target} = \frac{P_T G_{T,T} G_{R,T} \lambda^2 \sigma_B F_{T,T}^2 F_{R,T}^2}{(4\pi)^3 R_{T,T}^2 R_{R,T}^2 L_{T,T} L_{R,T}}, \tag{3.24}$$

where the extra T with respect to the notation defined in connection with (3.7) denotes target reflected signal. The bistatic clutter reflected signal may be analogously written as

$$S_{Clutter} = \frac{P_T G_{T,C} G_{R,C} \lambda^2 \sigma_B^0 F_{T,C}^2 F_{R,C}^2}{(4\pi)^3 R_{T,C}^2 R_{R,C}^2 L_{T,C} L_{R,C}}, \tag{3.25}$$

where $\sigma_B^0 = \gamma\sqrt{\sin\theta_i \sin\theta_s}$, is the scattering coefficient in the bistatic scatter region, and θ_i and θ_s are the incident and scattering angles respectively as defined in the bistatic chapter written by N. Willis in [60]. For convenience, γ will cover the terrain reflectivity as well as the urban reflectivity, realizing that this is an oversimplification. The extra C with respect to the notation defined in connection with (3.7) denotes clutter reflected signal. The direct signal may be written as

$$S_{DirectSignal} = \frac{P_T G_{T,D} G_{R,D} \lambda^2 F_D^2}{(4\pi)^2 R_D^2 L_D}, \tag{3.26}$$

where the D-notation denotes the direct signal, and R_D is the distance from the transmitter to the receiver, F_D is the pattern propagation factor, and L_D is all the other losses not accounted for in connection with the DSI.

The DSI interference is the ratio of signal-to-direct signal, S/D, which is

$$\frac{S}{D} = \frac{G_{T,T}}{G_{T,D}} \frac{G_{R,T}}{G_{R,D}} \frac{\sigma_B}{4\pi} \frac{F_{T,T}^2 F_{R,T}^2}{F_D^2} \frac{L_D}{L_{T,T} L_{R,T}} \frac{R_D^2}{R_{T,T}^2 R_{R,T}^2}. \tag{3.27}$$

In general, $G_{T,T} \neq G_{T,D}$, unless the target is on the baseline between transmitter and receiver, or on the extended baseline at the receiver side. Nevertheless, most broadcast transmitters are considered to be omni-directional, and it will be assumed $G_{T,T} = G_{T,D}$. The system losses are assumed to be $L_D = 1$, $L_{T,T} = 1$, and $L_{R,T} = 1$, while the target pattern propagation factors, $F_{T,T} = 1$ and $F_{R,T} = 1$, which leaves

$$\frac{S}{D} = \frac{G_{R,T}}{G_{R,D}} \frac{\sigma_B}{4\pi} \frac{1}{F_D^2} \frac{R_D^2}{R_{T,T}^2 R_{R,T}^2}. \tag{3.28}$$

Under the same conditions for the clutter case

$$\frac{S}{C} = \frac{G_{R,T}}{G_{R,C}} \frac{\sigma_B}{\sigma_B^0} \frac{1}{F_{T,C}^2 F_{R,C}^2} \frac{R_{T,C}^2 R_{R,C}^2}{R_{T,T}^2 R_{R,T}^2}. \tag{3.29}$$

These formulas will be part of the basis for the performance estimations of section 4.1.

3.4 Multipath

The multipath may be defined as all reflections off the target received in the receiver, excluding the transmitter-target-receiver path. One example may be the path transmitter-ground-target-receiver, which in principle will have a different Doppler shift than the transmitter-target-receiver path, which may pose problems for the target association. The time delay will be different, and might end up as an extra target detection. However, probably the most problematic issue about multipath (besides the DSI issue), is the destructive interference issue, where a target may not be detected due to the super positioning of the same signal resulting multipath. This is believed to be the reason for the systematically misdetections of the FM based PBR described in [41]. In the paper, a bistatic two way propagation model is used to investigate the received signal level at the receiver as a function of geometry. In addition to the traditional transmitter-target-receiver path, two additional paths are added: transmitter-ground-target, and target-ground-receiver. Analyzing the received signal level for these, the reported FM based PBR system's systematic misdetections during the trials are believed to be explained.

In many radar systems the multipath is also the cause of erroneous height estimates [86, Multipath error]. However, target height estimates in the broadcast based PBRs are not based on elevation lobing, but rather TDOA measurements, and then ellipsoidal intersections, and thus unless the multipath makes the TDOA measurements wrong, it is not believed that multipath will influence on target elevation estimates.

3.5 Signal processing

Figure 3.15 shows a generic passive radar processing scheme by Paul Howland [13]. Normally, the passive radar is exploiting transmitters of opportunity, and thus needs to record the transmitted signal as well as the target reflected signal. This is indicated in Howland's figure by the two antenna types, reference and surveillance antenna, resulting in two separate signal channels, reference channel and surveillance channel. The figure indicates that the reference channel is a single antenna, while the surveillance antenna is an array of many antennas. This is not necessarily the case, as the most prominent systems, Lockheed Martin's SS3 and Thales' HA100, both are using the same antenna array to record the direct signals, as well as the target reflected signals, though in separate channels. This means that the beamforming might be done for both the reference and surveillance channel.

The next step in the passive radar signal processing, is the signal conditioning. This

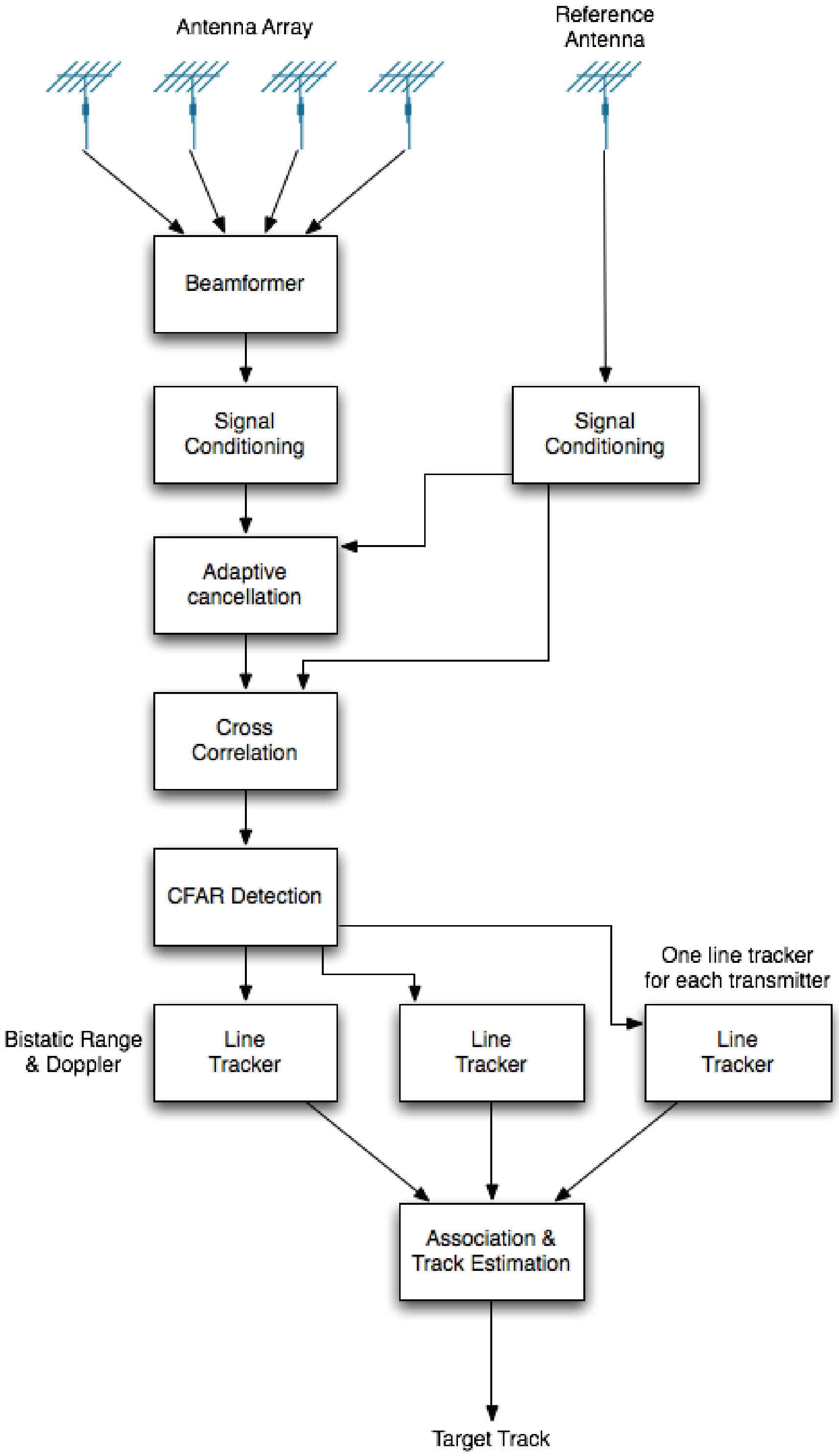

Figure 3.15: The figure shows a generic passive radar signal processing scheme, from [13].

step may include high quality analogue bandpass filtering of the signal, channel equalization to improve the quality of the reference signal, removal of unwanted structures in digital signals to improve the radar ambiguity function or even complete reconstruction of the reference signal from the received digital signal [13]. The main limiting detection factor is the reception/interference of the direct signal from the exploited transmitter in the surveillance channel, chapter 3.3. After the correlation process, the strong direct signal sidelobes may mask targets on the range-Doppler surface. Howland et. al. [44, pp. 108], illustrates this by an example from the NC3A system, where a target echo from a target at a range of $\sqrt{R_T R_R} = 150km$ given a RCS of $\sigma_B = 10dBSm$, would be $S_D/S_T = -90dB$ below the received direct signal if no signal interference rejection was applied. In order to avoid this, an adaptive filter is normally used in a least square process, [36], or more advanced versions of this might be developed [35]. The NC3A sensor's adaptive filtering is described in [23, pp. 292-295] and [44].

The next step in the signal processing is the correlation process, where the basis for the target detection and positioning is made. The correlation process produces the range-Doppler surfaces, where the targets are detected, and initial tracking is established after CFAR detection. The correlation process is the step where the reference and surveillance channels are processed together, and the reference and surveillance channels cease to exist. Although the reference and surveillance channels were processed together in the adaptive filtering step, they were still two separate channels. Only after the correlation step, where the bistatic range-Doppler surfaces are created, the CFAR, line tracking, and finally association and Cartesian track estimation are performed.

Figure 3.15 tells nothing about when the signals are digitized, which might be very system specific. If you digitize as early as possible, i.e. close to the antenna receiving elements, you gain flexibility, but might run into problems with A/D (Analog to Digital) dynamic range since the direct signal might be several orders of magnitude stronger than the target reflected signal, and you are receiving this at each element. On the other side, if you would like to do the beamforming and DSI cancellation before the digitalization process, you are trading flexibility for the relaxed dynamic range requirement.

The focus of this research is on the correlation process, and three of the most common ways to process the reference and surveillance channels follow. The two most straightforward algorithms are analogous to the calculation of the ambiguity function (3.22) [23, pp. 297-298],

$$|\Psi(\tau,\nu)| = \left| \sum_{n=0}^{N-1} e(n) d^*(n+\tau) e^{j2\pi\nu n/N} \right|^2 , \tag{3.30}$$

where j is the complex constant $j = \sqrt{-1}$, Ψ denotes the discrete amplitude-range-Doppler surface, $e(n)$ is the sampled filtered echo signal, and $d(n)$ is the sampled reference signal, τ is the time delay corresponding to the bistatic TDOA, and finally ν is the Doppler shift of interest [23, pp. 297-298]. There are two ways of interpreting this, as will be discussed in the next two sections.

3.5.1 Cross correlation approach

Equation (3.30) [23, pp. 297-298] may be interpreted as the correlation between $e(n)$ and $d(n)e^{j2\pi\nu(n/N)}$, where it is noted that the latter is a frequency shifted version of $d(n)$, and this can be very efficiently obtained by cyclic shifting the Discrete Fourier Transform (DFT)/Fast Fourier Transform (FFT) transformed version of $d(n)$. The correlation for all ranges, but one Doppler velocity is then calculated by multiplying each element of the DFT/FFT transformed $e(n)$ with each element of the shifted DFT/FFT transformed $d(n)$, and finally apply an Inverse Discrete Fourier Transform (IDFT)/Inverse FFT (IFFT) on the result vector. This will calculate (3.30) for all ranges, but one Doppler value ν. Further details are available in [23, pp. 297-298].

3.5.2 Discrete Fourier transform approach

On the other hand [23, pp. 297-298], if one is interested in all possible Doppler shifts, for one range, the most efficient way of doing this is by considering (3.30) as the Fourier transform of $e(n)d^*(n+\tau)$. This is easily achieved by element wise rotating, corresponding to the delay τ, in order to obtain $d^*(n+\tau)$, and then calculate the DFT/FFT of the element wise product of $e(n)$ and the rotated $d^*(n)$. This will calculate all the possible Doppler shifts for one range, corresponding to the delay τ. Further details are available in [23, pp. 297-298].

3.5.3 Efficient range Doppler processing

Both the above mentioned processing algorithms are efficient if only a few range cells or Doppler velocities shall be calculated. Normally, the interest is in a span of ranges and Doppler velocities, and the following algorithm provides an efficient way of achieving this. The method is briefly presented in [23, pp. 301-303], but full details can be found in [116, 117].

The CW transmitted and reflected surveillance signal is received, down converted, filtered and IQ sampled such that the resulting signal may be written[2], and section A.1,

$$U_{sur}(t_i) = \sum_{m=0}^{M-1} \xi_{sur}^m(t_i - \nu_m) u_{sur}^m(t_i - \nu_m) e^{j2\pi\left((f_c + f_D^m - f_{sur})t_i - f_c\nu_m - (t_R - t_L)f_D^m + \phi_c\right)}, \quad (3.31)$$

where M is the number of targets, $u_{sur}^m(t_i - \nu_m)$ is the received surveillance information signal, $\xi_{sur}^m(t_i - \nu_m)$ is a complex function accounting for time varying amplitude and phase shift, both functions for the mth target. $\nu_m = (t_T + t_R - t_L) = (R_T + R_R - L)/c$, from figure 3.2, while f_D^m is the assumed constant Doppler shift of the mth target, and f_c is the carrier/center frequency of the broadcasted signal/channel where ϕ_c is the initial phase of the broadcasted carrier/center frequency. f_{sur} accounts for the down conversion in the

---

[2] There exist several ways of realizing the reception, down conversion, (conditioning and adaptive) filtering and IQ conversion (if applied) of signals to baseband, figure 3.15. The alternatives require different mathematical formulations in order to be precise, however, the majority of them end up in a form like (3.31).

receiver, and the signal is sampled with sampling frequency f_s, yielding the sampling times $t_i = i/f_s$ for $i = 0, 1, 2, \ldots, S-1$, where $S > 0$ is the integer number of samples. [116] showed that (3.31) can in a logical way be recast in the two dimensional function

$$z_{sur}(i, s) \overset{\text{def}}{=} U_{sur}(t_{i+sN}), \tag{3.32}$$

for $i = 0, 1, 2, \ldots, 2N-1$, and $s = 0, 1, 2, \ldots, A-1$, where $N > 0$ and $A > 0$ are integers such that $(A+1)N \leq S$. Further rearranging terms in (3.31) and (3.32) yields

$$z_{sur}(i, s) = \sum_{m=0}^{M-1} \alpha_{sur}^m(t_{i+sN} - \nu_m) u_{sur}^m(t_{i+sN} - \nu_m) e^{j2\pi(f_c + f_D^m - f_{sur})t_{i+sN}}, \tag{3.33}$$

for $i = 0, 1, 2, \ldots, 2N-1$, and $s = 0, 1, 2, \ldots, A-1$, where

$$\alpha_{sur}^m(t_{i+sN} - \nu_m) = \xi_{sur}^m(t_{i+sN} - \nu_m) e^{j2\pi(-f_c\nu_m - (t_R - t_L)f_D^m + \phi_c)} \tag{3.34}$$

is a complex time dependent function.

The reference signal is after reception, down conversion, (conditioning) filtering and IQ sampling written as described in section A.1

$$U_{ref}(t_i) = \xi_{ref}(t_i) u_r(t_i) e^{j2\pi((f_c - f_{ref})t_i + \phi_c)}, \tag{3.35}$$

where $i = 0, 1, 2, \ldots, S-1$ for $S > 0$, an integer number of samples. $\xi_{ref}(t_i)$ plays the equivalent role for the direct path propagation as $\xi_{sur}(t_i)$ plays for the target reflected path, and f_{ref} is the frequency down conversion in the receiver. In the derivation of (3.35) in section A.1 the receiver's position was defined to be at zero range. Analogously to the surveillance signal,

$$z_{ref}(i, s) = \begin{cases} U_{ref}(t_{i+sN}) & i = 0, 1, 2, \ldots, N-1 \\ 0 & i = N, N+1, \ldots, 2N-1 \end{cases} \tag{3.36}$$

$s = 0, 1, 2, \ldots, A-1$, where $N > 0$ and $A > 0$ are integers such that $(A+1)N \leq S$. (3.36) inserted (3.35) yields

$$z_{ref}(i, s) = \begin{cases} C_i \alpha_{ref}(t_{i+sN}) u_{ref}(t_{i+sN}) e^{j2\pi(f_c - f_{ref})t_{i+sN}} & i = 0, 1, 2, \ldots, N-1 \\ 0 & i = N, N+1, \ldots, 2N-1 \end{cases}, \tag{3.37}$$

where C_i is a digital filter. The time varying complex function α_{ref} is

$$\alpha_{ref}(t_{i+sN}) = \xi_{ref}(t_{i+sN}) e^{j2\pi\phi_c}. \tag{3.38}$$

The cross-correlation between the two complex discrete functions $x(i)$ and $y(i)$, $i =$

$0, 1, 2, \dots, 2N-1$ is defined as

$$\hat{z}(i) \overset{\text{def}}{=} \sum_{n=0}^{2N-1} x^*(n) y(n+i) \tag{3.39}$$

where $x^*(n)$ is the complex conjugate of $x(n)$, and consequently the cross-correlation between $z_{ref}(i,s)$ and $z_{sur}(i,s)$ can after a minor rearranging of terms be written

$$\begin{aligned}\hat{z}(i,s) = &\sum_{n=0}^{N-1} \sum_{m=0}^{M-1} C_n \alpha_{ref}^*(t_{n+sN}) \alpha_{sur}^m(t_{n+i+sN} - \nu_m) u_{ref}^*(t_{n+sN}) u_{sur}^m(t_{n+i+sN} - \nu_m) \times \\ &e^{j2\pi(f_{ref} - f_{sur} + f_D^m)t_n} e^{j2\pi(f_{ref} - f_{sur} + f_D^m)t_{sN}} e^{j2\pi(f_c - f_{sur} + f_D^m)t_i}\end{aligned} \tag{3.40}$$

for $i = 0, 1, 2, \dots, 2N-1$ and $s = 0, 1, 2, \dots, A-1$.

Range estimate

The range is estimated by the correlation, and for a one reflector case, $\alpha_{sur}^m(t_{i+sN} - \nu_m) = 0$ for all $m \neq k$ for all values of i, and one value of s, since the situation will be comparable for all $s = 0, 1, 2, \dots, A-1$. Equation (3.40) can be written

$$\begin{aligned}\hat{z}(i,s) = &e^{j2\pi(f_{ref} - f_{sur} + f_D^k)t_{sN}} e^{j2\pi(f_c - f_{sur} + f_D^k)t_i} \sum_{n=0}^{N-1} C_n \alpha_{ref}^*(t_{n+sN}) \alpha_{sur}^k(t_{n+i+sN} - \nu_k) \times \\ &u_{ref}^*(t_{n+sN}) u_{sur}^k(t_{n+i+sN} - \nu_k) e^{j2\pi(f_{ref} - f_{sur} + f_D^k)t_n},\end{aligned} \tag{3.41}$$

leading to the absolute value

$$\begin{aligned}|\hat{z}(i,s)| = \Bigg| &\sum_{n=0}^{N-1} C_n \alpha_{ref}^*(t_{n+sN}) \alpha_{sur}^k(t_{n+i+sN} - \nu_k) \times \\ &u_{ref}^*(t_{n+sN}) u_{sur}^k(t_{n+i+sN} - \nu_k) e^{j2\pi(f_{ref} - f_{sur} + f_D^k)\frac{n}{f_s}} \Bigg|.\end{aligned} \tag{3.42}$$

Further, assume that there is no time dependent variations in the received signal as a consequence of anomalous propagation, i.e. one path direct propagation from transmitter to receiver, and no phase or amplitude variations due to inhomogeneous medias, leading (3.38) to

$$\alpha_{ref}(t_{n+sN}) = \xi_{ref}(t_{n+sN}) e^{j2\pi\phi_c} = \alpha_{ref} = \xi_{ref} e^{j2\pi\phi_c}, \tag{3.43}$$

where ξ_{ref} is a real positive constant. Equivalently for (3.34)

$$\begin{aligned}\alpha_{sur}^k(t_{n+i+sN} - \nu_k) = &\xi_{sur}^k(t_{i+sN} - \nu_k) e^{j2\pi(-f_c\nu_k - (t_R - t_L)f_D^k + \phi_c)} \times \\ = &\alpha_{sur}^k = \xi_{sur}^k e^{j2\pi(-f_c\nu_k - (t_R - t_L)f_D^k + \phi_c)},\end{aligned} \tag{3.44}$$

where ξ_{sur} is a real positive constant. The product $\alpha^*_{ref}(t_{i+sN})\alpha^k_{sur}(t_{n+i+sN}-\nu_k)$ in (3.42) can then be written

$$\alpha^*_{ref}(t_{i+sN})\alpha^k_{sur}(t_{n+i+sN}-\nu_k) = \alpha^*_{ref}\alpha^k_{sur} = \xi^*_{ref}\xi^k_{sur}e^{j2\pi(-f_c\nu_k-(t_R-t_L)f^k_D)}, \tag{3.45}$$

which is a product independent of time and the summing index n. The range to the target is found by maximizing the product of the two functions $u^*_{ref}(t_{n+sN})$ and $u^k_{sur}(t_{n+i+sN}-\nu_k)$ in (3.42) for the index i.

A general result, [118, pp. 143], of the autocorrelation function is that it attains its maximum value at the origin. The product of the two functions $u^*_{ref}(t_{n+sN})$ and $u^k_{sur}(t_{n+i+sN}-\nu_k)$ can be thought of as time shifted versions of each other, and thus the cross-correlation between them will be a time shifted version of the autocorrelation, and will attain its maximum value at $t=\nu_k$ instead of at the origin. Equation (3.42) inserted (3.45) for $C_n = 1$ $n = 0,1,2,\ldots,N-1$, $f_{ref} = f_{sur}$, and $f^k_D = 0$ is solved

$$\left|\sum_{n=0}^{N-1} u^*_{ref}(t_{n+sN})u^k_{sur}(t_{n+i+sN}-\nu_k)\right|_{\max} = \omega_{\max}(s), \tag{3.46}$$

for i, which yields $i = [\nu_k f_s]$, where $[x]$ means the integer value of x. The ambiguity functions for FM radio, DAB, and DVB-T signals have been extensively studied, and thus it might be concluded that equation (3.46) also will hold for $f^k_D \neq 0$ and f^k_D of realistic target Doppler dimensions, [27–34]. The correlation, (3.42), is now

$$|\hat{z}([\nu_k f_s], s)| \approx |\alpha^*_{ref}||\alpha^k_{sur}|\left|\sum_{n=0}^{N-1} C_n u^*_{ref}(t_{n+sN})u^k_{sur}(t_{n+sN})e^{j2\pi(f_{ref}-f_{sur}+f^k_D)\frac{n}{f_s}}\right|. \tag{3.47}$$

The informative exercise of choosing $C_n = 1$ and $u^*_{ref}(t_{n+sN})u^k_{sur}(t_{n+sN}) = 1$ for $n = 0,1,2,\ldots,N-1$ and $s = 0,1,2,\ldots,A-1$, results in the sum of (3.47) reducing to a geometrical sum which can be found in mathematical tables [119, 120] to be

$$\sum_{n=0}^{N-1}\left(e^{j2\pi(f_{ref}-f_{sur}+f^k_D)/f_s}\right)^n = \left\{\begin{array}{ll} N & f = 0,\pm1,\pm2,\ldots \\ \frac{\sin N\pi f}{\sin \pi f}e^{j(N-1)\pi f} & f \neq 0,\pm1,\pm2,\ldots \end{array}\right., \tag{3.48}$$

for $f = (f_{ref}-f_{sur}+f^k_D)/f_s$. The above sum's zeros are given by

$$(f_{ref}-f_{sur}+f^k_D) = \frac{f_s}{N}p \qquad p = 0,\pm1,\pm2,\ldots \quad \text{and} \quad p \neq mN,\ m = 0,\pm1,\pm2,\ldots . \tag{3.49}$$

This exercise shows that the correlation between the reference and surveillance signal will be degraded by the target's Doppler shift, and even nulls may appear, which might to some extent be filtered away as shown in figure 3.16. Figure 3.16 shows the effect of applying various filters, C_n for $n = 0,1,2,\ldots,N-1$ in the sum

$$\sum_{n=0}^{N-1}\left(C_n e^{j2\pi(f_{ref}-f_{sur}+f^k_D)/f_s}\right)^n, \tag{3.50}$$

as a function of target Doppler shift f_D^k, for no filter, Hamming, Hann and Blackman-Harris [121]. This is in principle the situation of $\alpha^*_{ref}(t_{n+sN})\alpha^k_{sur}(t_{n+i+sN} - \nu_k) = 1$ and $u^*_{ref}(t_{n+sN})u_{sur}(t_{n+sN}) = 1$, $i = [\nu_k f_s]$, and $f_{ref} = f_{sur}$ of equation (3.47). Two sets of parameters were applied, one FM radio like, where it was assumed that the sampling frequency was $f_s = 200kHz$, the carrier frequency of the transmitted signal was $f_c = 100MHz$, and it was required that maximum Doppler shift should be no higher than a velocity of $v_{\max} = \pm 300m/s$ with Doppler span $\Delta v = 600m/s$, resulting in (the span Pulse Repetition Frequency (PRF)) $f_s/N = 200Hz$, and $N = 1000$. For the DVB-T case, it was assumed that $f_s = 10MHz$, $f_c = 800MHz$, and required $v_{\max} = \pm 300m/s$, which resulted in $f_s/N = 1600Hz$, and $N = 6250$.

By carefully choosing the values of f_{ref} and f_{sur}, the correlation response of the correlation may be put at a frequency of choice (3.52). I.e. it might be handy to choose $f_{ref} - f_{sur} = 100Hz$, which would place the correlation response window at $\pm 100Hz$ in figure 3.16 for the FM radio example, in contrast to $f_{ref} = f_{sur}$, which means the window is ranging from $0Hz$ to $200Hz$.

The fraction N/f_s is the coherent correlation interval for *one correlation* vector, as is illustrated in figure 3.17c. The interval is determined by equations (3.32) and (3.37), which defines the reference signal for one row in the matrix to be N samples, which also might be considered to be the $PRF = N/f_s$ of the processing, which also will determine the unambiguous range to be $R_{unamb} = c/PRF = cN/f_s$. In the correlation $2N$ samples are processed, which is a result of the fact that one correlated range gate, is the result of a two channel correlation, each of N samples. The reference channel is defined in such a way that N filtered samples from the reference channel is followed by N trailing zeros, correlated against $2N$ samples from the surveillance channel, resulting in a N samples unambiguous range. The trailing zeros also ensures that the N samples range is not interfered by the cyclic FFT/IFFT methods used to perform the correlation.

Doppler estimate

In order to extract the target Doppler shift, $\alpha^m_{sur}(t_i - \nu_m) = 0$ for all $m \neq k$, equation (3.40) is recasted into

$$\begin{aligned}\hat{z}(i,s) =& e^{j2\pi(f_c - f_{sur} + f_D^k)t_i} \left[\sum_{n=0}^{N-1} C_n \alpha^*_{ref}(t_{n+sN}) \alpha^k_{sur}(t_{n+i+sN} - \nu_k) \times \right. \\ & \left. u^*_{ref}(t_{n+sN}) u^k_{sur}(t_{n+i+sN} - \nu_k)\; e^{j2\pi(f_{ref} - f_{sur} + f_D^k)t_n} \right] e^{j2\pi(f_{ref} - f_{sur} + f_D^k)\frac{N}{f_s}s}\end{aligned} \tag{3.51}$$

for $i = 0, 1, 2, \ldots, 2N-1$ and $s = 0, 1, 2, \ldots, A-1$, which in turn may be recast into

$$\hat{z}(i,s) = K(i,s,k) e^{j2\pi(f_{ref} - f_{sur} + f_D^k)\frac{N}{f_s}s}, \tag{3.52}$$

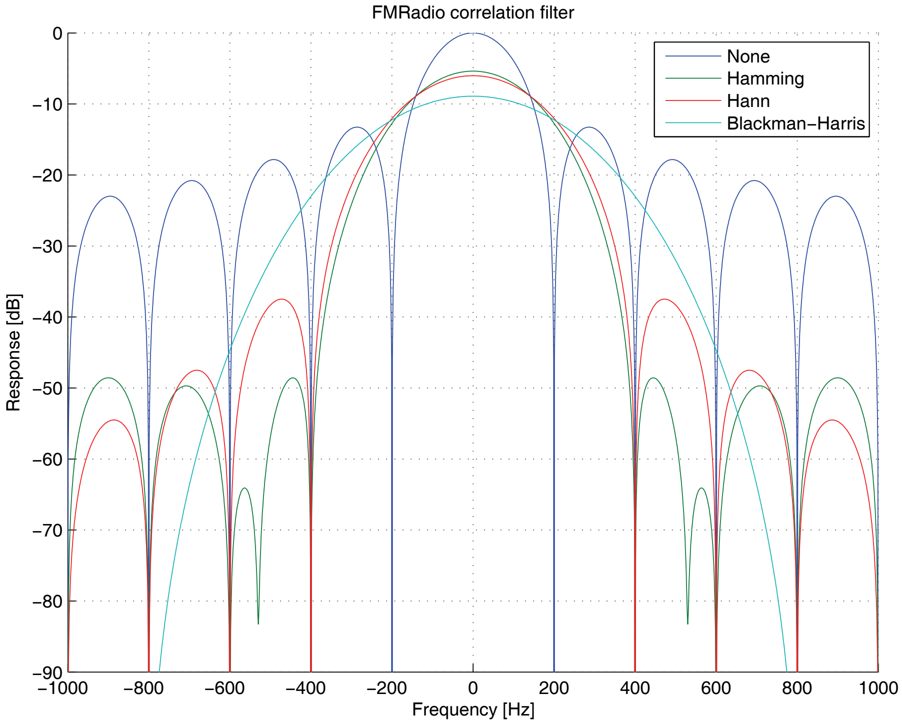

(a) The FM radio set of parameters, assuming $f_s = 200kHz$, $f_T = 100MHz$, and requiring $v_{\max} = \pm 300m/s$, yields $f_s/N = 200Hz$, and $N = 1000$.

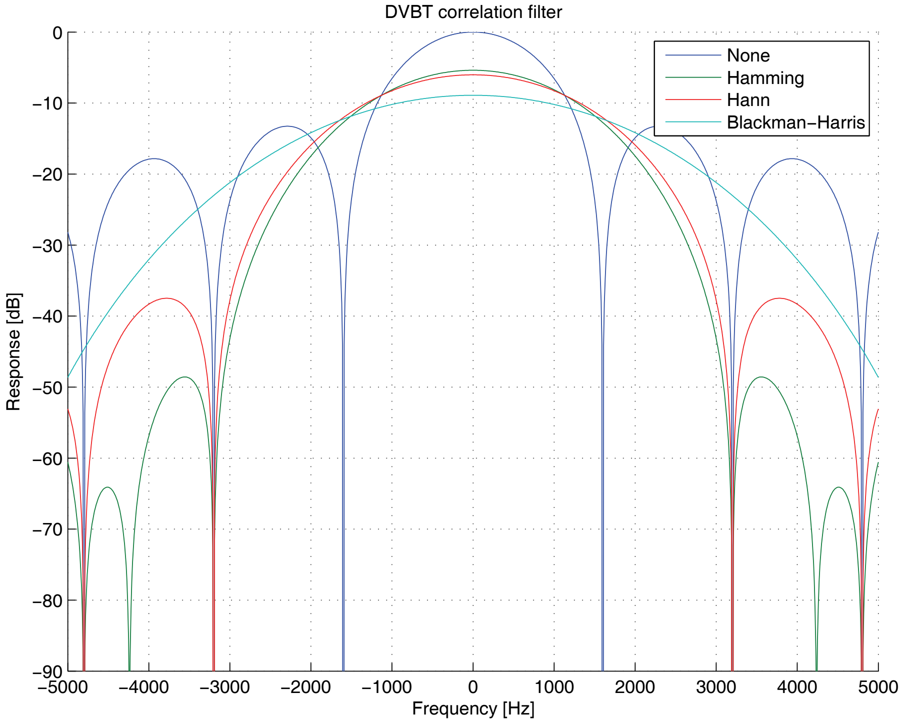

(b) DVB-T set of parameters, assuming $f_s = 10MHz$, $f_T = 800MHz$, and requiring $v_{\max} = \pm 300m/s$, yields $f_s/N = 1600Hz$, and $N = 6250$.

Figure 3.16: The filter effect, C_n, on the sum in (3.50), where the frequency on the x-axis refers to the Doppler shift, i.e. f_D^k.

where

$$\begin{aligned} K(i,s,k) = & e^{j2\pi(f_c - f_{sur} + f_D^k)t_i} \left[\sum_{n=0}^{N-1} C_n \alpha_{ref}^*(t_{n+sN}) \alpha_{sur}^k(t_{n+i+sN} - \nu_k) \times \right. \\ & \left. u_{ref}^*(t_{n+sN}) u_{sur}^k(t_{n+i+sN} - \nu_k)\ e^{j2\pi(f_{ref} - f_{sur} + f_D^k)t_n} \right], \end{aligned} \tag{3.53}$$

for $i = 0, 1, 2, \ldots, 2N-1$ and $s = 0, 1, 2, \ldots, A-1$. $K(i,s,k)$ depends on the correlation properties of $\alpha_{ref}(t_i)u_{ref}(t_i)$ and $\alpha_{sur}(t_i)u_{sur}(t_i)$ for $i = 0, 1, 2, \ldots, 2N-1$, and thus N, as well as the start of the processing, i.e. when is t_0. For each range correlation, i.e. fixed value of s and varying values of i, the variation of $K(i,s,k)$ can be interpreted as the target's response in the correlation process described in the previous section, modified by the correlation properties of $u(t_i)$, as well as the propagation contribution of $\alpha_{ref}(t_i)$ and $\alpha_{sur}(t_i)$. Stable electromagnetic conditions, (3.45), and the fact that $i = [\nu_k f_s]$ is considered a constant parameter (one range bin is considered), shows that the only time varying component in (3.53) is $u(t)$. In the case of a periodic $u(t)$, the PRF should be chosen PRF$=N/f_s$, in order to be equal to the periodicity of $u(t)$. In that case $K(i,s,k)$ is constant over $s = 0, 1, 2, \ldots, A-1$ for fixed values of i and k. This was the case of the Norwegian Multistatic radar system Digital Multistatic Radar (DiMuRa) [116, 122–125]. For PBR systems this cannot be expected to be the case, and thus it has to be taken into consideration that the function $u(t)$ is time varying, which will be treated in section 5.2. For the general case, it will be assumed that the variations of $u(t)$ over the chosen period is of such a character that $K(i,s,k)$ is relatively stable over $s = 0, 1, 2, \ldots, A-1$. Equation (3.52) clearly shows the need to compensate $\exp\left(j2\pi(f_{ref} - f_{sur} + f_D^k)sN/f_s\right)$ in (3.52) with a term $\exp\left(-j2\pi(f_{ref} - f_{sur})sN/f_s\right)$, which is readily implemented by a vector multiplication for all values of $s = 0, 1, 2, \ldots, A-1$.

As already mentioned, by carefully choosing the values of f_{ref} and f_{sur}, the correlation response may be placed at a frequency of choice (3.52). I.e. it might be handy to choose $f_{ref} - f_{sur} = 100Hz$, which would place the correlation response window at $\pm 100Hz$ in figure 3.16 for the FM radio example, in contrast to $f_{ref} = f_{sur}$, which means the window is ranging from $0Hz$ to $200Hz$.

The target's Doppler frequency is now found through a FFT of equation (3.52) for all $s = 0, 1, 2, \ldots, A-1$ for each of the ranges $i = 0, 1, 2, \ldots, M-1$[3], i.e. for all the M ranges of interest. A problem may arise when multiple range correlations are combined in the FFT of (3.52), where the correlation variations results in an amplitude modulated wave, which might be smeared in the FFT in contrast to the constant amplitude wave, which will not be smeared to the same extent. It should be noted that some amplitude modulations are not as severe as they might seem. Normally uniformly distributed noise will not affect the peak after the FFT seriously, while a linear function amplitude increase or decrease, or sinusoidal amplitude modulation, will deteriorate the peak of the FFT more.

---

[3] It is important to keep in mind that now the index i corresponds to one range bin, and $s = 0, 1, 2, \ldots, A-1$ corresponds to all the Doppler bins, i.e. looking at all Doppler velocities at one range bin. This argument can obviously be made for all the i range bins, and thus all ranges Doppler velocities are found.

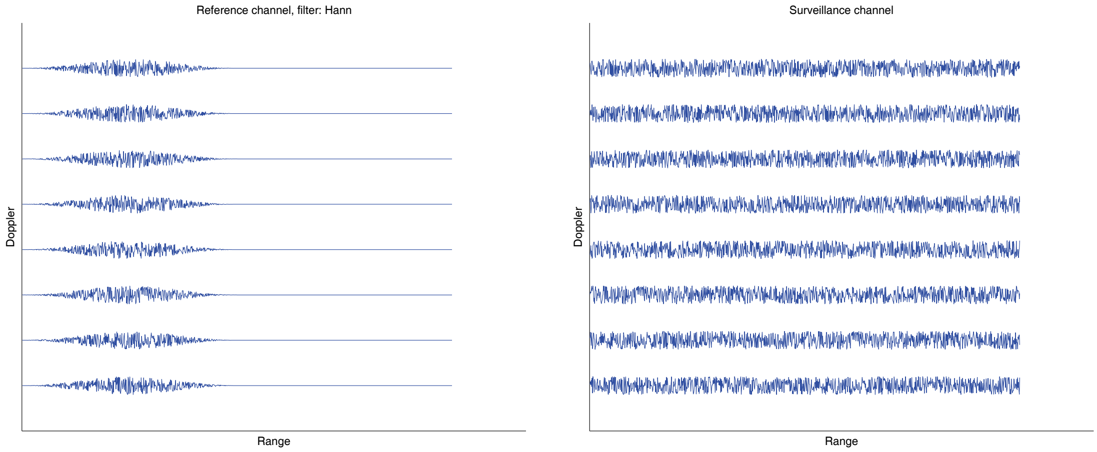

(a) Filtered reference channel

(b) Surveillance channel

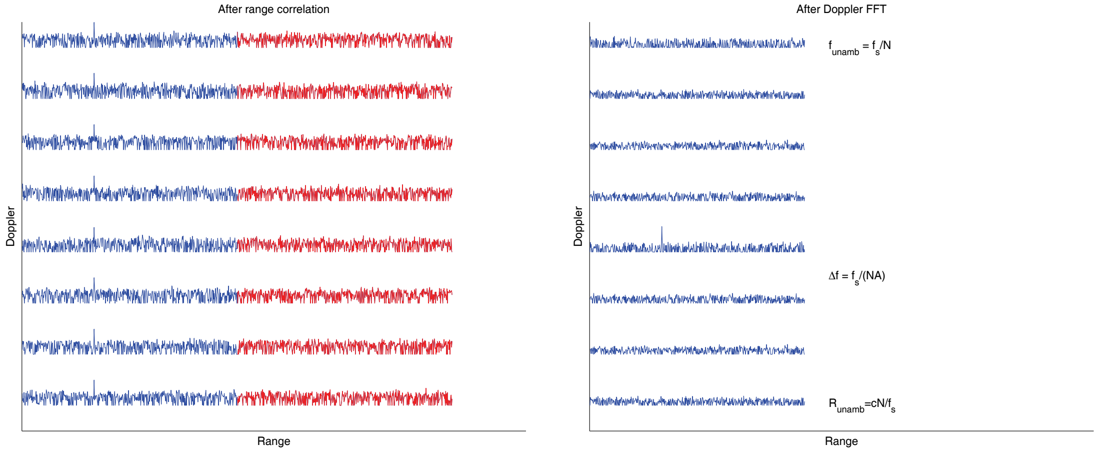

(c) After range correlation, red is discarded

(d) After Doppler FFT

Figure 3.17: The figure shows a schematic overview of the efficient range Doppler processing. Note that in figure c, the Doppler filter is not applied since it would make the target peaks at each Doppler bin nearly disappear (A=8, which is low).

However, for real life applications, there will be multipath effects, and time varying propagation conditions as well as time varying program content of the exploited broadcasted channels. The latter being severe for FM radio and well documented [3, 4, 22, 23, 26, 27, 29–31, 33, 36, 37, 40, 44]. For the digital waveforms the correlation stability due to waveforms are more predictable, as shown in [22, 23, 26, 31, 32, 40, 41, 116].

In order to lower the sidelobes of the FFT in the Doppler direction, a traditional window function/filter will be applied. Suitable filters are well described and the behavior documented in the well known work of Harris [121]. Mathematically, the filter will be denoted D_s, and be written (3.52)

$$\hat{z}(i,s) = K(i,s,k)D_s e^{j2\pi(f_{ref}-f_{sur}+f_D^k)\frac{N}{f_s}s} e^{-j2\pi f_p\frac{N}{f_s}s}, \tag{3.54}$$

for $s = 0, 1, 2, \ldots, A-1$ for all values of i, where the term $\exp\left(-j2\pi f_p sN/f_s\right)$ compensates for the term $\exp\left(j2\pi(f_{ref} - f_{sur})sN/f_s\right)$ of choice, normally this would be $f_p = f_{ref} - f_{sur}$.

Summary Range-Doppler Processing

The unambiguous range is $R_{unamb} = cN/(f_s) = c/PRF$, where the $PRF = f_s/N$ can be considered as "pulse repetition frequency". Further, the unambiguous Doppler is $f_{unamb} = f_s/N = PRF$, and the Doppler resolution is $\Delta f = f_s/(NA) = PRF/A$.

In summary, the efficient range-Doppler processing, also described in [23, pp. 301-303] and [116], consists of arranging the reference (3.35) and surveillance (3.32) sampled signals in two matrices, where a correlation along the range axis yields a response (not necessarily visible peak) at the correct target range. In the other direction, along the Doppler axis, a compensation term is applied, equation (3.54), and FFTs for all the ranges of interest in order to find the correct Doppler shift of the target is applied. The algorithm is very efficient since the correlation can be performed by use of FFT/IFFTs, and the Doppler FFTs is only required for the ranges of interest. Thus, target range and Doppler shift is calculated for all ranges and Doppler shifts within the limits as indicated above. Figure 3.17 illustrates the efficient range Doppler processing.

3.6 Summary

In summary, the classical theory of bistatic radar has been presented, with respect to PBR applications, and in particular resolution aspects. The definition(s) of bistatic radar was (were) reviewed in section 3.1.1, and a clear and unambiguous definition of bistatic radar is not yet formulated. This work defines bistatic radar according to the IEEE definition [82].

A generic passive radar signal processing scheme was briefly presented, as well as three ways of processing the range-Doppler surface (in the scheme called cross-correlation); the cross-correlation approach, the discrete Fourier transform approach, as well as the efficient range Doppler processing. The latter will be extended in chapter 5 in order to cope with multiple non-adjacent broadcasted channels.

Chapter 4

Hardware Design and Development

This chapter contains a brief description of the hardware used to collect real life data. The author has been supervising the top level design and ideas of the equipment (testing, functions, performance, dealing with the priorities, and finding the financing), but the credit for the technical as well as the practical solutions should be forwarded to the engineers at FFI, especially Steinar Johnsrud and Per Sørnes who designed the analog frontend for the DVB-T recordings. The author also recognizes the work performed by Jonas M. Christiansen, who has been managing the software (SW) installations and SW upgrades from the various manufacturers of the different subsystems. All SW supporting and organizing the data analysis of this thesis has been the work of the undersigned.

The driving motivation behind the data recording equipment were to be able to record both FM radio and DVB-T PBR target datasets of such a quality that analysis of longer periods, i.e. tens of minutes could be analyzed continuously. In addition to this, the whole FM band, as well as up to four non-adjacent DVB-T channels of choice, each of maximum $8MHz$ bandwidth, for both reference and surveillance channel should be recorded simultaneously. All this requirements were met by the equipment, as will be demonstrated in chapters 6 and 7.

4.1 Performance assessments

In order to gain insight into the performance expected from real life data collections, simple performance assessments based on the available system figures for the system will be presented. There are three geometries are explored for both FM radio and DVB-T, since all of them have powerful transmitters of both kinds with multiple frequencies being transmitted from all. Figure 4.1 shows the three transmitter sites of opportunity most suitable for PBR purposes in the Oslo region. The sites are Tryvannstaarnet (Tryvasshoegda for DVB-T), Holtberget (Kongsvinger for DVB-T), and Hoeyaas (Halden for DVB-T), while the receiver is placed on FFI premises. The trajectories of the commercial airliners going into Oslo airport Gardermoen are also displayed.

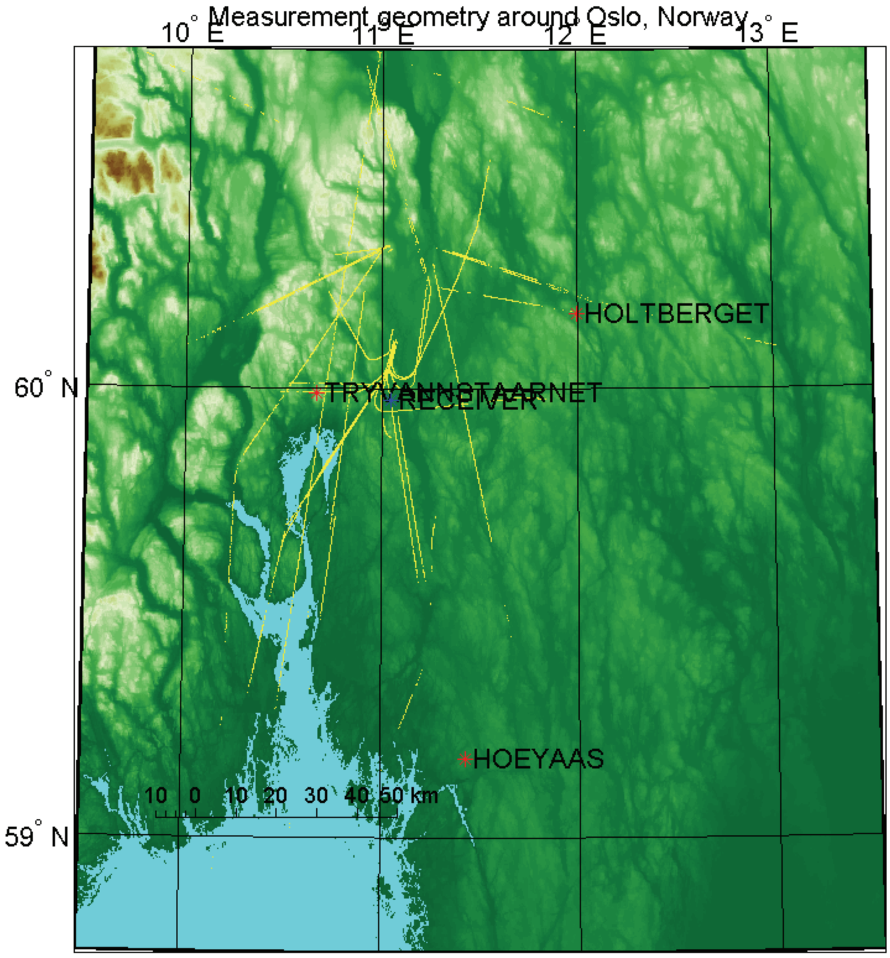

Figure 4.1: The PBR potential measurement geometries around Oslo, multiple frequency strong broadcasters in red, receiver position in blue, while the yellow lines indicates the commercial airline traffic going into Oslo airport Gardermoen.

Looking at the terrain cuts for the chosen geometries, the diffraction losses are seen to constitute an important part of the signal budget. The diffraction losses for the direct path between transmitter and receiver sites, F_D, were calculated using the ITU recommendation propagation by diffraction, P526-10 [14]. Table 4.1 shows the results for the diffraction calculations based on transmitter and receiver heights, the terrain profile between them from digital elevation maps, as well as a function of frequency. Examples of the one way diffraction losses for two geometries, and both the applicable frequencies, FM radio represented by $f = 100MHz$, and DVB-T represented by $f = 750MHz$ are shown in figures 4.2 and 4.3.

Due to the high level of irregular terrain which causes rather high diffraction losses (simple direct signal interference cancellation), it is believed that multipath with the direct path signal can be neglected in the calculations. However, being fully aware that the multipath still may cause signal scintillations, as is pointed out in the discussion in conjunction to figure 4.14a and is studied and modeled in [41]. Thus the performance is governed by the SNR described by equation (3.7), and the Signal to Direct signal Ratio (SDR) described by equation (3.28) together with the time-bandwidth product. The SNR

	Transmitter - FM radio		
Parameter	Tryvannstaarnet	Holtberget	Hoeyaas
90 $[MHz]$	24.0dB	36.4dB	41.5dB
100 $[MHz]$	24.0dB	36.8dB	42.1dB
110 $[MHz]$	24.1dB	37.2dB	42.7dB

	Transmitter - DVB-T		
Frequency	Tryvasshoegda	Kongsvinger	Halden
450 $[MHz]$	25.5dB	43.4dB	49.8dB
550 $[MHz]$	26.1dB	44.7dB	50.9dB
650 $[MHz]$	26.7dB	45.8dB	51.9dB
750 $[MHz]$	27.2dB	46.7dB	52.7dB
850 $[MHz]$	27.6dB	47.6dB	53.4dB

Table 4.1: The table shows the estimated diffraction losses as a function of transmitter and frequency.

for all systems, and geometries are calculated using equation (3.7), and the respective parameters are listed in table 4.2. In the same manner the SDR for all systems, and geometries are calculated using (3.28), and the corresponding parameters are listed in table 4.3. The calculations are summarized in table 4.4, and they show that all broadcasters probably will perform well with respect to SNR, however considering the DSI as well, the FM radio PBR relying of Tryvannstaarnet probably will not work due to the strong direct signal.

However, the interference and noise from adjacent channels is not included in the calculations. I.e. the single FM radio channel assigned band is $200kHz$, but way below the signal peak, the FM modulation turns out to be quite wide, maybe $1MHz$ wide, and this will cause problems in the processing, and it is claimed to limit the DSI suppression algorithms [22, 126]. This might be accounted for by subtracting dBs in the SNR from table 4.4, where for ranges of interest, the SNRs are quite high. And real life experiments show that the southern transmitter site (Hoeyaas/Halden) cannot work, probably due to the fact that it was hard to get a decent reference signal. According to the broadcasters channel plan, it should not be due to reuse of the frequencies, as there are no reuse of those at the eastern part of Norway. Subsequently, only the sites at Holtberget (FM radio and DVB-T), and Tryvannstaarnet (DVB-T only) will be considered.

Looking at the measured vertical antenna diagrams of some of the high power Norwegian FM radio broadcasters, it is noted that their vertical $-3dB$-beams are varying from 6 degrees to 8 degrees, while they all seems to be tilted one degree up. For the DVB-T broadcast antennas the elevation main beam is expected to be narrower, since from photos, the broadcast antenna arrays seem to be of the same rough size in elevation as the FM radio arrays. This might imply that a DVB-T PBR system will be less suitable for height coverage, and more suitable for low level coverage.

Table 4.5 shows the height coverage as a function of elevation, range, as well as the gain in elevation coverage due to the earth drop, or earth bulge, where the 4/3 earth's radius is applied in order to properly account for the refraction of radio waves in the atmosphere.

	Transmitter					
Parameter	Tryvannstaarnet FM radio	Tryvasshoegda DVB-T	Holtberget FM radio	Kongsvinger DVB-T	Hoeyaas FM radio	Halden DVB-T
P_T $[dB]$	40	35	37	37	40	38
ρ $[linear]$	1	1	1	1	1	1
G_T $[dB]$	10	10	10	10	10	10
G_R $[dB]$	8	22	8	22	8	22
t_c $[seconds]$	1	0.5	1	0.5	1	0.5
f_c $[MHz]$	100	750	100	750	100	750
σ_B $[dBsm]$	10	10	10	10	10	10
F_T $[dB]$	0	0	0	0	0	0
F_R $[dB]$	0	0	0	0	0	0
R_D $[km]$	21	21	57	57	91.5	91.5
R_T $[km]$	40	40	80	80	110	110
R_R $[km]$	20	20	20	20	20	20
L_T $[dB]$	0	0	0	0	0	0
L_R $[dB]$	0	0	0	0	0	0
L_sp $[dB]$	0	0	0	0	0	0
T_0 $[K]$	290	290	290	290	290	290
B $[kHz]$	50	8000	50	8000	50	8000
F $[dB]$	35	35	35	35	35	35

Table 4.2: The table lists the parameters and corresponding figures applied in (3.7) for SNRs calculation.

	Transmitter - FM radio		
Parameter	Tryvannstaarnet	Holtberget	Hoeyaas
$G_{R,D}$ $[dB]$	-10	-10	-10
F_D $[dB]$	-24	-37	-42
R_D $[km]$	21	57	91.5
$G_{R,T}$ $[dB]$	8	8	8
σ_B $[dBsm]$	10	10	10
$R_{T,T}$ $[km]$	40	80	110
$R_{R,T}$ $[km]$	20	20	20
B $[kHz]$	50	50	50
t_c $[seconds]$	1	1	1

	Transmitter - DVB-T		
Parameter	Tryvasshoegda	Kongsvinger	Halden
$G_{R,D}$ $[dB]$	-10	-10	-10
F_D $[dB]$	-26	-45	-50
R_D $[km]$	21	57	91.5
$G_{R,T}$ $[dB]$	20	20	20
σ_B $[dBsm]$	10	10	10
$R_{T,T}$ $[km]$	40	80	110
$R_{R,R}$ $[km]$	20	20	20
B $[kHz]$	8000	8000	8000
t_c $[seconds]$	0.5	0.5	0.5

Table 4.3: The table lists the specification, equation (3.28), figures for the evaluated FM radio and DVB-T based PBR geometries.

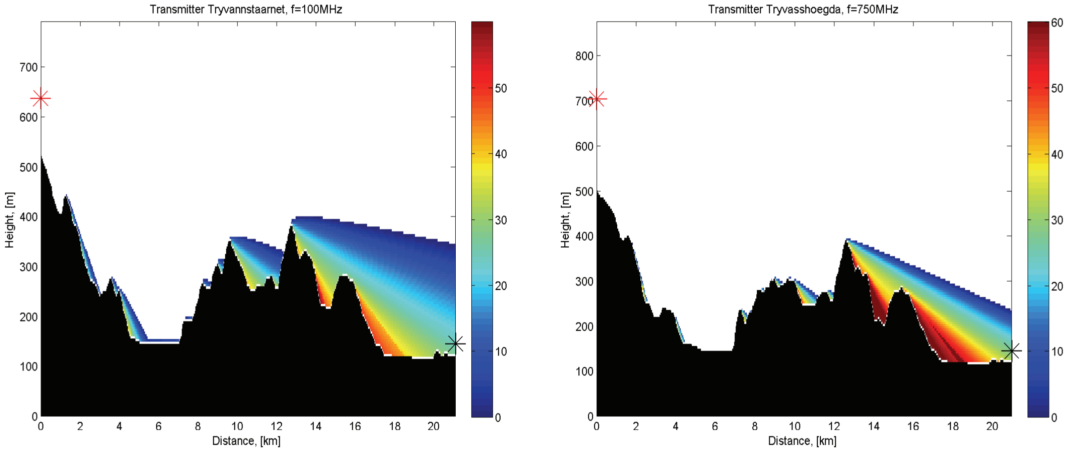

(a) $f = 100MHz$.

(b) $750MHz$.

Figure 4.2: The figure shows the diffraction loss as calculated using the ITU recommendation propagation by diffraction, P526-10 [14], for the (a) FM and (b) DVB-T transmitters at Tryvann.

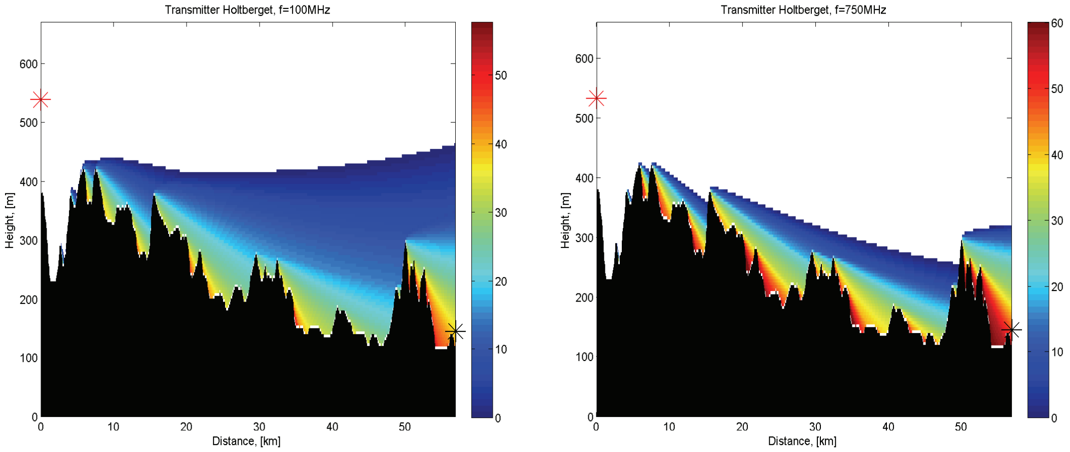

(a) $f = 100MHz$.

(b) $750MHz$.

Figure 4.3: The figure shows the diffraction loss as calculated using the ITU recommendation propagation by diffraction, P526-10 [14], for the (a) FM and (b) DVB-T transmitters at Kongsvinger.

	Transmitter - FM radio		
Parameter	Tryvannstaarnet	Holtberget	Hoeyaas
$S_{DR}[dB]$	-50.6	-35.0	-28.6
$TB\ [dB]$	47	47	47
$S_{DR}+TB\ [dB]$	-3.6	12.0	18.4
$SNR\ [dB]$	35.5	26.5	26.7

	Transmitter - DVB-T		
Parameter	Tryvasshoegda	Kongsvinger	Halden
$S_{DR}[dB]$	-36.6	-15.0	-8.6
$TB\ [dB]$	66	66	66
$S_{DR}+TB\ [dB]$	29.4	51.1	57.4
$SNR\ [dB]$	24.0	19.9	18.2

Table 4.4: The table shows the estimated performance figures for three PBR geometries for two types of transmitters, FM radio and DVB-T. TB is the time-bandwidth product.

$3dB$ point	Range				
$[Degrees]$	$10000m$	$30000m$	$50000m$	$100000m$	$200000m$
2	$349m$	$1048m$	$1746m$	$3492m$	$6984m$
4	$699m$	$2098m$	$3496m$	$6993m$	$13985m$
6	$1051m$	$3153m$	$5255m$	$10510m$	$21021m$
8	$1405m$	$4216m$	$7027m$	$14054m$	$28108m$
10	$1763m$	$5290m$	$8816m$	$17633m$	$35265m$
12	$2126m$	$6377m$	$10628m$	$21256m$	$42511m$
14	$2493m$	$7480m$	$12466m$	$24933m$	$49866m$

	Additional height coverage due to the earth's bulge				
	$10000m$	$30000m$	$50000m$	$100000m$	$200000m$
	$6m$	$53m$	$147m$	$589m$	$2355m$

Table 4.5: The upper table shows the height coverage in meters as a function of the angular elevation of the transmitter antenna $3dB$ upper point and range from the transmitter over flat earth, transmitter at zero altitude. The lower table shows in meters the additional height coverage (earth's bulge) due to the earth's curvature as a function of range for a transmitter at zero altitude. The 4/3-earth radius propagation by refraction is applied.

4.2 Description

The data recording equipment is mounted in a rack as shown in figure 4.4. The system consists of two storage servers with A/D capture cards inside, a control and processing computer with foldable screen and keyboard, an analog DVB-T frontend and an UPS. The rack also contains an Automatic Dependent Surveillance - Broadcast (ADS-B) receiver, which is used for recording the positions of the targets of opportunity.

The system is capable of recording two times (reference and surveillance) the FM radio band, $88 - 108MHz$, or 2×4 user selectable DVB-T channels in the UHF band ($474 - 850MHz$, channel 21-68, appendix B.4), each of $8MHz$ bandwidth. In order to intercept these signals, three types of antennas for the four input channels have been applied.

The FM radio band antennas are equal for the reference and surveillance channels. The two TRIAX FM (Band II - $87.5 - 108MHz$) Yagi antennas can be seen in figure 4.5a as the upper antenna (reference channel) and as the lower antenna in figure b (surveillance channel). The Yagi antenna has five elements, a reported gain of $8dB$, a front-to-back ratio of $20dB$, antenna beamwidth of 54 degrees, while the physical dimensions are $1932 \times 1577mm$, [127].

The DVB-T antennas for the reference and surveillance channels are not equal. The reference channel uses a Televes DAT75 Digital Tv Aerial with 75 elements [128]. The antenna is designed for the UHF channels $21 - 69$, which corresponds to the frequency band $474 - 858MHz$. It can be seen in figure 4.5a as the antenna below the FM antenna. The antenna has 75 elements, a reported gain close to $19dB$ at $800 - 850MHz$, while the gain nearly drops down to $12dB$ for $460MHz$. The front-to-back ratio is claimed to be $32dB$, the antenna beamwidth is believed to be around 20 degrees, and all these figures are believed to be valid for the higher frequencies, $800 - 850MHz$, [128]. No characteristics are made available for the lower frequencies, however the beamwidth is probably somewhere between 1.5 times (realistic) till 2 times (pessimistic, worst case) the size in both horizontal and vertical direction for the lowest frequencies compared to the highest frequencies.

The DVB-T antenna for the surveillance channel is a Funke Digital TV FFA4522 21/69 [129], and it can be seen in figure 4.5b as the antenna above the FM Yagi antenna. The antenna has a reported gain of gain $17dB$ for channel 21, and $24dB$ for channel 69. The horizontal beamwidth is for channel 21 reported to be 50 degrees, and for channel 69 reported to be 35 degrees, while the corresponding figures for the vertical beamwidth are 62 and 44 degrees, and finally the front-to-back ratio is claimed to be $26dB$, [129].

The antennas for the reference and surveillance channels are mounted on two large tripods, one for the reference channel's equipment, and one for the surveillance channel's equipment as partially seen in figure 4.5. Each tripod is equipped with a remotely controlled pan and tilt device and a videocamera. Normally the equipment is deployed on the roof of FFI, while being controlled from the indoor lab. This makes data collection fairly weather independent.

The two storage servers SAGAX SSS-3000 were bought from the Hungarian hardware manufacturer SAGAX [15]. Each of the servers have two RF inputs, one bandlimited channel, $88 - 112MHz$, and one channel with $200MHz$ analog bandwidth. In the following these channels are referred to as the FM (radio) channel and the wideband channel, respectively. The FM channel is built to record the FM radio spectrum, while the wideband channel is more versatile. In this work, the latter has been used to record the DVB-T signal(s), but in order to reflect the data recording equipment's versatility it is referred to as the wideband channel. The system is performing 14 bit (stored in 16 bits words) real sampling at $80MHz$, producing a data rate of 160MB/sec in each server. The servers are capable of recording data continuously for more than five hours. The servers may be controlled individually or together through a network as shown in figure 4.6.

The FM channel is designed to record the FM radio spectrum, and no additional hardware but an antenna with proper cable is required. However, in order to record the DVB-T signals an analog frontend was required. The frontend shown in figure 4.4, schematically in figure 4.7, was designed and developed by engineers[1] at FFI and has been named Dual Quad DVB-T Demodulator (DQD2). The DQD2 front-end comprises to identical channels, each capable of demodulating four programmable UHF channels, from channel 21 to channel 68, of $8MHz$ into one of the intervals I_n

$$I_n = [10(n-1)+1, 10(n-1)+9] \quad MHz, \tag{4.1}$$

where $n = 1, 2, 3, 4$ is referred to as DQD2 output channels. The reference and surveillance signals, now each consisting of up to four adjacent DVB-T channels, are each fed to a storage server wideband channel, sampled and finally stored at hard disks. The function of DQD2 is illustrated in figure 4.8.

A very special feature of the DQD2, coming from the hardware (HW) implementation, is the mirroring of each of the DQD2 output channels. Looking closer at figure 4.7, it can be seen that the input signal's carrier frequency, which is in the interval $[474MHz, 850MHz]$, is lower than LO1, which is in the interval $[869MHz, 1253MHz]$. The modulation results in a mirroring of the input signal, which is preserved throughout the rest of the signal chain and on to the hard disks. The signal's carrier frequency after LO1 is $395MHz$, and the signal is bandpass filtered and then modulated with LO2, which is $390MHz$, $380MHz$, $370MHz$, or $360MHz$ depending whether it is DQD2 output channel $1, 2, 3$ or 4 respectively. This means that if no post-mirroring is applied, the DQD2 output channels frequency axis, ranging from $0MHz$ to $40MHz$, written as $[0, 40MHz\rangle$, will look like

$$\langle 10 \quad 0 \,] \langle 20 \quad 10 \,] \langle 30 \quad 20 \,] \langle 40 \quad 30 \,] \; MHz \tag{4.2}$$

This might be digitally converted, previously referred to as post-mirroring, to

$$[\, 0 \quad 10 \rangle [\, 10 \quad 20 \rangle [\, 20 \quad 30 \rangle [\, 30 \quad 40 \rangle \; MHz \tag{4.3}$$

---

[1] The analog frontend DQD2 was designed and developed by the FFI engineers Steinar Johnsrud and Per Sørnes.

In the next section, the internal noise of the system is studied in further detail, and as long as DQD2 is not part of the signal chain, it is not necessary to take into account the mirroring of signals. Whether or not any post-mirroring is applied will be made clear in each case. It is underlined that the mirroring is not a problem for the FM channel.

The next section will deal with some basic properties of the receiver, and it might be helpful to understand that the FM radio channel is undersampled in the second Nyquist band. The A/D cards are running at $f_s = 80MHz$ real (one channel) sampling, which means that the analogically bandlimited FM radio signal in $88 - 108MHz$ shows up at $8-28MHz$ in the sampled data. The relationship between the not undersampled wideband channel and undersampled FM channel is

$$f_{FM} = f_{wideband} + 80MHz, \tag{4.4}$$

for $0 \leq f_{wideband} < 40MHz$.

Figure 4.4: The datarecording system mounted in a rack.

(a) Reference channel, FM radio antenna; TRIAX 5 element [127] (upper antenna), DVB-T antenna; Televes DAT75 Digital Tv Aerial [128] (lower antenna).

(b) Surveillance channel, DVB-T antenna; Funke Digital TV FFA4522 21/69 [129] (upper antenna), FM radio; TRIAX 5 element [127] (lower antenna).

Figure 4.5: The reference and surveillance channel antennas, mounted on a metal rod, on top of a pan- and tilt-device with video camera for remote (lab) operations.

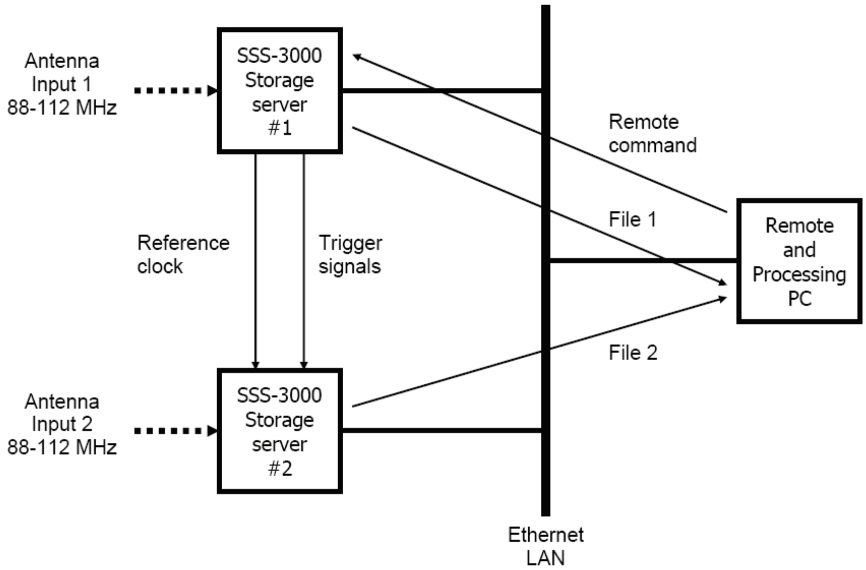

Figure 4.6: A schematic diagram of the two data recording PCs configured to record the FM radio band, $88 - 108MHz$, adapted from [15].

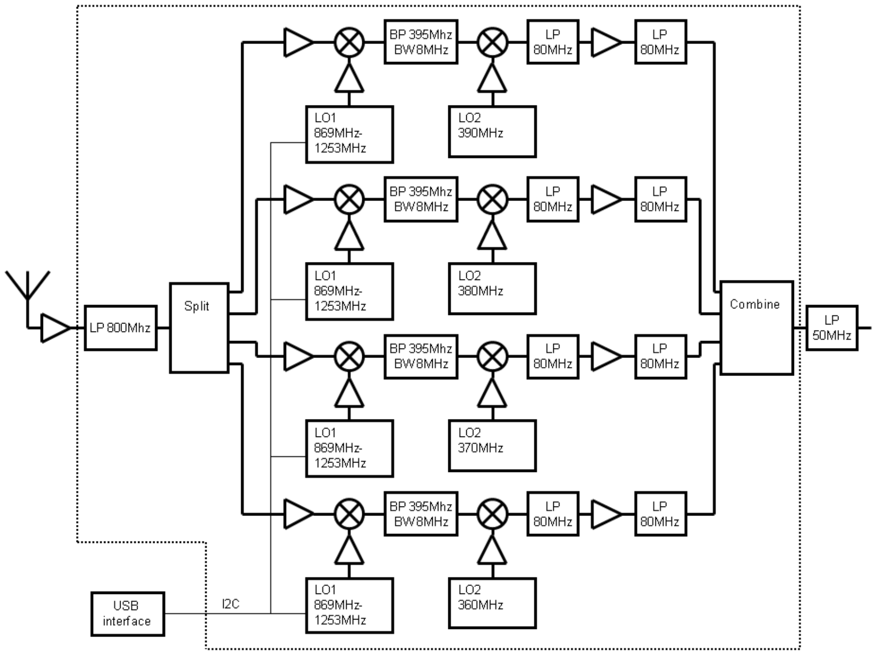

Figure 4.7: A schematic diagram of one of the two identical signal channels in DQD2, either the reference or the surveillance channel. Each channel consists of up to four non-adjacent DVB-T bands of choice, which are shifted down (figure 4.8) to the recording computers sampling band, i.e. $40MHz$ bandwidth.

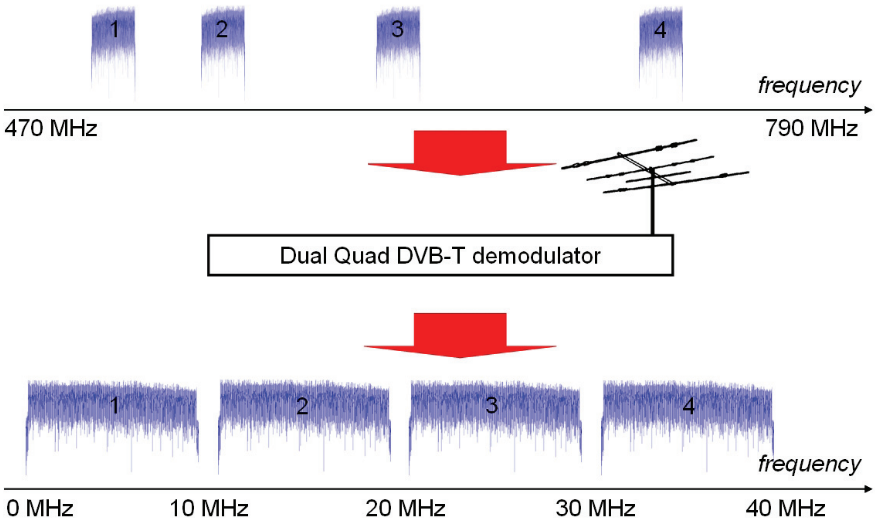

Figure 4.8: Operational sketch of DQD2. The indicated frequency band, $470 - 790 MHz$, along the frequency axes is the DVB-T licensed frequency band in Norway.

4.3 Receiver characteristics

The following section takes a closer look at the receiver characteristics with respect to interference and noise for the four input channels, reference and surveillance channel for both the FM and wideband (DVB-T) setup. This chapter will focus on the reference channel, but similar results have been achieved for the surveillance channel.

The DVB-T surveillance channel is equipped with an adjustable amplifier, which does not tell the actual gain, but once set, the gain stays the same until once again manually adjusted. In addition to this the DVB-T reference and surveillance antennas are different, further complicating direct comparisons of the two channels. This is not the case for the FM radio channels, where the equipment is identical for the two channels. However, roughly speaking, the following results for both the FM radio and DVB-T reference channel apply also to the surveillance channel.

The storage servers are SW controlled, and one of the options free to choose is the signal input attenuation. This is an analog SW controllable filter before the A/D converters. The filter is adjustable in steps of $10dB$, starting at $0dB$ (unattenuated), and it goes to $30dB$ (full attenuation). In the following discussion this filter will be actively applied in order to characterize the receiver, and the reference channel's antenna will be used to collect data.

Figure 4.9 shows the frequency spectra of the sampled open (no antenna) FM channel. The attenuation is varied in steps of $10dB$ from $0dB$ to $30dB$. The noise floor can for $0dB$ attenuation be regarded as relatively stable at $-50dB$, and it is only lowered a few dBs, to approximately $-52dB$ when increasing the attenuation to $30dB$.

In the first frequency spectrum, corresponding to $0dB$ attenuation, three major frequency components are seen, at $93.5MHz$, $100MHz$, and $106.5MHz$. The signal at $106.5MHz$ is pushed nearly $7dB$ down, to $-45dB$ going from $0dB$ to $10dB$ attenuation, but as the attenuation is increased additionally $10dB$, the signal is only lowered to $-50dB$, while increasing to $-48dB$ at $30dB$ attenuation. The frequency at $93.5MHz$ is stable at $-30dB$ for the $0dB$ and $10dB$ attenuation, while lowered to around $-40dB$ for $20dB$ and $30dB$ attenuation. The frequency at $100MHz$ is unaffected by the varying attenuation.

The same behavior can be observed for the wideband channel of the data recording equipment. Figure 4.10 shows the unmirrored (DQD2 is not part of the signal chain) frequency spectra of the terminated wideband channel for varying attenuation ranging from $0dB$ to $30dB$. The noise floor can be estimated to be slightly above $-50dB$ for $0dB$ attenuation, while for $30dB$ attenuation it is lowered to around $-52dB$. The signal at $20MHz$ frequency, corresponding to $100MHz$ in the FM channel, is unaffected by the attenuation. The signals at $13.5MHz$ and $26.5MHz$ are corresponding to $93.5MHz$ and $106.5MHz$ in the FM channel, and they are behaving in roughly the same way as before. They are close to unaffected by the $0dB$ and $10dB$ attenuation, and lowered $6-8dB$ for the $20dB$ and $30dB$ attenuation compared to the $0dB$ and $10dB$ attenuation. The wideband channel is wider, sampled bandwidth of $40MHz$, than the FM channel, which has a bandwidth of $20MHz$. Note signals at $6.7MHz$ and $33.5MHz$, behaving in roughly the same way as those at $13.5MHz$ and $26.5MHz$. These interferences are probably generated and/or intercepted within the PC's of the data recording system. At the FM channel input, a termination cannot be applied directly, due to a direct current at the terminals. This means that there is a high probability that the $93.5MHz$ and $100MHz$ frequency originates from a strong nearby FM transmitter which, amongst others, broadcast FM radio at those two frequencies at high power levels. However, also being present in the wideband channel, even when this is properly terminated, the frequencies are probably being intercepted somewhere inside the storage servers.

In summary, for all attenuations, there are strong frequency components (compared to the noise floor) at $93.5MHz$ (FM channel) and/or $13.5MHz$ (wideband channel) which should be kept in mind. Especially DQD2 output channel 2, $10-20MHz$, in the sampled wideband channel should be used with care. In the same way it should be kept in mind the $100MHz$ and/or $20MHz$ frequency. For the DVB-T applications using DQD2 this frequency will be between output channel 2 and 3, and will normally be filtered out, while the area around the $100MHz$ FM radio channel has to be used with care. If the attenuation is $20dB$ or more, normally the rest of the interfering frequencies can be expected to be within the noise floor, but care has to be taken if the attenuation is less than that, assuming that a sufficiently strong input signal is present.

Figure 4.11 shows the frequency spectra of the sampled FM channel for varying antenna azimuth directions while the attenuation is $0dB$. From the plots transmissions are seen to be intercepted in all directions, west being the most dominant one. To the west of the receiver there is a very strong transmitter which broadcasts FM radio at $88.7MHz$ ($P_T \approx 40dBW, G_T \approx 10dB$), $91.9MHz$ ($P_T \approx 20dBW, G_T \approx 10dB$), $93.0MHz$ ($P_T \approx 30dBW, G_T \approx 10dB$), $93.5MHz$ ($P_T \approx 37dBW, G_T \approx 10dB$), $100.0MHz$ ($P_T \approx 40dBW, G_T \approx 10dB$), and $103.9MHz$ ($P_T \approx 40dBW, G_T \approx 10dB$). In the frequency spectrum, the strongest signals are just below $0dB$, while $45dB$ down, the shoulders of the signals are close to $1MHz$ wide. The noise floor which was at $-50dB$ without input signal is now being severely distorted by the strong signals. For the other directions the same effect can be seen, although at a more moderate level since the input signals overall are weaker. The noise floor can be expected to be at $-50dB$ unless the input signals are so strong that their shoulders rise above the receiver noise. It should especially be noted that the $100MHz$ frequency is being broadcasted at high power from the nearby transmitter, and in the case of receiver antenna pointed at the transmitter (west), there is a signal/interference ratio of around $20dB$, in the north and south directions the corresponding figure is down to around $5dB$, and for east $7dB$.

Figure 4.12 shows the frequency spectra of the sampled wideband channel for varying antenna azimuth directions, while the attenuation is set to $30dB$, for the DVB-T channels numbered 52, 58, 61, and 58, appendix B.4. The plots are not corrected for the mirroring of the DQD2 output signals, the focus is on the interfering signals found in the terminated inputs case, and this will make the frequency comparisons easier. The signals will be followed from the terminated tests through the signal chain, thus no compensation will be made at this stage. The channels are being transmitted from Tryvann, which is $21km$ west of the receiver. Resulting in the western channel being around $10dB$ stronger than the others. While using the DQD2, it is expected that at integer multiples of $10MHz$ there will be interfering frequencies from the analog front-end, however these signals will be between the interesting regions, and will not corrupt the results. The $13.5MHz$ interfering frequency found in figure 4.10 is roughly $20dB$ below the reference signal in DQD2 output channel number 2. If this receiver was being used as a surveillance channel, pointing in the north direction, there will be signals of approximately the same magnitude, unless the attenuation is set to $0dB$, which will make the DSI and surveillance signal go up to $-10dB$, while the interfering signal will only rise to $-24dB$, resulting in a signal/interference ratio of $14dB$. However, DQD2 output channel number 2 should be used with care.

It is also noted that for the north, east and south azimuth directions, the noise floor between the down modulated DVB-T channels are around or below $-50dB$, with one exception, south direction at $20MHz$ where the noise is at $-45dB$. For the western direction, the noise floor is slightly higher, $20 - 25dB$ below the signal peak. This is above the European Telecommunications Standards Institute (ETSI) specification for the DVB-T standard, which states the shoulders of the signal shall be down by $40dB$ [12]. However, this mismatch is expected to be caused by the equipment, which not is of the highest quality available due to the limited development time as well as funding available for such a system.

Figure 4.13 shows the corresponding azimuthal directions for the DVB-T channels 24, 48, 55, and 48, while the attenuation is set to $10dB$. These DVB-T channels are broadcasted from the Kongsvinger transmitter which is $57km$ north-east of FFI, meaning none of the receiver antenna look angles will be directly at the transmitter. None of the plots have been corrected for the mirroring of the DQD2 output channels. The signals are weak for all directions, compared to the received signals when the reference antenna is directly aimed at the Kongsvinger transmitter, Figure 4.14a, same attenuation for all plots. In figure 4.13, the interferences at $13.5MHz$ is visible, while the expected integer multiples of $10MHz$ are clearly visible. In addition to these, there are several distinct frequencies present, i.e at $15MHz$ at $-28/-24dB$, and at $31MHz$ at $-31/-29dB$, visible in all azimuthal directions, roughly the same signal level. This indicates that the origin of the signal is in the area of the receiver, where the antenna far field beam is not formed. The strongest of those signals is at $15MHz$ at $-24dB$, when the antenna is pointing south. Figure 4.14a shows that when the receiver antenna is directed at the Kongsvinger transmitter, the signal level is varying from $-35dB$ to $-12dB$ across channels, with channel 55 experiences something looking like a deep null. This might indicate the presence of multipath.

Figure 4.14b, shows that each of the DQD2's channels have the same response for the same input signal, in this case the reference antenna is directed at Tryvann, the attenuation is 30dB, and the DQD2 input channels are all set to UHF channel 52.

Figure 4.14c, shows the adjacent channels to a DVB-T occupied one, channel 52, and it can be seen that there are activity in the band, in this case especially in channel 55, which is transmitted in a nearby area (Kongsvinger). This figure shows that the strong signal in channel 52 is not leaking into the adjacent channels above the noise floor.

Figure 4.14d shows the situation of looking into a direction, south, where there are supposed to be no DVB-T transmissions, nor any other spectral activity, for the selected input channels, 22, 28, 50 and 67. Spectral activity can be seen, as the signal level is above the receiver noise floor, and there are clearly visible frequency components revealing the presence of transmitted signals.

The target reflected surveillance signal's level will be way down in the receiver's noise floor, but a similar discussion will not be carried to here to the same detail. However, same results as those for the reference channel have been achieved for the surveillance channel.

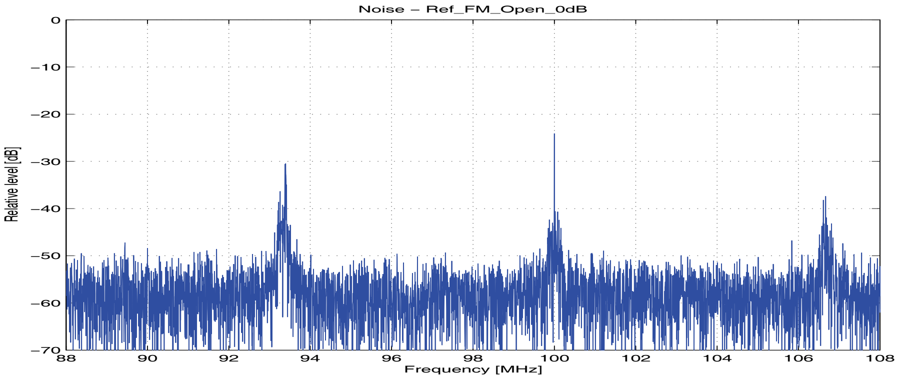

(a) $0dB$ attenuation.

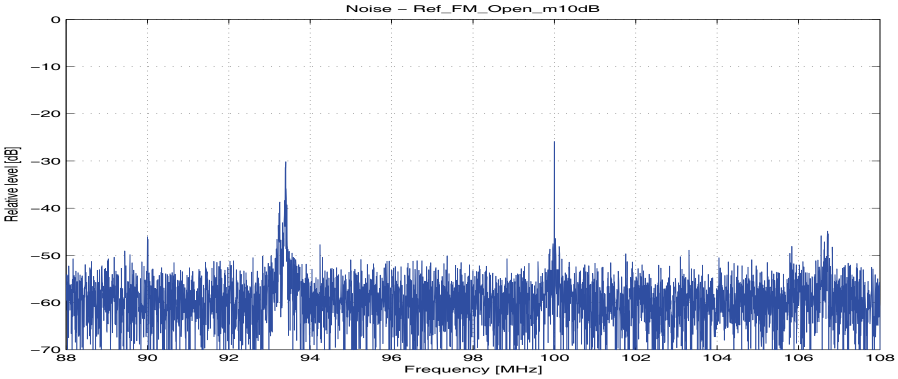

(b) $10dB$ attenuation.

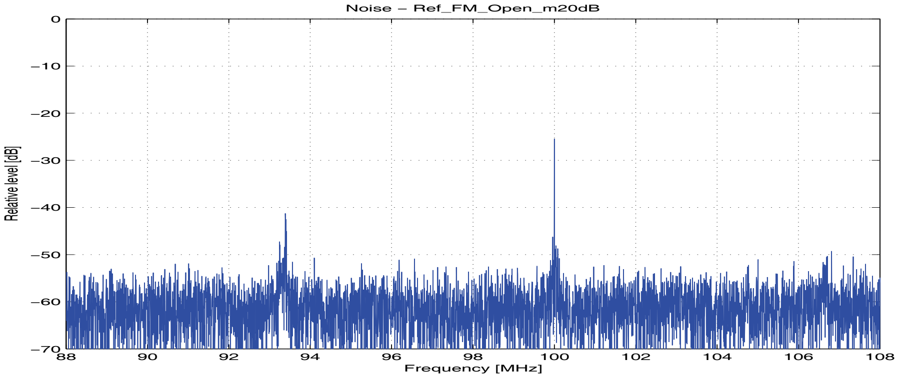

(c) $20dB$ attenuation.

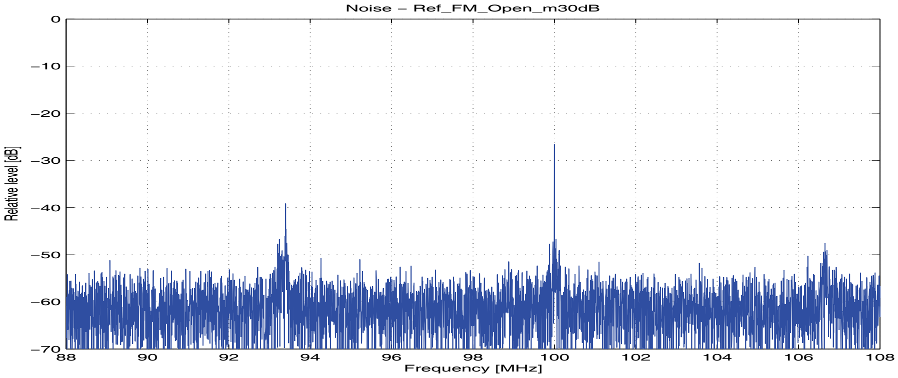

(d) $30dB$ attenuation.

Figure 4.9: Frequency spectra of the open (no antenna) FM reference channel with varying attenuation, ranging from $0dB$ to $30dB$.

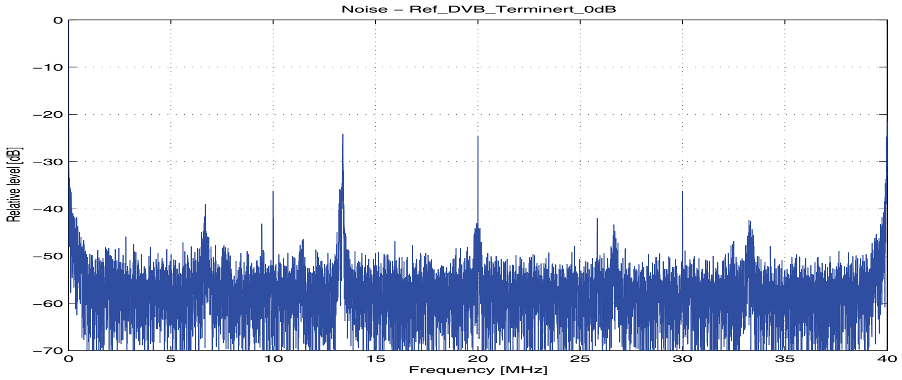

(a) $0dB$ attenuation.

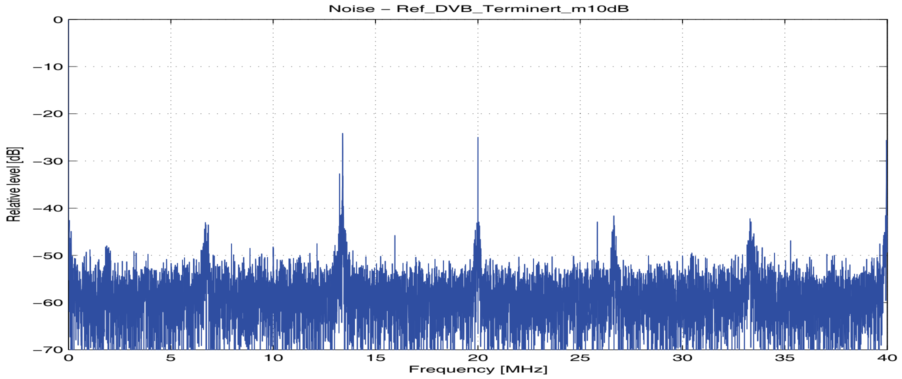

(b) $10dB$ attenuation.

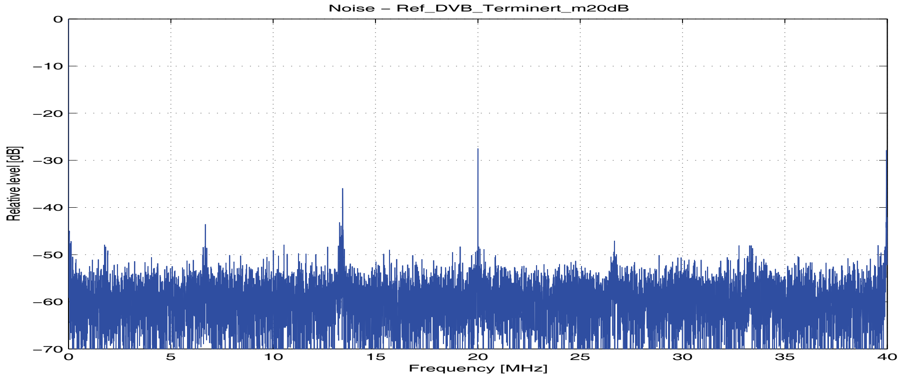

(c) $20dB$ attenuation.

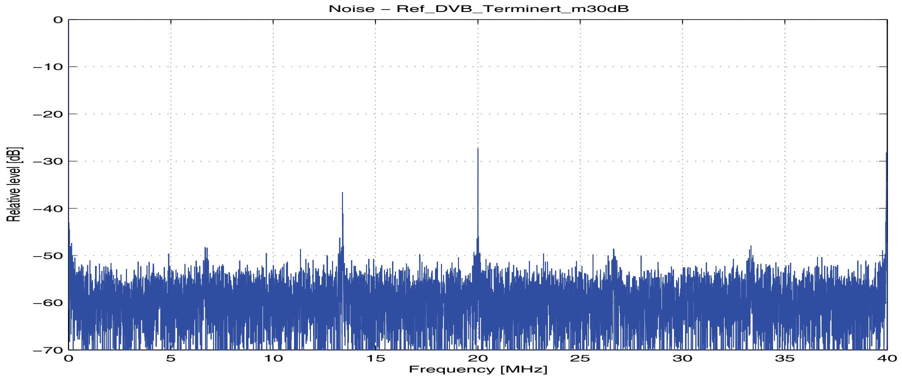

(d) $30dB$ attenuation.

Figure 4.10: Frequency spectra of the terminated wideband reference channel with varying attenuation, ranging from $0dB$ to $30dB$.

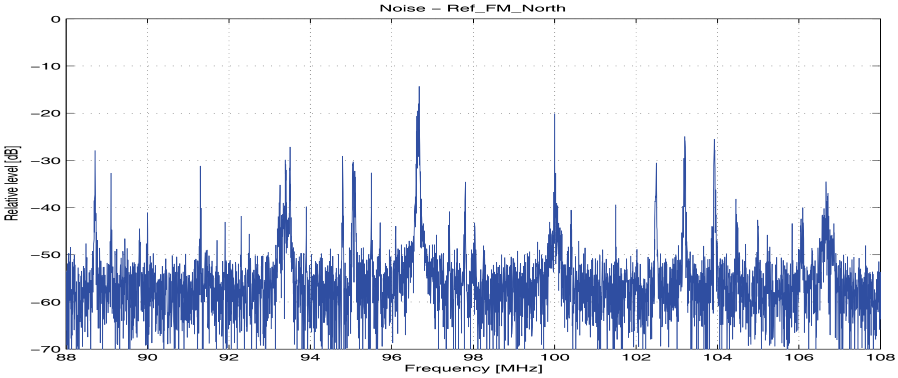

(a) North.

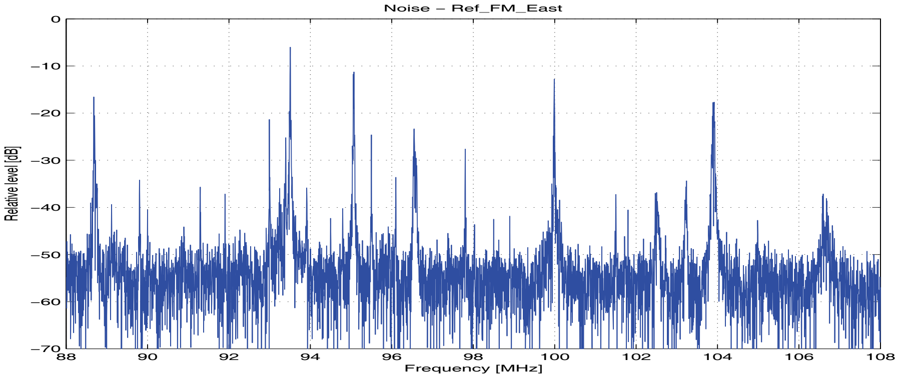

(b) East.

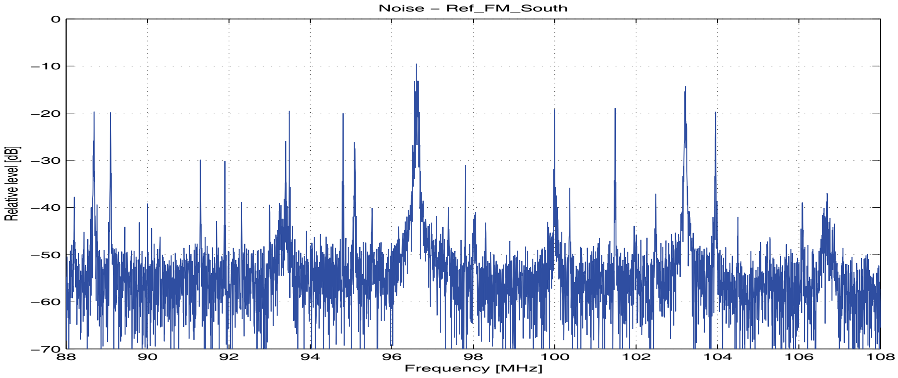

(c) South.

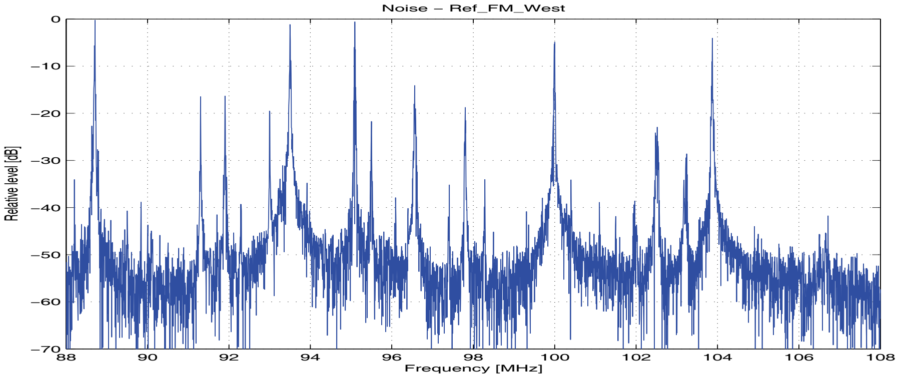

(d) West.

Figure 4.11: Frequency spectra of the sampled FM reference channel for varying antenna azimuth directions, the attenuation is $0dB$.

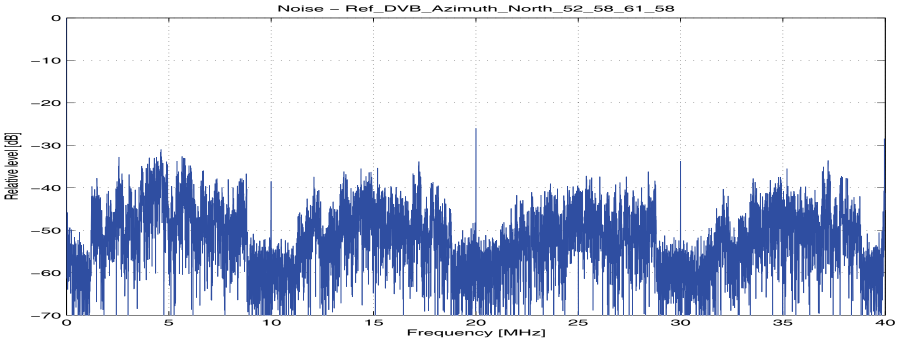

(a) North.

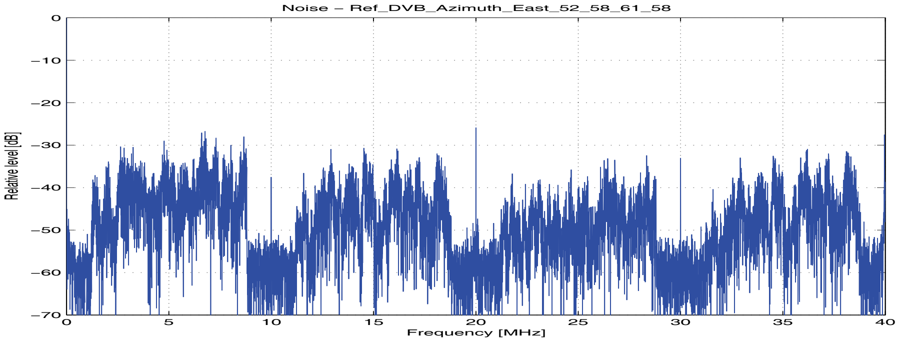

(b) East.

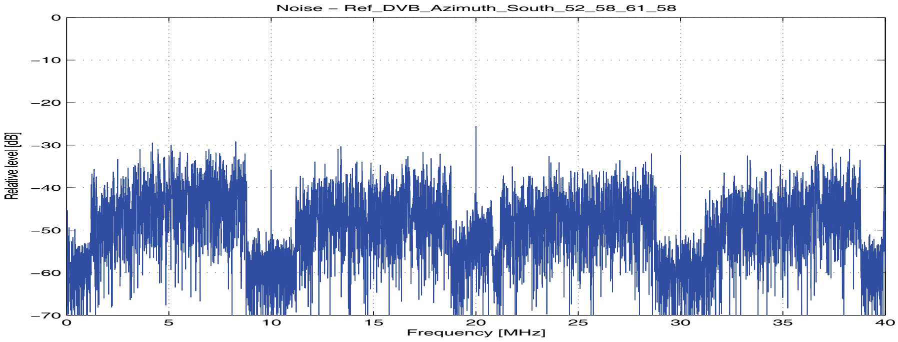

(c) South.

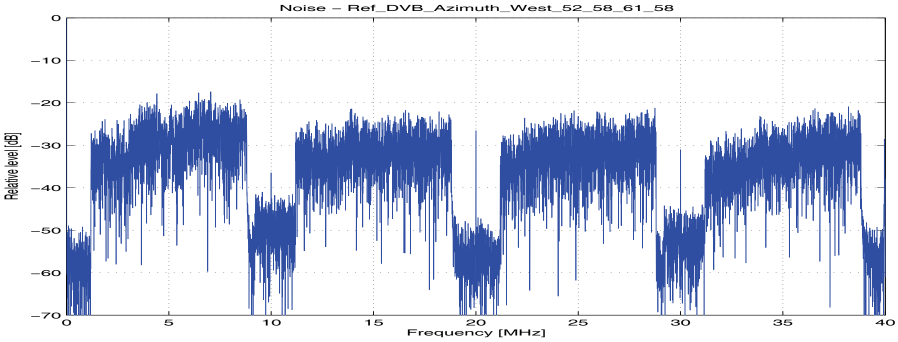

(d) West.

Figure 4.12: Frequency spectra of the sampled wideband reference channel for varying antenna azimuth directions, attenuation is set to $30dB$, and the DVB-T channels are number 52, 58, 61, and 58, corresponding to the Tryvasshoegda broadcast channels.

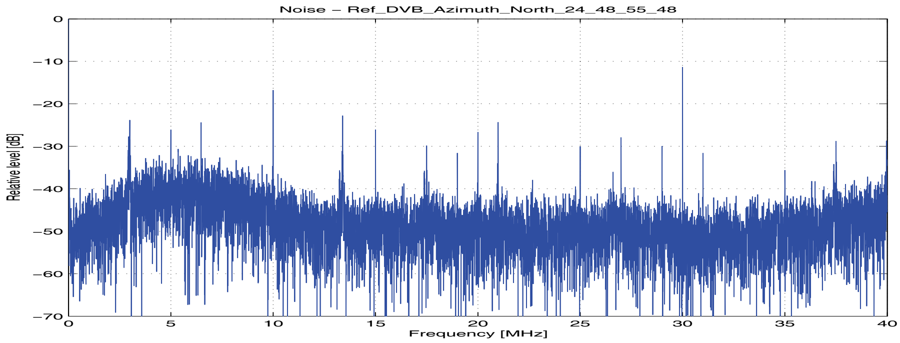

(a) North.

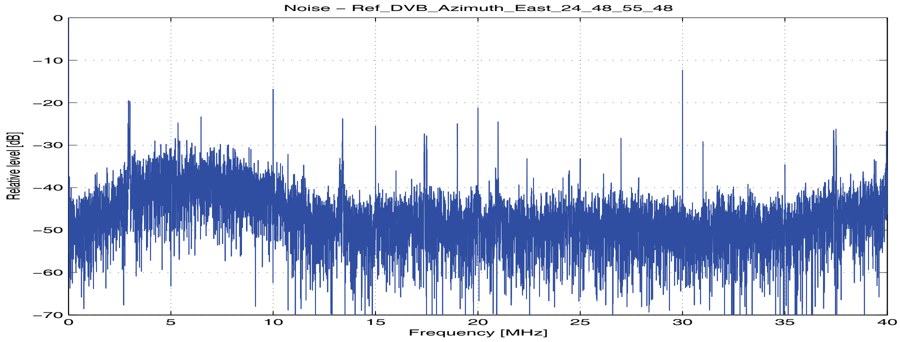

(b) East.

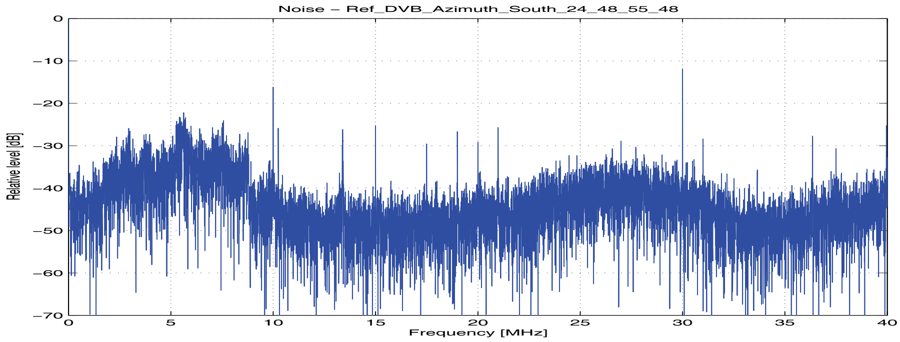

(c) South.

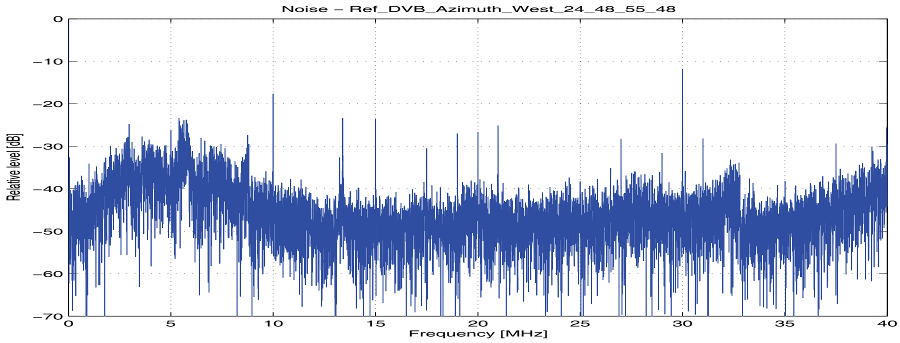

(d) West.

Figure 4.13: Frequency spectra of the sampled reference wideband channel for varying antenna azimuth directions, attenuation is set to $10dB$, and the DVB-T channels are 24, 48, 55, and 48, corresponding to the Kongsvinger broadcast channels.

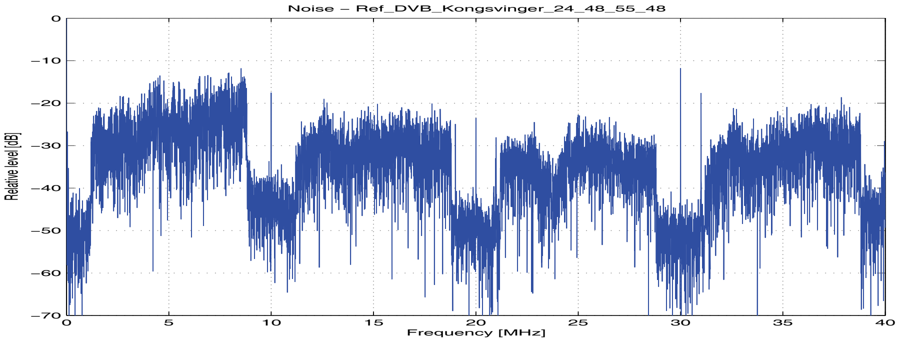

(a) Channel characteristics receiver antenna aimed at Kongsvinger, DQD2 set to DVB-T channels 24, 48, 55, and 48, attenuation set to $10dB$.

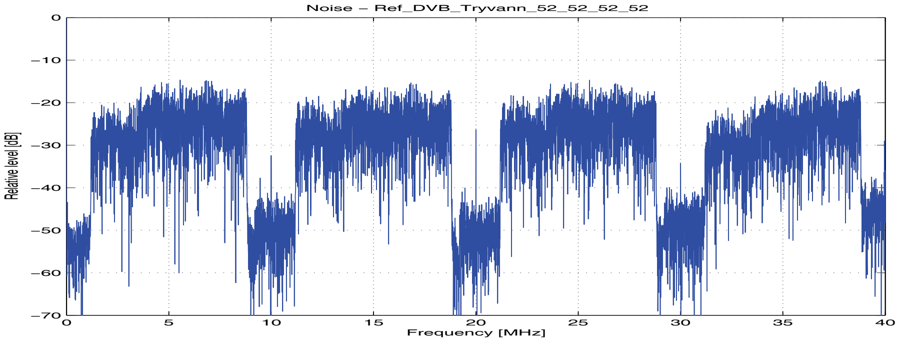

(b) Channel characteristics for DVB-T receiver antenna pointing at Tryvann, DQD2 set to DVB-T channels 52, 52, 52, and 52, attenuation set to $30dB$.

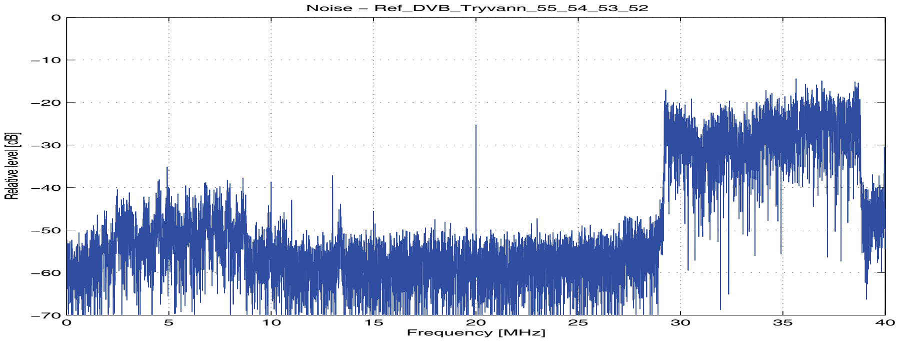

(c) Channel characteristics of DQD2 DVB-T channels 55, 54, 53, and 52. Receiver antenna pointing at Tryvann, attenuation set to $30dB$.

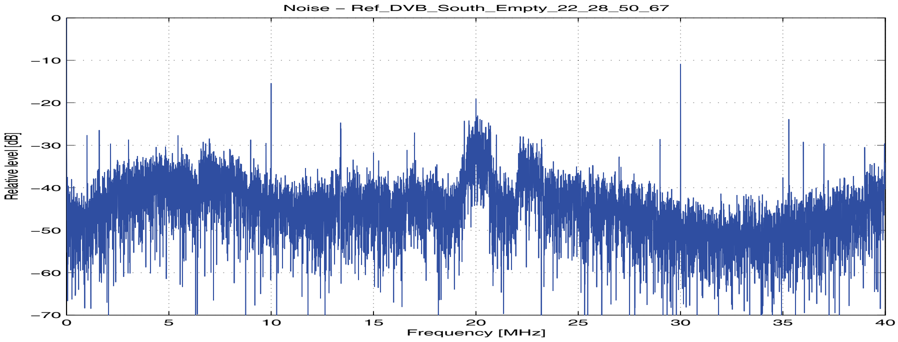

(d) Channel characteristics for receiver antenna pointing south, while DQD2 set to DVB-T channels 22, 28, 50, and 67, which are beleived to be not used, attenuation set to $10dB$.

Figure 4.14: The figure shows miscellaneous aspects of the DVB-T recording system's reference channel.

FM radio			DVB-T		
Frequency [MHz]	Attenuation $0-10dB$	Attenuation $20-30dB$	Frequency [MHz]	Attenuation $0-10dB$	Attenuation $20-30dB$
93.5	Present	Present	6.7	Present	Present
100.0	Present	Present	10.0	Present	Present
106.5	Present		13.5	Present	Present
			13.5	Present	Present
			20.0	Present	Present
			26.5	Present	
			30.0	Present	Present
			33.5	Present	

Table 4.6: The table lists the interfering frequencies in the receiver's FM radio and DVB-T signal path as a function of the applied attenuation. The table is valid for both the reference and surveillance channel.

4.4 Summary

In summary, initial performance estimates for a few of the promising geometries and strong multichannel broadcasters of opportunity in the Oslo region, figure 4.1, were made. The Hoeyaas/Halden geometries were not working in real life, probably due to the low quality on the received reference signal. The Tryvannstaarnet (FM radio) was not working due to the strong DSI as predicted. Thus, the applicable broadcasters were Holtberget (FM radio), Kongsvinger (DVB-T), and Tryvasshoegda (DVB-T).

In order to reduce complexity in the work, adaptive filtering as well as signal conditioning, figure 3.15, are avoided. These algorithms still undergo major research and development, are thus not easily applicable. The focus of this work should be on the exploitation of multiple broadcasted bands, and not the fine tuning of such algorithms. By considering the results of this chapter, it is believed that the estimated terrain shielding should be sufficient in order to avoid implementing the adaptive filtering. Some signal conditioning may be expected to be performed.

The top level design and ideas of the data recording equipment, i.e. testing, functions, performance, dealing with the priorities, as well as finding the financing, were performed by the undersigned, although the actual making of the system and practical solutions were performed by FFI engineers. All SW supporting and organizing the data analysis of this thesis has been the work of the undersigned.

The driving motivation behind the data recording equipment were to be able to record both FM radio and DVB-T PBR target datasets of such a quality that analysis of longer periods, i.e. tens of minutes could be analyzed continuously. In addition to this, the whole FM band, as well as up to four non-adjacent DVB-T channels of choice, each of maximum $8MHz$ bandwidth, for both reference and surveillance channel should be recorded. All this requirements were met by the equipment, as will be seen in chapters 6 and 7.

The analysis of the hardware and data recording equipment showed that the presence of interfering frequency components at various frequencies, their strength depending on the system's input attenuations. Especially, should DQD2 output channel number 2, i.e.

$10 - 20MHz$, in the sampled wideband channel be used with care, due to the $13.5MHz$ frequency which is strong compared to the noise floor, and present for all attenuations. In addition to this, the integer multiples of $10MHz$ when the DQD2 is part of the signal chain is clearly present, however these frequencies are between the signal regions of interest, and will normally be filtered out in the processing. Table 4.6 lists the interfering frequencies which should be kept in mind during in the future research for both the reference and surveillance channels.

When strong input DVB-T signals are present, the frequency spectrum seems to be as expected, i.e. the signal frequency response is relatively flat. However, when the input signal is weak (system attenuation $< 10dB$, and signal $< 20dB$ above the noise floor), the spectrum exhibits several distinct frequency components, which might cause problems for the future signal processing, especially if these signals are present both in the reference and surveillance signal.

Chapter 5

PBR Signal Processing Methodology

This chapter derives in detail the signal processing methodology. In particular, a method on how to coherently combine multiple broadcasted channels of opportunity of the same type (FM radio, DVB-T, DAB) is proposed. The channels may be non-adjacent and irregular spaced in frequency as well as of (time) varying bandwidth. The algorithm is mathematically derived, and this chapter limits the discussion to theoretical simulations of the algorithm's performance and behavior, while real life target analysis, results, and performances are presented in chapter 6 for the FM PBR, and in chapter 7 for the DVB-T PBR.

Much of the material in this chapter has been reported on in a series of conference papers [3–7] throughout or work with the thesis. The following section will briefly run through each of the papers and their contributions.

5.1 Motivation

It has been shown [38, 39] that the detection performance is improved by using several FM radio channels for detection, as frequency diversity is achieved as well as a robustness against the bandwidth fluctuations arising from the combination of the FM radio modulation technique and the time varying program content. The Norwegian high power FM transmitters seem to broadcast at least three high power FM radio channels, as is also the case for the DVB-T system, where each DVB-T transmitter was, until fall 2010, broadcasting three COFDM bands as seen in table 1.1. Sometime fall 2010 this was changed to five bands from each transmitter.

This work is aiming at adding another capability to the single transmitter PBR work on detection and tracking, namely improved target range estimation as explained in section 1.2. The focus is on how to improve the range resolution in the range correlation of the matched filter processing by exploiting multiple broadcasted channels from a single transmitter. The latter requirement is important in order to achieve the same geometry for all channels for the same target, i.e. same time-delayed processing. It is believed that this work will fit nicely in a future system design alongside the improved detection performance of [38, 39], and the single transmitter target tracking of [43]. No attempts on trying to coherently add multiple geographically separated broadcasted channels are performed. However, the algorithm lays the foundation for research into this field (figure 6.7 and related discussion).

[64] focused on how to improve the range resolution in PBR systems by using multiple FM radio channels. The paper describes the autocorrelation function for several equally and non-equally spaced FM radio channels. Specifically, [64] showed that the range resolution (autocorrelation function) can be improved by combining several FM radio channels at the cost of ambiguities, exemplifying this for channel separation ranging from $\Delta f = 150kHz$ to $\Delta f = 250kHz$.

[3] showed that in a multichannel FM radio autocorrelation, it is advantageous to use lower channel correlation bandwidth in order to avoid ambiguities in the range dimension rather than increase the channel correlation bandwidth and risk getting ambiguities. It is also beneficial to adaptively tune the FM radio bandwidth in the range correlation process to the actual available bandwidth. This work was followed by [4], which showed results from the processing of multiple FM-radio frequency bands based on real life datasets, of both reference and surveillance channels, where the latter were containing targets of opportunity. The results showed that the range resolution was improved, although the cross-correlation function in range was very peaky, as described in [3, 64].

[5] presented a general mathematical algorithm on how to improve the range resolution by using multiple broadcasted channels from a single transmitter in the range correlation. The algorithm builds on the ideas presented in [3,4], and the work mathematically demonstrated how to deal with different non-regular spaced carrier frequencies, independent and non-correlated signals, in order to optimize the target resolution.

Finally, [7] extended the work of [5], where the mathematical framework was presented with an emphasis on exploiting FM radio waveforms. For the more general case, [7] assumed that the broadcasted signal was modulated onto a carrier frequency, being FM radio, DAB, or DVB-T, or pure noise of a given bandwidth. Schematics of the ideas are illustrated for FM radio and DVB-T signals of opportunity in figures 4.8 and 5.1 respectively.

The work in this thesis has been inspired by the work being performed on high resolution radar, where multiple stepped frequency waveforms are synthesized together in order to achieve high range resolution, well described in [46]. The continuous discrete frequency coding technique [46, pp. 142-149, 197-220] transmits a continuous wave signal, which is stable in frequency for a time T, and is then stepped Δf in frequency. This is repeated n times, giving a repetition period of nT. By requiring the step frequency to be $\Delta f = 1/T$, it is ensured that at the time of each of the steps, the phase of the signal is the same, and the resulting transmitted signal over time is continuous, and the point target return reduces to a geometrical sum of a complex exponentials. The unambiguous delay results in $R_u = nc/\Delta f$, and the corresponding resolution is $\Delta R = c/(n\Delta f)$. The research of this thesis might be considered an extension of the work on continuous discrete

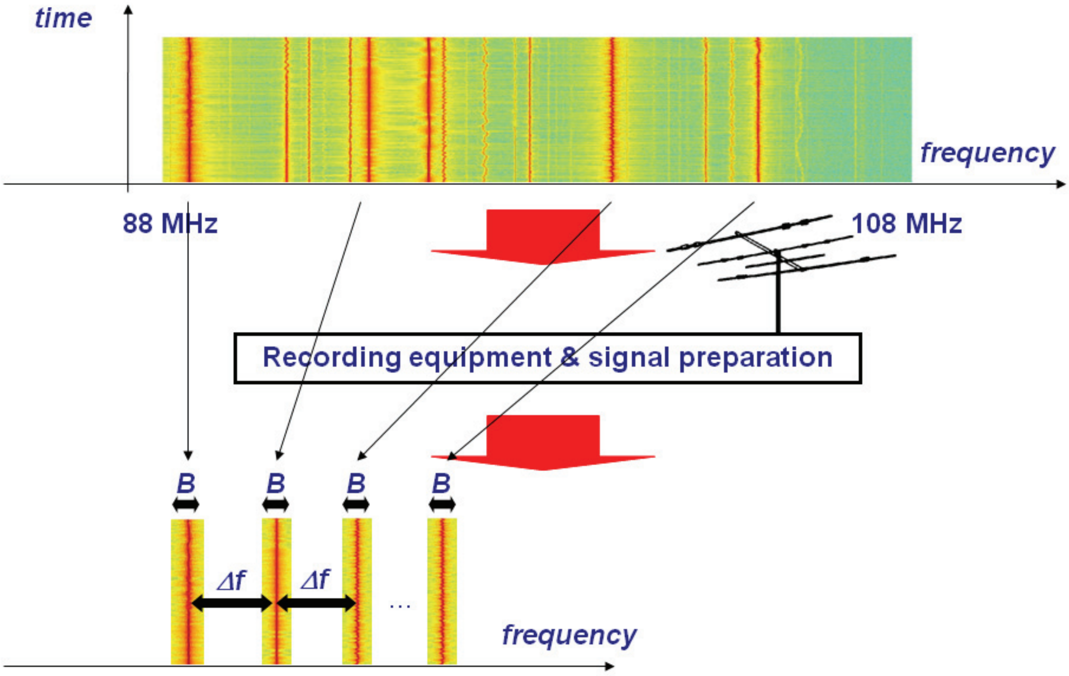

Figure 5.1: Schematics of the FM radio case. In the plots, red color represents strong signal, while green represents no signal.

Table 5.1: Target monostatic Doppler shift, i.e. maximum bistatic (3.18) with $\beta = \delta = 0$, as a function of transmitter center frequency and target velocity.

System	Center frequency	Target velocity			
		$50m/s$	$100m/s$	$150m/s$	$300m/s$
FM radio	$88MHz$	$29.3Hz$	$58.7Hz$	$88.0Hz$	$176.0Hz$
	$98MHz$	$32.7Hz$	$65.3Hz$	$98.0Hz$	$196.0Hz$
	$108MHz$	$36.0Hz$	$72.0Hz$	$108.0Hz$	$216.0Hz$
DVB-T	$500MHz$	$166.7Hz$	$333.3Hz$	$500.0Hz$	$1000.0Hz$
	$600MHz$	$200.0Hz$	$400.0Hz$	$600.0Hz$	$1200.0Hz$
	$700MHz$	$233.3Hz$	$466.7Hz$	$700.0Hz$	$1400.0Hz$
	$800MHz$	$266.7Hz$	$533.3Hz$	$800.0Hz$	$1600.0Hz$

frequency coding techniques [46, pp. 142-149, 197-220], in order to make it applicable for PBR systems. The following differences are noted:

1. In the PBR case, no control of the transmitted waveforms, or the spacing Δf between different frequency channels, nor the carrier frequency of those can be controlled. Meaning that it is not possible to require $\Delta f = 1/T$, even though T is free to choose. As seen in table 1.1, the spacing of the carrier frequencies of a few powerful Norwegian FM radio and DVB-T transmitters are not regular.

2. In addition to this, the work in [46] is not considering coded waveforms for stepped frequency applications, and are thus transmitting non-modulated continuous waveforms processed in sequence. The research of this thesis is considering independently broadcasted signals, consisting of an information carrying signal modulated to a carrier frequency. All channels are broadcasted simultaneously, as well as are processed simultaneously. This calls for an understanding of the importance of in-channel cross-correlation between the reference and surveillance channels, as well as the out-of-channel cross-correlation between reference and surveillance channels, as will be seen later.

3. Finally, by using different broadcasted channels in the correlation process, each of the channels will result in different Doppler shifts from the same targets, as each of the channels are using different carrier frequencies, and examples of this is seen in table 1.1. A PBR strategy in order to cope with this is to keep the coherent integration time low, and thus reducing the Doppler resolution, making all shifts end up in the same Doppler cell, [4, 38]. This work it will demonstrate why this to some extent will work and show that it might not always be the case. However, [46] suggests a phase correction term for each frequency (band), and it will be shown how this can be extended to the PBR case for waveforms of opportunity.

Figure 5.2 illustrates the target Doppler shift for a target traveling at $v = 100m/s$ (along the bistatic extended baseline, equation (3.18) where $\beta = \delta = 0$). The figure also

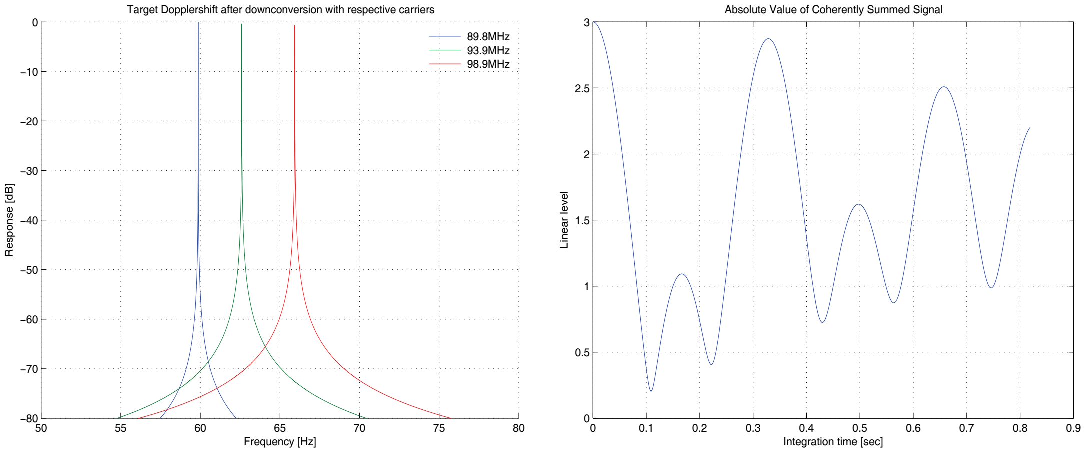

(a) Doppler shifted responses - FM radio. (b) Coherent sum response - FM radio.

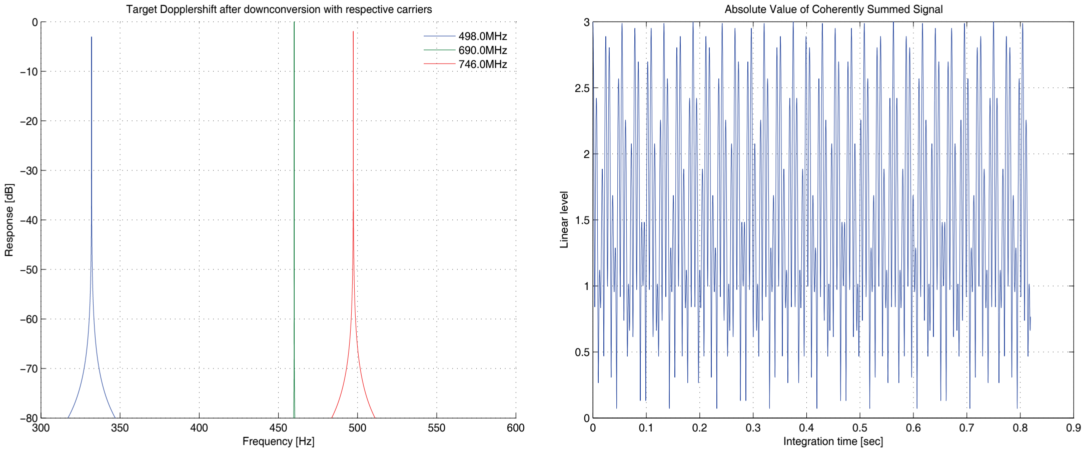

(c) Doppler shifted responses - DVB-T. (d) Coherent sum response - DVB-T.

Figure 5.2: The figures show the monostatic (maximum bistatic) Doppler shift, equation (3.18) where $\beta = \delta = 0$, for a target traveling at $v = 100m/s$ for the respective carrier frequencies, and the resulting coherent direct sum of the returns.

shows effects of simply summing the target response for FM radio and the DVB-T like signals in this case. The principles will be the same for other bistatic geometries as well. For the PBR FM radio systems the integration time is around $0.5sec$, and for DVB-T systems around $0.1sec$, [26]. This means that the Doppler resolution of FM radio PBR will be $2Hz$, and correspondingly the Doppler resolution of PBR DVB-T systems will be $10Hz$, and the Doppler shifts easily exceeds these numbers as seen in table 5.1 and figure 5.2.

In order to illustrate the performance and importance of the assumptions for the proposed algorithm to be explained, a pseudo random code generated for P simulated channels was used. The code has been band limited to bandwidth B, the frequency distance between the down modulated signals is Δf, while the initial frequency offset is f^{p0}, f^{q0}. The two sets of parameters for the simulations are tabulated in table 5.2, one set mimicking the FM radio parameters, and one set mimicking the DVB-T parameters.

Table 5.2: The parameter set for the simulations with the pseudo random code.

System	Number of channels P	Channel bandwidth B	Channel separation Δf	Initial offset frequency f^{p0}, f^{q0}	Signal IQ-sample f_s
FM radio	3	$100kHz$	$150kHz$	$50kHz$	$400kHz$
DVB-T	3	$8MHz$	$10MHz$	$4MHz$	$28MHz$

5.2 Signal processing

Schematics of the data collection and down modulation for the signal processing are illustrated in figures 4.8 and 5.1 for FM radio and DVB-T signals of opportunity respectively. A brief overview of the proposed processing scheme may be formulated as follows, and is also described in the flow chart of figure 5.3: The sampled reference and surveillance channels are organized according to (5.2) and (5.6) after the individual channels have been down modulated according to (5.22) and (5.23) as illustrated in figures 4.8 and 5.1. Each of the individual channel's phase is estimated from the single channel correlation, a readily available result from the detection process (5.27), and adjusted for accordingly in each channel before the range correlation which is described in (5.9). Section 5.2 goes through the correlation process and the range estimation, followed by an analysis of the processing scheme's Doppler sensitivity in section 5.2.3. The advantage of this scheme is that it ensures maximum signal-to-noise ratio on the target, while the major drawback is that the optimization is for one Doppler velocity only. But as shall be seen, the algorithm is rather robust for small Doppler variations. Optimization for multi-target Doppler processing has been out of the scope of this work, which has been focused on maximizing the multi-channel return for a single target while improving the range resolution, and maintaining the Doppler information and resolution.

The first stages of the algorithm do not require the range and Doppler information of the target, even though it is known a priori, and this might be slightly confusing. However, this is a simple way of explaining the algorithm using the efficient range-Doppler processing principles as in section 3.5. All of the major computations of the algorithm may be performed efficiently by FFT/IFFT algorithms.

5.2.1 The signal model

In appendix A the general form of the reference and surveillance channel's signals are presented in equations (A.14) and (A.15) respectively. Until now, only a single broadcasted channel has been exploited. The following will extend the signal processing of chapter 3.5 to the exploitation of multiple broadcasted channels from a single transmitter, i.e. single geometry for multiple channels, as in figure 3.2.

This work will disregard the target's acceleration. In order to incorporate this effect, strategies like in [130, 131] might be applied.

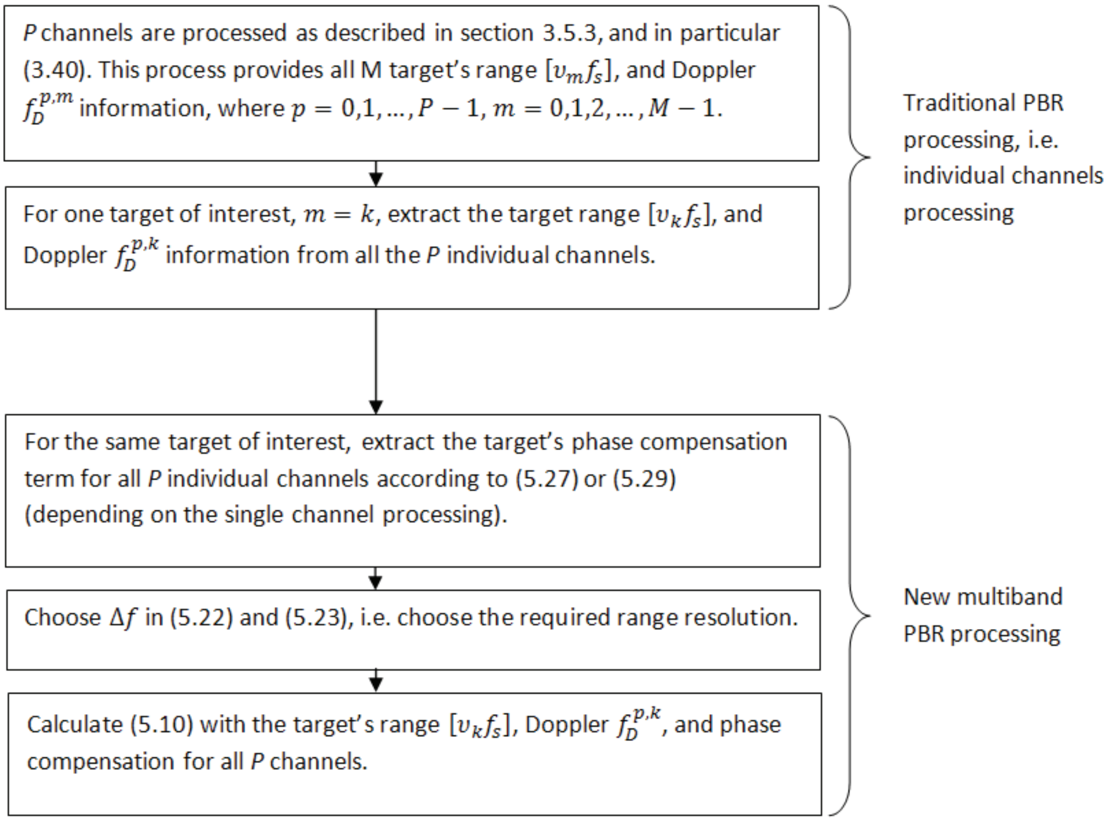

P channels are processed as described in section 3.5.3, and in particular (3.40). This process provides all M target's range $[\upsilon_m f_s]$, and Doppler $f_D^{p,m}$ information, where $p = 0,1,\dots,P-1$, $m = 0,1,2,\dots,M-1$.

For one target of interest, $m = k$, extract the target range $[\upsilon_k f_s]$, and Doppler $f_D^{p,k}$ information from all the *P* individual channels.

For the same target of interest, extract the target's phase compensation term for all *P* individual channels according to (5.27) or (5.29) (depending on the single channel processing).

Choose Δf in (5.22) and (5.23), i.e. choose the required range resolution.

Calculate (5.10) with the target's range $[\upsilon_k f_s]$, Doppler $f_D^{p,k}$, and phase compensation for all *P* channels.

Figure 5.3: The figure shows a flow chart of the multiband signal processing as is described in section 5.2.

Since the focus is on signals broadcasted from the same transmitter position, the geometries are identical for all frequencies in question for the same point target. An analogue argument as for (A.14) and (A.15) can be made for the multiple channels case, and thus the received reference signal, after reception, down conversion, (conditioning) filtering and IQ sampling may be written as

$$U_{ref}(t_i) = \sum_{p=0}^{P-1} \xi_{ref}^{p}(t_i) u_{ref}^{p}(t_i) e^{j2\pi((f_c^p - f_{ref}^p)t_i + \phi_c^p)}, \tag{5.1}$$

where $i = 0, 1, 2, \ldots, S-1$ for $S > 0$, an integer number of samples, P is the number of channels, and $p = 0, 1, 2, \ldots, P-1$ is the channel number, and $t_i = i/f_s$, where f_s is the IQ-sampling frequency. (For $P = 1$, (5.1) reduces to (3.35)). $u_{ref}^{p}(t_i)$ is the received reference channel's information signal, the complex time varying function $\xi_{ref}^{p}(t_i)$ is accounting for the potentially time varying target reflectivity in amplitude as well as phase, and for clear air effects like multipath, gaseous absorption, diffraction, and refraction, and non-clear air effects like precipitation and clouds. f_c^p is the carrier/center frequency of the pth channel, f_{ref}^p is the receiver down conversion, and ϕ_c^p is the initial phase for the pth channel.

[116] showed that (5.1) can in a logical way be recast in the two-dimensional function

$$z_{ref}(i, s) \overset{\text{def}}{=} \begin{cases} C_i U_{ref}(t_{i+sN}) & i = 0, 1, 2, \ldots, N-1 \\ 0 & i = N, N+1, \ldots, 2N-1 \end{cases} \tag{5.2}$$

where $N > 0$ and $A > 0$ are integers such that $(A+1)N \leq S$, and C_i is an identical filter for each value of $s = 0, 1, 2, \ldots, A-1$. (5.2) inserted (5.1) yields

$$z_{ref}(i, s) = \begin{cases} \sum_{p=0}^{P-1} C_i \alpha_{ref}^{p}(t_{i+sN}) u_{ref}^{p}(t_{i+sN}) e^{j2\pi(f_c^p - f_{ref}^p)t_{i+sN}} & i = 0, 1, 2, \ldots, N-1 \\ 0 & i = N, \ldots, 2N-1 \end{cases} \tag{5.3}$$

and

$$\alpha_{ref}^{p}(t_{i+sN}) = \xi_{ref}^{p}(t_{i+sN}) e^{j2\pi\phi_c^p}. \tag{5.4}$$

P channels of the CW transmitted and reflected surveillance signal is received, down converted, filtered and IQ sampled such that the resulting signal may be written

$$U_{sur}(t_i) = \sum_{p=0}^{P-1} \sum_{m=0}^{M-1} \xi_{sur}^{p,m}(t_i - \nu_m) u_{sur}^{p,m}(t_i - \nu_m) e^{j2\pi\left((f_c^p + f_D^{p,m} - f_{sur}^p)t_i - f_c^p \nu_m - (t_R - t_L) f_D^{p,m} + \phi_c^p\right)}, \tag{5.5}$$

where M is the number of targets, and $m = 0, 1, 2, \ldots, M-1$, is the target number. (For $P = 1$, (5.5) reduces to (3.31)). $u_{sur}^{p,m}(t_i - \nu_m)$ is the received information signal in the surveillance channel, the complex time varying function $\xi_{sur}^{p,m}(t_i)$ is accounting for the potentially time varying target reflectivity in amplitude as well as phase, and for clear air effects like multipath, gaseous absorption, diffraction, and refraction, and non-clear air effects like precipitation and clouds. f_c^p is the carrier/center frequency of the pth channel, $f_D^{p,m}$ is the mth target's Doppler shift based on the pth channel, and f_{sur}^p is

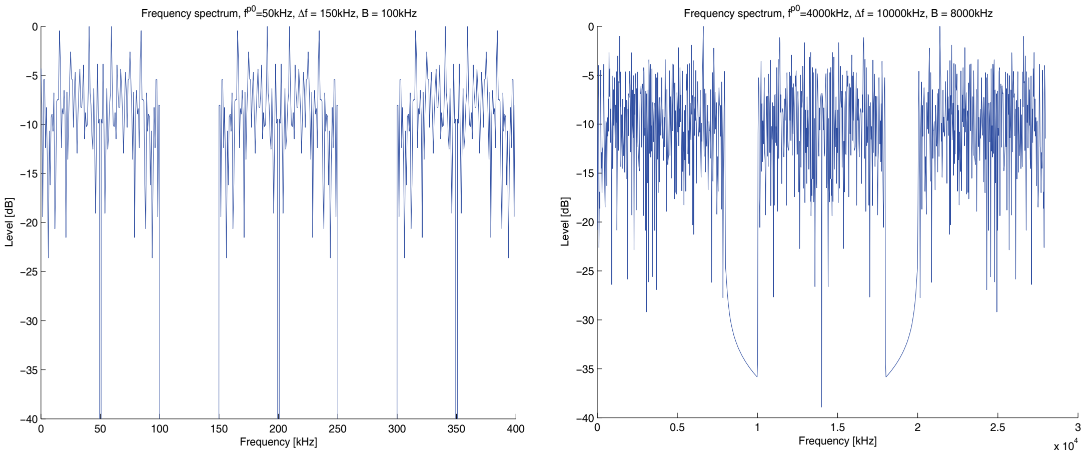

(a) FM radio parameters.

(b) DVB-T parameters.

Figure 5.4: Frequency spectrum for the bandlimited pseudo random generated noise. The parameters are defined in table 5.2

the receiver down conversion for the pth channel. A single geometry for each target (all transmitter(s) and receiver(s) at the same position) as seen in figure 3.2 is considered. For each single point target, the reflected signals arrives simultaneously at the receiver ν_m later for $m = 0, 1, 2, \ldots, M-1$, as derived in appendix A. $\nu_m = t_T + t_R - t_L$ for $t_T = R_T/c$, $t_R = R_R/c$, and $t_L = L/c$, where R_T, R_R, and L refers to figure 3.2. The signals initial phase ϕ_c^p for the pth is as for the reference channel (5.1).

As for the reference channel, (5.5) is recasted in the two dimensional function

$$z_{sur}(i, s) \overset{\text{def}}{=} U_{sur}(t_{i+sN}), \tag{5.6}$$

for $i = 0, 1, 2, \ldots, 2N-1$, and $s = 0, 1, 2, \ldots, A-1$, where $N > 0$ and $A > 0$ are integers such that $(A+1)N \leq S$. Further rearranging terms (5.5) and (5.6) yields

$$z_{sur}(i, s) = \sum_{p=0}^{P-1} \sum_{m=0}^{M-1} \alpha_{sur}^{p,m}(t_{i+sN} - \nu_m) u_{sur}^{p,m}(t_{i+sN} - \nu_m) e^{j2\pi(f_c^p + f_D^{p,m} - f_{sur}^p) t_{i+sN}}, \tag{5.7}$$

for $i = 0, 1, 2, \ldots, 2N-1$, and $s = 0, 1, 2, \ldots, A-1$, where

$$\alpha_{sur}^{p,m}(t_{i+sN} - \nu_m) = \xi_{sur}^{p,m}(t_{i+sN} - \nu_m) e^{j2\pi\left(-f_c^p \nu_m - (t_R - t_L) f_D^{p,m} + \phi_c^p\right)}. \tag{5.8}$$

The cross-correlation between two discrete functions is defined in (3.39), and applying this to (5.3) and (5.7) yields

$$\begin{aligned}\hat{z}(i,s) &= \sum_{n=0}^{2N-1} z_{ref}^{*}(n,s) z_{sur}(n+i,s)\\ &= \sum_{n=0}^{N-1}\sum_{q=0}^{P-1} C_n \alpha_{ref}^{q*}(t_{n+sN}) u_{ref}^{q*}(t_{n+sN}) e^{-j2\pi(f_c^q - f_{ref}^q)t_{n+sN}} \times\\ &\quad \sum_{p=0}^{P-1}\sum_{m=0}^{M-1} \alpha_{sur}^{p,m}(t_{n+i+sN}-\nu_m) u_{sur}^{p,m}(t_{n+i+sN}-\nu_m) e^{j2\pi(f_c^p + f_D^{p,m} - f_{sur}^p)t_{n+i+sN}},\end{aligned} \tag{5.9}$$

which, according to the distributive law of mathematics, can be written

$$\begin{aligned}\hat{z}(i,s) &= \sum_{n=0}^{N-1}\sum_{q=0}^{P-1} C_n \sum_{p=0}^{P-1}\sum_{m=0}^{M-1} \alpha_{ref}^{q*}(t_{n+sN}) \alpha_{sur}^{p,m}(t_{n+i+sN}-\nu_m) \times\\ &\quad u_{ref}^{q*}(t_{n+sN}) u_{sur}^{p,m}(t_{n+i+sN}-\nu_m) \times\\ &\quad e^{j2\pi\left((f_{ref}^q - f_c^q)+(f_c^p - f_{sur}^p)+f_D^{p,m}\right)t_{n+sN}} e^{j2\pi\left(f_c^p - f_{sur}^p + f_D^{p,m}\right)t_i},\end{aligned} \tag{5.10}$$

for $i = 0,1,2,\ldots,2N-1$ and $s = 0,1,2,\ldots,A-1$.

5.2.2 Range estimation

The range is estimated by the correlation, and this will be analyzed for a one reflector case, $\alpha_{sur}^{p,m}(t_{i+sN}-\nu_m) = 0$ for all $m \neq k$ for all values of p, i, and for all $s = 0,1,2,\ldots,A-1$. Thus

$$\begin{aligned}\hat{z}(i,s) &= \sum_{q=0}^{P-1}\sum_{p=0}^{P-1} e^{j2\pi\left((f_{ref}^q - f_c^q)+(f_c^p - f_{sur}^p)+f_D^{p,k}\right)t_{sN}} e^{j2\pi\left(f_c^p - f_{sur}^p + f_D^{p,k}\right)t_i} \times\\ &\quad \sum_{n=0}^{N-1}\Big[C_n \alpha_{ref}^{q*}(t_{n+sN}) \alpha_{sur}^{p,k}(t_{n+i+sN}-\nu_k) u_{ref}^{q*}(t_{n+sN}) u_{sur}^{p,k}(t_{n+i+sN}-\nu_k) \times\\ &\quad e^{j2\pi\left((f_{ref}^q - f_c^q)+(f_c^p - f_{sur}^p)+f_D^{p,k}\right)\frac{n}{f_s}}\Big],\end{aligned} \tag{5.11}$$

The sum over n in (5.11) depends on the product $\alpha_{ref}^{q*}(t_{n+sN}) u_{ref}^{q*}(t_{n+sN}) \alpha_{sur}^{p,k}(t_{n+i+sN} - \nu_k) u_{sur}^{p,k}(t_{n+i+sN}-\nu_k)$. As for the single channel case, it is further assumed that there is no time dependent variations in the received signal as a consequence of anomalous propagation, i.e. one path directly propagation from transmitter to receiver, and no phase or amplitude variations due to inhomogeneous medias, leading (5.4) to

$$\alpha_{ref}^p(t_{i+sN}) = \xi_{ref}^p(t_{i+sN}) e^{j2\pi\phi_c^p} = \alpha_{ref}^p = \xi_{ref}^p e^{j2\pi\phi_c^p} \tag{5.12}$$

where the complex time varying function $\xi^p_{ref}(t)$ now is considered a real positive constant ξ^p_{ref}. Equivalently for (5.8)

$$\begin{aligned}\alpha^{p,k}_{sur}(t_{i+sN}-\nu_k) &= \xi^{p,k}_{sur}(t_{i+sN}-\nu_k)e^{j2\pi\left(-f^p_c\nu_k-(t_R-t_L)f^{p,k}_D+\phi^p_c\right)} \\ &= \alpha^{p,k}_{sur}=\xi^{p,k}_{sur}e^{j2\pi\left(-f^p_c\nu_k-(t_R-t_L)f^{p,k}_D+\phi^p_c\right)} \qquad (5.13)\end{aligned}$$

where $\xi^{p,k}_{sur}$ is a real positive constant. The product $\alpha^{q*}_{ref}(t_{n+sN})\alpha^{p,k}_{sur}(t_{n+i+sN}-\nu_k)$ can then be written

$$\alpha^{q*}_{ref}(t_{n+sN})\alpha^{p,k}_{sur}(t_{n+i+sN}-\nu_k)=\alpha^{q*}_{ref}\alpha^{p,k}_{sur}=\xi^q_{ref}e^{-j2\pi\phi^q_c}\xi^{p,k}_{sur}e^{j2\pi\left(-f^p_c\nu_k-(t_R-t_L)f^{p,k}_D+\phi^p_c\right)}, \qquad (5.14)$$

leading to

$$\begin{aligned}\hat{z}(i,s) &= \sum_{q=0}^{P-1}\sum_{p=0}^{P-1}e^{j2\pi\left((f^q_{ref}-f^q_c)+(f^p_c-f^p_{sur})+f^{p,k}_D\right)t_{sN}}e^{j2\pi\left(f^p_c-f^p_{sur}+f^{p,k}_D\right)t_i}\times \\ &\quad \xi^q_{ref}\xi^{p,k}_{sur}e^{j2\pi\left(-f^p_c\nu_k-(t_R-t_L)f^{p,k}_D+\phi^p_c-\phi^q_c\right)}\times \\ &\quad \sum_{n=0}^{N-1}C_nu^{q*}_{ref}(t_{n+sN})u^{p,k}_{sur}(t_{n+i+sN}-\nu_k)e^{j2\pi\left((f^q_{ref}-f^q_c)+(f^p_c-f^p_{sur})+f^{p,k}_D\right)\frac{n}{f_s}}. \qquad (5.15)\end{aligned}$$

The target range is found by the correlation peak, and the behavior of the sum over n in equation (5.15) will be elaborated on. Defining

$$C^{p,q}(i,s)=\sum_{n=0}^{N-1}C_nu^{q*}_{ref}(t_{n+sN})u^{p,k}_{sur}(t_{n+i+sN}-\nu_k)e^{j2\pi\left((f^q_{ref}-f^q_c)+(f^p_c-f^p_{sur})+f^{p,k}_D\right)\frac{n}{f_s}}, \qquad (5.16)$$

for $p,q=0,1,2,\dots,P-1$. The product of the two functions $u^{q*}_{ref}(t_{n+sN})$ and $u^{p,k}_{sur}(t_{n+i+sN}-\nu_k)$ for $p=q$, can be thought of as time shifted versions of each other, and thus the cross-correlation between them will be a time shifted version of the autocorrelation, and will obtain its maximum value at $t=\nu_k$ instead of at the origin. For $p=q$ and $f^p_{ref}=f^p_{sur}$, the maximum of $C^{p,p}(i,s)$ as a function of i

$$C^{p,p}_{\max}(s)=\left|\sum_{n=0}^{N-1}C_nu^{p*}_{ref}(t_{n+sN})u^{p,k}_{sur}(t_{n+i+sN}-\nu_k)e^{j2\pi f^{p,k}_D\frac{n}{f_s}}\right|_{\max}, \qquad (5.17)$$

yields $i=[\nu_kf_s]$, where $[x]$ means the integer value of x. The filter C_n, for $n=0,1,\dots,N-1$, will widen (and lower) the target correlation peak as well as lower the sidelobes. The target's Doppler shift $f^{p,k}_D$ will also reduce the target peak, and it is well described in section 3.5.3, and especially in figure 3.16.

Setting $i=[\nu_kf_s]$ in (5.16)

$$C^{p,q}([\nu_kf_s],s)\approx\sum_{n=0}^{N-1}C_nu^{q*}_{ref}(t_{n+sN})u^{p,k}_{sur}(t_{n+sN})e^{j2\pi\left((f^q_{ref}-f^q_c)+(f^p_c-f^p_{sur})+f^{p,k}_D\right)\frac{n}{f_s}}. \qquad (5.18)$$

Further, setting $C_n = 1$, and $u_{ref}^{q*}(t_{n+sN})u_{sur}^{p,k}(t_{n+sN}) = 1$ for $n = 0, 1, 2, \ldots, N-1$, as well as $s = 0, 1, 2, \ldots, A-1$, for pairs of values for $p, q = 0, 1, 2, \ldots, P-1$ the sum in (5.18) will be a geometrical series [119,120], and for $f = (f_{ref}^q - f_c^q) + (f_c^p - f_{sur}^p) + f_D^{p,k}$

$$\sum_{n=0}^{N-1} \left(e^{j2\pi f/f_s}\right)^n = \begin{cases} N & f = lf_s \qquad l = 0, \pm 1, \pm 2, \ldots \\ \frac{\sin(N\pi f/f_s)}{\sin(\pi f/f_s)} e^{j(N-1)\pi f/f_s} & f \neq lf_s \qquad l = 0, \pm 1, \pm 2, \ldots \end{cases} . \tag{5.19}$$

The above sum's zeros are given by

$$f = \frac{f_s}{N} l \qquad l = 0, \pm 1, \pm 2, \ldots \qquad \text{and} \qquad l \neq mN,\ m = 0, \pm 1, \pm 2, \ldots, \tag{5.20}$$

which show that, the correlation between the reference and surveillance signal will be degraded depending on the value of $f = (f_{ref}^q - f_c^q) + (f_c^p - f_{sur}^p) + f_D^{p,k}$. Section 3.5.3 showed the effect of this for the target's Doppler shift, but now it is seen that also the choices on f_{ref}^q, f_c^q, f_{sur}^p as well as $f_D^{p,k}$ contributes to this reduction in correlation peak. This might be applied as an advantage, by letting $f = (f_{ref}^q - f_c^q) + (f_c^p - f_{sur}^p) + f_D^{p,k}$ take a value so that the sum ends up close to a zero for the values of $p \neq q$. However, this might be hard to achieve as the sum in real world is dependent on the function $u(t)$, and thus this might turn out to be a time dependent calculation. It is a topic for further fine tuning of the algorithm. The results from section 3.5.3 still applies with the single choices of p and q.

However, all contributions from $C^{p,q}(i, s)$ for $p \neq q$ are still contributing in the full sum as seen in equation (5.15), and their impact needs to be accounted for, which shortly will be attend to.

The function $u(t)$, the origin of $u_{ref}(t)$ and $u_{sur}(t)$ is in general a time varying function, as is indicated in equations (5.16) and (5.17) by the dependence on $s = 0, 1, 2, \ldots, A-1$. This is necessarily not correct, and the error is illustrated by two examples in figure 5.5 for the pseudo random bandlimited noise code with FM radio and DVB-T parameters. Especially for real life FM radio waveforms this assumption is in general violated due to the program content dependent information signal. However, for shorter time segments, N low, even the FM radio waveforms might be considered constant with time. The problem arises when multiple of these are going to be integrated over time, and especially for the Doppler processing, which are explained in the next chapter. In order to mitigate the time varying response, there are two options. The first being extending the coherent range correlation processing interval, as seen in figure 5.5a for the same parameters as in figure 5.5c except each range correlation interval is four times longer, although the total $CPI \approx 1.3 sec$ is the same. Figure 5.5d shows the range correlation response for a repeating code, where the periodicity of the code is equal to the processing time's PRF=N/f_s, and thus the correlation should behave exactly the same way for each range correlation interval. This is the signal form used in the Norwegian multistatic radar DiMuRa, and further information can be found in [116,122–125].

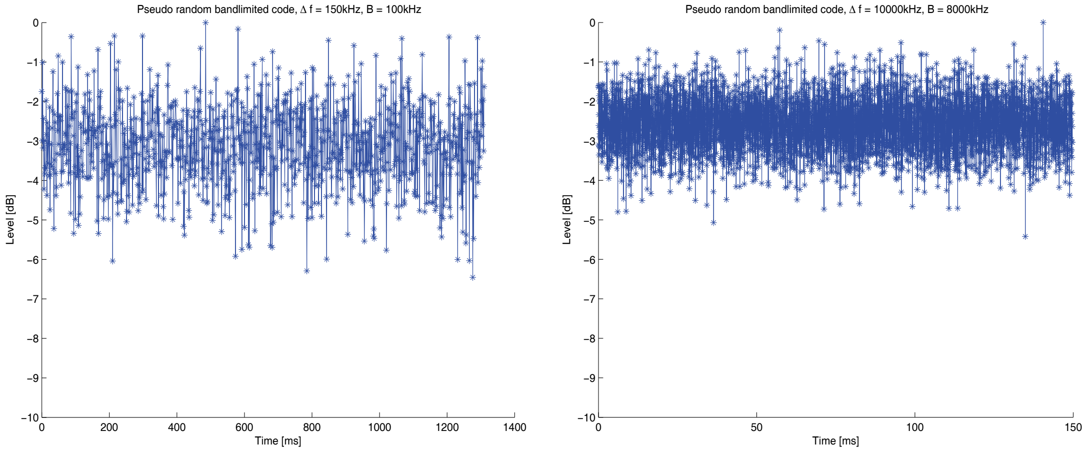

(a) FM radio parameters, $CPI \approx 1.3sec$, $N = 512,\ A = 1024$.

(b) DVB-T parameters, $CPI \approx 0.15sec$. $N = 1024,\ A = 4096$.

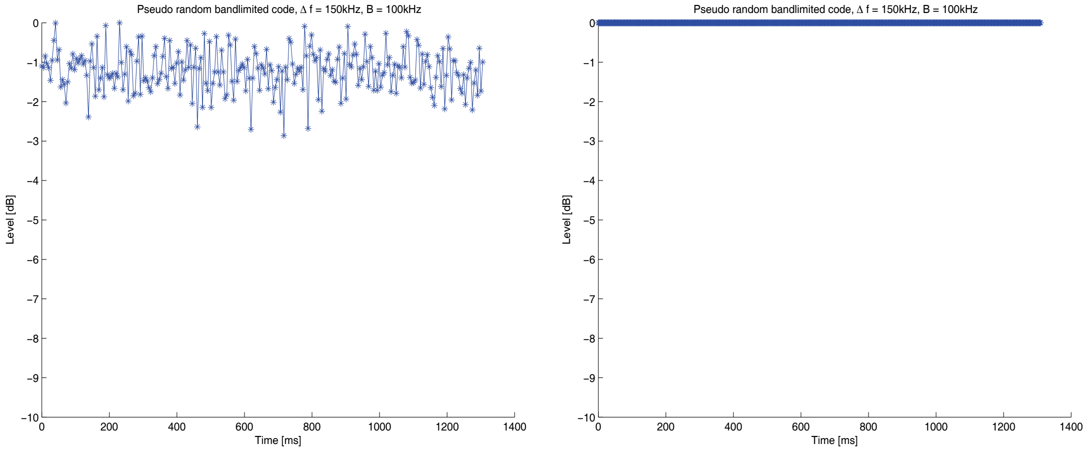

(c) FM radio parameters, $CPI \approx 1.3sec$. $N = 2048,\ A = 256$.

(d) FM radio parameters, repeating code. $N = 512,\ A = 1024$.

Figure 5.5: Range correlation stability as a function of time for the bandlimited pseudo random generated noise. The simulation parameters are listed in table 5.2.

Equation (5.15) shows that for the multichannel situation, the resulting coherent sums are not necessarily at their maximum values. Setting $i = [\nu_k f_s]$ in (5.15) yields

$$\begin{aligned}\hat{z}([\nu_k f_s], s) \quad = \quad & \sum_{q=0}^{P-1}\sum_{p=0}^{P-1} e^{j2\pi\left((f_{ref}^{q}-f_c^q)+(f_c^p-f_{sur}^p)+f_D^{p,k}\right)t_{sN}} e^{j2\pi\left(f_c^p-f_{sur}^p+f_D^{p,k}\right)\frac{[\nu_k f_s]}{f_s}} \times \\ & \xi_{ref}^{q}\xi_{sur}^{p,k}e^{j2\pi\left(-f_c^p\nu_k-(t_R-t_L)f_D^{p,k}+\phi_c^p-\phi_c^q\right)} \times \\ & \sum_{n=0}^{N-1} C_n u_{ref}^{q*}(t_{n+sN})u_{sur}^{p,k}(t_{n+[\nu_k f_s]+sN}-\nu_k)e^{j2\pi\left((f_{ref}^{q}-f_c^q)+(f_c^p-f_{sur}^p)+f_D^{p,k}\right)\frac{n}{f_s}},\end{aligned} \tag{5.21}$$

for $s = 0, 1, 2, \ldots, A-1$. Equation (5.21) shows that in contrast to the single channel case, section 3.5 where $P = 1$, even if the correct target range is estimated by the algorithm, the target response will not necessarily be at its maximum value due to the double sum of complex values not necessarily being in phase, nor at the same frequency. Further, the modulating exponentials at different frequencies due to the down modulating and target's Doppler shift in (5.21) will make the coherent sum oscillate, and thus a ranging error might be induced if not properly handled. This is in principle the situation illustrated in figure 5.2.

In order to optimize the value of the sum in equation (5.21), and be ensured the required bandwidth in the range correlation, it is decided to optimize the efforts on a single target, and thus f_{ref}^{q} is chosen

$$f_{ref}^{q} = q\Delta f + f_c^q + f_{ref}^{q0} + lf_s \tag{5.22}$$

and f_{sur}^{p} is chosen

$$f_{sur}^{p} = p\Delta f + f_c^p + f_D^{p,k} + f_{sur}^{p0} + l'f_s, \tag{5.23}$$

for $l, l' = 0, \pm1, \pm2, \ldots$, and f_{ref}^{q0}, f_{sur}^{p0} being the initial frequency offsets. This means that

$$\Delta f = \frac{f_{ref}^{q} - f_c^q}{q} = \frac{f_{sur}^{p} - f_c^p}{p} \tag{5.24}$$

for $f_D^{p,k} = 0$, $f_{ref}^{q0} = f_{sur}^{p0} = 0$, and $l = l' = 0$. Δf is the difference between the broadcasted channel's carrier frequency and the down modulation in the receiver for the reference or surveillance channel. The schematics of this is shown in figure 4.8 and figure 5.1. In (5.24) Δf is described as a fixed quantity for all $p, q = 0, 1, 2, \ldots, P-1$. This is a choice of convenience, and not a mathematical requirement. The general case of not using the same difference in frequency between the down modulated channels could have been described here. However, that would only clutter the presentation of the method without justifying the increased complexity in notation. No results from such an approach are included in this thesis. However, simple experiments suggested the effect being less predictable ambiguities in both amplitude and range, as is believed also to be supported by [64]. Equation (5.21) inserted (5.22) and (5.23) then reduces to

$$\begin{aligned}\hat{z}([\nu_k f_s], s) \;=\; & \sum_{q=0}^{P-1}\sum_{p=0}^{P-1} e^{j2\pi\left((q\Delta f+f_{ref}^{q0})-(p\Delta f+f_{sur}^{p0})\right)t_{sN}} e^{-j2\pi\left(p\Delta f+f_{sur}^{p0}\right)\frac{[\nu_k f_s]}{f_s}} \times \\ & \xi_{ref}^{q}\xi_{sur}^{p,k} e^{j2\pi\left(-f_c^p\nu_k-(t_R-t_L)f_D^{p,k}+\phi_c^p-\phi_c^q\right)} \times \\ & \sum_{n=0}^{N-1} C_n u_{ref}^{q*}(t_{n+sN})u_{sur}^{p,k}(t_{n+[\nu_k f_s]+sN}-\nu_k) e^{j2\pi\left((q\Delta f+f_{ref}^{q0})-(p\Delta f+f_{sur}^{p0})\right)\frac{n}{f_s}},\end{aligned} \tag{5.25}$$

for $s = 0, 1, 2, \ldots, A-1$.

For $p \neq q$, (5.16)-(5.17), $C_{\max}^{p,q}(s) \leq C_{\max}^{p,p}(s)$, $s = 0, 1, 2, \ldots, A-1$, as the best fit for the function is the function itself. Further, looking at the properties of the ambiguity function in [22,27,30–32,37,42,44], it is expected that $C_{\max}^{p,q}(s) \ll C_{\max}^{p,p}(s)$ for $p \neq q$, as is also shown in figure 5.6. Figure 5.6 shows the simulated co- and cross-channel correlation for both examples mimicking FM radio and DVB-T signal parameters. The co-channel correlations ($p = q$) are on the diagonal, while off the diagonal are the cross-channel correlations ($p \neq q$). It is seen that the cross-channel correlation is down by at least $10dB$ for both the FM radio and the DVB-T case. Based on the auto- and cross-correlation properties of $u_{ref}(t)$ and $u_{sur}(t)$ as seen in (5.16) and (5.17), it is expected $C_{max}^{p,q}(s) \ll C_{\max(s)}^{p,p}$ for $p \neq q$, meaning that the cross-correlations for non-corresponding reference and surveillance channels will be dominated by the correlations from corresponding reference and surveillance channels as seen in figure 5.6. Further, it is reasonable to choose $f_{ref}^{q0} = f_{sur}^{p0}$. This, as well as setting equation (5.18) in (5.25)

$$\hat{z}([\nu_k f_s], s) \;\approx\; \sum_{p=0}^{P-1} C^{p,p}([\nu_k f_s], s)\xi_{ref}^{p}\xi_{sur}^{p,k} e^{-j2\pi\left(p\Delta f+f_{sur}^{p0}\right)\frac{[\nu_k f_s]}{f_s}} e^{j2\pi\left(-f_c^p\nu_k-(t_R-t_L)f_D^{p,k}\right)}, \tag{5.26}$$

for $s = 0, 1, 2, \ldots, A-1$. Equation (5.26) shows the need to compensate for the phase of the resulting correlation for each of the individual channels, as well as two exponential complex terms originating from the Δf value and f_{sur}^{p0} which is both known figures. The first part of the compensation can be achieved for the range and Doppler shift in question by considering the result of the correlation (5.9) for the individual channels, $P = 1$ for each of the channels as described in [116]

$$\hat{z}'([\nu_k f_s], s) = C^{w,w}([\nu_k f_s], s)\xi_{ref}^{w}\xi_{sur}^{w,k} e^{-j2\pi\left(w\Delta f+f_{sur}^{w0}\right)\frac{[\nu_k f_s]}{f_s}} e^{j2\pi\left(-f_c^w\nu_k-(t_R-t_L)f_D^{w,k}\right)}, \tag{5.27}$$

for $p = w$, for $w = 0, 1, 2, \ldots, P-1$ and $s = 0, 1, 2, \ldots, A-1$. The term $\hat{z}'([\nu_k f_s], s)$ in (5.27) will be used to align the phases for the individual channels before range correlation, and this is a figure that should be readily available from the correlation of the individual channels (as most likely already are used for target detection and tracking). In real life situations, the phase might not be available individually for each $s = 0, 1, 2, \ldots, A-1$,

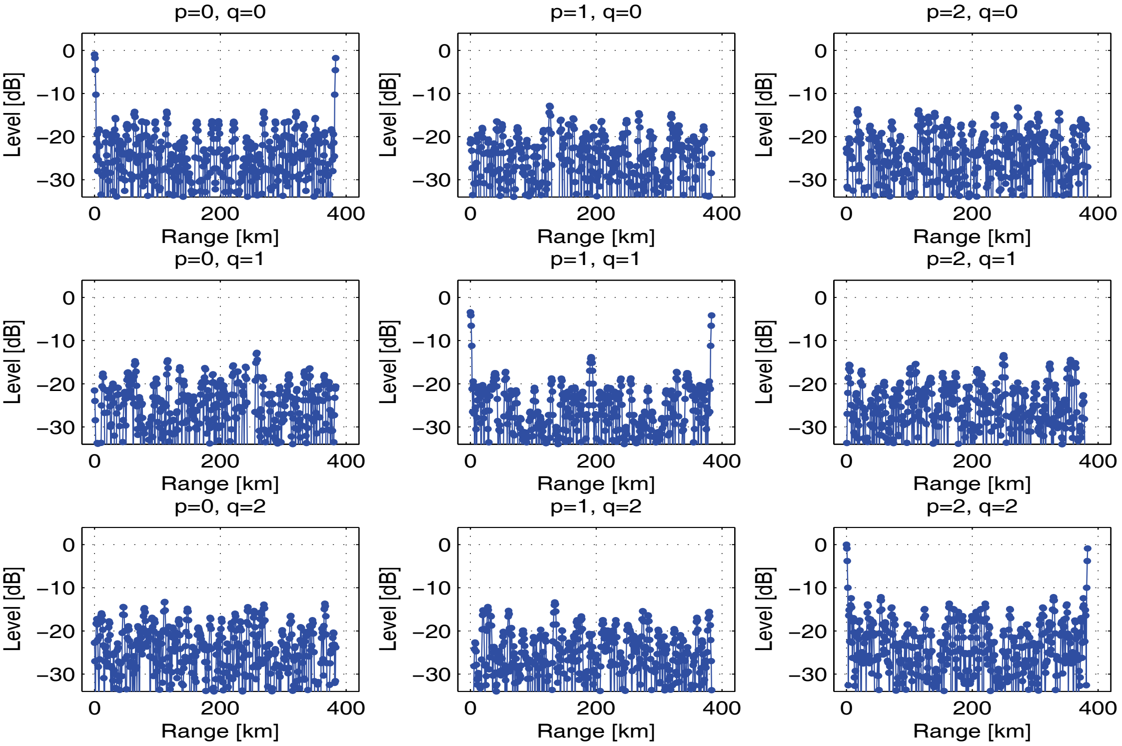

(a) FM radio parameters, table 5.2.

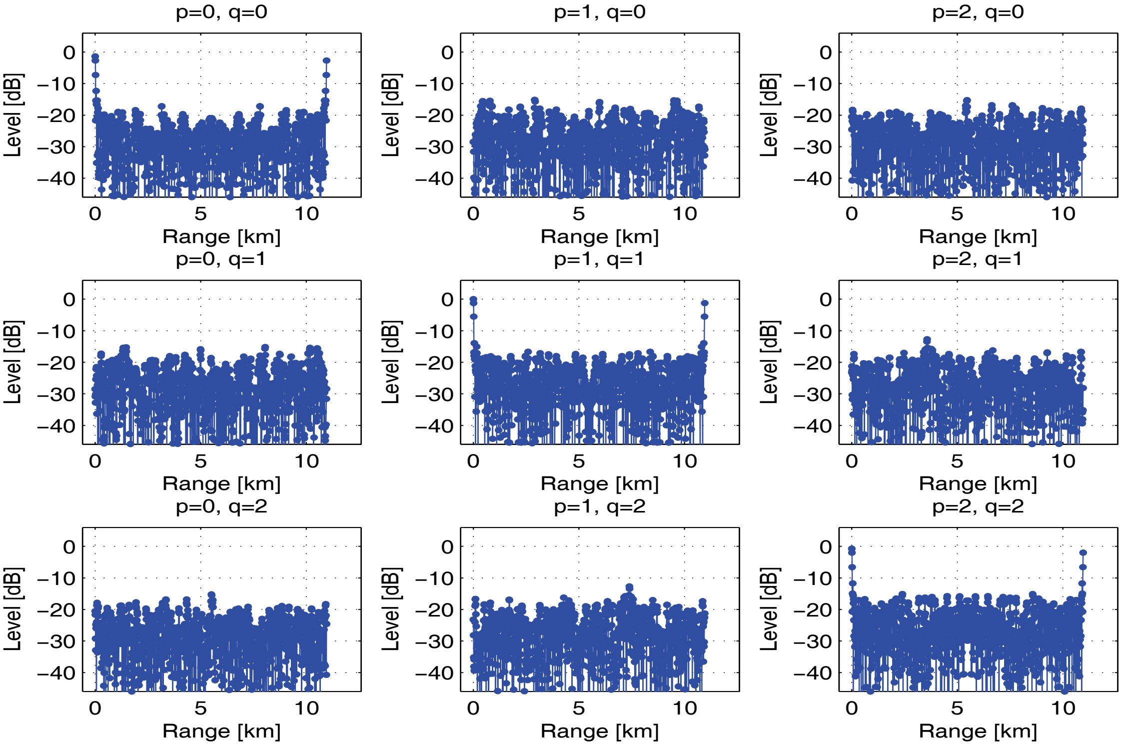

(b) DVB-T parameters, table 5.2.

Figure 5.6: Simulated, equation (5.9), co- and cross-channel correlation for the $P = 3$ channels. The frequency spectra for the applied signals are shown in figure 5.4.

or an averaged value might be sought, in order to counter the variation of $C^{w,w}([\nu_k f_s], s)$ with s. In this case, the target's peak value after the Doppler processing might be applied, which for equation (5.27) means that this is the zero frequency/velocity bin of the FFT, i.e. average value, as all target responses are shifted to this bin, (5.22)-(5.23).

This approach cannot be used if the phase correction term is to be extracted from the single channel's processing. The target will in the single channel's processing be shifted according to its Doppler-shift, and this should be corrected for. This applies whether the term is taken from each range correlation, or from the fully processed range-Doppler matrix. By setting (3.45) in (3.41),

$$\begin{aligned}\hat{z}(i,s) &= e^{j2\pi f_D^k t_{sN}} \xi_{ref}\xi_{sur}^k e^{j2\pi(f_c - f_{sur} + f_D^k)t_i} e^{j2\pi(-f_c\nu_k - (t_R - t_L)f_D^k)} \times \\ & \sum_{n=0}^{N-1} C_n u_{ref}^*(t_{n+sN}) u_{sur}^k(t_{n+i+sN} - \nu_k) e^{j2\pi f_D^k t_n}, \end{aligned} \tag{5.28}$$

which by applying the notation of equation (5.16), and inserting $i = [\nu_k f_s]$ reduces to

$$\begin{aligned}\hat{z}'([\nu_k f_s], s) &= e^{j2\pi f_D^k t_{sN}} C^{w,w}([\nu_k f_s], s)\xi_{ref}\xi_{sur}^k \times \\ & e^{j2\pi(f_c - f_{sur} + f_D^k)\frac{[\nu_k f_s]}{f_s}} e^{j2\pi(-f_c\nu_k - (t_R - t_L)f_D^k)}. \end{aligned} \tag{5.29}$$

Two differences between (5.27) and (5.29) are noted. First, the term $e^{j2\pi f_D^k t_{sN}}$, which means that the single channel processing places the target at its correct Doppler shift in the range-Doppler matrix as expected. Second, there is the difference between the term $e^{-j2\pi\left(w\Delta f + f_{sur}^{w0}\right)\frac{[\nu_k f_s]}{f_s}}$ from (5.27) and the term $e^{j2\pi(f_c - f_{sur} + f_D^k)\frac{[\nu_k f_s]}{f_s}}$ from (5.29), which means that the single channel case never go above $p = 0$, as this is a single channel range-Doppler processing. Both these terms needs to be accounted for if the phase term shall be taken directly from the single channel's processing, i.e. equation (5.29). The brute force approach would be to process single channels directly according to (5.27), and thus get the phase correction term.

By doing this, both the different Doppler shifts, as well as the unknown phases of each of the Doppler shifted frequencies are compensated, and the correlation peak of the target will achieve its maximum value.

5.2.3 Doppler processing

The multiple channels range correlation is now stable with time and target Doppler shift. The focus will now be shifted to the algorithm's Doppler tolerance for a one reflector case, $\alpha_{sur}^{p,k}(t_{n+i+sN} - \nu_k) = 0$ for all $m \neq k$ for one value of i, and all values of s. The Doppler shift is known a priori through the target detection and tracking process for the individual channels, and has also been compensated for in (5.22) and (5.23). In order to achieve the required time-bandwidth product in the signal processing, and thus suppress clutter Doppler processing is introduced. The focus here will also be on the processing scheme's robustness for the target's Doppler variations. Doppler variations coming either from uneven translational movement, rotational Doppler from non-radial movement or maneuvering, and/or micro Doppler from internally moving parts on the target.

The Doppler processing is performed by a FFT over the s-dimension, as for the single channel case in section 3.5.3. Equation (5.26) showed that the perfectly Doppler matched compensation (equations (5.22) and (5.23)) shifts the target to the stationary Doppler bin, and thus the range result of (5.26) for this bin is independent of s, and thus time. The importance of small target Doppler variations which are not compensated for will in further detail be considered. Thus the previous discussion is revisited, with the Doppler shift notation now according to

$$f_D^{p,k} \rightarrow f_D^{p,k} + \delta_D^{p,k}, \tag{5.30}$$

where $\delta_D^{p,k}$ is a small Doppler shift on top of the regular translational Doppler shift $f_D^{p,k}$ for target number k for channel number p. (5.22), (5.23), and (5.30) inserted into (5.21), with for $C_{max}^{p,q}(s) \ll C_{\max(s)}^{p,p}$ for $p \neq q$, and $f_{ref}^{q0} = f_{sur}^{p0}$ yields

$$\begin{aligned} \hat{z}([\nu_k f_s], s) \quad = \quad & \sum_{p=0}^{P-1} e^{-j2\pi\left(p\Delta f + f_{sur}^{p0} - \delta_D^{p,k}\right)\frac{[\nu_k f_s]}{f_s}} \xi_{ref}^{p} \xi_{sur}^{p,k} e^{j2\pi\left(-f_c^p \nu_k - (t_R - t_L)(f_D^{p,k} + \delta_D^{p,k})\right)} \times \\ & \left(\sum_{n=0}^{N-1} C_n u_{ref}^{p*}(t_{n+sN}) u_{sur}^{p,k}(t_{n+[\nu_k f_s]+sN} - \nu_k) e^{j2\pi\delta_D^{p,k}\frac{n}{f_s}} \right) e^{j2\pi\delta_D^{p,k}\frac{N}{f_s}s}, \end{aligned} \tag{5.31}$$

for $s = 0, 1, 2, \ldots, A-1$. Once the phase term (5.27) of each of the P channels have been compensated for (multiplied by the complex conjugate of (5.27)), (5.31) is recasted into

$$\begin{aligned} \hat{z}'([\nu_k f_s], s) \quad = \quad & \sum_{p=0}^{P-1} D_s \left(\xi_{ref}^{p} \xi_{sur}^{p,k} \right)^2 e^{j2\pi\delta_D^{p,k}\frac{[\nu_k f_s]}{f_s}} e^{-j2\pi(t_R - t_L)\delta_D^{p,k}} \times \\ & \left(\sum_{n=0}^{N-1} C_n u_{ref}^{p*}(t_{n+sN}) u_{sur}^{p,k}(t_{n+[\nu_k f_s]+sN} - \nu_k) \right)^* \times \\ & \left(\sum_{n=0}^{N-1} C_n u_{ref}^{p*}(t_{n+sN}) u_{sur}^{p,k}(t_{n+[\nu_k f_s]+sN} - \nu_k) e^{j2\pi\delta_D^{p,k}\frac{n}{f_s}} \right) e^{j2\pi\delta_D^{p,k}\frac{N}{f_s}s}, \end{aligned} \tag{5.32}$$

for $s = 0, 1, 2, \ldots, A-1$. In order to lower the sidelobes of the FFT in the Doppler direction, a traditional window function/filter has been applied in (5.32), D_s, for $s = 0, 1, 2, \ldots, A-1$. Suitable filters are well described and the behavior thoroughly documented in the renowned work of Harris [121].

Equation (5.32) shows that if the variations of each of the $s = 0, 1, 2, \ldots, A-1$ range correlations, i.e. n-sums, is neglectable, the only s-dependence is in the last term. By performing a FFT over the s-direction of the matrix, $\delta_D^{p,k}$ is found under the condition that the resolution of the FFT allows it. This discussion is actually parallel to the one in section 3.5.3 and illustrated in figure 3.16. I.e. it is applicable for values of $\delta_D^{p,k}$. The $\delta_D^{p,k}$ will reduce the peak of the range correlation as previously described, but for each

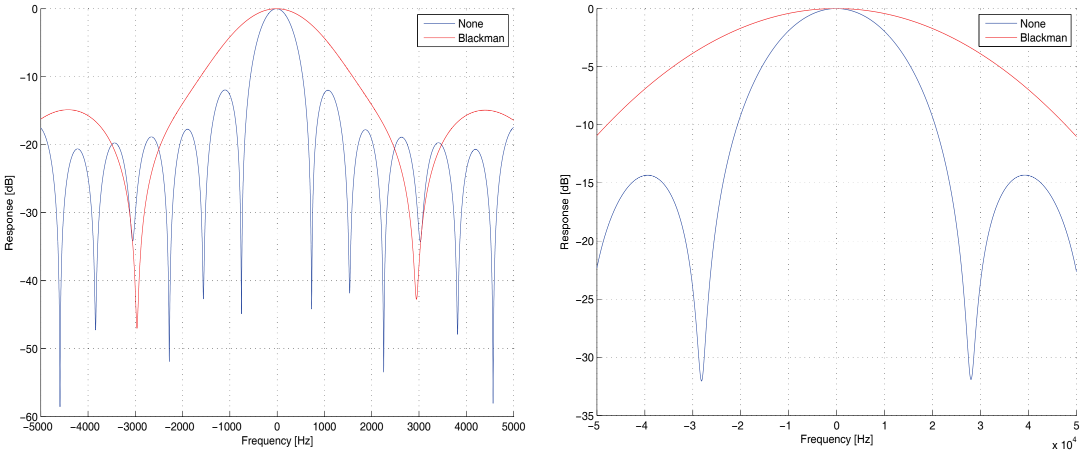

(a) FM radio parameters, $N = 512,\ f_s = 400kHz$.

(b) DVB-T parameters, $N = 1024,\ f_s = 28MHz$.

Figure 5.7: The algorithms Doppler response for the two examples from FM radio and DVB-T parameter sets as described in table 5.2.

range gate's values of $s = 0, 1, 2, \ldots, A-1$ the value range correlation's value might be considered constant over s.

The target's Doppler frequencies is now found through a FFT of equation (5.32) for all $s = 0, 1, 2, \ldots, A-1$. And for the full matrix, for each of the ranges $i = 0, 1, 2, \ldots, M-1$[1], i.e. for all the M ranges of interest in (5.10).

From equation (5.20) it is seen that the Doppler response of the signal processing is as for the single channel case, dependent on the sampling frequency f_s, number of samples in the range correlation processing N, as well as the applied range filter. Figure 5.7 shows the response of the FM radio and DVB-T parameters for no range filter, as well as one Blackman-Harris filter for the pseudo random code with parameters as in table 5.2. This is the multichannel version of figure 3.16 although the numbers are different, the principles remains the same.

It is important to note that the goal is not to compensate for the influence of the term $\delta_D^{p,k}$, but to map the importance of the extra Doppler term in the processing. The single channel processing of section 3.5.3 was compensating $f_p = f_{ref} - f_{sur}$, equation (3.52), for the difference in the down modulation in the reference and surveillance channels. For the multiple frequency case, this is already compensated for in equation (5.23). The difference between the two in principle very similar processing schemes of section 3.5.3 and this section is that the former is focusing on target detection and producing detections for target track, while the latter is focusing on better range resolution performance for single targets as well as maintaining the Doppler resolution of the long integration time, in order to improve target resolution and/or extract individual target information.

For real life applications, there will be multipath effects, and time varying propagation

---

[1] It is important to keep in mind that now the index i corresponds to one range bin, and $s = 0, 1, 2, \ldots, A-1$ corresponds to all the Doppler bins, i.e. looking at all Doppler velocities at one range bin. This argument can obviously be made for all the i range bins, and thus all ranges Doppler velocities are found.

conditions as well as time varying program content of the exploited broadcasted channels. The latter being severe for FM radio as is well documented [3,4,22,23,26,27,29–31,33,36, 37,40,44]. For the digital waveforms the correlation stability due to waveforms is more predictable, as shown in [22,23,26,31,32,40,41,116].

In the algorithm development, it was assumed the same target response for all frequencies/channels. This is not necessary, but a choice of convenience in order to ease the presentation of the algorithm. The algorithm can easily be extended to cope with the individual channel equalization directly, but that would only complicate the picture unnecessarily. In real life the target's RCS may be expected to be frequency dependent as well as the broadcast parameters and propagation. This will result in varying target response in the processing, and in order to make the algorithm behave predictable, this should be equalized for each channel for the target. For the FM radio PBR this is not expected to happen, as the frequency span is only $20MHz$, as well as the carrier frequencies are low, $88 - 108MHz$, for the targets of interest. However, once looking at DVB-T, the frequency span is larger $320MHz$, as well as the frequencies higher, $470 - 790MHz$. From real life target analysis, the target response equalization was found necessary for the DVB-T waveform, chapter 7, but not for the FM radio waveform.

5.2.4 Algorithm simulations

In this section the performance of the algorithm will be presented. The algorithm simulations were made by using the signals with parameters of table 5.2 in equation (5.10) for $M = 1$. Figures 5.8 and 5.9 show all the combinations of target response in the signal processing while compensating for the Doppler frequency (5.22)-(5.23), as well as compensating for the phase term (5.27) as a function of time (total CPI) and Doppler frequency ($\delta_D^{p,k}$ in (5.30)). All plots show the time varying surface fluctuations ($< 5dB$) which arise from the time varying range correlation properties from the code, as seen in figure 5.5, where it also is shown that the fluctuations may be countered by increasing the range correlation CPI. The fluctuations may be removed by using a repetitive signal of same length as the range correlation interval. However, this is not in general possible once relying on broadcasted signals of opportunity, even if the range correlation interval might be free to choose.

Figures 5.8a and 5.9a show the straightforward summation of target responses of all exploited channels. The response is time varying as well as the initial processing response is low (around $-35dB$). Figures b of 5.8 and 5.9 show that getting the phase right is important due to signal levels at the start of the processing only ($0dB$). The phase compensation ensures maximum target response in the signal processing only at the start of the processing, while compensating for the Doppler frequencies makes the target response stationary, but not necessarily at its maximum, figures c of 5.8 and 5.9. By compensating for both the phase and the frequency, stable target response at maximum value from the signal processing's point of view are achieved, figures d of 5.8 and 5.9. Although stable here means variations below $5dB$ due to the code correlation properties as a function of time. It is noted that the analyzed Doppler segment shows that the small additional Doppler

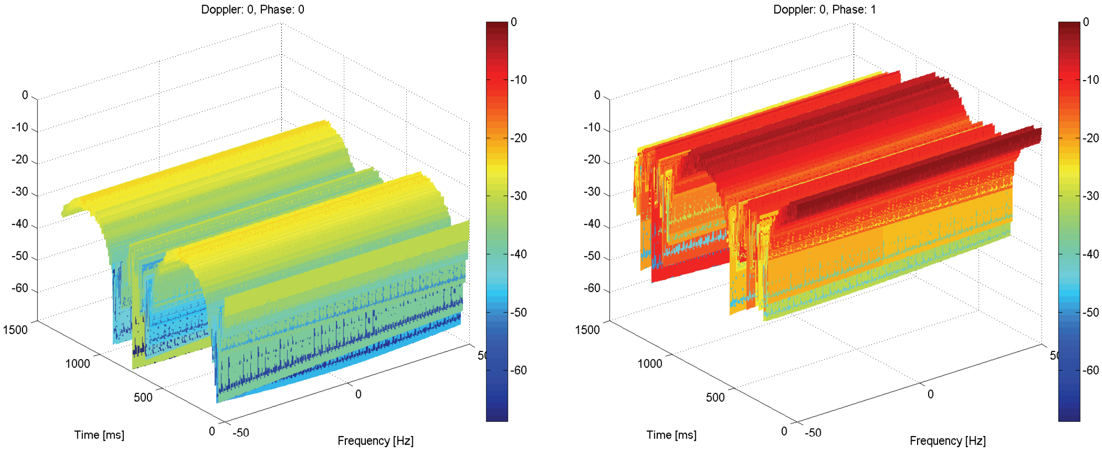

(a) No Doppler nor phase compensation. (b) No Doppler, phase only compensation.

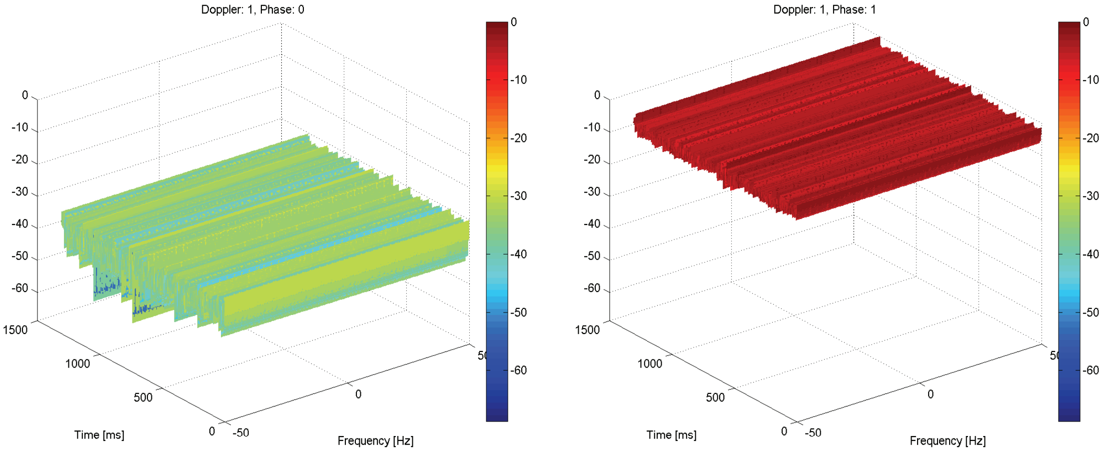

(c) Only Doppler, no phase compensation. (d) Both Doppler and phase compensation.

Figure 5.8: The figure shows all the combinations of target response in the signal processing while compensating for the Doppler frequency (5.22)-(5.23), as well as compensating for the phase term (5.27) as a function of time (total CPI) and Doppler frequency ($\delta_D^{p,k}$ in (5.30)) for the PBR signal processing for FM radio parameters.

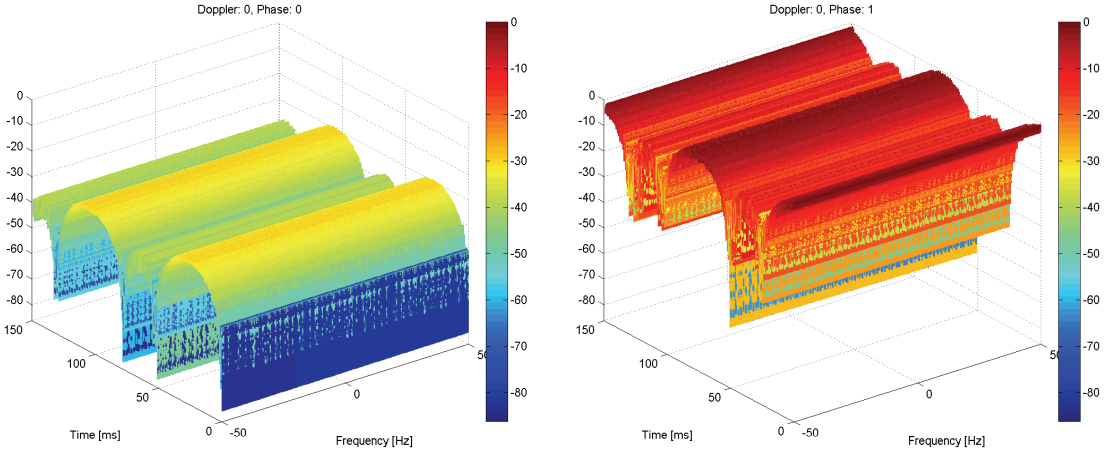

(a) No Doppler nor phase compensation. (b) No Doppler, phase only compensation.

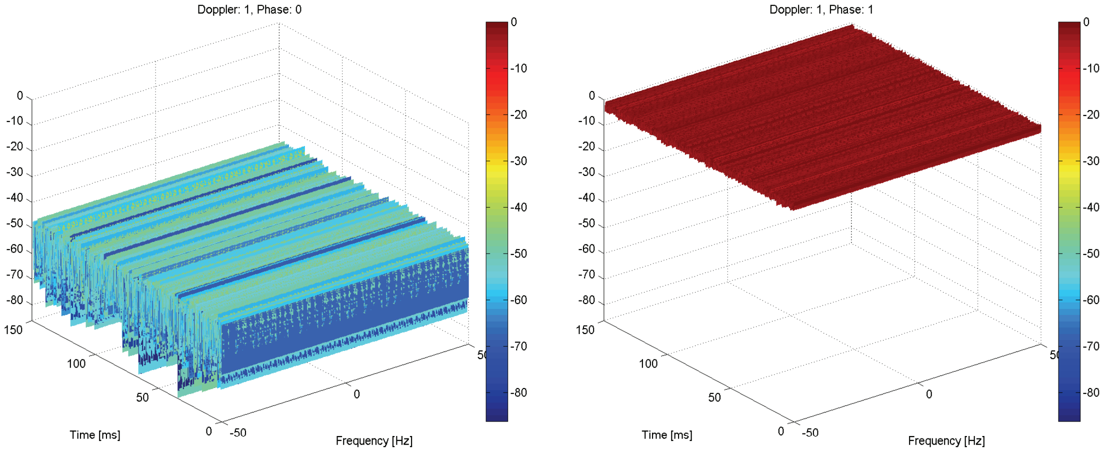

(c) Only Doppler, no phase compensation. (d) Both Doppler and phase compensation.

Figure 5.9: The figure shows all the combinations of target response in the signal processing while compensating for the Doppler frequency (5.22)-(5.23), as well as compensating for the phase term (5.27) as a function of time (total CPI) and Doppler frequency ($\delta_D^{p,k}$ in (5.30)) for the PBR signal processing for DVB-T parameters.

shift analyzed in equation (5.30)-(5.32) will not impact destructively on the algorithm.

The now higher range correlation resolution in combination with the maintained Doppler resolution from the relatively long integration time motivates ISAR imaging of targets. In order to do so, it is of high interest to reduce the target response's oscillations as a function of time due to the time varying code correlation properties. However, both the FM radio and the DVB-T signal's time varying correlation properties as plotted in figure 5.5 indicate that from the algorithm's point of view, stable enough correlation properties with time should be achievable in both range and Doppler, and hence ISAR imaging of targets based on multiple broadcasted signals from the same transmitter should be possible to achieve.

In the analysis of real targets it shall be seen, chapters 6 and 7, that the low frequency $88 - 108MHz$, and $470 - 790MHz$ combined with the motion of the targets results in a very low Doppler shifts, and thus ISAR images for the applied integration times are not possible to obtain. However, simple HRR analysis of two targets of opportunity, section 7.4 will be presented.

5.3 Summary

A mathematical processing scheme has been developed. The algorithm is inspired by the high range resolution approaches used in HRR radar systems, on how to exploit multiple non-adjacent broadcasted channels/bands in the PBR range correlation in order to achieve higher range resolution, while maintaining the Doppler resolution from the relatively long integration times. The broadcasted channels/bands are assumed to be from a single transmitter. The following problems were addressed and solved:

- By using broadcasted signals at different carrier frequencies, the target Doppler shift will be different, and the proposed method takes this into account.

- By using time varying waveforms (signals of opportunity, i.e. FM, DAB, DVB-T, or pseudo noise) in the range correlation, a time varying result is achieved. If this becomes an issue, it should be countered by increasing the range correlation time. This might be achieved either by increasing the total CPI, or by keeping the CPI constant and reducing the Doppler resolution.

- Combining multiple bands results in co-channel correlation as well as cross channel correlation. While only the former is sought, it was showed that the cross terms may be neglected due to their correlation properties with respect to each other. This is also helped by the fact that they contain a destructive frequency component from the de-modulation.

- Even though good individual correlation performances are achieved for single channels/bands, summing the correlation contributions for the different channels/bands might cause an out of phase summation which will modulate the range correlation peak in a way that may cause erroneous range estimates to be made. The algorithm

> estimates a phase correction term that once applied make all contributions in phase, and thus the erroneous range estimates, as well as destructive summing of target responses, are avoided.

The method was tested on pseudo random generated noise signals with FM radio and DVB-T like parameters. The pseudo random noise signals were chosen in order to some extent use a predictable code in the presentation of the algorithm. The FM radio signals are highly time varying signals, and the DVB-T signal contains deterministic components that results in predictable ambiguities [23, pp. 315-338]. In order to mitigate these signal specific effects in the performance presentation of the algorithm, a pseudo random noise signal which behaved predictable was generated.

In summary, this chapter has shown the development of a processing scheme enabling the simultaneous processing of multiple broadcast channels in order to improve the range correlation's bandwidth. The algorithm developed has been derived mathematically and tested using simulated signals. This work forms the basis for developing high range resolution imaging and ISAR capabilities in the PBR systems under consideration. In the next two chapters experimental evaluation of the algorithm developed using real FM and DVB-T broadcasts and commercial aircraft targets are reported.

Chapter 6

FM PBR Results and Analysis

This chapter presents the performance analysis of the FM radio waveform using the algorithm developed in chapter 5. Using both simulation and real target data it will be shown that the proposed algorithm offers improved range resolution capability. All datasets were collected with the hardware described in chapter 4.

6.1 FM waveform analysis

For the FM radio waveform, a simple signal conditioning was applied, figure 3.15. The target's response across single channels were equalized, and thus each of the individual channel's signal level were adjusted so that the target's peak response of each of the individual channels after full range Doppler processing are equal. Testing showed no major performance improvement, the target seems stable, and the range sidelobes seem to behave like before. It is expected that the time varying waveform is impacting the performance more than the difference in target signal response. The FM radio target response differences (figure 6.3 $< 6dB$) were also less than for the DVB-T case (figure 7.2 $< 14dB$), and combined with the difference in bandwidth this may cause the difference in performance. For the DVB-T case, the same waveform conditioning was successful. It should be noted that this topic has not been studied in full depth, and further studies are required before solid conclusions are made.

The basics of the FM radio waveform is presented in appendix B, in particular the FM modulation in section B.1. A short survey is presented in section B.2 of the various bandwidth considerations coming from the communication research. It is shown that these considerations are not suitable for radar purposes, as they are focusing on providing sufficient bandwidth for proper channel quality and stability, while efficiently exploiting the limited frequency available. Finally, section B.3 provides a mathematically formulated version (in the nomenclature of this thesis, section B.1), of a FM SW radio demodulation algorithm [98]. This is the SW digital demodulation scheme used in order to produce figure 6.2, as well as listen to the audio in the recorded signals, table 6.1. With respect to the nomenclature of appendix B, the Norwegian FM radio broadcast system is using modulation index $\beta = 5$, and frequency deviation $\Delta f = 75kHz$.

Figure 1.3 shows a snapshot of the entire FM radio band, ranging from $88MHz - 108MHz$. The focus of this thesis is to exploit multiple channels from the same FM radio tower, and the algorithm was explained in detail in chapter 5 for a pseudo random noise signal. This section applies real FM radio signals recorded in the reference channel of the equipment to gain insight into the algorithm's performance using FM radio signals. The reference antenna is pointed at a strong nearby transmitter, and thus a strong and clear signal is recorded. The signal potentially contains multipath, even though it is diffracted from transmitter to receiver as seen in figure 4.2a. The sampled reference signal is digitally substituted in the surveillance signal, and thus the following situation is achieved: Data analysis with real life propagation, full match with the reference and surveillance channel's signals, and thus the FM radio waveform's performance is analyzed in the signal processing described in chapter 5.

The FM radio wave is explained in appendix B, and in figure 6.1 the schematic diagram of the decoded FM radio signal or unmodulated information signal is shown. The information signal, equation (B.1), is occupying $100kHz$, and it consists of multiple parts. Ranging from $30Hz$ to $15kHz$ is the mono audio section, which consists of the sum of the stereo left and right channels. This is the part which all FM radio receivers can decode. Then there is the $19kHz$ stereo pilot, which has two functions: First the mere presence decides whether the transmission is stereo or mono by definition. Second, if the pilot is present, this carrier is used in the receiver to decode the stereo audio as seen as the double sideband centered at $38kHz$, ranging from $23kHz$ to $53kHz$, being the difference of the stereo left and right channels. And also, the double sideband modulated Radio Data System (RDS) information at $57kHz = 3 \times 19kHz$. In the rest of the band national adaptations may apply, and no traces of a regular broadcasted signal above the RDS information as seen in figure 6.2 have been found.

The FM radio signal is highly time varying, as seen in figure 1.3, and especially in the detailed figure 6.2, further summarized in table 6.1. The left sub figures show 30 seconds of the broadcasted FM radio signal, while the right sub figures show the corresponding decoded FM radio signal, as illustrated in figure 6.1. Table 6.1 gives a high level description of the program content of each of the channels. The bandwidth of the FM radio signal with respect to program content has been extensively covered in the literature [27–34]. However, figure 6.1 may lead to the conclusion that a stereo signal has a wider bandwidth than the mono signal, and thus are better suited for radar applications. Looking at figure 6.2 it is clearly seen that this is not necessarily the case. All shown broadcasted signals are stereo signals by definition since the $19kHz$ stereo pilot clearly is present. But only the two music playing channels, figure 6.2b and d contain substantial stereo information in the stereo audio band $23kHz - 53kHz$. Figure 6.2a shows scattered stereo information, while c shows nearly no stereo information, even though both signals by definition are containing stereo information. The presence of the $19kHz$ stereo pilot is necessary but not sufficient condition for the presence of signal in the stereo audio channel. In summary, the stereo signal may be broadcasting a close to mono signal as the stereo information is broadcasted as the sum $30Hz - 15kHz$ and difference $23kHz - 53kHz$ of the stereo audio

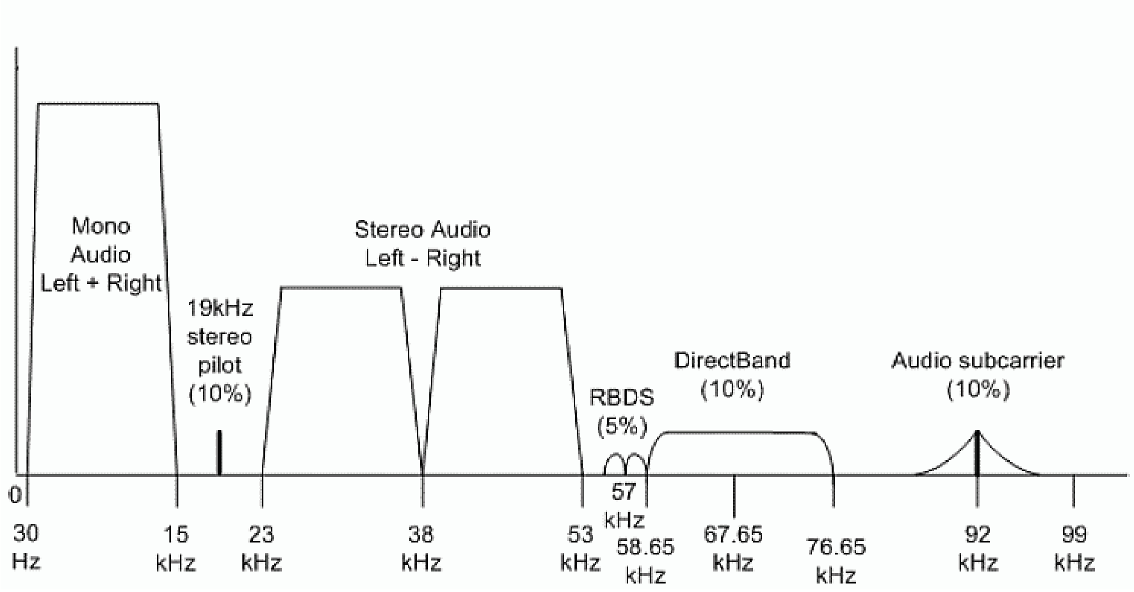

Figure 6.1: Schematic diagram of the frequency content of the decoded FM radio signal or the unmodulated information signal. National adaptations may apply [16]. The figure is from [17].

Table 6.1: Program content and description of the strong Tryvann FM radio channels.

Frequency	Program content and description
$88.7MHz$	Two men talking calmly together in studio.
$93.5MHz$	Music, the group Guns N' Roses playing the former hit "Paradise City"
$100.0MHz$	Man talking very calmly in studio, then playing chanting.
$103.9MHz$	Music, the group No Doubt playing the hit "Don't speak".

channels, at different parts of the band.

It is also noted that especially in figure 6.2c, that when there is no or low bandwidth in the information signal, distinct lines appear at the integer value of the $19kHz$ stereo pilot. This is not a HW failure, and it is explained mathematically in appendix B.1.

The surveillance channel $R_T + R_T - L = 15km$ is delayed so that the target, $v = 100m/s$ radial velocity ($\beta = \delta = 0$, (3.18)) shows up at $15km$ in the figures. Figure 6.3 shows the single channel target peak from the range Doppler matrix processed as described in section 3.5.3, where the datasets are from the recordings shown in figure 6.2. The range resolution is seen to be varying across channels, and the best resolution is achieved by the two music playing channels, table 6.1. Further analysis of these channels resolution performances will be performed later.

The theoretical formula from literature for stepped continuous wave signals range resolution ($-4dB$ width) is [46, pp. 148], combined with the radar world's definition of the resolution to be the half $-3dB$-width (divide by two)

$$\Delta R = \frac{c}{2N\Delta f}, \tag{6.1}$$

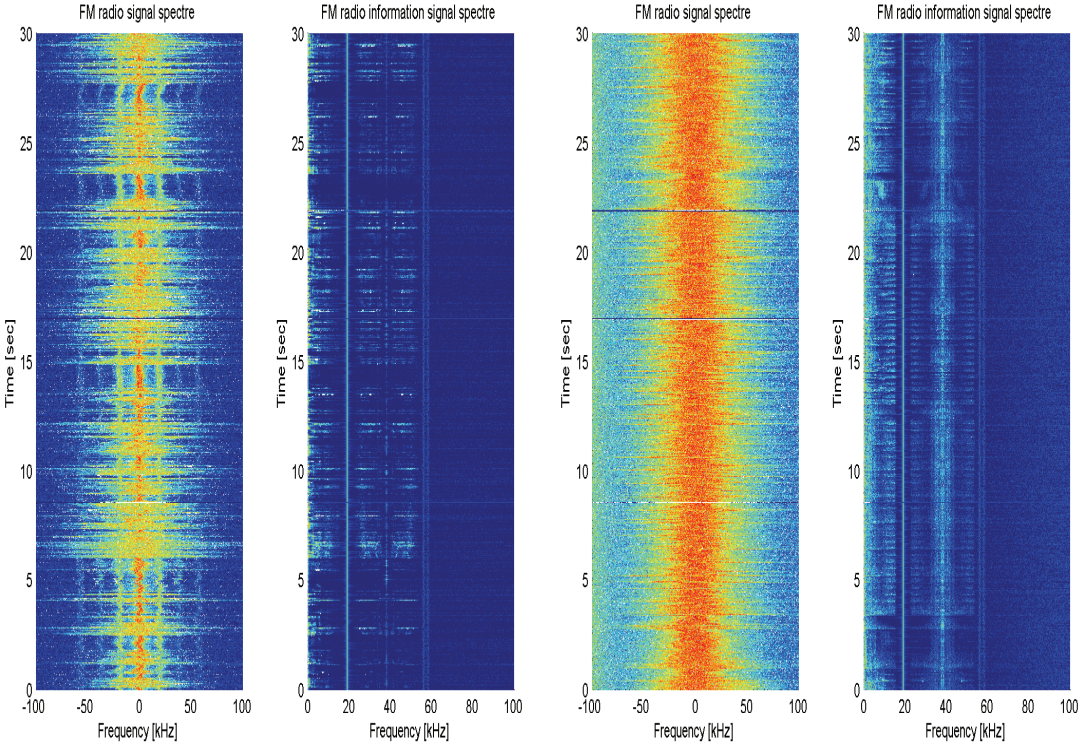

(a) $88.7 MHz$.

(b) $93.5 MHz$.

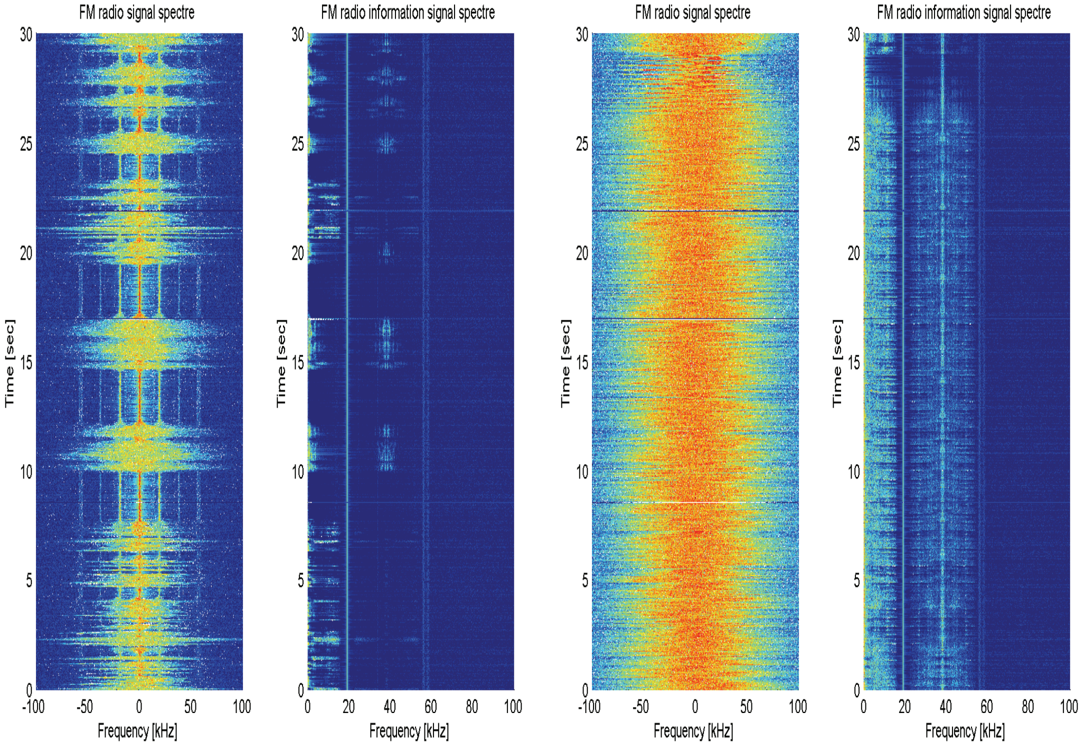

(c) $100.0 MHz$.

(d) $103.9 MHz$.

Figure 6.2: The left sub figures show 30 seconds of the broadcasted FM radio signal, while the right sub figures show the corresponding decoded FM radio signal, figure 6.1.

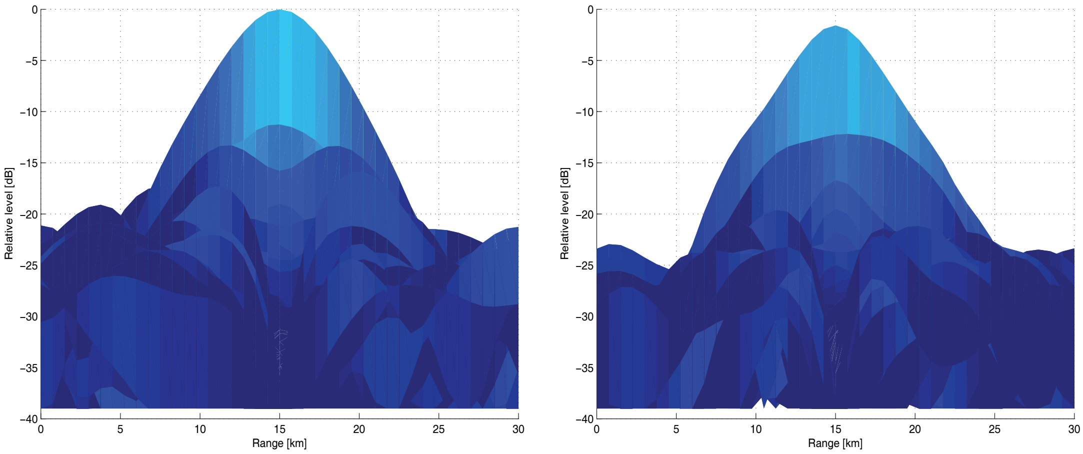

(a) $88.7 MHz$. (b) $93.5 MHz$.

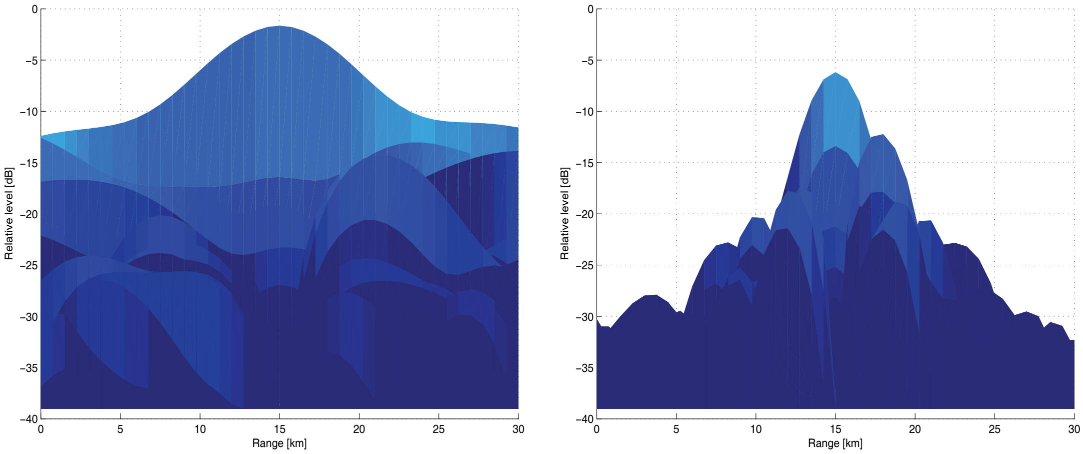

(c) $100.0 MHz$. (d) $103.9 MHz$.

Figure 6.3: The single channel's auto correlation. The datasets are the same as shown in figure 6.2. CPI= $329 ms$.

Table 6.2: Ambiguity distance $c/\Delta f$, combined waveform resolution $c/(N\Delta f)$, and sampling resolution c/f_s for $N = 4$ as a function of Δf.

Δf	Ambiguity distance $c/\Delta f$	Combined distance $c/(N\Delta f)$	Sampling distance c/f_s	Ratio $f_s/\Delta f$	Ratio $f_s/(N\Delta f)$
$50kHz$	$6000m$	$1500m$	$750.0m$	8.0	2.0
$150kHz$	$2000m$	$500m$	$375.0m$	5.3	1.3
$300kHz$	$1000m$	$250m$	$187.5m$	5.3	1.3

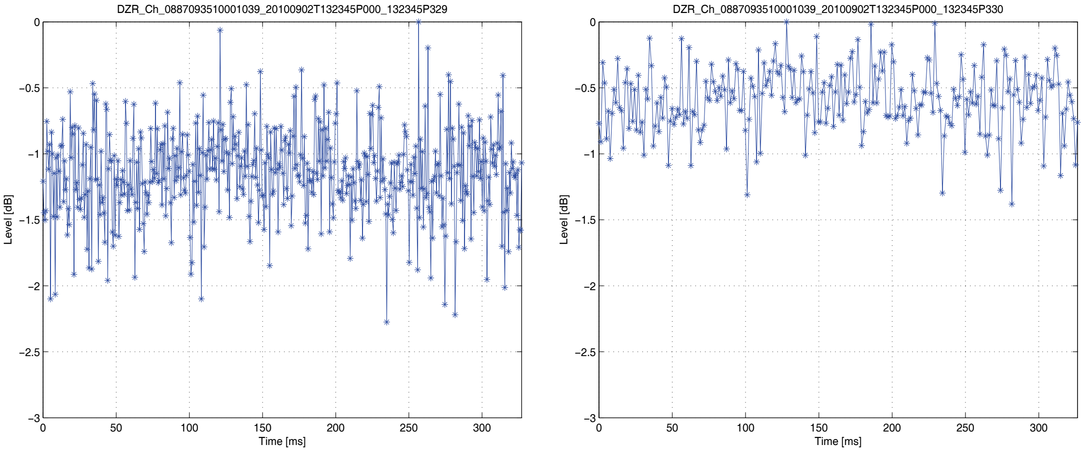

(a) Range correlation fluctuations, each range-CPI= $0.64ms$.

(b) Range correlation fluctuations, each range-CPI= $1.28ms$.

Figure 6.4: The stability of the individual range correlations each consisting of range-CPI= $0.64ms$ and range-CPI=$1.28ms$. Both plots result from the overall CPI≈ $329ms$, $\Delta f = 50kHz$, and $N = 4$.

where c is the speed of propagation, N is the number of combined channels, and Δf is as before. Table 6.2 summaries the expected performance for the chosen parameters. The range ambiguities are expected to be occurring at

$$R_{ambiguity} = R \pm K\frac{c}{\Delta f}, \tag{6.2}$$

for $K = 0, 1, 2, \ldots$ for a single point target. The signal's bandwidth mainly contributes to lower the sidelobes of the ambiguities, while it is the distance between the signals that defines the main target peak.

Figure 6.4 shows the time stability of the range correlation for the combined signal for $\Delta f = 50kHz$, $N = 4$, and CPI≈ $329ms$ for two range-CPIs, range-CPI=$0.64ms$ and range-CPI=$1.28ms$. In this case, the overall CPI is kept constant, at CPI≈ $329ms$. By increasing the range-CPI, the stability with time also improves, as is in accordance with the results from chapter 5, where similar results were obtained for the pseudo-random noise.

Finally, before simulations with real life signals, it should be noted that the highly time varying FM radio signal makes simulations/analysis challenging, as one ends up with all

Table 6.3: Synthetic target parameters.

Δf	Target 1, $v = 100m/s$	Target 2, $v = 100m/s$
$50kHz$	$R = 15.0km$, $0dB$	$R \in [15.0km, 21.0km]$, $-3dB/-6dB$
$150kHz$	$R = 15.0km$, $0dB$	$R \in [15.0km, 17.0km]$, $-3dB/-6dB$
$300kHz$	$R = 15.0km$, $0dB$	$R \in [15.0km, 16.0km]$, $-3dB/-6dB$

kinds of possible combinations of signal bandwidth, number of channels, carrier frequencies, program contents and so on. The FM radio work in this chapter is based on four individual FM radio channels for a 10 seconds time segment containing a representative mix of variations of bandwidths and program types.

6.1.1 Single point target

The aim of this section is to 1) improve on the single target positioning resolution, and 2) demonstrate the importance of the phase term correction as was described in chapter 5.

Figure 6.5 shows all the combinations of compensating for the Doppler frequency (5.22)-(5.23), and compensating for the phase term (5.27). As expected, the situations without Doppler compensations a and b are the most severe, although in this case the main peak is at correct range. This will in general not be the case even for Doppler compensation, as will be seen shortly. In this example, once the Doppler shift of the target with respect to the carrier frequency in question has been compensated for, the phase compensation seems to have no effect on this real life datasets, figure 6.5c and d. By using the sampled reference channel signal also as the surveillance signal, the cross-correlation reduces to the autocorrelation, which means any phase term will be canceled due to the product of the function by itself complex conjugated, and thus all phase terms should be zero. The results of the phase estimation for all range correlations are shown in figure 6.6, and they behave as expected, close to zero with small variations.

The Norwegian transmitters (one transmitter for each FM radio channel) are not physically synchronized, but all the transmitters are synchronized by GPS PPS-pulse, and thus they behave like they are synchronized, and the phase synchronization term may be obsolete. In order to illustrate the importance of the phase term, the same processing is applied on a deliberately phase distorted data segment, where the importance of the phase correction term is obvious as seen in figure 6.7. The phase term is now seen to be not zero, plots a-d, and the resulting range correlation is shown in plot e-f. It is clear that no phase compensation makes the target range wrong, while compensating for the phase term, figure 6.7, makes the range correct, and the situation of figure 6.5, plots c and d is restored.

However, for both the FM radio system as well as for the DVB-T system the results with and without the phase term correction will be presented. This is due to differences in real life data and simulations, where the latter not always grasps the finer details of the real world.

Two ideas on algorithm applications spring to mind: First, if the broadcast transmit-

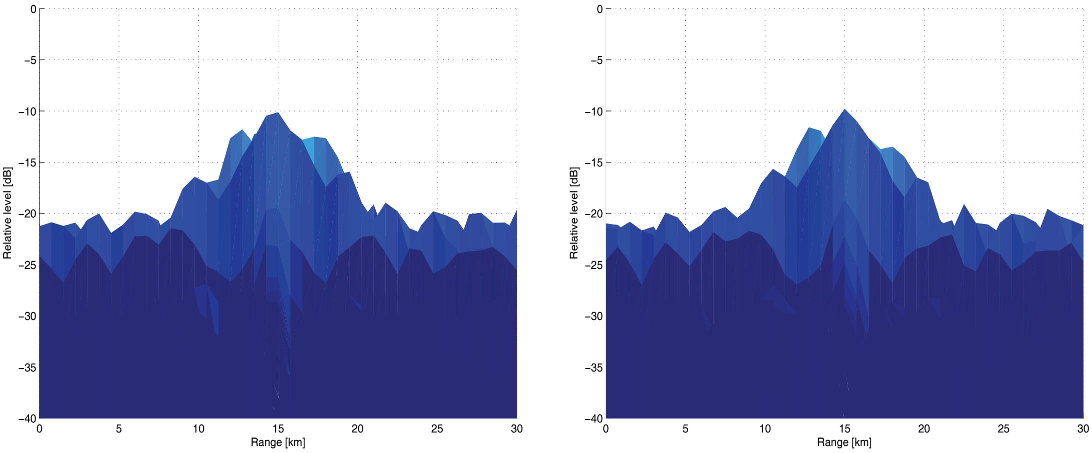

(a) No Doppler nor phase compensation. (b) No Doppler, phase only compensation.

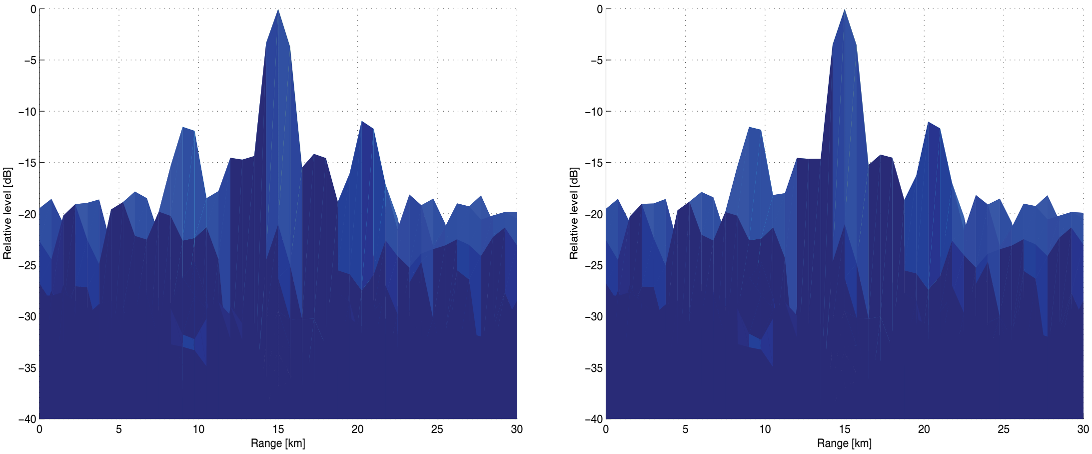

(c) Doppler only, no phase compensation. (d) Both Doppler and phase compensation.

Figure 6.5: All the combinations of compensating for the Doppler frequency (5.22)-(5.23), and compensating for the phase term (5.27). CPI= $329ms$, $\Delta f = 50kHz$, $N = 4$.

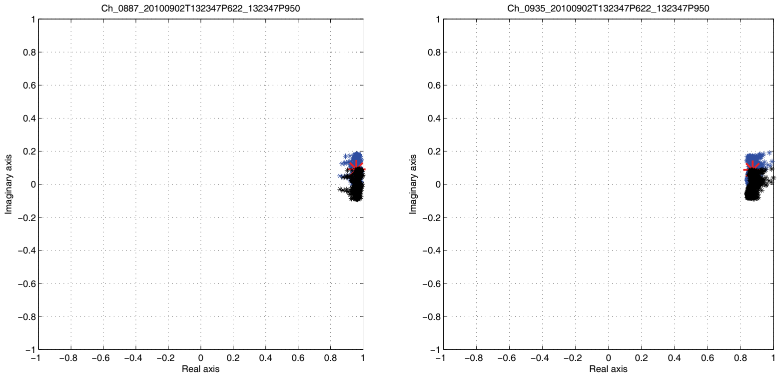

(a) $88.7MHz$. (b) $93.5MHz$.

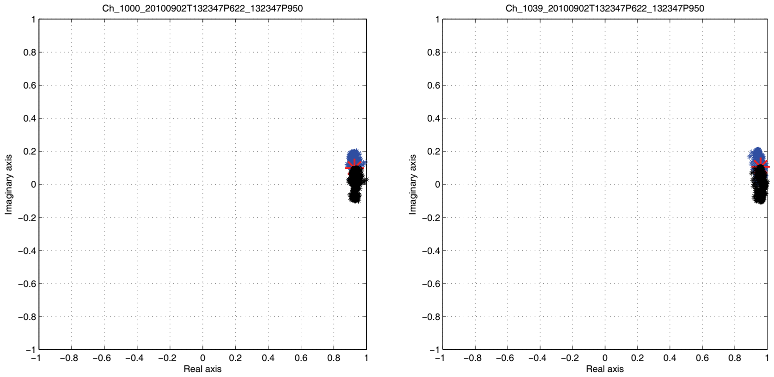

(c) $100.0MHz$. (d) $103.9MHz$.

Figure 6.6: The plots displays the phase normalised on the unit circle. Phase estimation (blue), averaged correction term (red), and phase compensated correlations (black). CPI= $329ms$, $\Delta f = 50kHz$, $N = 4$.

ters are synchronized to a high quality level, this may call for the phase to be estimated across channels, and thus make a more robust estimation of the phase term from (5.27). This may work since it is the same geometry, as well as an assumed point target for all FM radio frequencies (this is not necessarily the case for the DVB-T system as will be seen in section 7.4). Second, if one is going to combine broadcasted signals from different geometries, both the Doppler (obvious and simple to compensate for) and the phase term are important to compensate for, and in this case, they have to be estimated for all geometries. Once the range and Doppler have been compensated for, the situation may be as illustrated in figure 6.7, and without compensation, the target response may be as in figure e, while the fully compensated situation is shown in f. For the FM radio system (and also the DAB and DVB-T), there normally are multiple synchronized channels in each geometry and thus for each geometry the phase may be very reliable accounted for, and thus the algorithm illustrated in figure 6.7 may be applied with success. Dealing with this has been tempting, but the latter idea is way out of the scope of this thesis, although the first idea would be interesting to follow up, there is no time within this thesis' work.

The figures 6.8a, c, and e show the range view of the range-Doppler matrix after full range-Doppler processing as described in chapter 5, for CPI= $329ms$, and $N = 4$. The range ambiguities are quite conspicuous, and these plots show what the FM radio waveform is capable of resolving in range due to the waveform using the proposed algorithm.

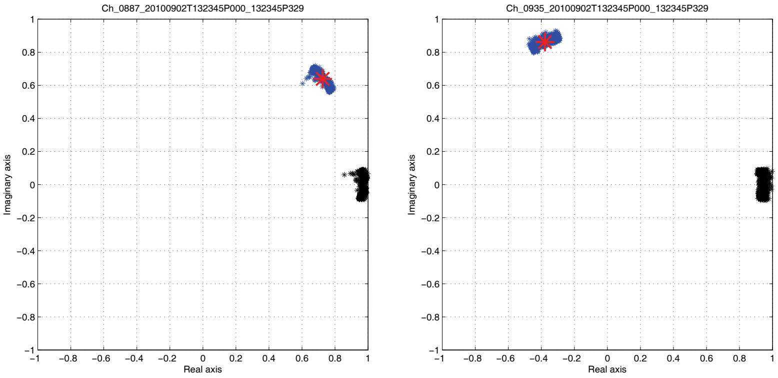

(a) 88.7MHz. (b) 93.5MHz.

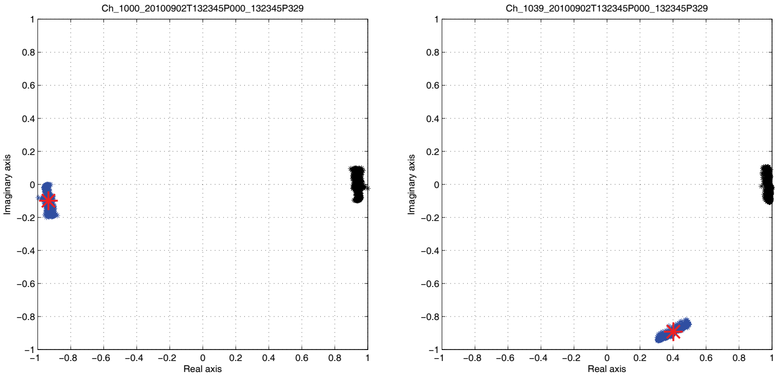

(c) 100.0MHz. (d) 103.9MHz.

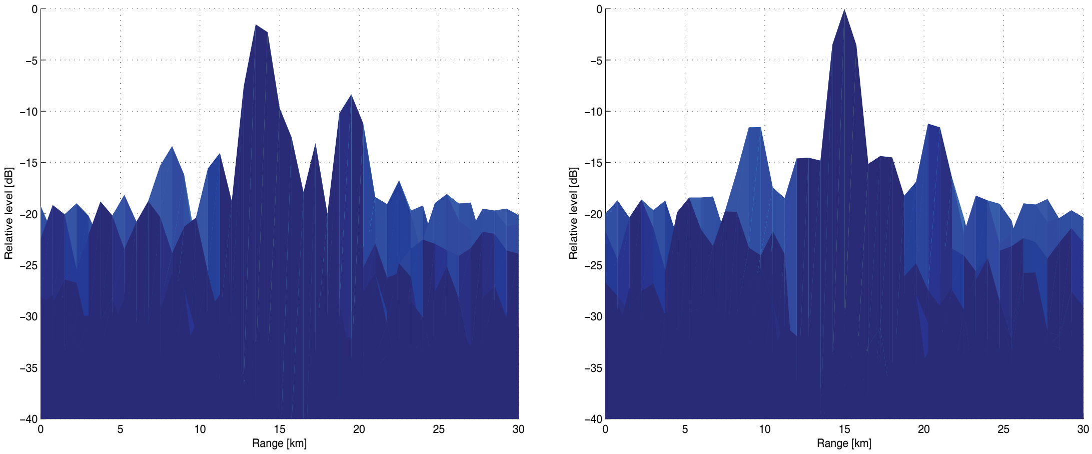

(e) Doppler only, no phase compensation. (f) Both Doppler and phase compensation.

Figure 6.7: (a-d): Distorted phase (blue), averaged correction term (red), and phase compensated correlations (black), normalised to the unit circle. Figure (e) and (f) show the Doppler/no phase and Doppler/phase corrected range correlations. CPI= 329ms, $\Delta f = 50kHz$, $N = 4$.

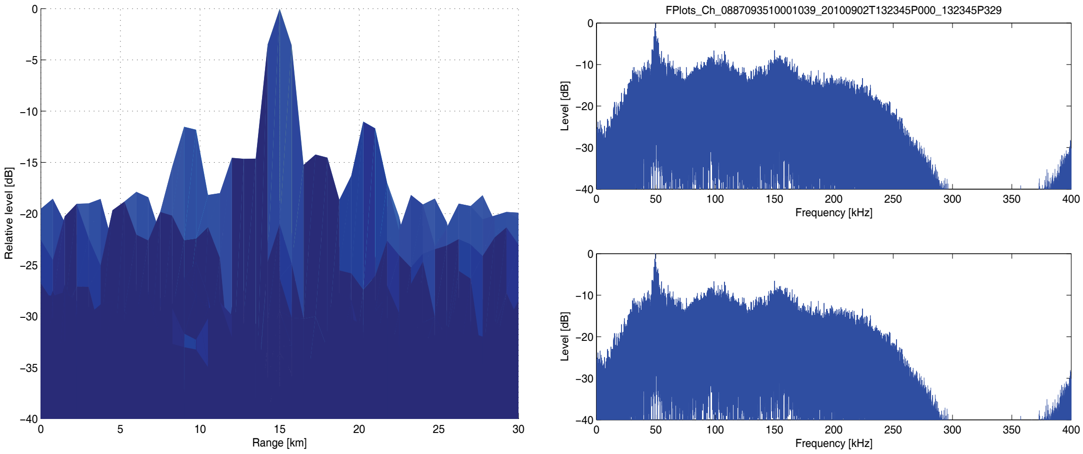

(a) Range view, $\Delta f = 50kHz$.

(b) Frequency spectrum, $\Delta f = 50kHz$, $f_s = 400kHz$.

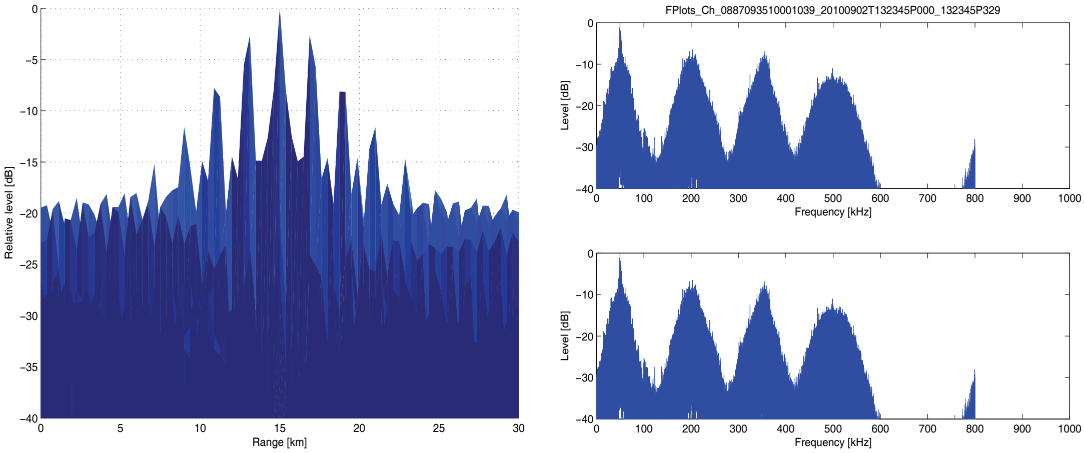

(c) Range view, $\Delta f = 150kHz$.

(d) Frequency spectrum, $\Delta f = 150kHz$, $f_s = 800kHz$.

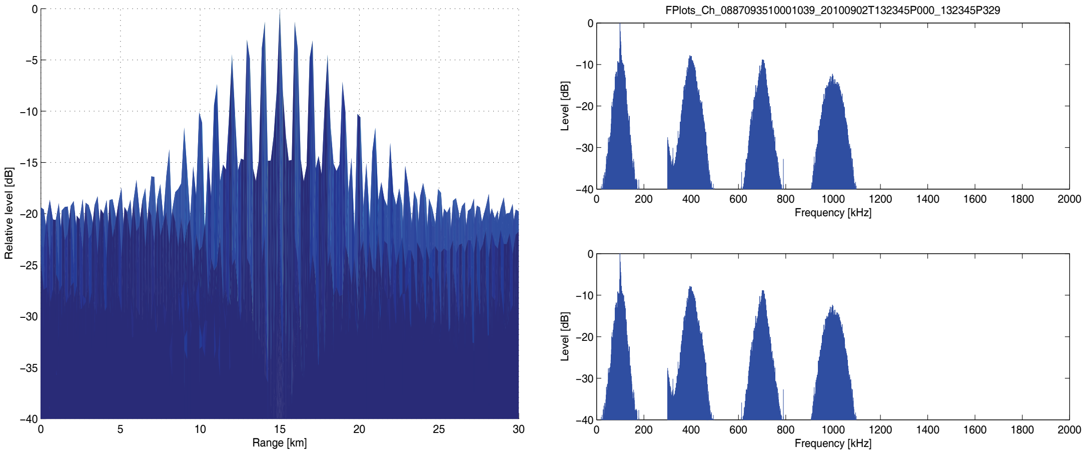

(e) Range view, $\Delta f = 300kHz$.

(f) Frequency spectrum, $\Delta f = 300kHz$, $f_s = 1600kHz$.

Figure 6.8: The figures (a), (c), and (e) show the range view of the full range-Doppler processing as described in chapter 5, for CPI$= 329ms$, $N = 4$. Figures (b), (d), and (f) show the corresponding combined frequency spectra.

Table 6.4: Autocorrelation peak width for both single channel as well as for the combined channels with $N = 4$ and as a function of Δf.

		$-3dB$ peak width	$-6dB$ peak width	$-9dB$ peak width	Sampling resolution f_s, c/f_s
Single channel	$88.7MHz$	$> 10.0km$	$> 10.0km$	$> 10.0km$	$1600kHz$, $187.5m$
	$93.5MHz$	$5.0km$	$8.0km$	$10.0km$	$1600kHz$, $187.5m$
	$100.0MHz$	$> 10.0km$	$> 10.0km$	$> 10.0km$	$1600kHz$, $187.5m$
	$103.9MHz$	$3.4km$	$4.6km$	$6.0km$	$1600kHz$, $187.5m$
Multi channel	$\Delta f = 50kHz$	$1.500km$	$1.500km$	$3.000km$	$400kHz$, $750m$
	$\Delta f = 150kHz$	$0.750km$	$0.750km$	$1.500km$	$800kHz$, $375m$
	$\Delta f = 300kHz$	$0.375km$	$0.375km$	$0.750km$	$1600kHz$, $187.5m$

In Doppler the resolution depends only on the coherent processing interval, at least for processing intervals of interest, i.e. CPI$\leq 1sec$. Figures a, c, and e show that between the expected ambiguities around $15dB$ of dynamic range can be achieved. I.e. in order to resolve two targets in range with a range difference below the ambiguity distance, they have to be below $15dB$ in signal level difference, but probably much less. The next section looks at the behavior when two point targets are present. Figures b, d, and f show the corresponding combined frequency spectra.

Figures 6.8 is for one CPI=$328ms$ only. In order to see the performance as a function of time, the width of the target main peak as a function of time and the $-3dB$, $-6dB$, and $-9dB$ points on each side of the main target peak has been extracted. The latter taken to be the closest sampling value exceeding the required threshold. The results can be seen in figure 6.9 for the single channels of $88.7MHz$, $93.5MHz$, $100.0MHz$, and $103.9MHz$, as well as the coherently combination of these channels for $\Delta f = 50kHz$, $\Delta f = 150kHz$, and $\Delta f = 300kHz$.

Figure 6.9 shows the $-3dB$, $-6dB$, and $-9dB$ points on each side of the main target peak at $15km$ for a dataset corresponding to the first $10sec$ of figure 6.2. Figures 6.9a, c, e, and g show the width of the single channels target peak. The target is seen as the blue line at $15km$ throughout the plot, while the various thresholds are the color coded lines. It is seen that the target is stable, but the resolution is highly time varying. By applying full (both frequency and phase compensated) algorithm, it is seen that the resolution is stable with time. The resolution is also improved with respect to the single channel case. A summary of the behavior is found in table 6.4.

Table 6.4 may lead to the conclusion that the resolutions are not in correspondence with the theory, but that is not the case. The closest range sample that fulfills the target range resolution requested width, being either $-3dB$, $-6dB$, or $-9dB$ is taken as the peak width. This is usually the case in real life systems, as the sampling frequency is tuned against the signal bandwidth. However, by interpolating between samples and extracting the true $-3dB$ range bandwidth, the performance of the real life data is in accordance

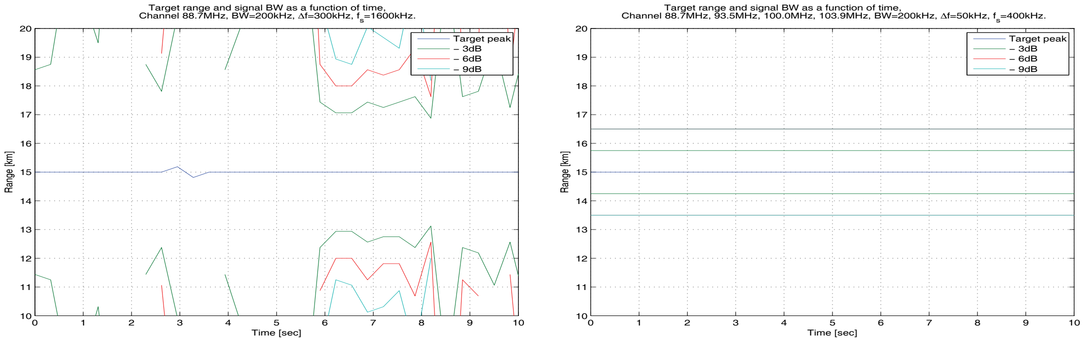

(a) $88.7MHz$. (b) $\Delta f = 50kHz$.

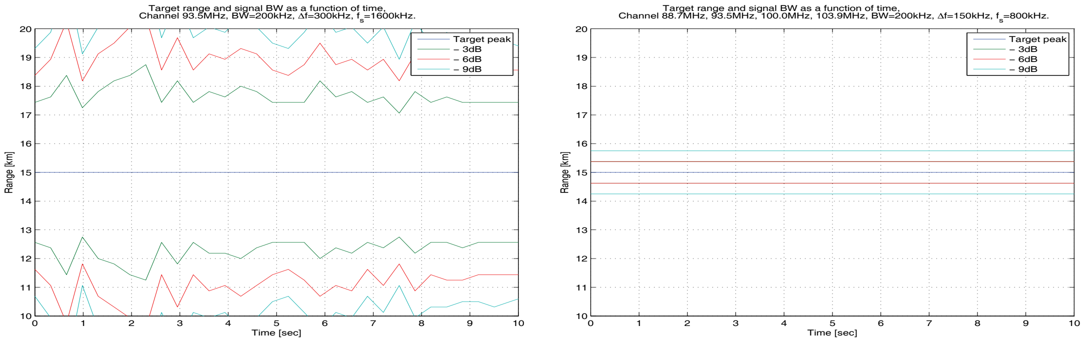

(c) $93.5MHz$. (d) $\Delta f = 150kHz$.

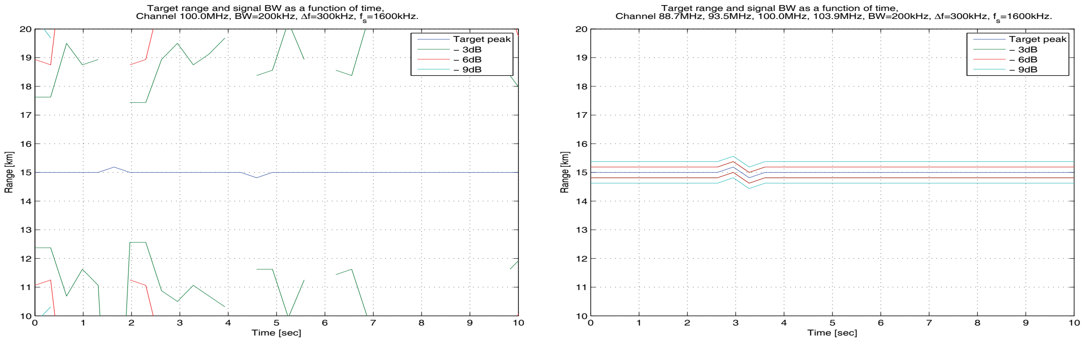

(e) $100.0MHz$. (f) $\Delta f = 300kHz$.

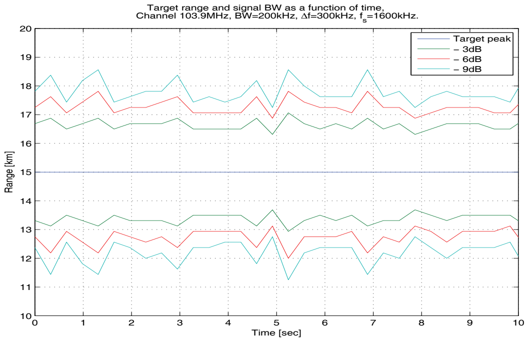

(g) $103.9MHz$.

Figure 6.9: The peak $-3dB$, $-6dB$, and $-9dB$ point as a function of time for the first ten seconds from figure 6.2. The left column shows the single channels target resolution, while the right column shows the combined channels target resolution as function of Δf. CPI$= 329ms$, $N = 4$.

with (6.1).

6.1.2 Two point targets

The ability to resolve two scatterers will be investigated in this section. The synthetic target parameters are listed in table 6.3. The surveillance channel is time-delayed N_{bins}, amplitude adjusted, and phase adjusted according to the following two formulas

$$\Delta\phi = 2\pi \frac{2f_{carrier} + f_{Doppler}}{2f_{sampling}} N_{bins}, \qquad \text{and} \qquad \Delta\phi = 2\pi \frac{f_{carrier} + f_{Doppler}}{f_{sampling}} N_{bins}, \tag{6.3}$$

where $f_{carrier}$ is the broadcast carrier frequency, and $f_{Doppler}$ is the target induced Doppler frequency of that frequency. The two different formulas were applied in order to avoid being in a(n) (un)fortunate situation, and by that reporting performance that is not representative. The first formula corresponds to a scatterer $N_{bins}/2$ behind the first one in a monostatic fashion, and the second one is of more arbitrary nature. However, the algorithm performed equally for both phase delays, and the following plots will be from the latter formula. This means a second point target at another distance, but the same velocity, is mimicked. The time delay has been adjusted in accordance with the reference/surveillance channel's sampling frequency in order to avoid interpolating the delayed signal between sampling points. This was also found convenient in order to avoid rounding the delay to the same nearest range sampling for adjacent second target delays.

The second target is not resolved in any of the individual FM radio channels, $88.7MHz$, $93.5MHz$, $100.0MHz$, or $103.9MHz$, except from some scattered occurrences in channel $103.9MHz$. In the other channels the target is seen to impact on the correlation peak in the range-Doppler plot, but it is definitely not resolved.

It has been showed that the estimation of the phase is of high importance, but once there are two closely spaced targets, the algorithm may not estimate the phase correctly, and thus the results might be erroneous, and the phase estimation techniques is one of the improving points of the algorithm.

Figure 6.10 shows the results of systematic delaying the second target between the first target range at $R = 15.0km$, and the Target 2 end range parameters of table 6.3. The targets relative levels are also tabulated, and in the following plots, a difference of $3dB$ between the two scatterers to be presented has been chosen.

Figure 6.10 is interpreted as follows: The first target is at $15km$, while the second target is stepped in range, and the actual target range is indicated in the leftmost column of the plots, numbers edgewise, i.e. the numbers $15.000, 15.750, \ldots, 20.250$ for the upper plot. Next/below to these numbers is the dataset duration in seconds, for the upper plot, that are the numbers 0 and 5. The x-axis of the plots, is the processing range in kms. Plots in the left column are not phase compensated, while the right column's plots is phase compensated.

The range resolution should be as in (6.1) according to theory for a single point target as also verified in previous section. The figure shows multiband processing for three variations of Δf, for $\Delta f = 50kHz$, $\Delta f = 150kHz$,, and $\Delta f = 300kHz$, ten seconds of the dataset seen in 6.2. The figure shows target position 1 at $15km$, and then the second target is stepped systematically from target 1 to the first range ambiguity in steps of the sampling resolution's corresponding range. This means that even though all plots in figure 6.10 are from different Δf, phase/no phase compensation, and sampling, the overall figure is close to normalized with respect to the ambiguity distance, which is the range interval of interest.

Looking at figures (a) and (b), it is seen that the second target is fully resolved from $17.25km$ to $18.75km$, which yields a target peak-to-peak full resolution capability of $2.25km$ between targets differing by $3dB$. Passing $18.75km$, the target is approaching the range ambiguity at $21.000km$. In figures (e) and (f) the target is fully resolved from $15.375km$ to $15.563km$, although being very weak phase compensated case (f), and it is noted that the ranging is not fully as expected.

In figures (c) and (d) there is something going on. The second target is clearly there, a comparison with the single target situation ($15.000km$) verifies that. The range of the second scatterer seems to be wrong, and no good explanation for this has been found. The analyzed dataset is ten seconds so it is not believed that this is a waveform issue, nor is it expected to be a simulation artifact. Table 6.2 shows the ratios $f_s/\Delta f$, and $f_s/(N\Delta f)$, which for the $\Delta f = 150kHz$, and $\Delta f = 300kHz$ is the same and lower (5.3/1.3) than for the $\Delta f = 50kHz$ case (8.0/2.0). Most likely, the algorithm is breaking down as a function of signal input in combination with some simulation artifacts, i.e. very black/white situations. For target multiple scatterers resolution, with the FM radio waveforms the ratios $f_s/\Delta f$, and $f_s/(N\Delta f)$ should be noted, and they should not be too low, and the line might have crossed for $\Delta f = 150kHz$ and $\Delta f = 300kHz$. This is also common sense, as just increasing Δf will not result in the corresponding range resolution capabilities, also due to the fact that the range ambiguities will come closer, but at some point there should be some signal bandwidth present in order to resolve targets.

Looking at figure 6.10 (a) and (b) it is noted that there is very little difference between the phase and no phase compensated situation. This difference increases in the plots (c)-(f), although at large, they behave similarly. It should be noted that the main peak of the range correlation has been adjusted to the exact position of target 1, information that is a priori known, as it is assumed that target 1 is fully tracked, and now the goal is to estimate the real number of targets in this single PBR track. The algorithm sometimes results in a ranging error, which causes only a shift of all peaks, and thus the figure would be impossible to read properly. The stability was not improved by increasing the coherent integration time, no real performance improvement was found. Thus, only results from CPI$= 328ms$ was presented, but all have been processed in parallel for CPI$= 328ms$, and CPI$= 984ms$. However, as shall be seen for real life data, there is a difference.

6.1.3 Summary

The straightforward technique of interpolating to the correlation peak is not resolving targets, only improving on the single target's position. By improving the range resolution one of the major shortfalls of current FM radio based PBR systems is countered. Although

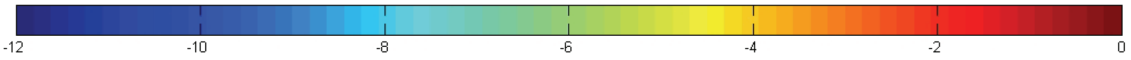

The figure's color coding in dB.

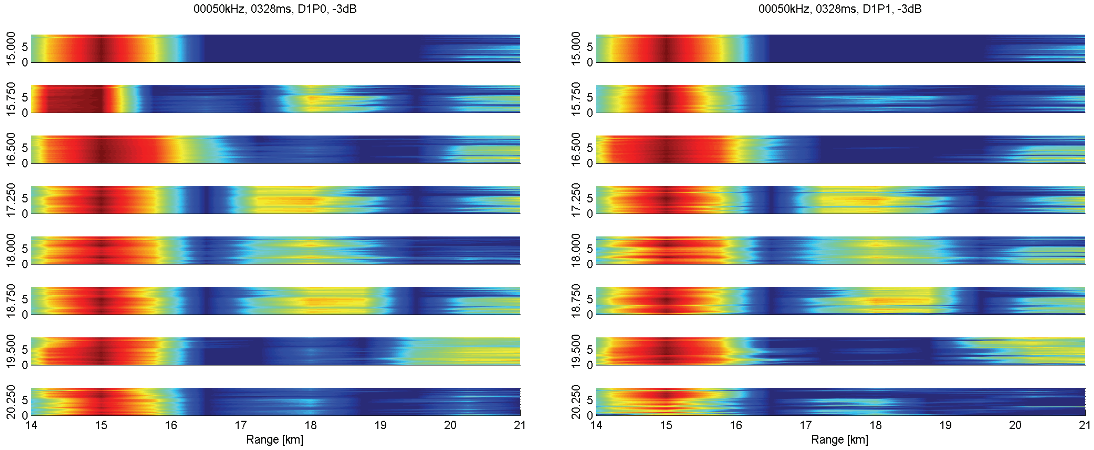

(a) $\Delta f = 50kHz$, no phase compensation. (b) $\Delta f = 50kHz$, phase compensated.

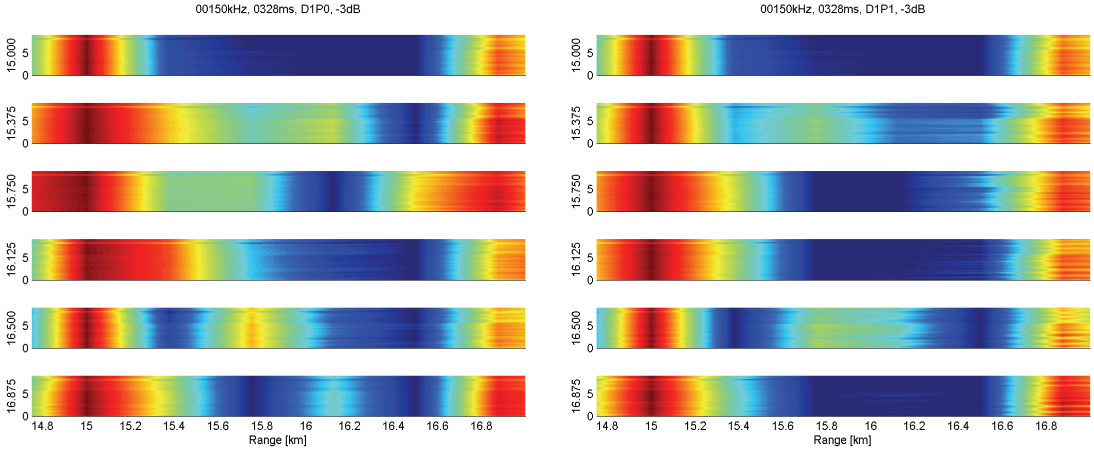

(c) $\Delta f = 150kHz$, no phase compensation. (d) $\Delta f = 150kHz$, phase compensated.

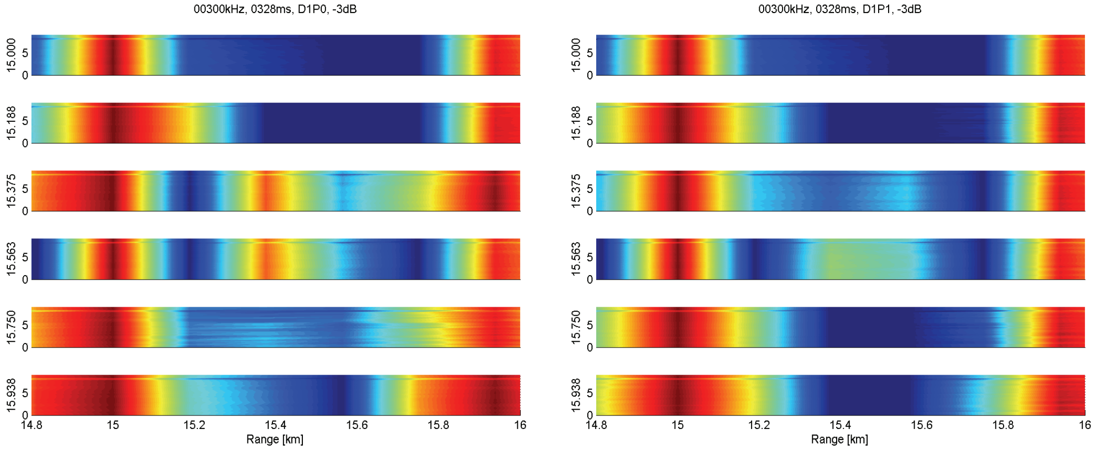

(e) $\Delta f = 300kHz$, no phase compensation. (f) $\Delta f = 300kHz$, phase compensated.

Figure 6.10: Systematic testing of the algorithm's resolution capabilities for two scatterers varying according to table 6.3. CPI= $329ms$, $N = 4$.

the good Doppler resolution of such systems is helping resolving targets, the capability to exploit the better range resolution for targets at exactly the same velocity and close in range should be able aid the tracking process, as well as raise some operational interest by military clients.

Simulations based on real life FM radio waveforms show that the algorithm is capable of improving the range resolution according to theory for single scatterers as is summarized in table 6.4. For multiple scatterers, the algorithm is impacted by the FM radio's time varying behavior. The bandwidth contributes to lowering the range ambiguities sidelobes, and as the bandwidth is fluctuating, the sidelobes are fluctuating as well.

In order to investigate the algorithm's resolution performance a second scatterer with respect to the first one was systematically delayed, table 6.3, from zero distance and out to first ambiguity distance as tabulated in table 6.2. As an example, the case of two targets separated by bistatic range of $2.250km$ ($1.1250km$ equivalent monostatic resolution) was simulated. The targets were not resolved in the single channel case, but being fully resolved by processing $N = 4$ channels together for $\Delta f = 50kHz$, while the results became more dubious for the $\Delta f = 150kHz$, and $\Delta f = 300kHz$ cases. For target multiple scatterers resolution, with the FM radio waveforms the ratios $f_s/\Delta f$, and $f_s/(N\Delta f)$, should be kept in mind. They should not be too low, and this line might have been crossed for $\Delta f = 150kHz$ and $\Delta f = 300kHz$, which for the $\Delta f = 150kHz$, and $\Delta f = 300kHz$ is the same and lower (5.3/1.3) than for the $\Delta f = 50kHz$ case (8.0/2.0).

The simulations showed no real performance improvement by increasing the coherent integration interval. Some "averaging" effects were observed, as more data is processed together, but no significant performance improvements were observed.

6.2 Real life target: Airliner analysis

This section applies the proposed algorithm presented in chapter 5, on real life target data collected with the data recording equipment presented in chapter 4. The target is an airliner of opportunity, exemplified in figure 6.11, heading for Gardermoen airport outside Oslo in Norway. The exploited FM radio broadcaster, Holtberget, is a powerful transmitter, and the broadcasted channels are listed in tables 1.1 while simple performance assessments are presented in section 4.1.

All targets of opportunity, i.e. exclusively airliners, included in this FM radio based PBR research have been behaving like single scatterers, see section 6.1.

The transmitter, target, and receiver geometry is shown in figure 6.12, and the reference and surveillance antenna's sectors are also indicated. Figure b is a zoom of figure a in order to show the target trajectory for ten seconds of analysis. The target position is recorded by Kinetic Mode-S receiver [19]. The data was recorded in 2009, when the Mode-S receiver system definitely not was operational, and thus they cannot be used for system accuracy performance calculations. The Mode-S target position is mainly used here as a rough guide to what to be expected from the calculations.

Figure 6.13 shows the FM radio PBR target Doppler shift induced from the geometry

Figure 6.11: Example of type of airliner target, a Scandinavian Airlines System's Boeing 737, [18].

and target trajectory/velocity as presented in figure 6.12. The transmitter's carrier frequency is $f = 89.8MHz$. From the figure it is seen that ISAR imaging based on the target motion would in these data be very hard to achieve due to the low Doppler shift differences, $f_D \in [14.34Hz, 14.58Hz]$, mainly caused by the low carrier frequency. However, in the datasets there were targets spreading in Doppler probably due to the irregular movement in the air caused by turbulence or wind. For the limits of the FM band, the spreading is for $f = 88.0MHz$, $f_D \in [14.00Hz, 14.28Hz]$, and $f = 108.0MHz$, $f_D \in [17.25Hz, 17.55Hz]$. This requires a Doppler resolution of $\Delta f_D = 0.3Hz$ in order to reach the spreading, and a Doppler resolution of $\Delta f_c = 0.03Hz$ in order to have ten Doppler bins over the target. The former requires an integration time of CPI= $3sec$, while the latter a CPI= $30sec$, which is unrealistic. It should also be noted that the target spreading in range is low, below $50m$.

From the Holtberget transmitter, the three frequencies $89.8MHz$, $93.9MHz$, and $98.9MHz$, are exploited, using $\Delta f = 50kHz$, $\Delta f = 150kHz$, and $\Delta f = 300kHz$ in the processing. The presented datasets are all ten seconds.

The target's range and Doppler single channel's detections, as well as stability with time is shown in figure 6.14 for CPI= $329ms$, and CPI= $984ms$. The results are obtained by the effective range-Doppler processing of section 3.5.3. It is seen that the longer integration time, thus more stable results. This is mainly due to the "averaging" effect which comes from increasing the integration time.

Figure 6.15 shows the single channel detections for CPI=$329ms$, and CPI=$984ms$ as a

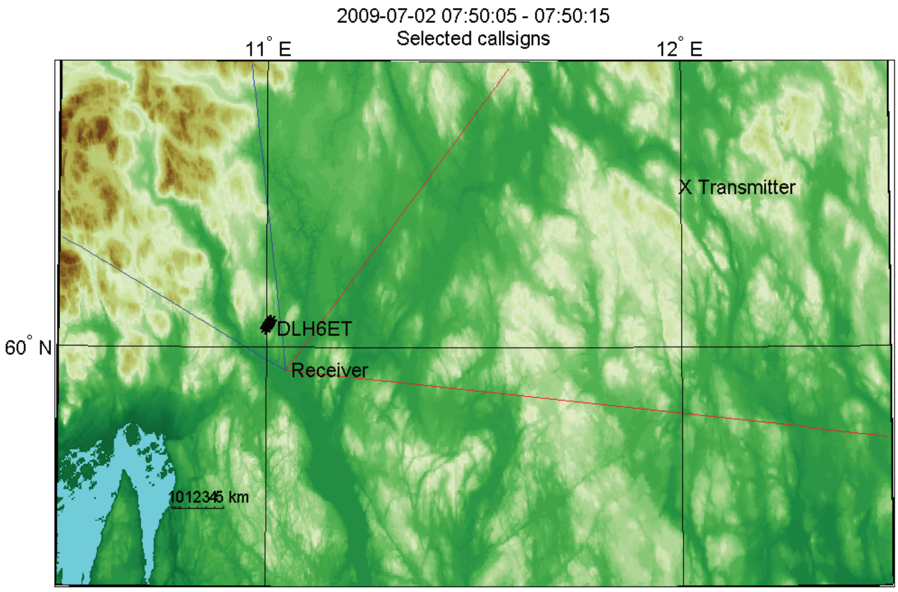

(a) Transmitter, target, and receiver geometry.

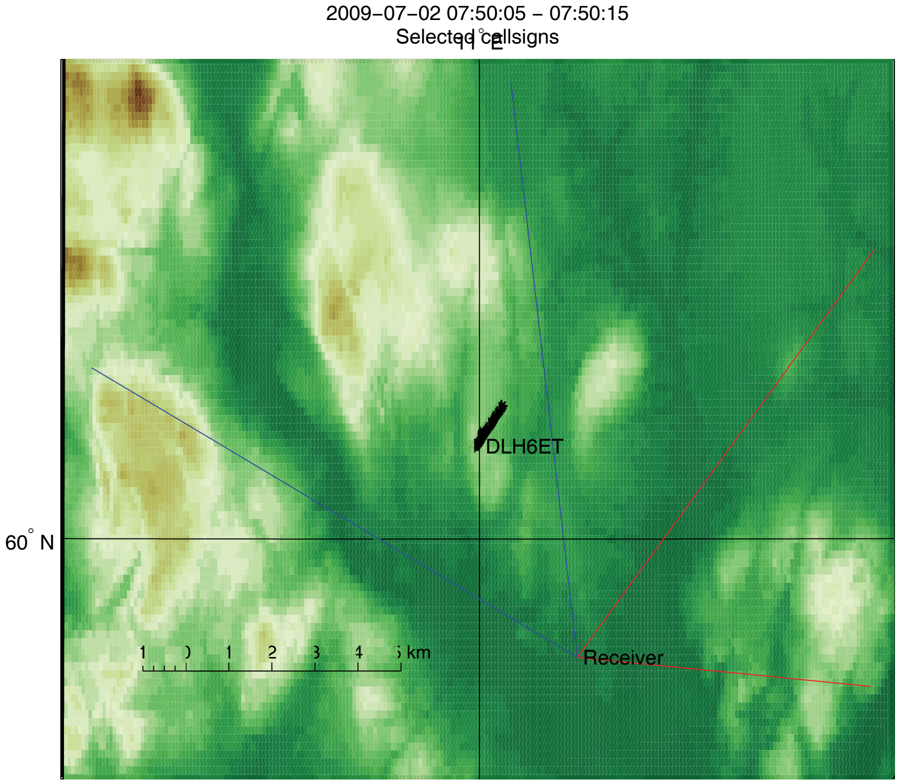

(b) Zoom of (a), detailing the target (black curve) trajectory.

Figure 6.12: The figure shows the geometry for the passive bistatic radar setup, including the target of opportunity's position recorded by the Kinetic Mode-S receiver [19]. The sectors indicates the reference (red) and surveillance (blue) channels beam directions and widths.

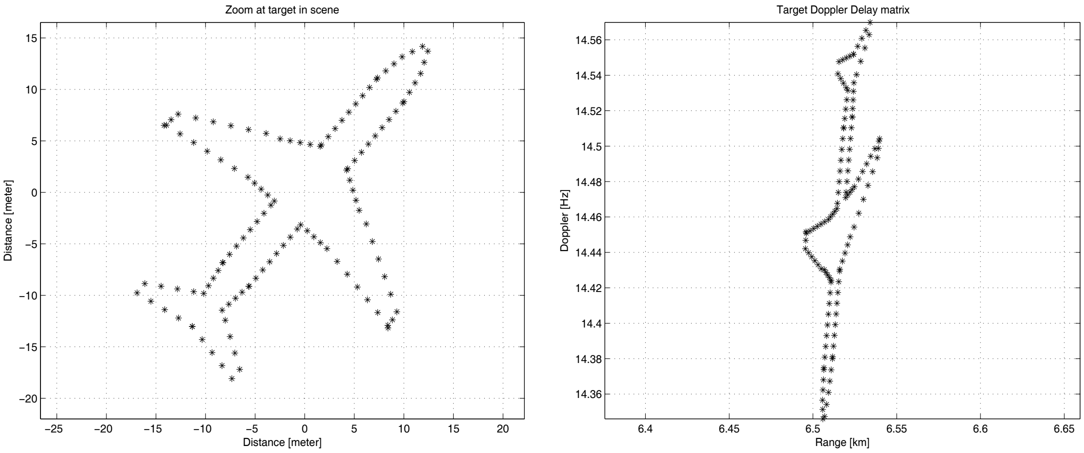

(a) Zoom at target in scene, north up. (b) Target range-Doppler profile.

Figure 6.13: FM radio PBR target Doppler shift induced from the geometry and target trajectory/velocity as presented in figure 6.12. The transmitter's carrier frequency is $f = 89.8MHz$.

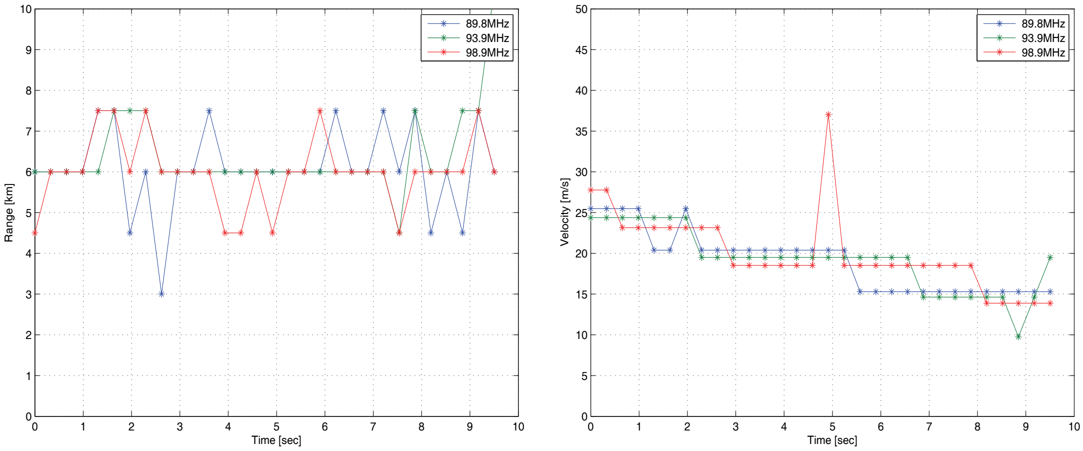

(a) Time-range, CPI=329ms. (b) Time-velocity, CPI=329ms.

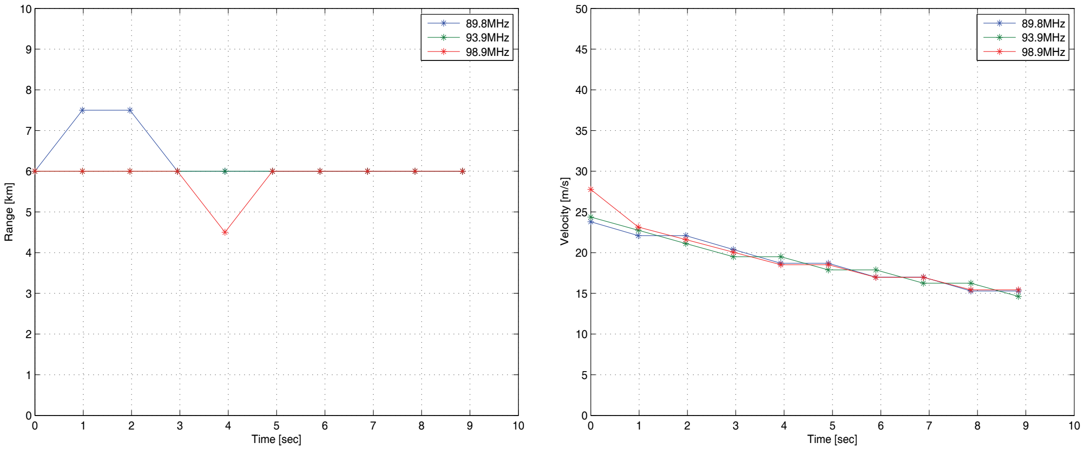

(c) Time-range, CPI=984ms. (d) Time-velocity, CPI=984ms.

Figure 6.14: FM radio PBR target range and velocity as functions of time. The geometry and target trajectory is presented in figure 6.12. The processed data is also presented as a function of CPI.

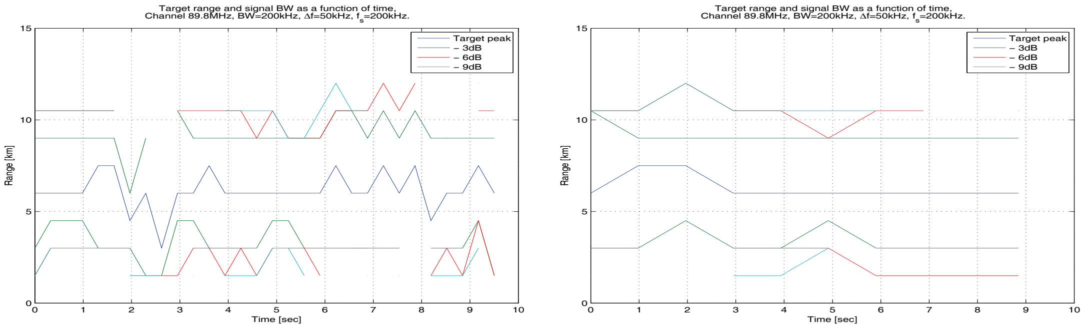

(a) 89.8MHz, CPI=329ms.   (b) 89.8MHz, CPI=984ms.

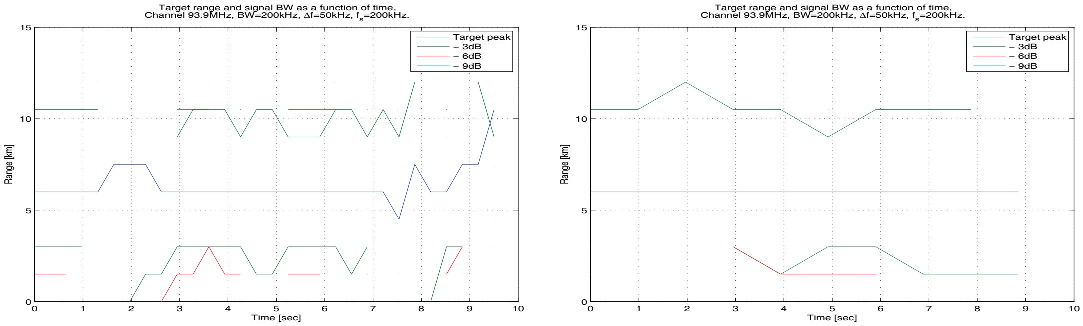

(c) 93.9MHz, CPI=329ms.   (d) 93.9MHz, CPI=984ms.

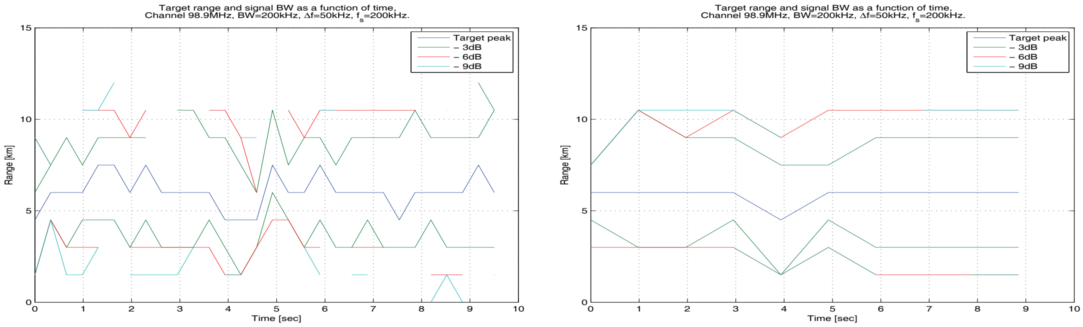

(e) 98.9MHz, CPI=329ms.   (f) 98.9MHz, CPI=984ms.

Figure 6.15: Single channel detections for CPI=329ms, and CPI=984ms.

function of target peak width and time. The target peak's range, and $-3dB$, $-6dB$, and $-9dB$ widths as functions of time are measured. The stability is clearly much better for the longer integration time. Comparing these results with figure 6.9, where the waveform's performance was analyzed, it is seen that the real life situation is more complicated. The target is now changing both range and Doppler with respect to the radar system, as well as multipath, and signal levels are much lower. Figure 6.9 was the perfect situation, strong and clean signals (surveillance being a replica of the reference channel), while figure 6.15 reflects the real world.

Figures 6.16, 6.17, and 6.18 show the results of the algorithm presented in chapter 5 applied on the real life target data sets presented in figures 6.12-6.15.

The first observation is that the algorithm works better with phase compensation than without. Comparing figure 6.16 a and b it is clearly seen that the stability of the target are better, i.e. the range is not varying as much from CPI to CPI. In the non-phase compensated plots there seems to be a periodicity which is not present in the phase

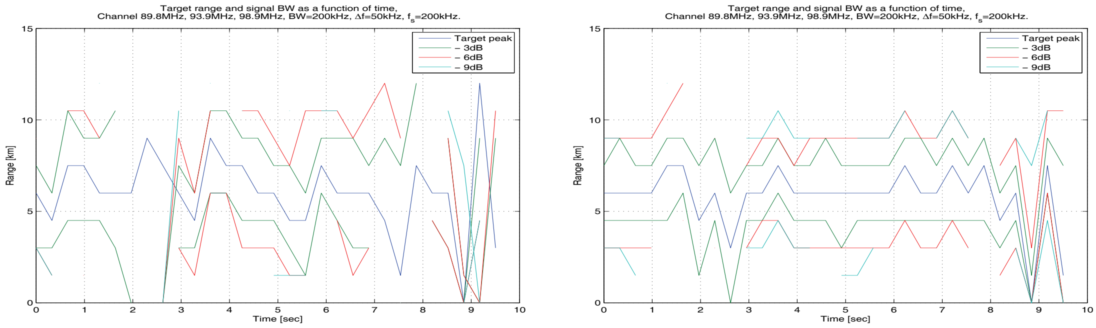

(a) Doppler only, no phase compensation, CPI=329ms (b) Both Doppler and phase compensation, CPI=329ms

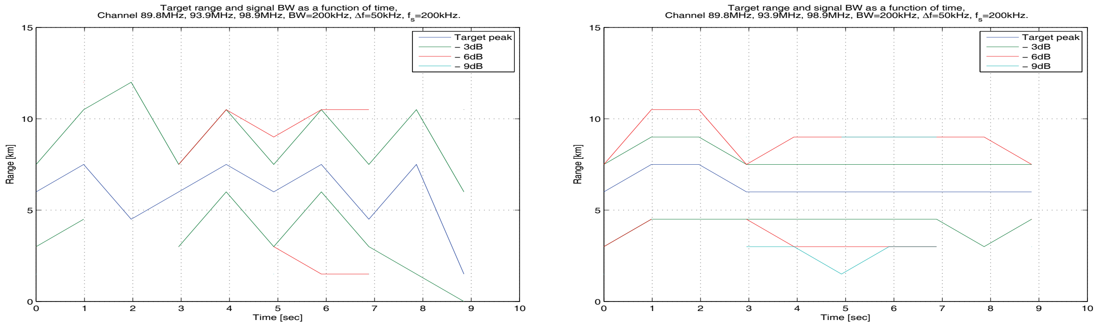

(c) Doppler only, no phase compensation, CPI=984ms (d) Both Doppler and phase compensation, CPI=984ms

Figure 6.16: Target peak width $(-3/-6/-9dB)$ as a function of CPI and time for $\Delta f = 50kHz$.

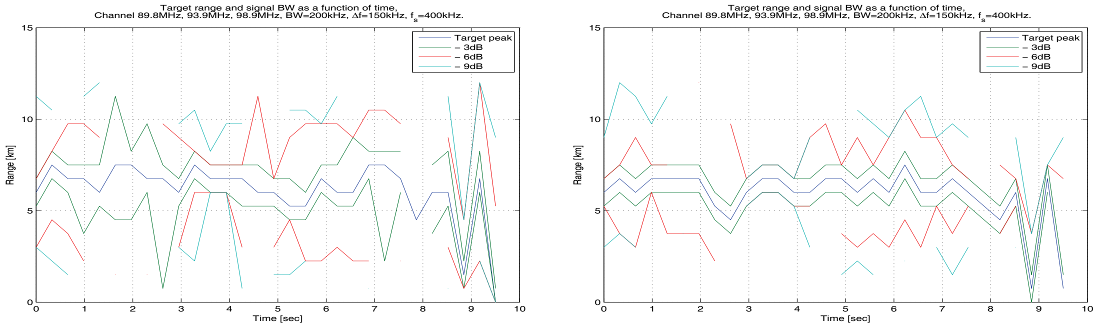

(a) Doppler only, no phase compensation, CPI=329ms (b) Both Doppler and phase compensation, CPI=329ms

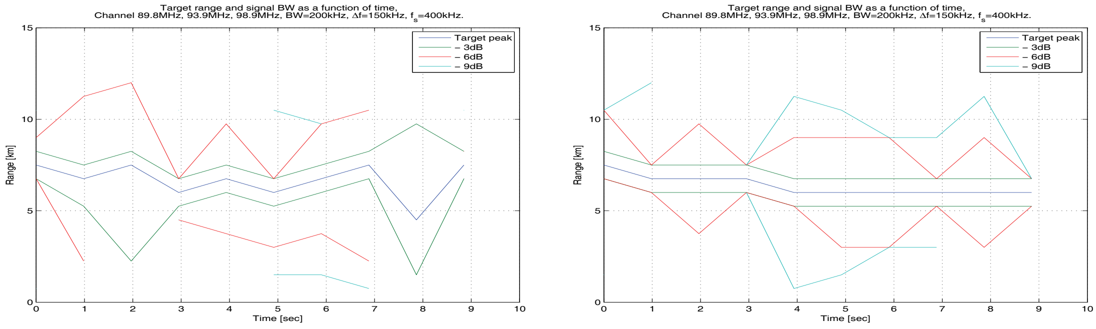

(c) Doppler only, no phase compensation, CPI=984ms (d) Both Doppler and phase compensation, CPI=984ms

Figure 6.17: Target peak width $(-3/-6/-9dB)$ as a function of CPI and time for $\Delta f = 150kHz$.

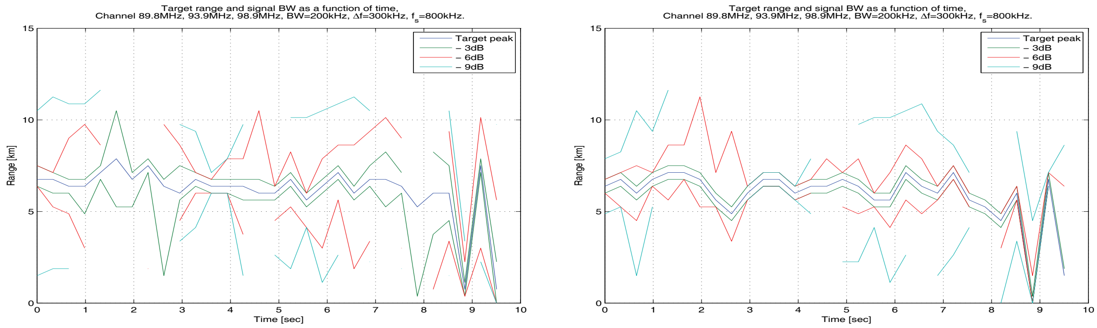

(a) Doppler only, no phase compensation, CPI=329ms (b) Both Doppler and phase compensation, CPI=329ms

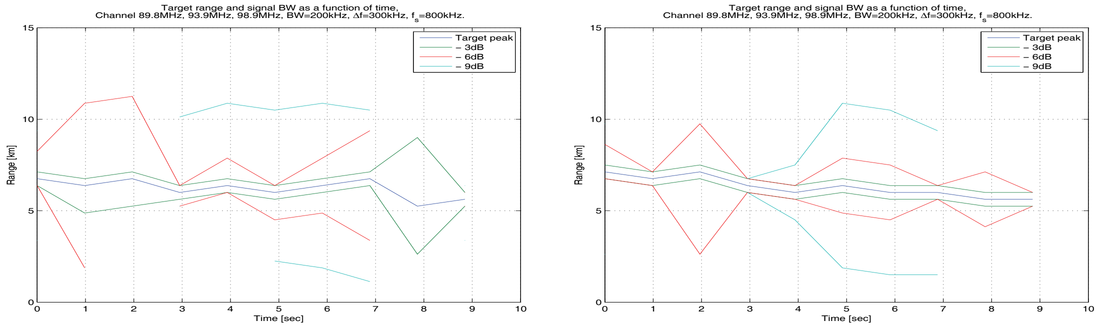

(c) Doppler only, no phase compensation, CPI=984ms (d) Both Doppler and phase compensation, CPI=984ms

Figure 6.18: Target peak width $(-3/-6/-9dB)$ as a function of CPI and time for $\Delta f = 300kHz$.

compensated plots, this is especially visible in figure 6.16a versus b. The same performance can be noted in the rest of the plots, figure 6.16-6.18.

The second observation is that the width of the target's peak seems to be narrower for the phase compensated case. Comparing figure 6.17a and b, and c and d, between $1-3$ seconds, it is seen that the phase compensated plots have the $-3dB$ width behaving like the target, while the non-phase compensated plots are the $-3dB$ width jumping randomly. Similar examples can be found for other segments of the plots and CPIs. Counter examples can be found, but they are outnumbered by the plots supporting the claim, as well as the theory of chapter 5. None of the above mentioned results were observed in the waveform simulated cases of the previous sections.

Looking at the plot which is believed to be the most target position accurate 6.18d, where both Doppler and phase compensation have been applied, the CPI$= 984ms$, and the $\Delta f = 300kHz$. It is seen that the target is behaving as expected, i.e. slowly monotonically approaching the radar in range, with no range jumps at all. The $-3dB$ points are following the target, the $-6dB$ are close to following, but in a non-random pattern. The $-3dB$ width is throughout the ten presented seconds $750m$, yielding the half width resolution to be $\Delta R = 375m$.

Comparing the results for the single channel case 6.15 to the multiband processing, figures 6.16-6.18, it is clearly seen that the width of the peak has been narrowed. Looking at CPI$= 984ms$, in figure 6.15b, d, and e, the target $-3dB$ width is $6000-8000m$, while

Table 6.5: Target peak width for both single channels as well as for the $N = 3$ combined Holtberget channels as a function of frequency and Δf, phase corrected case.

		$-3dB$ peak width	$-6dB$ peak width	$-9dB$ peak width	Sampling resolution, f_s, c/f_s
Single channel CPI=329ms	89.8MHz	ca 6km	ca 6km	6km	200kHz, 1500m
	93.9MHz	ca 7km	n/a	n/a	200kHz, 1500m
	98.9MHz	ca 5km	ca 6km	n/a	200kHz, 1500m
Multi channel CPI=329ms	$\Delta f = 50kHz$	3.00km	6.00km	6.00km	200kHz, 1500m
	$\Delta f = 150kHz$	1.50km	n/a	n/a	400kHz, 750m
	$\Delta f = 300kHz$	0.75km	n/a	n/a	800kHz, 375m
Single channel CPI=984ms	89.8MHz	ca 6km	ca 7km	ca 8km	200kHz, 1500m
	93.9MHz	ca 8km	n/a	n/a	200kHz, 1500m
	98.9MHz	ca 6km	ca 8km	ca 8km	200kHz, 1500m
Multi channel CPI=984ms	$\Delta f = 50kHz$	3.00km	6.00km	6.00km	200kHz, 1500m
	$\Delta f = 150kHz$	1.50km	6.00km	n/a	400kHz, 750m
	$\Delta f = 300kHz$	0.75km	3.00km	ca 9km	800kHz, 375m

the corresponding numbers for the multiband cases of $\Delta f = 50kHz$, $\Delta f = 150kHz$, and $\Delta f = 300kHz$ are 3000m, 1500m, and 750m respectively. And thus the half width range resolutions are improved from around 4000m to 1500m, 750m, and 375m respectively. All this is summarized in table 6.5, although the single channel plots are highly fluctuating, and the target peak widths in these cases are merely indicated. In some cases the fluctuations were so bad that the peak width could not be estimated, and this is in the table termed n/a.

6.3 Summary

Simulations based on real life FM radio waveforms show that the algorithm is capable of improving range resolution according to theory for single scatterers as is summarized in table 6.4. For multiple scatterers, the algorithm is impacted by the FM radio's time varying behavior, although less than expected. The bandwidth contributes to lowering the range ambiguities sidelobes, and as the bandwidth is fluctuating, the sidelobes are fluctuating as well.

By exploiting multiple broadcasted channels the simulations show that the single point scatterer resolution is improved from $3km - 10km+$ for the single channels target peak widths down to $1.5km/0.750km/0.375km$, for the $\Delta f = 50kHz/150kHz/300kHz$ case. All results are tabulated in table 6.4.

As an example, the case where two targets were separated by bistatic range of 2.250km (1.1250km equivalent monostatic resolution) was presented. The targets were not resolved in the single channel cases, but being fully resolved by processing $N = 4$ channels together for $\Delta f = 50kHz$, while the results became more dubious for the $\Delta f = 150kHz$, and $\Delta f = 300kHz$ cases. For target multiple scatterers resolution, with the FM radio waveforms one should be aware of the ratios $f_s/\Delta f$, and $f_s/(N\Delta f)$, which should not be too low, and this line might have been crossed for $\Delta f = 150kHz$ and $\Delta f = 300kHz$, which for the $\Delta f = 150kHz$, and $\Delta f = 300kHz$ is the same and lower (5.3/1.3) than for the $\Delta f = 50kHz$ case (8.0/2.0).

The simulations showed no real performance improvement by increasing the coherent integration interval. Some "averaging" effects were observed, as more data is processed together, but no significant performance improvement was observed. Also, the phase term seemed not to be too important. However, by analyzing real data, it was found that the phase correction term is important for the FM radio waveform. The results were much more stable, as well as sensible as far as the work in this thesis was able to verify. It was also found that the increased CPI resulted in much more stable, and believable results. This was exemplified by what is believed to be the best performance of the algorithm, figure 6.18d, where both the Doppler and phase has been corrected for, and the CPI=984ms. It was shown that the target was slowly and monotonically approaching the radar in range, with no range jumps at all.

The range resolution on real target position is improved from the $N = 3$ single channels case of $6 - 8km$, down to $3.00km$, $1.50km$, and $0.75km$, for the three exploited channels from the Holtberget broadcaster by using $\Delta f = 50kHz$, $\Delta f = 150kHz$, and $\Delta f = 300kHz$ respectively, as seen in table 6.5, where full results for the PBR's resolution improvement for the airliner are available.

Further, the mathematics of chapter 5 showed that once the high range resolution is in place, the ISAR image formation should be readily available under the constraint that sufficient target maneuvering is available, which not at all might be the case for these frequencies, see figure 6.13. The low carrier frequency combined with the motion of the airliner makes target ISAR imaging based on target Doppler spread very hard for the FM radio frequencies and realistic integration times.

Chapter 7

DVB-T PBR Results and Analysis

This chapter presents the performance analysis of the DVB-T radio waveform using the algorithm developed in chapter 5. It will be shown that the proposed algorithm offers improved range resolution capability as previously demonstrated for FM transmissions. As in the previous chapter, all datasets were collected with the hardware described in chapter 4. This chapter also presents novel PBR HRR results from two different targets of opportunity.

The generation of the DVB-T signal is well described in [12], and the ambiguity behavior properly treated in [23, 32]. The relatively high bandwidth of DVB-T combined with the relatively long integration times may cause range and Doppler walk, and strategies for meeting those are treated in [132, 133]. These publications are interesting once improved range resolution and/or increased integration times are sought.

The DVB-T system is a single frequency network consisting of multiple single frequency networks operating in adjacent areas at different frequencies as seen in figure 7.1, appendix B.4. The figure shows the situation north of Oslo, where the receiver was placed on the roof of FFI. For the DVB-T work, comprises both waveform analysis and real target data analysis based on the Tryvasshoegda and Kongsvinger transmitters, which are parametrically described in table 1.1. Simple performance assessments are presented in section 4.1.

Section 7.1 maps the DVB-T waveform's capabilities for improved range resolution, motivated both by single scatterer positioning, but also multiple scatterer resolution. The chapter further investigates the algorithm's performance in two real life situations: Section 7.2 for an airliner of opportunity, figure 6.11, while section 7.3 for a propeller aircraft of opportunity, figure 7.13. The targets were recorded at different days, using different trajectories, and broadcasters of opportunity yielding different bistatic geometries. Finally, section 7.4 presents some observations of the algorithm's performance with respect to NCTR aspects, i.e. HRR, (and thus potentially ISAR).

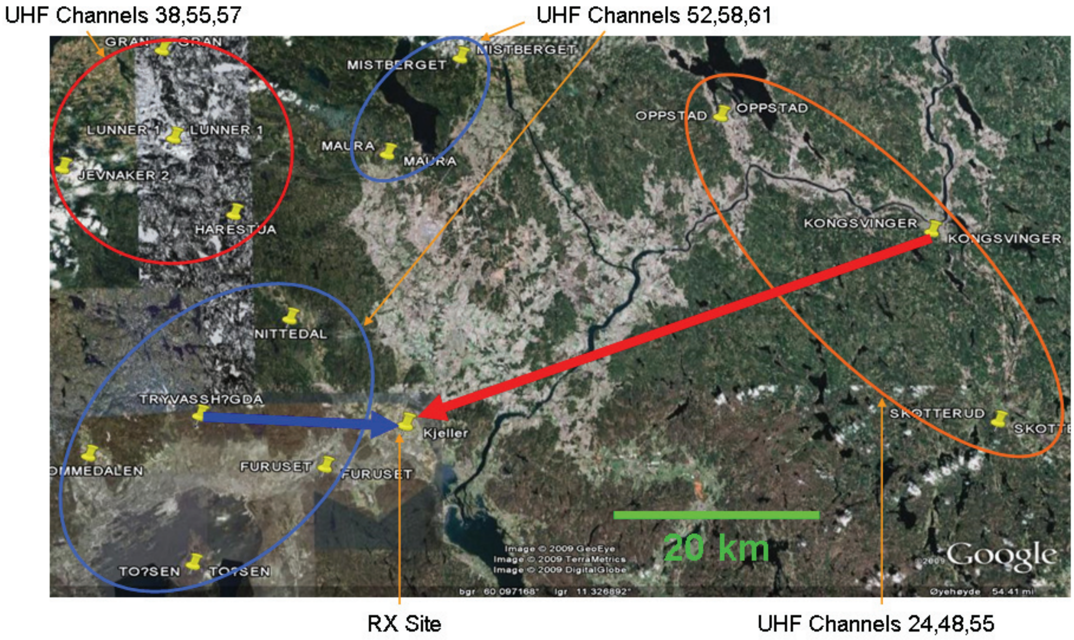

Figure 7.1: The Norwegian DVB-T network is based on multiple single frequency networks operating in adjacent areas at different frequencies. March 2009, north of Oslo, Norway.

7.1 DVB-T waveform analysis

In order to show the potential of the DVB-T waveform, the nearby and powerful Tryvasshoegda transmitter was used as signal source for the simulations. The signal was recorded and then synthetic targets according to table 7.1 were generated, and the results are presented in the following sections. Table 7.2 presents important parameters and numbers associated with the algorithm of chapter 5, and these will be referenced to in the following.

Table 7.1 shows the ambiguity distance $c/\Delta f$, combined waveform theoretical resolution $c/(N\Delta f)$, and sampling resolution c/f_s for $N = 3$ as a function of Δf.

7.1.1 Waveform conditioning

Figure 3.15 shows the generic processing scheme for passive radar signal processing. Until now, the focus has been on the passive radar range cross-correlation and its properties in light of exploiting the available broadcasted bandwidth, avoiding beamforming, signal conditioning, and adaptive cancellation. Although a simple waveform conditioning for the FM radio has been applied, it was not until the processing the DVB-T signals started it

Table 7.1: Synthetic target parameters.

Δf	Target 1, $v = 100m/s$	Target 2, $v = 100m/s$
$4MHz$	$R = 15.0km$, $0dB$	$R \in [15.0km, 15.1km]$, $-3dB/-6dB$
$8MHz$	$R = 15.0km$, $0dB$	$R \in [15.0km, 15.1km]$, $-3dB/-6dB$

Table 7.2: Ambiguity distance $c/\Delta f$, combined waveform resolution $c/(N\Delta f)$, and sampling resolution c/f_s for $N = 3$ as a function of Δf.

Δf	Ambiguity distance $c/\Delta f$	Combined distance $c/(N\Delta f)$	Sampling distance c/f_s	Ratio $f_s/\Delta f$	Ratio $f_s/(N\Delta f)$
$4MHz$	$75.0m$	$25.0m$	$7.5m$	10.0	3.3
$8MHz$	$37.5m$	$12.5m$	$7.5m$	5.0	1.7

was realized that the waveform conditioning really was necessary.

A single target (Target 1) according to table 7.1 was generated, and for each of the individual channels ($722MHz$, $770MHz$, and $794MHz$) the response after full range Doppler processing is shown in figure 7.2 a-c. The second channel is $8dB$ below the first, with the third being $6dB$ below the second, and thus $14dB$ below the first. If the algorithm for processing multiple bands is applied directly, the response is as shown in d and e. The target's response across channels are equalized, and thus each of the individual channel's signal level are adjusted so that the target's peak response of each of the individual channels after full range Doppler processing are equal as seen in figure 7.3 a,c, and e. Then the target peak response for the combined processing as seen in figure 7.4a and b is achieved. Comparing this with figure 7.2d and e, it is seen that the target's response main peaks are narrower, but the sidelobe level remains the same.

This was not the case for the FM radio, were no apparent performance improvement by signal conditioning were found. For the FM radio, the differences in simulated target peaks are less than $6dB$, while the differences of $8dB$ and $14dB$ for the DVB-T peaks are seen in figure 7.2. In the algorithm development in chapter 5 the same target response for all frequencies/channels was assumed. This is not necessary, but a choice of convenience in order to present the algorithm. The algorithm can easily be extended to cope with the channel equalisation directly, but that would only complicate the picture unnecessarily. For the rest of the DVB-T results, the target response variations have been compensated for.

For real life targets, both the multipath and target RCS may be expected to be frequency dependent, and thus frequency dependent target response should be taken into account. For the FM radio PBR this is not expected to happen to the same extent as for DVB-T, as the frequency span is only $20MHz$, as well as the carrier frequencies are low, $88-108MHz$, for the targets of interest. However, once looking at DVB-T, the frequency span is larger $320MHz$, as well as the frequencies higher, $470-790MHz$. From real life target analysis, it was found that the target response equalisation was necessary for the DVB-T waveform, chapter 7, but not for the FM radio waveform.

7.1.2 Single point target

For the FM radio case the aim of this section was to 1) improve on the single target positioning resolution, and 2) demonstrate the importance of the phase term correction as

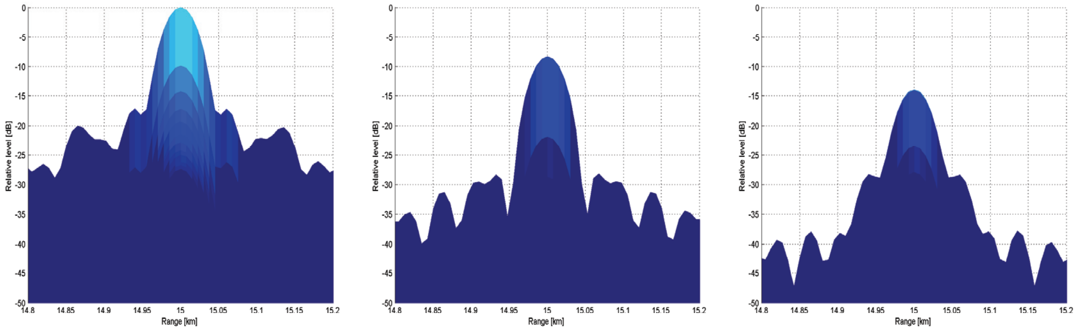

(a) $722MHz$. (b) $770MHz$. (c) $794MHz$.

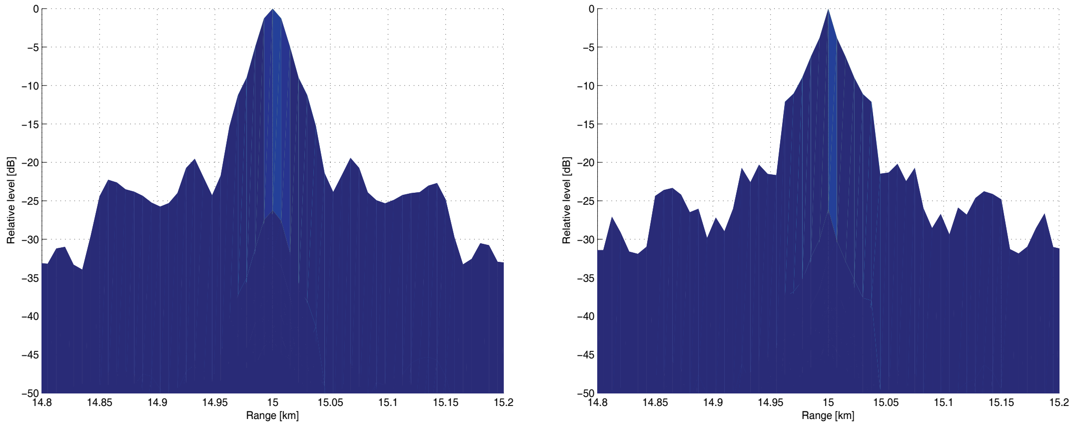

(d) Combined, $\Delta f = 4MHz$, $N = 3$. (e) Combined, $\Delta f = 8MHz$, $N = 3$.

Figure 7.2: (a-c): The single channel's auto correlation for CPI$= 105ms$. Figures (d) and (e) show the combined target peak.

Table 7.3: Autocorrelation peak width for both single channel as well as for the combined channels with $N = 3$ and as a function of Δf.

		$-3dB$ peak width	$-6dB$ peak width	$-9dB$ peak width
Single channel	$722MHz$	45.0m	60.0m	75.0m
	$770MHz$	45.0m	60.0m	75.0m
	$794MHz$	45.0m	60.0m	75.0m
Multi channel	$\Delta f = 4MHz$	30.0m	30.0m	45.0m
	$\Delta f = 8MHz$	15.0m	30.0m	30.0m

described in chapter 5. For the DVB-T case the goals are slightly different. The resolution is to begin with so good that improving on that seems to be of less interest, [26, 63]. However, the focus will be on single target containing of multiple scatterers in order to achieve HRR capabilities, and if that is possible, the generation of ISAR images should be straightforward, once the target exhibits the necessary Doppler spreading as shown in section 5.2.3. The FM radio system is operating both at a lower frequency $88MHz - 108MHz$ and bandwidth $< 100kHz$ than the DVB-T system, which is broadcasting in the $470MHz - 790MHz$ band at $8MHz$ bandwidths. The DVB-T operates at channel bandwidths of $6MHz$, $7MHz$, or $8MHz$, and the latter has been chosen in Norway.

Figure 7.3a, c, and e show the autocorrelation of three of the reference channels recorded when the antenna was pointing at the Tryvasshoegda transmitter 7.1, which is a nearby strong transmitter, and thus a strong DVB-T signal is received. Figures b, d and f show each of the channel's autocorrelation peak widths for a synthetic target generated at $15km$. The $-3dB$ width is $40m$, the $-6dB$ width is $60m$, and the $-9dB$ width is $80m$, which yields $-3/dB - 6dB/ - 9dB$ radar resolution of $20m/30m/40m$ respectively.

Figure 7.3a, and e show that the range sidelobes are $17.1dB$ and $20.0dB$ below the main peak, while figure c shows that the sidelobes are $14.2dB$ below the main peak. This result is stable with time, as is expected, since the COFDM is trying to mimic as random signal as possible. However, the OFDM ambiguities remains, [23, pp. 315-337].

Figure 7.3b, d, and f show the main peak width for the single channel's range correlation as a function of time. Five processing intervals are displayed, each of CPI=$105ms$ duration. The width is, as expected, stable with time, and thus no more than these 5 processing cycles are displayed. By measuring this peak width to the closest sampling point as tabulated in table 7.2, the results summarized in table 7.3 are achieved.

Figure 7.4 shows the main target peak for the combined channel range processing. The peak is shown for the cases of $\Delta f = 4MHz$, and $\Delta f = 8MHz$, in figure 7.4a and b. Figure c and d show the extracted peak width for the $-3dB/ - 6dB/ - 9dB$ peak width. The results are summarized in table 7.2. It is seen that the target resolution is improved from $45m/60m/75m$ for the $-3dB/ - 6dB/ - 9dB$ peak widths respectively to $30m/30m/45m$, for the $\Delta f = 4MHz$ case, and $15m/30m/30m$, for the $\Delta f = 8MHz$ case.

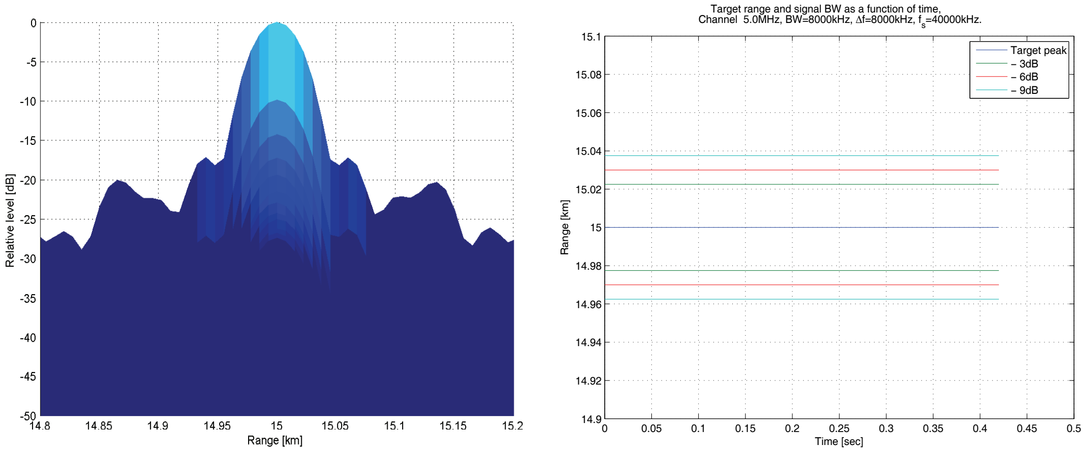

(a) Single channel correlation, $f = 722MHz$.

(b) Target peak width.

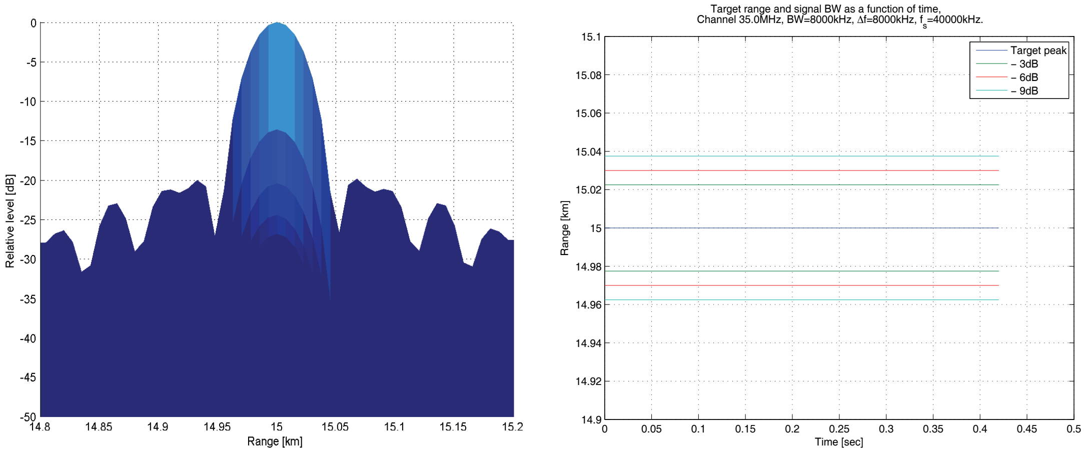

(c) Single channel correlation, $f = 770MHz$.

(d) Target peak width.

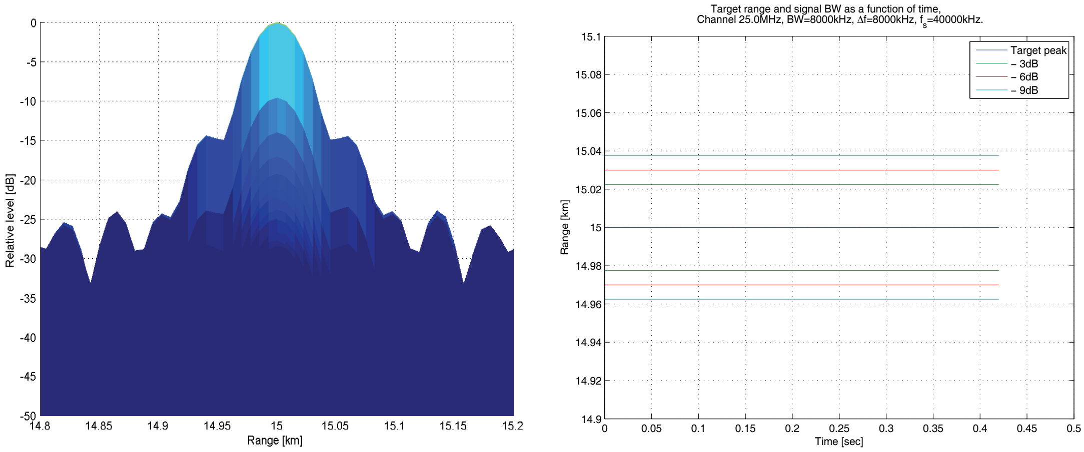

(e) Single channel correlation, $f = 794MHz$.

(f) Target peak width.

Figure 7.3: The single channel's auto correlation for CPI= $105ms$. The peak width variations with time is shown in figure b, d, and f.

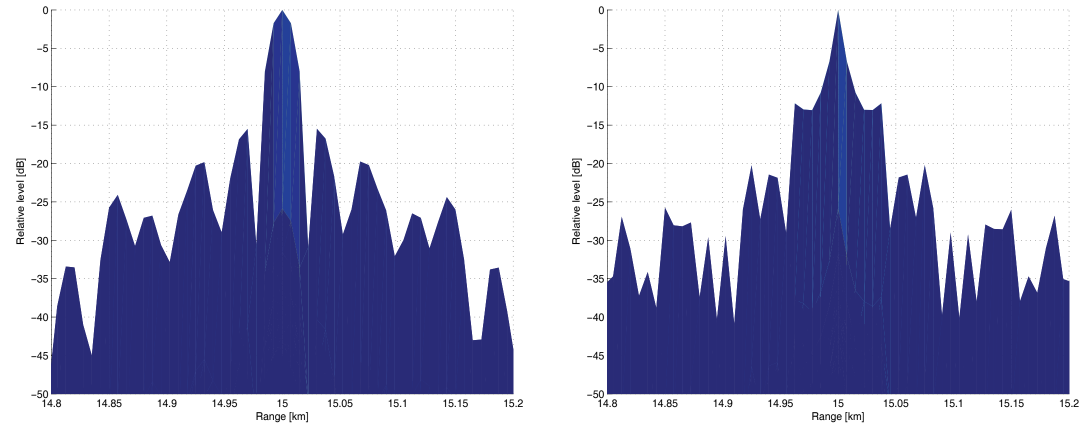

(a) $\Delta f = 4MHz$.

(b) $\Delta f = 8MHz$.

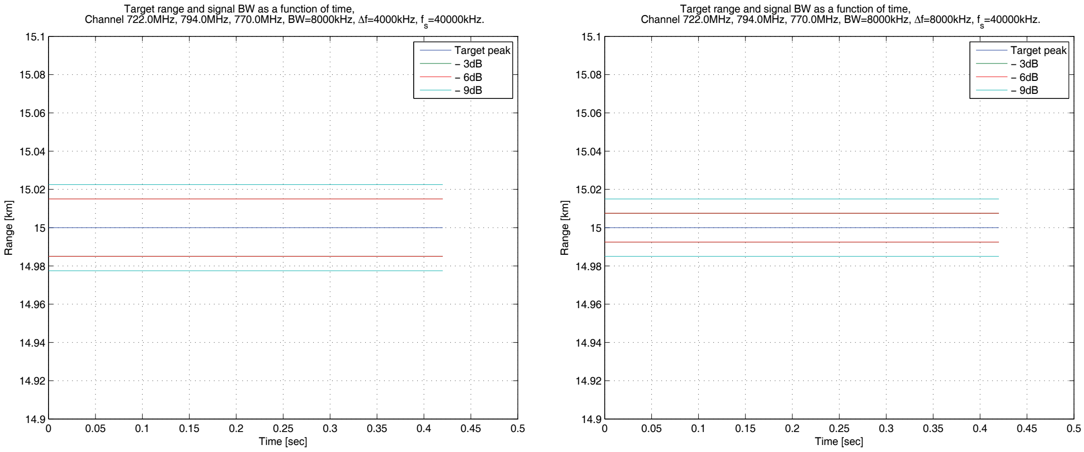

(c) $\Delta f = 4MHz$.

(d) $\Delta f = 8MHz$.

Figure 7.4: The combination of multiple channels for CPI= $105ms$, $N = 3$.

7.1.3 Two point targets

The ability to resolve two scatterers will be investigated in this section. The synthetic target parameters are listed in table 7.1. The surveillance channel is time-delayed, amplitude and phase adjusted according to (6.3) in order to mimic a second point target at another distance, $3dB$ weaker, but at the same velocity. If the velocity differs, the Doppler processing will help distinguish the two scatterers. The time delay has been adjusted in accordance with the reference/surveillance channel's sampling frequency in order to avoid interpolating the delayed signal between sampling points. This was convenient in order to avoid rounding the delay to the same nearest range sample for adjacent second target delays.

Figures 7.5 and 7.6 are interpreted as follows: The first target is at $15km$, while the second target is stepped in range, and the actual target range is indicated in the leftmost column of the plots, numbers edgewise, i.e. the numbers $15.000, 15.008, \ldots, 15.080$ for the upper plot. Next/below to these numbers is the dataset duration in seconds, for the upper plot, that are the numbers 0 and 0.2. The y-axis of the plots, is the processing range in kms. Plots in the left column are not phase compensated, while the right column's plots are phase corrected.

Figure 7.5 shows that the three exploiting channels are not behaving in the same way. The second scatterer are fully resolved for channels with carrier frequencies $770MHz$, and $794MHz$ at $15.060km$, while hints of the second scatterer are visible in channel corresponding to $722MHz$. Channels $722MHz$ and $794MHz$ are fully resolving the second scatterer at $15.038km$, and $722MHz$ also at $15.030km$. From these plots, it is hard to conclude on a proper resolution capabilities. However, what is more important, is to note the difference, or gain in range resolution capabilities, which is demonstrated in figure 7.6 in the multiple channels case. The single channels presented are the same that are being coherently combined and presented in figure 7.6.

The importance of the phase term is also presented, and figure 7.6a and c are the phase uncompensated versions, while figures b and d show the phase compensated resolution plots. In principle, there is little difference between the phase, and non-phase compensated plots apart from the fact that the phase compensated plots are range adjusted according to the highest peak in the plot. In the multiple channels case, the ambiguities are expected to be occurring according to (6.2) and table 7.2, while the range resolution should be as in (6.1) according to theory for a single point target.

Figure 7.6a and b show the case for $N = 3$, with $\Delta f = 4MHz$, and with/without phase correction. The target second scatterer is stepped in range from $15km$ (single target) to $15.060km$. The second scatterer is clearly resolved for $15.030km$, although at a slightly wrong range, but this is probably due to the fact that the second scatterer is interacting with the main scatterer at $15.000km$, as well as the effective rounding to the closest range sampling. It is noted that due to the overlapping frequency spectra, little range sidelobes and ambiguities are experienced.

For the $N = 3$, and $\Delta f = 8MHz$ case, it is seen that the second scatterer have impact at the plot already at $15.008km$, strongly at $15.015km$, but the second scatterer is not

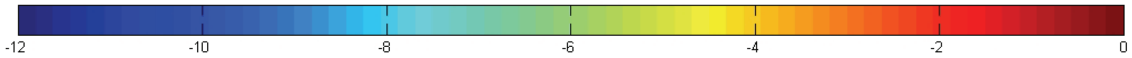

The figure's color coding in dB.

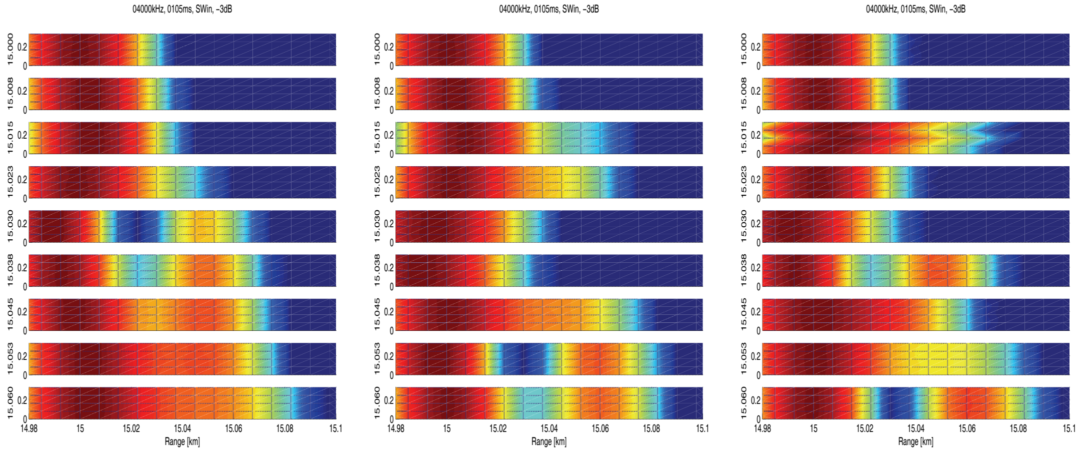

(a) $722MHz$. (b) $770MHz$. (c) $794MHz$.

Figure 7.5: Systematic testing of the algorithm's resolution capabilities for two scatterers varying according to table 7.1, where the second scatterer is $3dB$ below the main scatterer. CPI= $105ms$.

fully resolved before $15.023km$, although the ambiguity situation is slightly worse than for the $\Delta f = 4MHz$ case. The ambiguity distance, table 7.2, is $37.5m$, and thus folding of the second target around this distance should be present. There are some signs of this effect, however less pronounced than expected.

It should be noted that the main peak of the range correlation is range shifted to the exact position of target 1, since the algorithm sometimes results in a ranging error, which causes a shift of all peaks, and thus the figure would be impossible to read properly. The reader is reminded that the target is already detected and tracked, so the information on target position is known.

7.1.4 Summary

Simulation results from using real life DVB-T recorded signals have been presented. The focus has been on mapping the DVB-T waveform's behavior and performance in the proposed algorithm by using real life strong recorded broadcasted signals from nearby broadcasters.

By exploiting multiple broadcasted channels the simulations show that the single point scatterer resolution is improved from $45m/60m/75m$ for the $-3dB/-6dB/-9dB-$ single channels target peak widths to $30m/30m/45m$, for the $\Delta f = 4MHz$ case, and $15m/30m/30m$, for the $\Delta f = 8MHz$ case. All results are tabulated in table 7.3.

It is also showed that the combination of multiple DVB-T channels in the range correlation improves on the PBR system's capabilities to resolve nearby scatterers. The resolution capabilities was improved from around $60m$ to $30m/23m$ for the $\Delta f = 4MHz/\Delta f = 8MHz$ by using three DVB-T channels in the range correlation with varying spacing. The theoretical range performance of the algorithm is summarized in table 7.2. By using

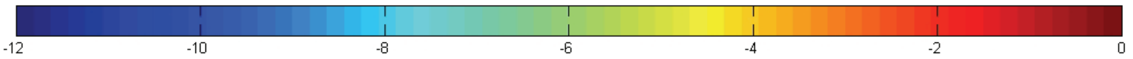

The figure's color coding in dB.

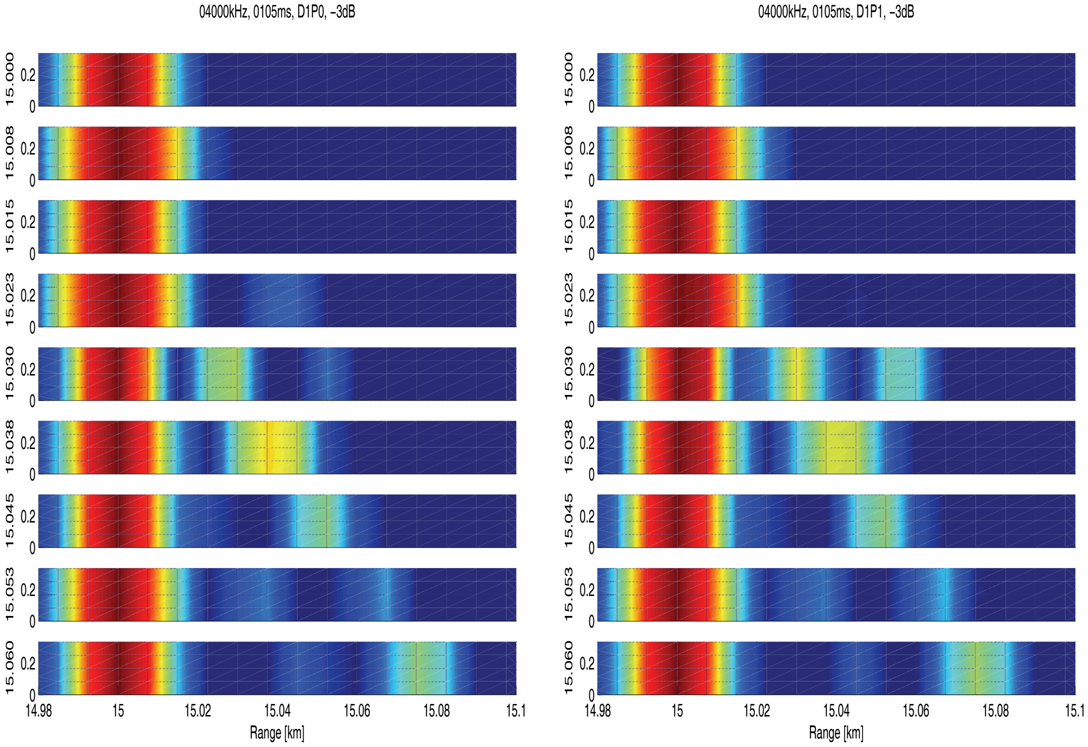

(a) $\Delta f = 4MHz$, no phase compensation. (b) $\Delta f = 4MHz$, phase compensated.

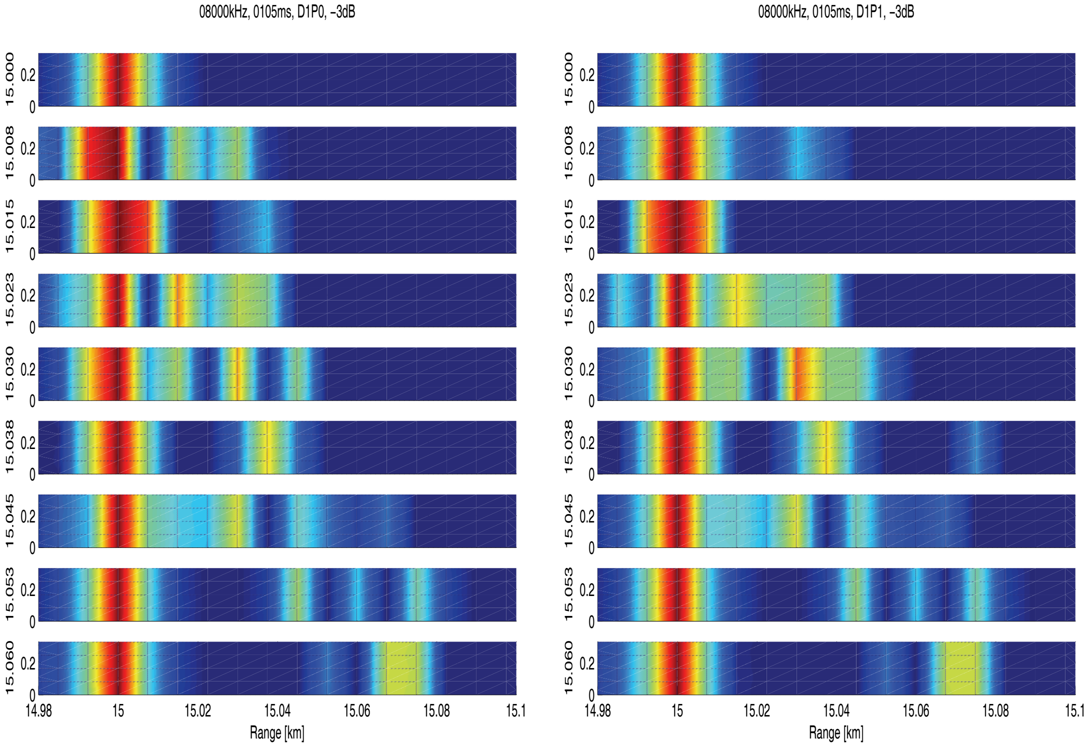

(c) $\Delta f = 8MHz$, no phase compensation. (d) $\Delta f = 8MHz$, phase compensated.

Figure 7.6: Systematic testing of the algorithm's resolution capabilities for two scatterers with varying range, and one $3dB$ below the first, parameters varying according to table 7.1. CPI$= 105ms$, $N = 3$.

overlapping/adjacent bands $\Delta f < B/2$, some of the ambiguities in the range correlation is avoided, while by allowing frequency gaps, $\Delta f > B/2$, ambiguities which may complicate the picture are introduced. How to properly tune this will be the radar designer's choice to make once the application has been decided.

As with the FM radio waveform, the phase term seems not to be very important once simulations like these are presented, while as shall be seen, in the real life target analysis, the phase term is important.

7.2 Real life target: Airliner analysis

This section will apply the proposed algorithm presented in chapter 5, on real life target data collected with the data recording equipment presented in chapter 4. Performance against an airliner of opportunity will be presented. The airliner is exemplified in figure 6.11, and it was heading for Gardermoen airport outside Oslo in Norway. The exploited DVB-T radio broadcaster Kongsvinger, figure 7.1, is a powerful transmitter, and the broadcasted channels are listed in tables 1.1 while simple performance assessments are presented in section 4.1.

The transmitter, target, and receiver geometry is shown in figure 7.7, and the reference and surveillance antennas sectors are also indicated. Figure b is a zoom of figure a in order to show the target trajectory for the ten seconds of analysis. The target position is recorded by Kinetic Mode-S receiver [19]. The data was recorded in 2009, when the Mode-S receiver system definitely not was operational, and thus the Mode-S data cannot be used for system accuracy performance calculations. The Mode-S target position is mainly used here as a rough guide to what should be expecting from the calculations.

Figure 7.8 shows the DVB-T PBR target Doppler shift induced from the geometry and target trajectory/velocity as presented in figure 7.7 for transmitter's carrier frequency of $f = 498MHz$. From the figure it is seen that ISAR imaging based on the target motion would in these data be very hard to achieve due to the low Doppler shift differences, $f_D \in [14.34Hz, 14.58Hz]$, mainly caused by the relatively low carrier frequency. However, in the recorded datasets there is present target spreading in Doppler probably due to the irregular movement in the air caused by turbulence or wind. For the limits of the dataset recorded from Kongsvinger (table 1.1), the spreading is for $f = 498MHz$, $f_D \in [329.3Hz, 329.8Hz]$, and $f = 746MHz$, $f_D \in [493.25Hz, 494.05Hz]$. This requires a best case Doppler resolution of $\Delta f_D = 0.8Hz$ in order to reach the spreading, and a Doppler resolution of $\Delta f_c = 0.08Hz$ in order to have ten Doppler cells over the target. The former requires an integration time of CPI$= 1.25sec$, while the latter a CPI$= 12.5sec$, and especially the latter is highly unrealistic since the range resolution for a single channel is around 20m! [132,133] presented work on countering the range-Doppler migration in order to meet the high bandwidth combined with the long integration times. It is also noted that the target spreading in range is low, below $50m$, which means that there is $2-3$ range bins on a target of opportunity.

Figure 7.9 shows the single channel's target detections for range and velocity as func-

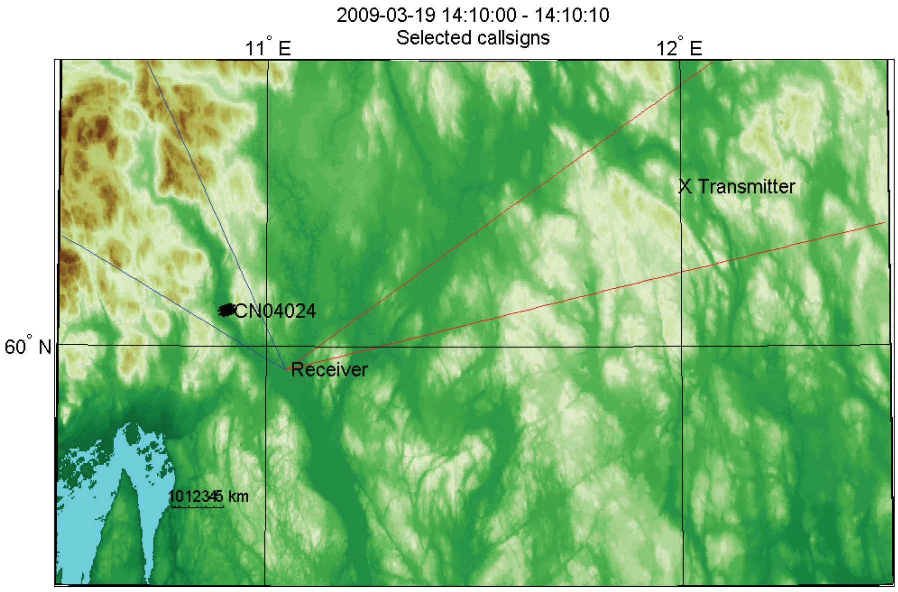

(a) Transmitter, target, and receiver geometry. The red sector mimics the receiver antenna reference channel beam direction and width, while the blue sector is the beam direction and width for the surveillance channel.

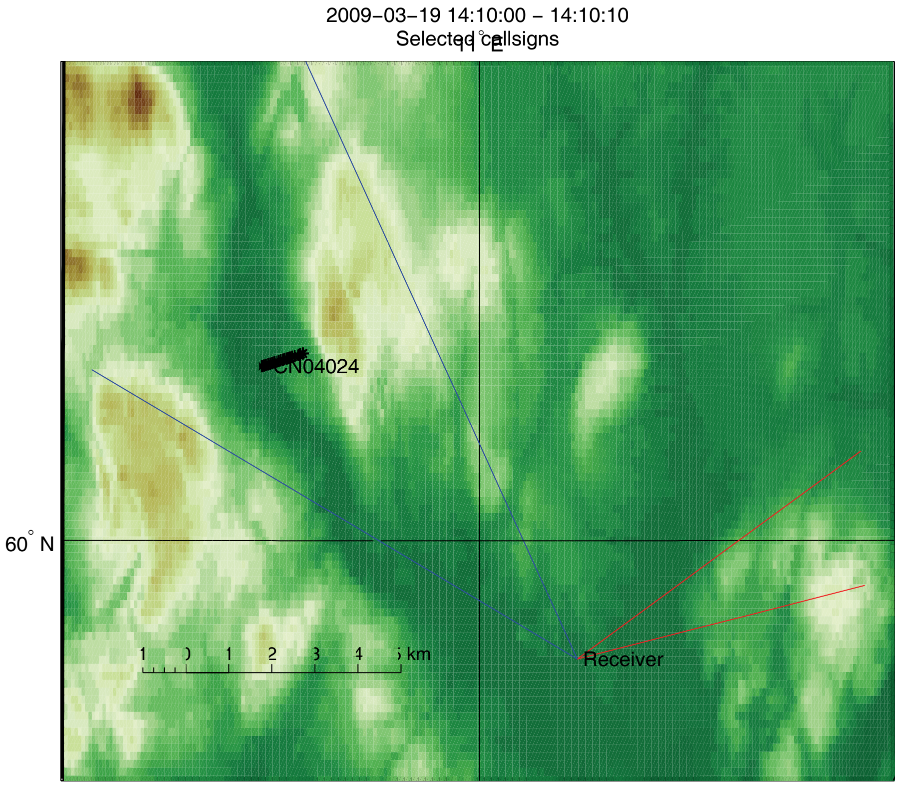

(b) Zoom of the figure (a) above. The target (black curve) trajectory with respect to the receiver is shown.

Figure 7.7: The figure shows the geometry for the passive bistatic radar setup, including the target of opportunity's position recorded by the Kinetic Mode-S receiver [19].

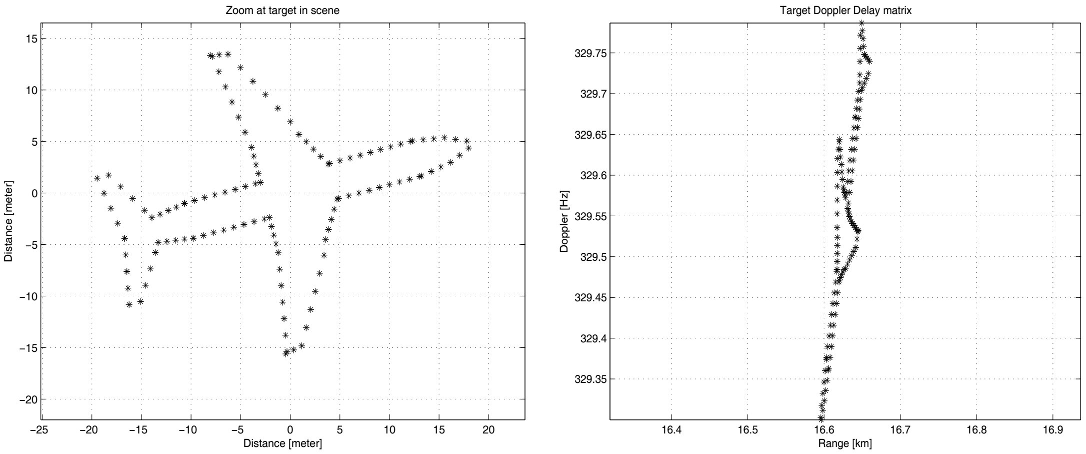

(a) Zoom at target in scene, north up. (b) Target range-Doppler profile.

Figure 7.8: DVB-T PBR target Doppler shift induced from the geometry and target trajectory/velocity as presented in figure 7.7. The transmitter's carrier frequency is $f = 498MHz$.

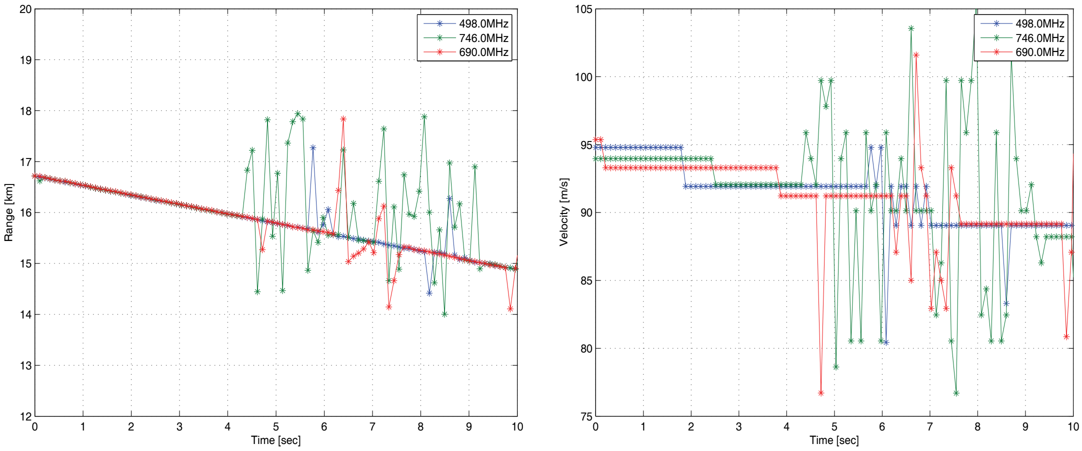

(a) Time-range. (b) Time-velocity.

Figure 7.9: DVB-T PBR target range and velocity as functions of time. The geometry and target trajectory is presented in figure 7.7, for CPI=105ms.

tions of time, for the target trajectory presented in figure 7.7. Figure 7.9 is based on a signal processing time of CPI=105ms.

All figures 7.10-7.12 show the full time-range plot in the left column, i.e. figures a, c, (and e). The right column represent a zoom of the figures in the left column, since the dataset is long compared to the range resolution, and thus the left column only would be hard to use for shedding light on the range resolutions.

Figure 7.10 shows the single channel detections for CPI=105ms, as a function of target peak width and time. The target peak's range as well as the $-3dB$, $-6dB$, and $-9dB$ peaks widths as a function of time is measured. Comparing these results with figure 7.3, where the waveform's performance was analyzed, it is seen that the real life situation is more complicated. The target is now changing both range and Doppler with respect to the radar system, and signal levels are much lower. Figure 7.3 showed the perfect situation, strong and clean signals (surveillance being a replica of the reference channel), while the real world is represented in figure 7.10.

Figure 7.10 shows that the target is not constantly detected, sometimes there is a hardware glitch, as seen around 5.8, 6, 8.2, and 8.7 seconds, where all channels go wrong. Sometimes there is no target detections in one/two of the channels, while the two/one other clearly detects the target, as seen between 7 and 8 seconds. As target range-Doppler values for the algorithm, the average of the individual channels range-Doppler values have been used. This is a very simple approach, but the focus has been on the algorithm development and mapping of its performance, and not on single channel detection improvement. For that it is referred to the papers described in the literature critique's section 2.2.

Figures 7.11 and 7.12 show the results of the algorithm presented in chapter 5 applied on the real life target data sets presented in figures 7.7-7.10.

The first observation is that the algorithm works better with phase compensation than without. Comparing figure 7.11-7.12, show that the stability is improved once the phase correction is applied. Comparing figure 7.11a and c to 7.12a and c it is visible, however might be hard to see properly. IN figures b and d of the same plots the difference is evident. The target trajectory in the non phase compensated plots is jumping irregularly, as is not the case in the phase compensated plots. These results are consistent with the results from the simulations in section 5.2, and also from the real life target data analysis of the FM radio PBR results presented in chapter 6.

The Kongsvinger broadcaster was broadcasting three DVB-T channels at 498MHz, 690MHz, and 746MHz. Table 7.4 shows each of these three channel's target peak widths for $-3dB$, $-6dB$, and $-9dB$, averaged over 4 seconds of high quality detection data. The $-3dB$ target peak width is 51.7m, 48.4m, and 53.4m for the three channels, yielding an averaged single channel performance of 51.3m. Comparing this to the corresponding numbers for the algorithm for $\Delta f = 4MHz$ and $\Delta f = 8MHz$, 30.2m and 15.0m respectively, it is seen that the resolution is improved by a factor of 1.7 and 3.4. This means that the obtained half peak width (classic resolution) in this case is 15.1m, and 7.5m. All results are available in table 7.4 for the airliner of opportunity.

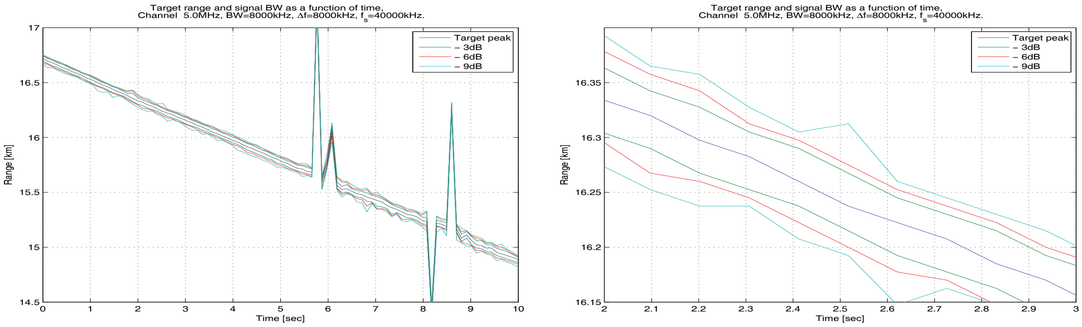

(a) $f = 498MHz$.

(b) Zoom of figure (a).

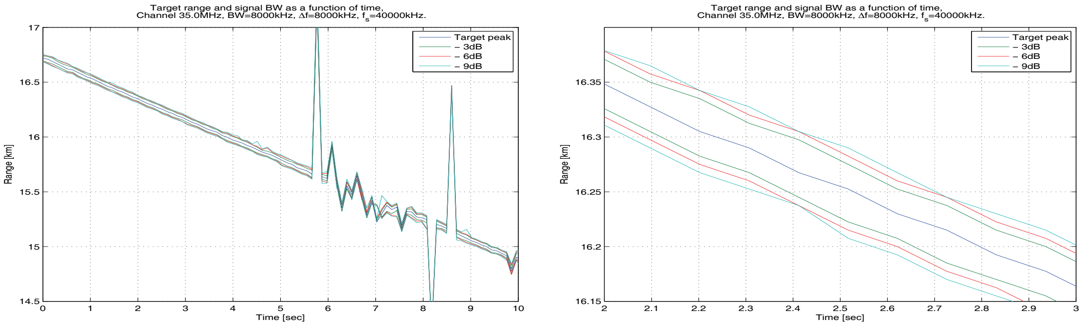

(c) $f = 690MHz$.

(d) Zoom of figure (c).

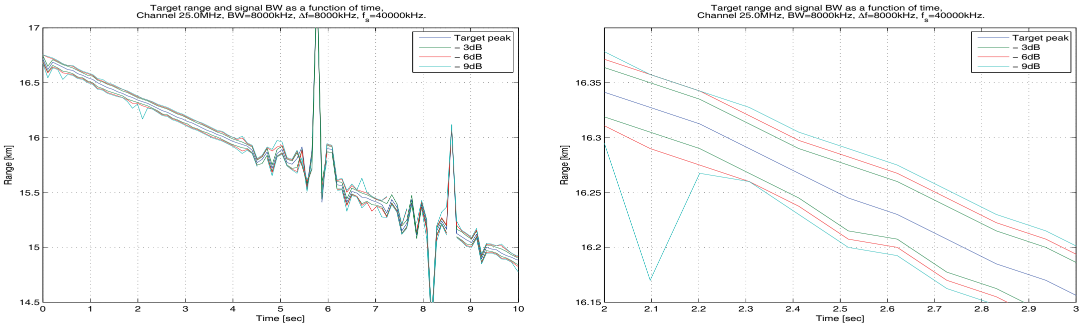

(e) $f = 746MHz$.

(f) Zoom of figure (e).

Figure 7.10: Single channel detections for CPI=105ms.

Table 7.4: Averaged target peak width for both single channels as well as for the $N = 3$ combined Kongsvinger channels as a function of frequency and Δf, phase corrected case, CPI= 105ms.

		$-3dB$ peak width	$-6dB$ peak width	$-9dB$ peak width
Single channel	$498MHz$	$51.7m$	$71.6m$	$93.9m$
	$690MHz$	$48.4m$	$65.3m$	$76.9m$
	$746MHz$	$53.4m$	$74.6m$	$94.3m$
Average	All channels	$51.3m$	$70.5m$	$88.4m$
Multi channel	$\Delta f = 4MHz$	$30.2m$	$33.9m$	$43.3m$
	$\Delta f = 8MHz$	$15.0m$	$23.6m$	$30.9m$

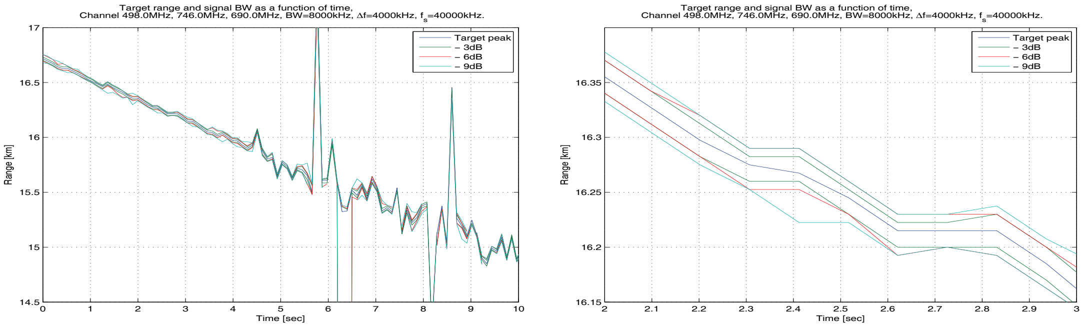

(a) $\Delta f = 4MHz$. (b) Zoom of figure (a).

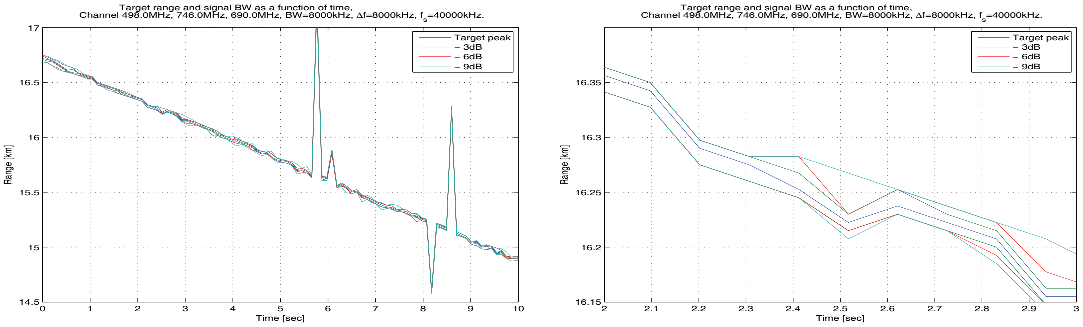

(c) $\Delta f = 8MHz$. (d) Zoom of figure (c).

Figure 7.11: Multiple channel detections for CPI=105ms, no phase fix.

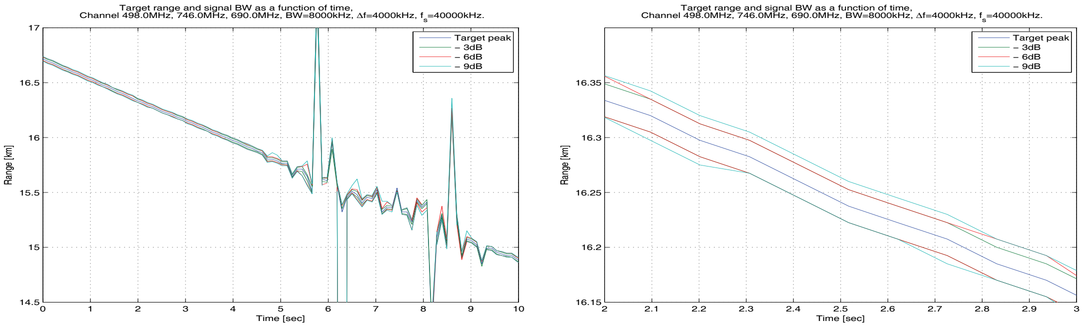

(a) $\Delta f = 4MHz$. (b) Zoom of figure (a).

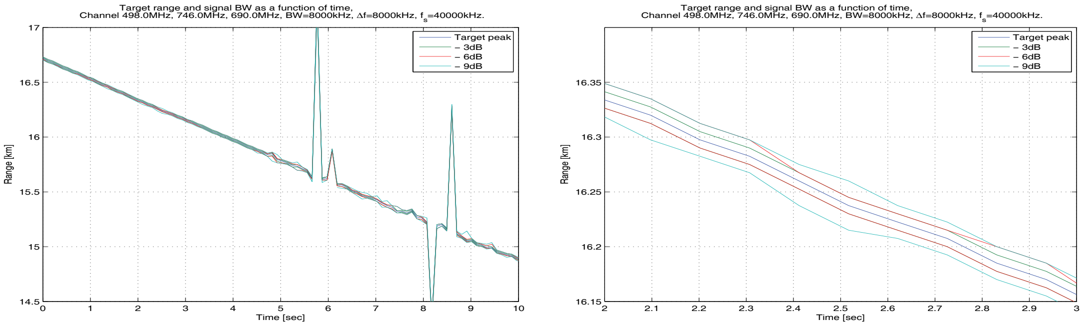

(c) $\Delta f = 8MHz$. (d) Zoom of figure (c).

Figure 7.12: Multiple channel detections for CPI=105ms, phase fix.

7.3 Real life target: Propeller aircraft analysis

In order to cross check the results, a second aircraft is included, this time a propeller aircraft taking off from a nearby airfield. With respect to the airliner in the previous section, this is a target of different type, flying a different trajectory, combined with exploiting a different DVB-T broadcaster which is offering different frequencies. The propeller aircraft is believed to be a Cessna 172 as pictured in 7.14, and the transmitter, target, receiver geometry is shown in figure 7.14. The transmitter of opportunity is now the DVB-T broadcaster Tryvasshoegda, figure 7.1, operating at $722MHz$, $770MHz$, and $794MHz$ as tabulated in table 1.1. The PBR system's expected performance is addressed in section 4.1.

This was a target of opportunity which presented itself during another data recording, and thus no GPS or ground truth reference is available for the target. However, the target was lifting off, towards north-west, from the nearby airfield, and was flying a straight line (with respect to the runway) throughout the recording. And thus, the geometry of figure 7.14 is believed to be moderately accurate. But as shall be seen in the data recordings, both the range and speed of the target is increasing with respect to the PBR. This is in contrast to the indicated trajectory, which is seen to approach the PBR baseline, and thus both the range and Doppler are expected to approach zero. Most likely the target turned slightly, and it might also have been accelerating, and in such a way countering the geometric impact on the velocity.

The surveillance antenna was pointed at the target, and was following the target for around 30 seconds, target trajectory indicated in the figure with the black asterisk. The red sector mimics the receiver antenna reference beam direction and width, while the blue sector is the instantaneous beam direction and width for the surveillance channel, and it should be noted that for this data recording the surveillance antenna was constantly pointing at the target.

Figure 7.15 shows 10 seconds of time-range as well as time-velocity of the data of highest quality from the recording. The data is presented in time-range/velocity instead of range/velocity, as that plot would be very hard to read due to mis-detections in the dataset. The time-range/velocity plots were found to be far more robust in this respect. The target is well detected in all three channels, and as target range-Doppler values for the algorithm, the average of the individual channels range-Doppler values are used. This is a very simple approach, but the focus has been on the algorithm development and mapping of its performance, and not on single channel detection improvement. Further information on the latter may be found in the literature critique's section 2.2.

Figure 7.16 shows the single channel's detections target peak width in the bistatic range-Doppler plots. The peak is extracted, and the width to the nearest sampling point's value is measured. In the zoomed plots it is seen that the individual channels behave similar, except for the section where channel $794MHz$ goes off. Once a channel goes off, the applied peak estimator tends to find very narrow measures, and thus all such data are excluded in the calculations.

Figure 7.13: Example of propeller aircraft target, a Cessna 172, [20].

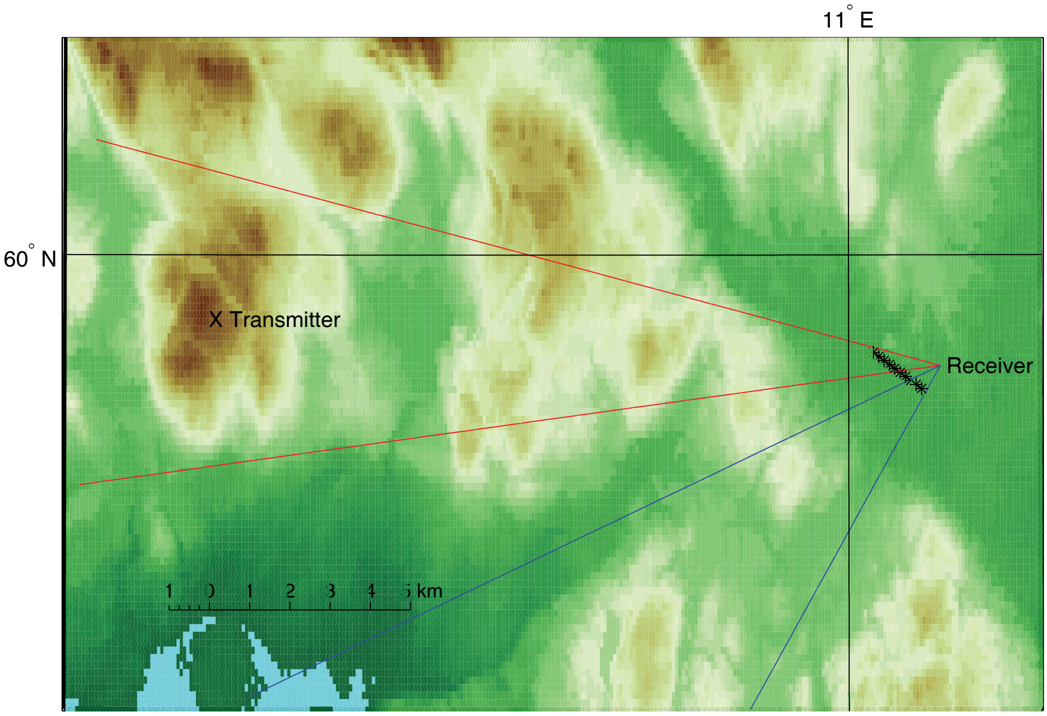

Figure 7.14: The figure shows the geometry for the passive bistatic radar setup, including the propeller target's flight direction (black asterisk). The red sector mimics the receiver antenna reference beam direction and width, while the blue sector is the beam direction and width for the surveillance channel. It should be noted that for this recording, the surveillance antenna was pointed at the target as it flew away from the receiver.

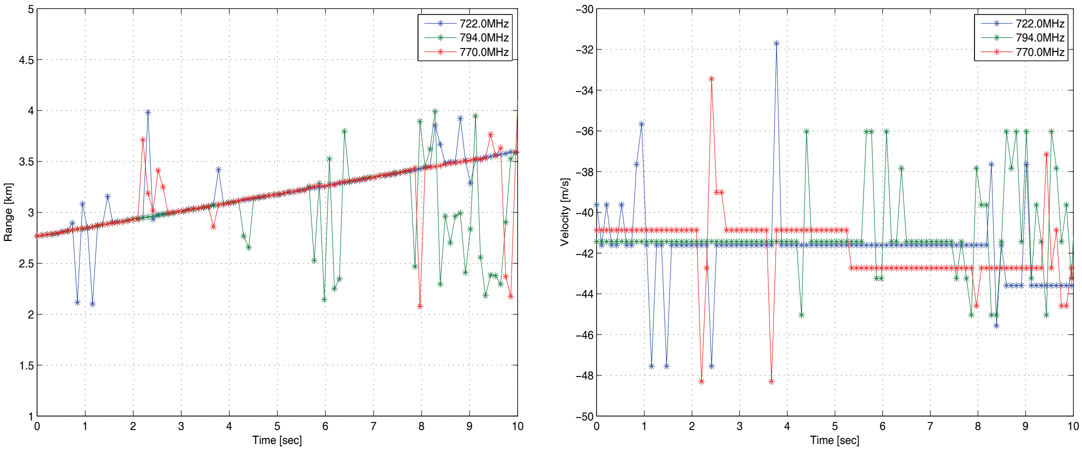

(a) Time-range.

(b) Time-velocity.

Figure 7.15: DVB-T PBR target range and velocity as functions of time. The geometry and target trajectory is presented in figure 7.14. CPI= $105ms$.

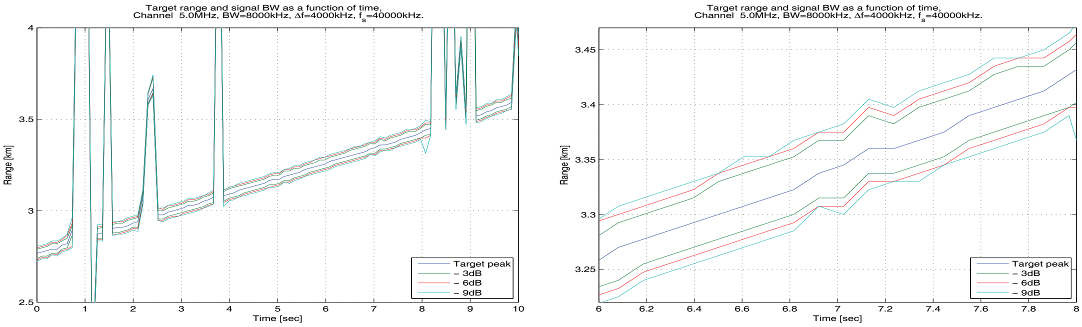

(a) $f = 722MHz$.

(b) Zoom of figure (a).

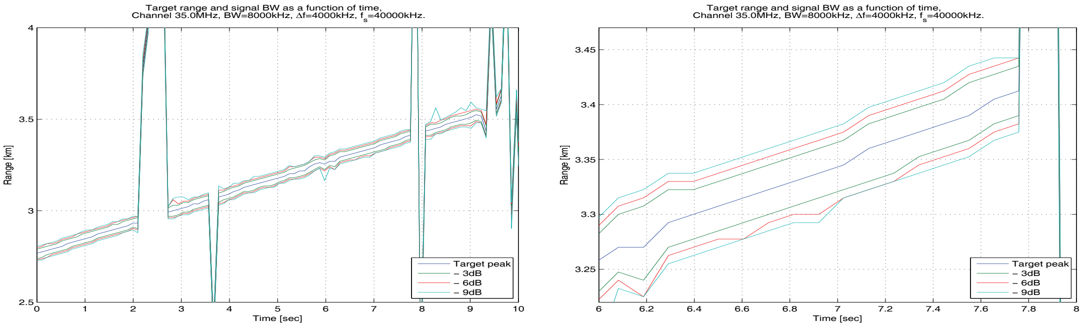

(c) $f = 770MHz$.

(d) Zoom of figure (c).

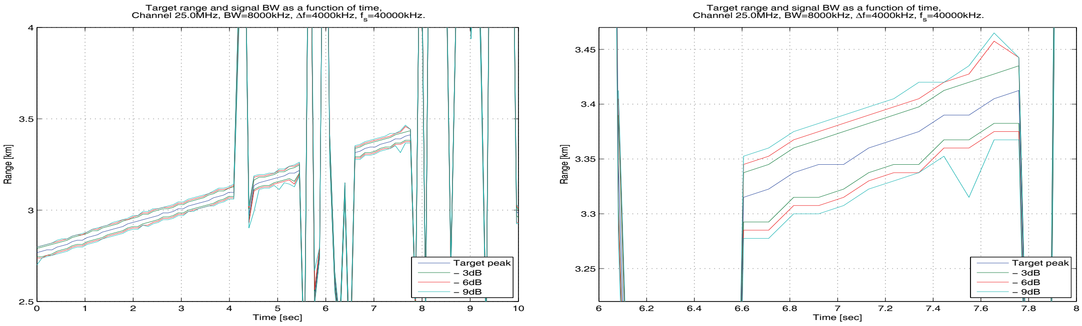

(e) $f = 794MHz$.

(f) Zoom of figure (e).

Figure 7.16: Single channel detections for CPI=$105ms$.

Table 7.5: Averaged target peak width for both single channels as well as for the $N = 3$ combined Tryvasshoegda channels as a function of frequency and Δf, phase corrected case, for CPI= $105ms$.

		$-3dB$ peak width	$-6dB$ peak width	$-9dB$ peak width
Single channel	$722MHz$	$49.3m$	$64.5m$	$76.9m$
	$770MHz$	$48.9m$	$64.7m$	$76.9m$
	$794MHz$	$49.3m$	$65.1m$	$83.1m$
Average	All channels	$49.2m$	$64.8m$	$79.0m$
Multi channel	$\Delta f = 4MHz$	$30.0m$	$35.1m$	$43.5m$
	$\Delta f = 8MHz$	$15.0m$	$24.0m$	$30.2m$

The target response peak widths for the propeller aircraft is averaged, as in the previous section for the airliner, for $-3dB$, $-6dB$, and $-9dB$. The dataset for averaging is chosen so that each of the individual channels are producing high quality target data, and thus mis-detections seen in the figure are excluded. Channels $722MHz$, $770MHz$, and $794MHz$ result in peak widths of $49.3m$, $48.9m$, and $49.3m$ respectively, yielding an overall channel average of $49.2m$. This procedure was repeated for the $-6dB$ and $-9dB$ case, and all results are tabulated in table 7.5.

Figures 7.17 and 7.18 show the results of the algorithm presented in chapter 5 applied on the real life target data sets presented in figures 7.14-7.16.

The first observation is that as for the airliner, the algorithm works better with phase compensation than without. Comparing figure 7.17 and 7.18, shows that the stability is improved once the phase correction is applied. In the full $10sec$ target plots in figures a and c the improvement might be hard to see, but in the zoomed plots b and d, the improvement is evident. Even the target mis-detections of channel $794MHz$ is countered by applying the phase correction. These results are consistent with the results from the simulations in section 5.2, and also from the real life target data analysis of the FM radio PBR results presented in chapter 6 as well as for the airliner of previous section.

Table 7.5 shows the averaged target peak width for both single channels as well as for the $N = 3$ combined Tryvasshoegda channels as a function of frequency and Δf for the phase corrected case where the CPI= $105ms$. The expected performance is shown in table 7.2. The aircraft's target peak is averaged over the periods where all the individual channels are performing well, and were producing good target detections, and thus the algorithm is expected to perform well.

Comparing the single channels range resolution performance numbers to the corresponding numbers for the algorithm using $\Delta f = 4MHz$ and $\Delta f = 8MHz$, $30.0m$ and $15.0m$ respectively, it is seen that the resolution is improved by a factor of 1.6 and 3.3. This means that the obtained half peak width (classic resolution) in this case is $15.0m$, and $7.5m$. All results are available in table 7.5 for the propeller aircraft of opportunity.

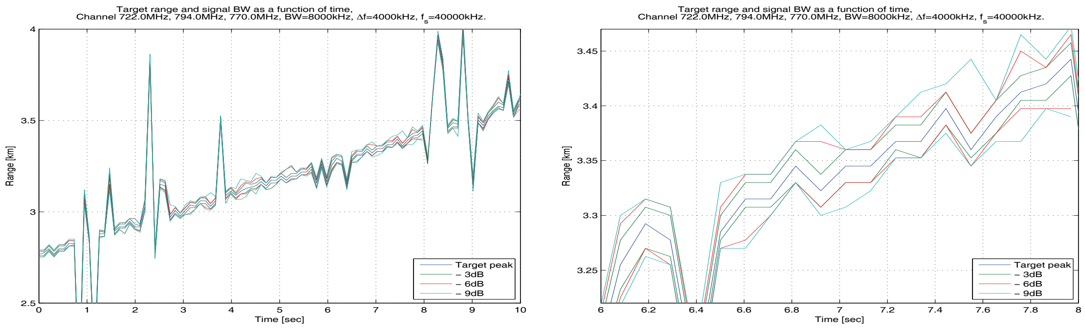

(a) $\Delta f = 4MHz$. (b) Zoom of figure (a).

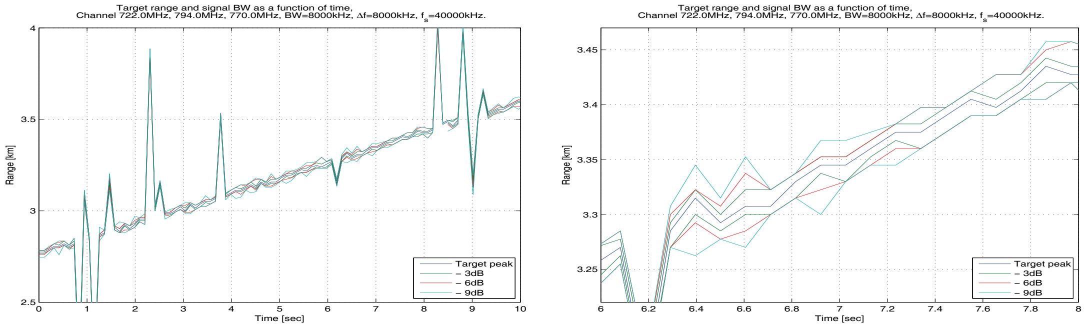

(c) $\Delta f = 8MHz$. (d) Zoom of figure (c).

Figure 7.17: Multiple channel detections for CPI=105ms, no phase fix.

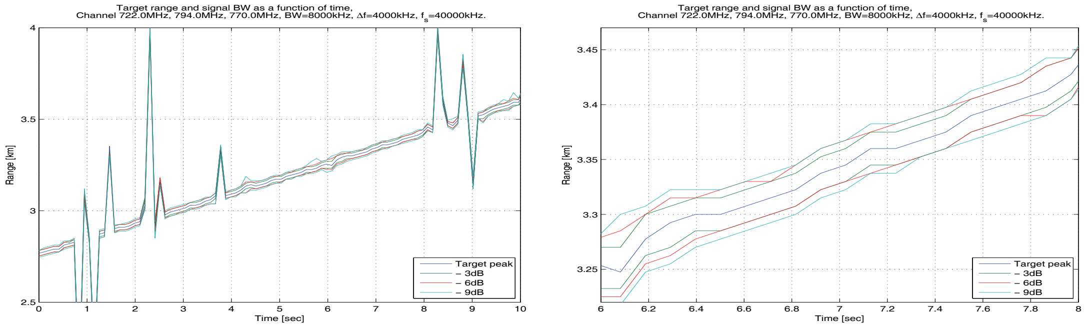

(a) $\Delta f = 4MHz$. (b) Zoom of figure (a).

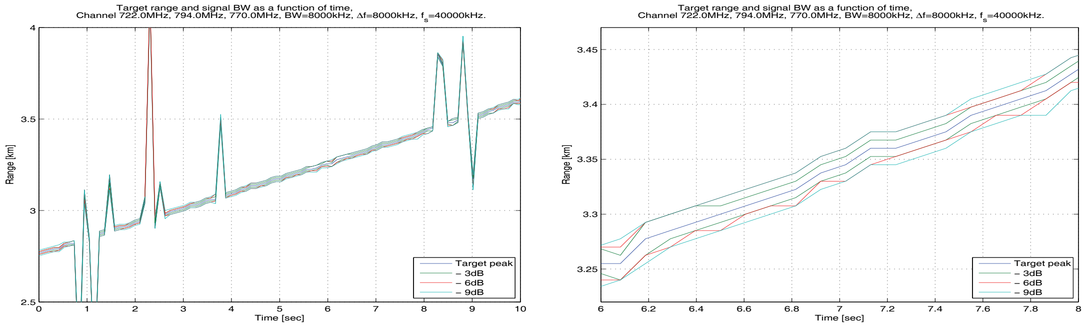

(c) $\Delta f = 8MHz$. (d) Zoom of figure (c).

Figure 7.18: Multiple channel detections for CPI=105ms, phase fix.

7.4 Range profile analysis

This section presents the range behavior of two different targets in (unfortunately) two different geometries for the DVB-T based PBR system. The system is exploiting multiple channels in two different geometries as described and analyzed in sections 7.2 and 7.3 as well as also producing the individual channels for each of the broadcasters. It is realized that further studies and systematic testing of the algorithm and its results are required before firm conclusions on real life HRR performance can be made. However, some observations made by simply testing the algorithm on the available real life data sets will be addressed. Further systematic data analysis is recommended on data of higher quality than what was acquired during the work with this thesis. Especially would different targets flying the same trajectories be of high interest, something this work did not find room for. Proper signal conditioning and adaptive filtering/direct path signal cancellation are also recommended before further testing is performed.

Comparing tables 7.4 and 7.5, it might be concluded that there is no reason to follow up on the HRR and ISAR capabilities for DVB-T based PBR. However, those tables are only considering the main scatterer's behavior and are not providing the deeper results present in the data.

Figure 7.19 shows an instant from the range-Doppler surface along the Doppler axis for both the airliner and propeller aircraft targets. Plots a-f show the individual channels target peak widths, while plots g-j show the performance of the coherently combined single channels. At first glance, these channels seem to behave very alike, and the results of sections 7.2-7.3, tables 7.4 and 7.5 did not indicate any noticeable differences. However a deeper analysis will reveal some interesting differences.

Looking at plots a-f it is noticed that for both targets the signal to noise ratio is equal to, or over $10dB$ for the two targets across their respective channels. For the airliner at channels $498MHz$, $690MHz$, and $746MHz$, the signal to noise levels are $15dB$, $18dB$, and $12dB$ respectively, while the corresponding numbers for the propeller aircraft for channels $722MHz$, $770MHz$, and $794MHz$, are $10dB$, $15dB$, and $13dB$. It is noted that the absolute level is slightly different, which really does not mean that much, since the primary interest are in the relative levels between signal and noise/interference floor. The individual channel's target peak responses are adjusted so that for both the airliner and the propeller aircraft, the target peaks are at $0dB$. The assumption is that the DVB-T waveform is sufficiently content independent, so the variations in performance are produced by the target. In addition to this it is believed that the geometry differences are countered by the fact that the two targets are so different, that they should be able to distinguish despite the differences in geometry. However, looking at the two geometries of figure 7.7 and 7.14, it is noted that in both cases the target is in the bistatic geometry north of and close to the receiver, and thus the two geometries might be considered to be similar, but not equal. The exercise may be considered a "proof of concept", as well as a necessary but not sufficient condition for target HRR analysis.

For the airliner, the main scatterer is seen to be at $16.25km$, and that in plot a, there

Table 7.6: Typical target parameters for the airliner in figure 6.11, and the propeller aircraft in figure 7.13. The numbers are from [18, 20].

Target type	Length	Wingspan	Height	Weight
Boeing 737 (300/400/500)	$31 - 37m$	$29m$	$11m$	$31 - 68$ tons
Cessna 172	$8m$	$11m$	$3m$	$0.8 - 1.1$ tons

is an indication of a second scatterer at $16.3km$, while this is not visible in plots c and e. However, in plots c and e, there are signs of a second scatterer at $16.12km$, and for plot e also a third one at $16.16km$. By combining the single channels, plots g and i are produced for $\Delta f = 4MHz$, and $\Delta f = 8MHz$. For both of these, the main scatterer is clearly visible, and the target peak narrower as reported on in section 7.2. In plot g, the other scatterers in the individual channels are not clearly visible, but traces of the one at $16.16km$ might be seen, as well as modest peaks at $16.21km$ and $16.27km$, which might be sidelobes of the main peak. In plot i, all the described scatterers show up clearly as well as resolved.

The target peaks of the propeller aircraft, plots b, d, and f are all simpler, with no distinct peaks in addition to the main peak, except for the peak at $3.44km$ in plot f. This is $100m$ bistatic range from the main peak, in this geometry, close to $50m$, which definitely puts it outside the target as seen in table 7.6. For the combined plots, the main target peak is narrower as expected, while there is no signs of second scatterers activity, apart from the ambiguity sidelobes of plot j at $3.29km$ and $3.36km$. The latter two sidelobes coincides both in range and level relative the main target peak of plots i and j, and it is thus expected that they are waveform dependent, since that is the only common denominator here.

Equation (6.2) and also table 7.2 describes the ambiguity distance, and this is tabulated in table 7.7 in order to ease the interpretation of figure 7.20.

Figure 7.20 shows ten consecutive CPI=$105ms$ intervals, figure 7.19 being the first. It is dangerous to conclude on general performances based on CPI=$105ms$ of data, and thus figure 7.20 is intended to give an indications of the performance with time. The main target peak is put at zero distance as well as zero level, since both targets are moving and fluctuating, and thus constantly changing range and level. The plots are thresholded at $-20dB$, i.e. below main target peak.

In addition to the discussion from figure 7.19, figure 7.20 tells that the scatterers following the airliner at $-130m$ and $-90m$ relative to the main scatterer is relatively stable for $690MHz$, and $746MHz$, while they are not visible in plot a for $498MHz$. It should be noted that the vague contours of a not resolved weak scatterer in plot a for the $498MHz$ case might be seen. The main target peak seems to be wider when passing $-10dB$, and this indicates a second (or more) not resolved scatterers. The differences between the lowest, and the two highest frequencies are $192MHz$ and $248MHz$ while the difference between the two latter frequencies is only $56MHz$. Corresponding plots for the propeller aircraft, plots b, d, and f seems to be more consistent between themselves and the frequency differences are all below $72MHz$. There might be lots of other explanations for this, however, this is merely brought to the reader's attention.

It might be tempting to conclude that based on the geometry, figure 7.7, as well as the second scatterer at $100m/2 = 50m$ relative main scatterer, the length of the target being roughly $50m$, and thus it is an airliner. And the propeller aircrafts plots show no second scatterer, and thus the target is below $60m/2 = 30m$ in range. That might be correct in this case, but in general, the internal propagation of the targets are not known, and thus internal target multipath which results in delayed and multiple scatterers in the HRR plots could be expected. Meaning that if classification is to be performed based on this approach, all targets to be recognized should be tabulated, with lots of statistics for each, as functions of time, frequency and geometry. However, the difference in range resolution plots for the two targets are duly noted, and this seems promising.

From the corresponding plots of the combined processing, plots g-j, it can be seen that the algorithm suppresses scatterers that is not present in all individual channels. This is as expected, as the algorithm might be considered an averaging of contributions across frequency (different broadcasted channels) as well as across range. This is maybe most clearly visible in plots b and f for the propeller aircraft, where there exist scattered strong sidelobes varying in range as well as time up to levels of $-5dB$ with respect to main scatterer. These are suppressed in plots h and j, where corresponding numbers are around $-10dB$. Unfortunately, this effect works on real scatterers as well.

Figure 7.21 shows the averaged range-level plots of figure 7.20. Especially it is noted that the single channel propeller aircraft plots b, d, and f exhibits a single stable main peak. For the airliner, the situation is different. The main peak is accompanied by the peaks at $-90m$ and $-130m$ as described before. The first of these stands clearly out in the averaged case for the two upper frequencies $690MHz$ at $-11dB$ and $746MHz$ at $-10dB$, while not visible at all for the lower frequency $498MHz$. The second scatterer is visible for $746MHz$ only, but at $-8dB$.

By averaging the combined plots, it is seen that the target peak response from the propeller aircraft is largely approaching the performance of a single scatterer, section 7.1, and particularly figure 7.4a. For the airliner, it seems as the ambiguities from the main peak is showing up. But the interesting thing to notice is that they are only showing up roughly in accordance with the single channels scatterers, and better resolved. For the combined plots, g/i, the single channel scatterer at $-130m$ seems to be shifted slightly to (just below) $-150m$ at $-15dB/-16dB$, while the peak at $-90m$ remains at $-13dB/-12dB$. For the $\Delta f = 8MHz$ there is also a peak showing up at $-120m$ at $-13dB$, which at first glance might be an ambiguity, but it might as well also be the resolving of two close scatterers, as seen in plot e, which as in section 7.1.3 may result in a slight ranging error. And then there is the potential hidden scatterer in the main peak for plot a for $498MHz$.

In the investigations of the ambiguities, they always seemed to be symmetric around the main target peak, but this might be a result of simulations artifacts due to the extreme similar (the same) signal applied in section 7.1. Comparing plots g, i and h, j, it is seen

Table 7.7: Relative ambiguity distance based on equation (6.2) for a main target scatterer at $0m$ for $N = 3$.

$\Delta f = 4MHz$	$0m$		$\pm 75.0m$		$\pm 150.0m$
$\Delta f = 8MHz$	$0m$	$\pm 37.5m$	$\pm 75.0m$	$\pm 112.5m$	$\pm 150.0m$

that the right side of the main scatterer, i.e. all positive ranges, may be considered target independent. The plots are practically equal for the positive ranges. The same peaks are visible, and at roughly the same level, i.e. $\pm 1dB$. The main difference between plots g, i and h, j lies to the left of the main scatterer, i.e. negative ranges with respect to the main peak. For the airliner there are multiple scatterers present, which is not present for the propeller aircraft. In addition to this, all scatterers are better resolved compared to the individual channels, while slightly suppressed due to the fact that they are not present and of equal strength in all the combined channels.

In summary, it might be speculated in all directions with all sorts of plausible conclusions on what the various peaks of the plots are. However, until controlled experiments with a properly tuned algorithm as well as better hardware may be carried out, it should be concluded that there is good reasons to believe that the two target responses presented here are different enough so that there is reasons for further investigations on the topic of NCTR with this algorithm. It should also be stated that the assumption that the two targets responds sufficiently different in the signal processing to be categorized correctly in a future manual PBR NCTR mode, i.e. a zoom display for an operator, has been supported.

Further, the mathematics of chapter 5 showed that once the high range resolution is in place, the ISAR image formation should be readily available under the constraint that sufficient target maneuvering is available, which not at all might be the case for these frequencies, see figure 7.8.

It seems that the algorithm will work best if the target is responding equally on the applied frequencies, which calls for as adjacent broadcasted channels as possible. This is not surprisingly, and also supported by the mathematics of chapter 5. In order for the algorithm to meet these prospects further testing and tuning of the algorithm is necessary, in order to make sure ambiguities can be separated from real target scatterers. It is also recommended to include adaptive filtering in order to suppress the direct path signal.

The work has demonstrated that the DVB-T PBR system seems to produce range plots of different character for two different targets, despite different geometries and broadcasted channel's carrier frequencies. The results had to be averaged over multiple CPIs (10 CPIs, each of $105ms$) in order to be trusted with respect to stability. The range responses for an airliner of opportunity as well as a propeller aircraft were studied. This is two very different targets, table 7.6, and the idea was to make a proof of concept study, in which differences due to the targets, and not the waveform, carrier frequencies, nor the geometry was demonstrated. The research in this thesis shows that this has been achieved.

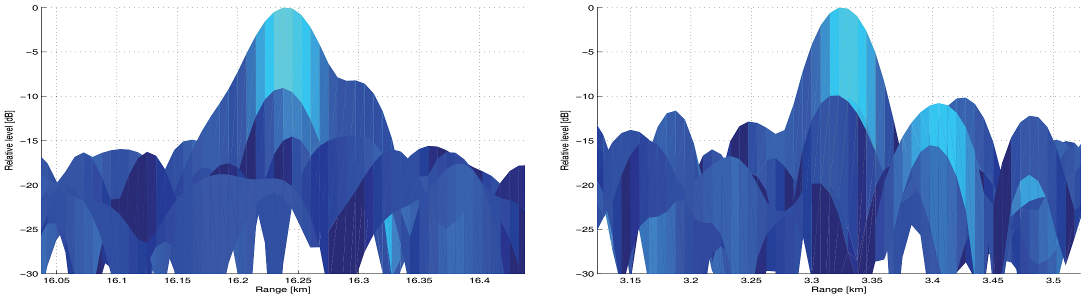

(a) $f = 498MHz$, airliner. (b) $f = 722MHz$, propeller aircraft.

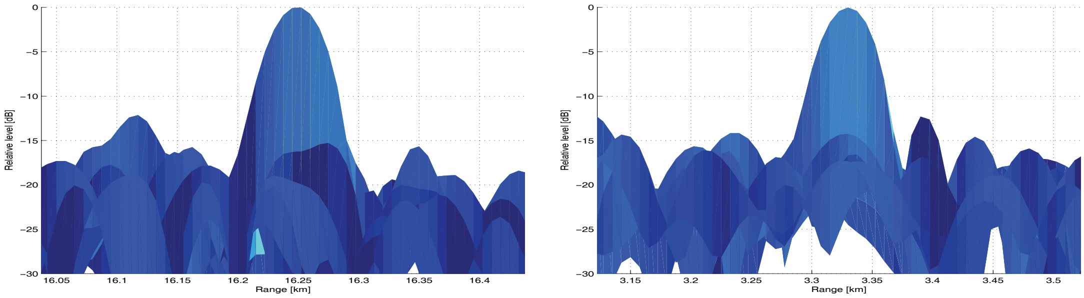

(c) $f = 690MHz$, airliner. (d) $f = 770MHz$, propeller aircraft.

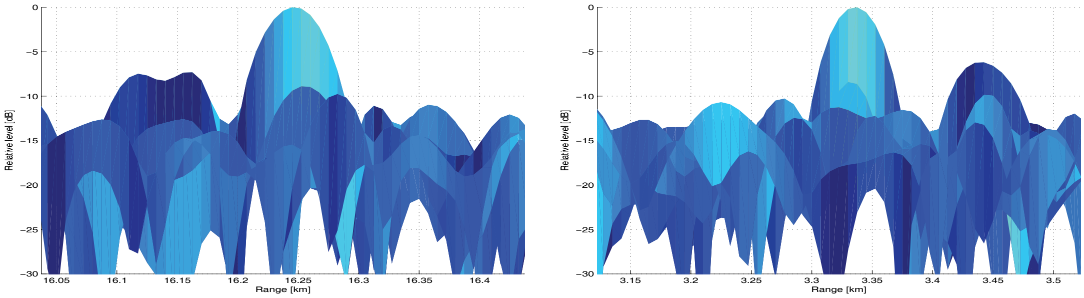

(e) $f = 746MHz$, airliner. (f) $f = 794MHz$, propeller aircraft.

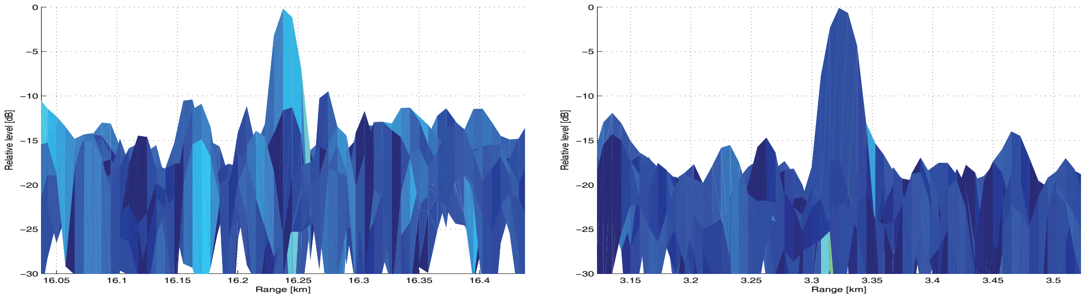

(g) All, $\Delta f = 4MHz$, airliner. (h) All, $\Delta f = 4MHz$, propeller aircraft.

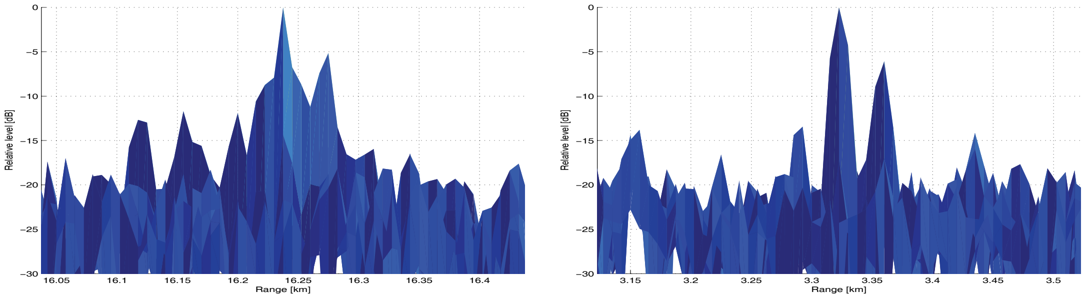

(i) All, $\Delta f = 8MHz$, airliner. (j) All, $\Delta f = 8MHz$, propeller aircraft.

Figure 7.19: Instant of the range view detection of airliner and propeller aircraft from sections 7.2 and 7.3. (a-f): Single channel detections, (g-j): Coherently combined single channel's detections.

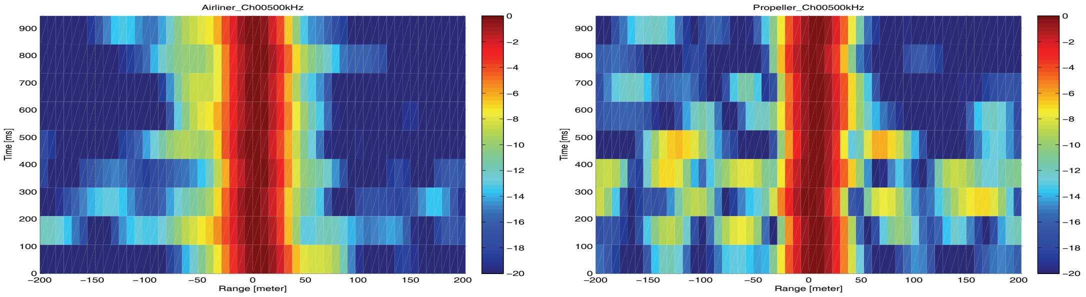

(a) $f = 498MHz$, airliner. (b) $f = 722MHz$, propeller aircraft.

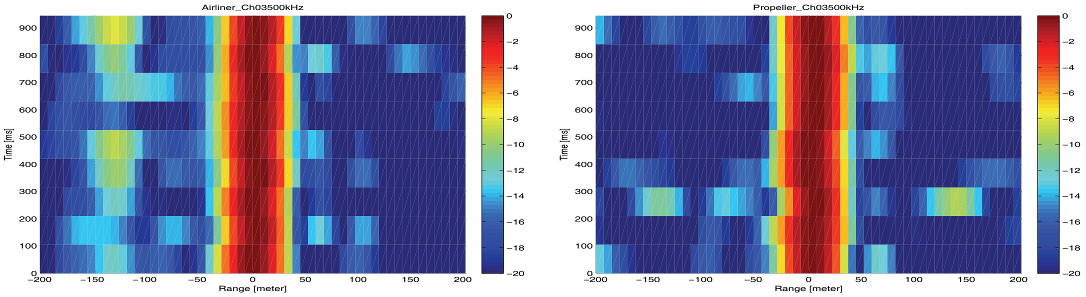

(c) $f = 690MHz$, airliner. (d) $f = 770MHz$, propeller aircraft.

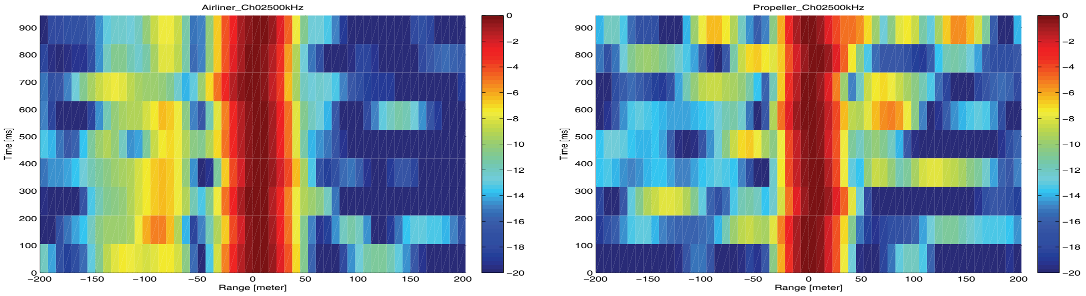

(e) $f = 746MHz$, airliner. (f) $f = 794MHz$, propeller aircraft.

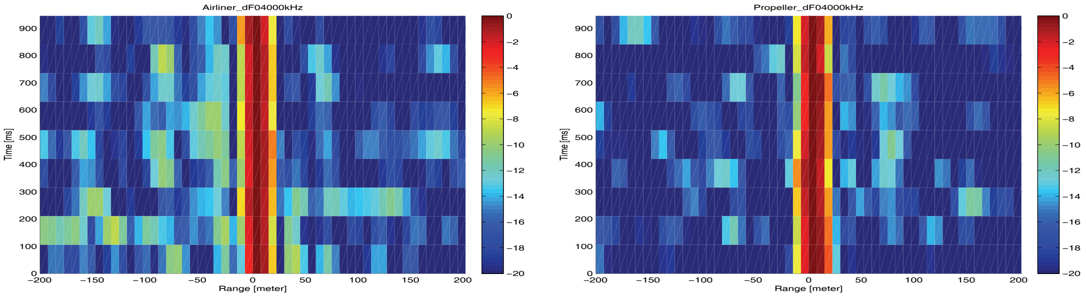

(g) All, $\Delta f = 4MHz$, airliner. (h) All, $\Delta f = 4MHz$, propeller aircraft.

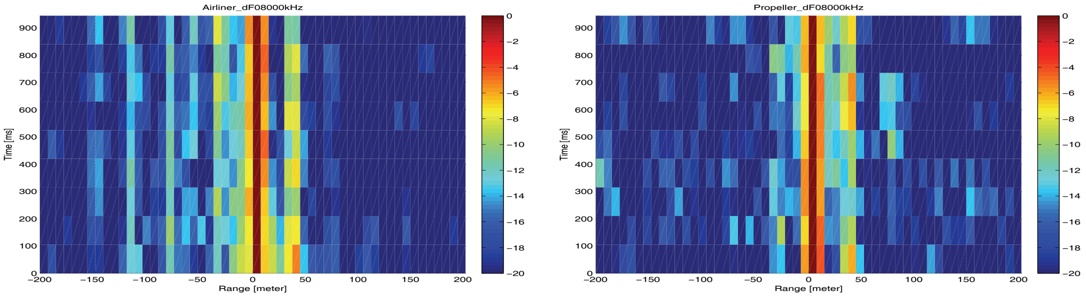

(i) All, $\Delta f = 8MHz$, airliner. (j) All, $\Delta f = 8MHz$, propeller aircraft.

Figure 7.20: One second of range view detection of airliner and propeller aircraft from sections 7.2 and 7.3. (a-f): Single channel detections, (g-j): Combined single channel's detections.

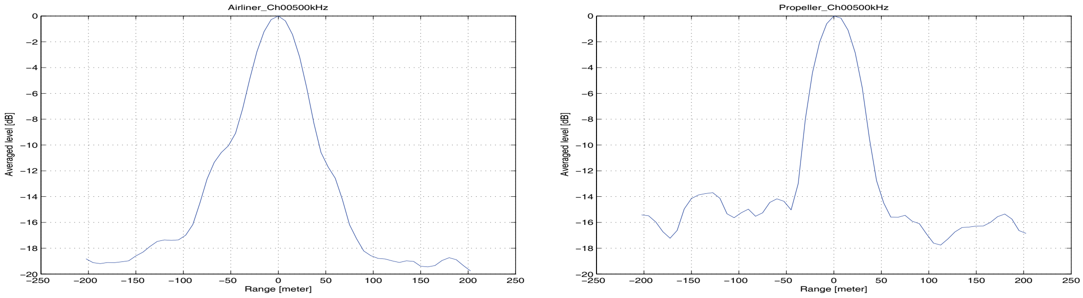

(a) $f = 498MHz$, airliner. (b) $f = 722MHz$, propeller aircraft.

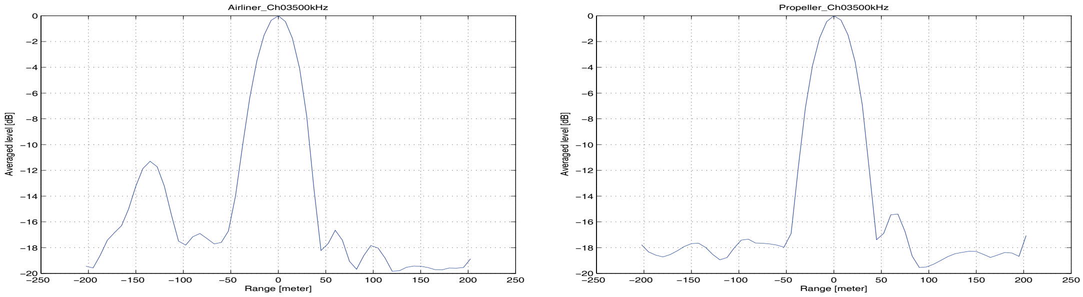

(c) $f = 690MHz$, airliner. (d) $f = 770MHz$, propeller aircraft.

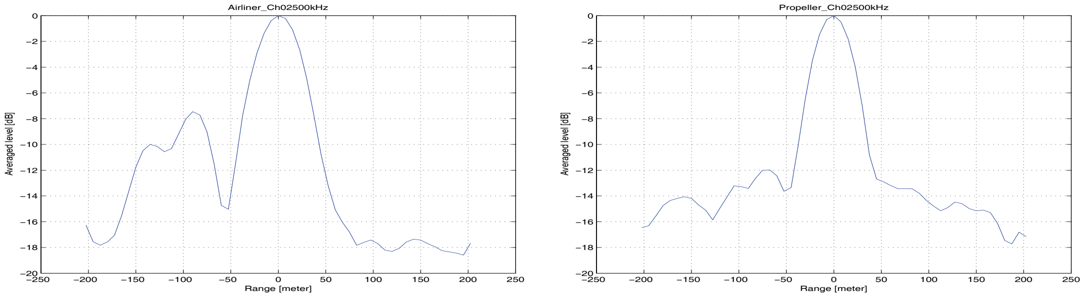

(e) $f = 746MHz$, airliner. (f) $f = 794MHz$, propeller aircraft.

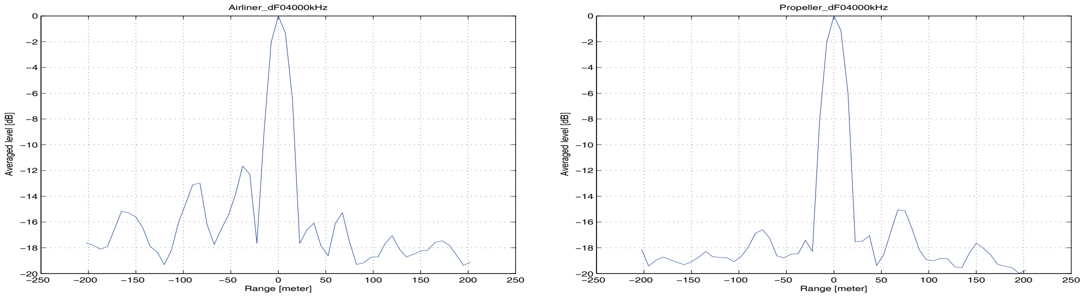

(g) All, $\Delta f = 4MHz$, airliner. (h) All, $\Delta f = 4MHz$, propeller aircraft.

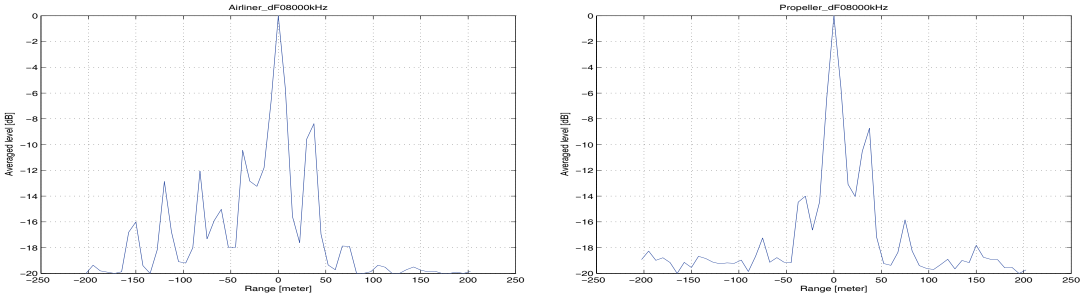

(i) All, $\Delta f = 8MHz$, airliner. (j) All, $\Delta f = 8MHz$, propeller aircraft.

Figure 7.21: Averaged plots of the one second of range view detection of airliner and propeller aircraft from figure 7.20. (a-f): Single channel detections, (g-j): Combined single channel's detections.

7.5 Summary

Results from simulations of the DVB-T waveform's behavior and performance by using strong recorded broadcasted signals from a nearby broadcaster have been presented.

By exploiting multiple broadcasted channels the simulations show that the single point scatterer resolution is improved from $45m/60m/75m$ for the $-3dB/-6dB/-9dB$ single channels target peak widths to $30m/30m/45m$ for the $\Delta f = 4MHz$ case, and $15m/30m/30m$, for the $\Delta f = 8MHz$ case. All results are tabulated in table 7.3.

It is also shown that that the combination of multiple DVB-T channels in the range correlation improves on the PBR systems capabilities to resolve nearby scatterers. The research under this thesis improved the resolution capabilities from around $60m$ to $30m/23m$ for the $\Delta f = 4MHz/\Delta f = 8MHz$ by using three DVB-T channels in the range correlation with varying frequency spacing. The theoretical range performance of the algorithm is summarized in table 7.2. By using overlapping/adjacent frequency down converted bands $\Delta f < B/2$, some of the ambiguities in the range correlation were avoided, while by allowing frequency gaps, $\Delta f > B/2$, ambiguities which may complicate the picture were introduced. How to properly tune this will be the radar designer's choice to make once the application has been decided.

By studying two cases of real target data it was shown that the phase correction presented in chapter 5, and also verified in chapter 6, is important also for the coherent combination of multiple DVB-T bands. The stability of the real targets trajectories were shown to be strongly improved.

The Kongsvinger broadcaster were broadcasting three DVB-T channels at $498MHz$, $690MHz$, and $746MHz$ and all channels were exploited in the case of an airliner target of opportunity, as seen in figure 6.11. Table 7.4 shows each of these three channel's target peak widths for $-3dB/-6dB/-9dB$ averaged over 4 seconds of high quality detection data. The $-3dB$ target peak width is $51.7m$, $48.4m$, and $53.4m$ for the three channels, yielding an averaged single channel performance of $51.3m$. Comparing this to the corresponding numbers for the algorithm for $\Delta f = 4MHz$ and $\Delta f = 8MHz$, $30.2m$ and $15.0m$ respectively, the resolution is improved by a factor of 1.7 and 3.4. This means that the obtained half peak width (classic resolution) in this case is $15.1m$, and $7.5m$. All results are available in table 7.4 for the airliner of opportunity.

Similarly, for an propeller aircraft of opportunity the target response for $-3dB/$, $-6dB$, and $-9dB$ peak widths were averaged. The broadcaster of opportunity were Tryvasshoegda, transmitting channels $722MHz$, $770MHz$, and $794MHz$, which resulted in $-3dB$ peak widths of $49.3m$, $48.9m$, and $49.3m$ respectively, yielding an overall channel average of $49.2m$. Comparing the single channels range resolution performance numbers to the corresponding numbers for the algorithm using $\Delta f = 4MHz$ and $\Delta f = 8MHz$, $30.0m$ and $15.0m$ respectively, the resolution is improved by a factor of 1.6 and 3.3. This means that the obtained half peak width (classic resolution) in this case is $15.0m$, and $7.5m$. Full results are available in table 7.5 for the propeller aircraft of opportunity.

Comparing tables 7.4 and 7.5, there seems to be no reason to follow up on the HRR and

ISAR capabilities for DVB-T based PBR, as the performances are very similar. However, a deeper look at the results proved otherwise, and it was shown that the two targets responses are sufficiently different in order to follow up with work on PBR NCTR aspects. It was obviously not possible to pinpoint scatterers on the two targets in the HRR plots produced since this was an uncontrolled experiment, and the speculations might go in all directions with all sorts of plausible conclusions on what the various peaks in the plots were. However, until controlled experiments with a properly tuned algorithm as well as better hardware may be carried out, there is reason to conclude that the two target responses presented are different enough so that there are reasons for further investigations on the topic of NCTR with this algorithm. This research has provided support of the claim that the two targets respond sufficiently different in the signal processing to be categorized correctly in a future manual PBR NCTR mode. This may be implemented as simple as a zoom display for an operator in first instance.

Further, the mathematics of chapter 5 showed that once the high range resolution is in place, the ISAR image formation should be readily available under the constraint that sufficient target maneuvering is available, which not at all is the case for these frequencies, see figure 7.8.

The algorithm will work best if the target is responding equally on the applied frequencies, which calls for as adjacent broadcasted channels as possible. This is not surprisingly, and also supported by the mathematics of chapter 5. In order for the algorithm to meet these prospects further testing a tuning of the algorithm is necessary, in order to make sure ambiguities can be separated from real target scatterers. It is also recommended to include adaptive filtering in order to suppress the direct path signal.

It has been shown that the DVB-T PBR system produces range plots of different character for two different targets, despite different geometries and broadcasted channel's carrier frequencies. The results had to be averaged over multiple CPIs (10 CPIs, each of $105ms$) in order to be trusted with respect to stability, and the range response for an airliner and a propeller aircraft of opportunity were studied. This is two very different targets, table 7.6, and the idea was to make a proof of concept study, in which the differences due to the targets were shown, and not the waveform, carrier frequencies, nor the geometry. The research conducted under this thesis has provided support for that.

Chapter 8

Conclusions and Future Work

In this chapter the main contributions and achievements of the work are summarized. The algorithm development and key results are summarized along with suggestions for further work.

The work has been based on the premise that exploitation of the available (frequency scattered) bandwidth broadcasted from single FM radio and DVB-T transmitter towers may be achieved by coherently combining each of the individual channels/bands in order to improve the range resolution. This thesis supports that claim, and it was shown that higher target range resolution is achieved for both FM radio and DVB-T waveforms of opportunity. In addition to this, for the DVB-T waveform, simple examples of PBR HRR were performed. The aim of the thesis has been to develop the foundations for an PBR operator zoom function in order to make her/him able to decide whether there are one, two or more targets present in the scene (FM radio and DVB-T), or classify targets (DVB-T).

The work started with simple performance predictions for various strong transmitters of opportunity in the southeastern parts of Norway, in particular around Oslo. It was shown that target detections and real life data recording should be possible for ranges of interest to the research. The data recording equipment was designed, produced and made working, and which was used to record the full FM radio band, as well as up to four non-adjacent DVB-T channels of choice for both reference and surveillance channel. Normally 10-20 minutes recording time was used, and all datasets were analyzed. In parallel, the mathematics was developed and an algorithm for coherently combining the non-adjacent single channels/bands was implemented. The performance of the algorithm was supported by theoretical simulations using pseudo random generated signals, as well as simulations using real recorded FM radio and DVB-T signals from nearby strong transmitters. Finally, the algorithm's performance was also supported by real data analysis of targets of opportunity for both FM radio and DVB-T PBR. In the DVB-T case, simple analysis of HRR profiles for two different targets of opportunity were included: An airliner and a propeller aircraft, which is claimed behaved differently enough for an operator to classify them as targets of different type.

8.1 Contributions and conclusions

The major contributions of this thesis may be divided into the following parts: Hardware design and development, algorithm development, simulations, real target data analysis, and finally NCTR and HRR considerations. Each of them are summarized below.

8.1.1 Hardware design and development

The author has been supervising the top level design and ideas of the equipment (testing, functions, performance, dealing with the priorities, as well as finding the financing), but the credit for the technical as well as the practical solutions should be forwarded to the engineers at FFI, especially Steinar Johnsrud and Per Sørnes who also designed the analog frontend for the DVB-T recordings. The author also recognizes the work performed by Jonas M. Christiansen, who has been managing the SW installations and SW upgrades from the various manufacturers of the different subsystems. All SW for the testing of the equipment, and supporting and organizing the data analysis of this thesis has been the work of the undersigned.

The driving motivation behind the data recording equipment was to be able to record both FM radio and DVB-T PBR target datasets of such a quality that data analysis of longer time segments, i.e. tens of minutes could be analyzed continuously. The data recording was achieved, although this thesis presents datasets limited to ten seconds of continuous data. The research required that the whole FM band, as well as up to four non-adjacent DVB-T channels of choice, each of maximum $8MHz$ bandwidth, for both reference and surveillance channel should be recorded. All requirements were met by the equipment.

An analog DVB-T frontend named DQD2 was designed and manufactured at FFI. DQD2 down modulates up to four DVB-T channels ($8MHz$ wide) of choice to the SAGAX servers bandwidth, real sampling $80MHz$, both reference and surveillance channels. The SAGAX servers were equipped with a filtered analog FM radio channel, in which the servers sampled the entire FM band directly. Thus, it was possible to record data according to the fundamental idea of the thesis as illustrated in figures 4.8 and 5.1.

Analysis of the data recording equipment showed that the system is not of the highest quality, but should be working for this thesis' purpose, as long as the identified spurious signals and problem areas of table 4.6 are taken into account. This interference was identified to come from within the data recording system as well as from nearby transmissions. Unidentified transmissions in the DVB-T regulated bands were found, even if they were not supposed to be there according to channel plans. It is believed that they come from test transmissions somewhere, however the undersigned was not able to find or get confirmation of any such activity. In order to quantify the effect of adjacent channel transmissions, tests in order to detect folding into, and cross talk from, adjacent channels were performed, but no traces of such behavior were found.

The data recording equipment was found suitable for the purpose of this research. Performance estimates as well as practical tests with the equipment showed that for the strong multichannel broadcasters of opportunity in the Oslo region, figure 4.1, one FM radio and two DVB-T PBR geometries worked for real targets data recording: Holtberget (FM radio), Kongsvinger (DVB-T), and Tryvasshoegda (DVB-T).

8.1.2 Algorithm development

A mathematical processing scheme was developed. The scheme was inspired by the high range resolution approaches used in HRR radar systems [46]. The algorithm exploits multiple non-adjacent broadcasted channels/bands in the PBR range correlation in order to improve the range resolution, while maintaining the Doppler resolution from the relatively long integration times. The broadcasted channels/bands are assumed to be from a single transmitter in order to obtain a single bistatic geometry as in figure 3.2. The following problems were addressed and solved:

- By using broadcasted signals at different carrier frequencies, the target Doppler shift will be different, and the proposed method takes this into account.
- By using time varying waveforms (signals of opportunity, i.e. FM, DAB, DVB-T, or pseudo noise) in the range correlation, a time varying result is achieved. If this becomes an issue, it should be countered by increasing the range correlation time. This might be achieved either by increasing the total CPI, or by keeping the CPI constant and reducing the Doppler resolution.
- By combining multiple bands coherently, co-channel correlation as well as cross-channel correlation is made. Only the former is of interest, and it was shown that the cross terms may be neglected due to their correlation properties with respect to each other. This is also helped by the fact that they contain a destructive frequency component from the de-modulation.
- Even though good individual correlation performances are achieved for single channels/bands, summing the correlation contributions for the different channels/bands might cause an out of phase summation which will modulate the range correlation peak in a way that may cause erroneous range estimates to be made. The algorithm estimates a phase correction term that once applied make all contributions in phase, and thus the erroneous range estimates, as well as destructive summing of target responses, are avoided.

The method's performance was simulated by using pseudo random generated noise signals with FM radio and DVB-T like parameters. The pseudo random noise signals were chosen in order to some extent use a predictable code in the ”theoretical” verification of the algorithm. The FM radio waveform is highly time varying, and the DVB-T signal contains deterministic components that results in predictable ambiguities [23, pp. 315-338]. In order to mitigate these signal specific effects in the performance presentation of the algorithm, a pseudo random noise signal which behaved predictable and controllable was generated.

In summary, an algorithm for the simultaneous exploitation of multiple non-adjacent broadcasted channels/bands in the PBR range correlation in order to improve the range resolution, while maintaining the Doppler resolution from the relatively long integration times has been mathematically presented. The algorithm has also been tested on simulated noise signals. This work forms the theoretical foundation for developing high range resolution analysis as well as ISAR imaging capabilities in the PBR systems under consideration.

8.1.3 Simulations

Simulations based on real life FM radio waveforms showed that the algorithm is capable of improving range resolution according to theory for single scatterers as is summarized in table 6.4. The performance of the algorithm was impacted by the fluctuating behavior of the FM radio signal, although less than expected. The simulations also showed that two targets not resolved in the individual channels, are resolved by using the proposed algorithm properly. Single scatterer targets are significantly better positioned by the improved resolution capabilities, i.e. ten times of the best performing individual channel.

The algorithm's performance with the DVB-T waveform was more predictable, and all simulation results are tabulated in table 7.3. The simulations showed that for the DVB-T waveform, single scatterer targets will be up to three times more accurately positioned by the increased range resolution algorithm, $-3dB$ target peak width down to $15m$ ($7.5m$ equivalent monostatic range resolution) compared to single channel range processing, target $-3dB$ peak width of $45m$ ($22.5m$ equivalent monostatic range resolution), for the three DVB-T channels in this example.

Considering multiple targets and/or multiple scatterer targets, the simulations showed that the DVB-T waveform and current processing algorithms offers target separation, i.e. bistatic target peak widths of around $60m$. The two examples provided in this thesis showed target resolution capabilities of $30m$ and $23m$. By using the monostatic equivalent range resolution the numbers corresponds to $30m$ improved down to $15m$ and $11.5m$, meaning targets separated by around $10m$ distance will be resolved in *range*, before Doppler separation is considered.

8.1.4 Real target data analysis

For the FM radio waveform, only airliners of opportunity were recorded, and all targets analyzed behaved like single scatterer targets. The full results of the range resolution improvement are available in table 6.5. The range resolution on target position was for the FM radio waveform significantly improved from around $6-8km$ bistatic range, down to $750m$ for the highest synthesized bandwidth applied, but this can further improved by using more channels of opportunity as well as fine tuning the algorithm.

For the DVB-T waveform, two types of targets of opportunity were recorded and analyzed, and the airliner behaved like a multiple scatterer target, while the propeller aircraft behaved like a single scatterer target. However, the main scatterer of both targets behaved consistently with respect to each other, and full results of the range resolution are available in tables 7.4 and 7.5. The simulation findings were supported in terms of resolution, and the target's $-3dB$ bistatic range peak width is improved from around $50m$ down to $15m$ for the highest performing set of parameters.

8.1.5 NCTR and HRR considerations

The DVB-T offers single channel bandwidth which is of the order of $30m$ monostatic range resolution. For air targets, this is a range resolution which offers 1-2 range cells on the largest targets, and very good range resolution for target detection and tracking. Thus, the resolution may be claimed to be between applications. Apart from recent work, [66, 67, 73] where some of it [66, 67] was partly supported by this thesis' in terms of providing target data recordings, no efforts on improving the range resolution has been found.

Inspired by the high range resolution achievements of section 7.1, the airliner's and the propeller aircraft's PBR range profiles were analyzed in greater detail. The two targets were shown to behave sufficiently different in the signal processing to be categorized correctly as two targets of different type. The airliner's main scatterer was accompanied by other weaker frequency dependent scatterers already in the single channels range-Doppler plots. However by applying the proposed algorithm, finer details of the scatterers were revealed.

In a future manual system, the HRR capability may be realized as simple as a target zoom display for an operator.

8.1.6 Conclusions

PBR of today is mimicking monostatic radar. And compared to monostatic radar, it is a very complex radar. The deployment is not straightforward, despite the advantage of no required frequency allocations. There is a requirement of sufficient distance and spreading of transmitters with respect to the scene. For the FM radio PBR the program content is also an issue. In principle, the undersigned claims that current PBR systems have shown that the technology works, now it is time for the technology to take advantage of the benefits of being PBR. I.e. the emergence of the next generation PBR systems with additional capabilities with respect to current PBR systems and monostatic radars.

[43] suggests that PBR tracking down to one transmitter is achievable, as is indirectly supported by [26] for the DVB-T case. Single transmitter tracking will drastically improve PBR performance. Single transmitter tracking will be made robust by considering using all broadcasted frequencies from a tower. [38, 39] showed that the detection performance is improved by using several FM radio channels for detection, as frequency diversity is achieved as well as a robustness against the bandwidth fluctuations arising from the combination of the FM radio modulation technique and the time varying program content.

The findings of this thesis will add nicely to the capabilities of the multi frequency PBR capable of single transmitter tracking. The improved range resolution may aid the deghosting process by making the range ellipsoids narrower, and thus resolving ghost targets, which emerge from the wide range resolution's overlapping of intersections as is illustrated in [22, pp. 164, figure 6.40]. The PBR tracking process might also be aided since the finer range resolution may provide better information of target maneuvering. The improved target resolution may better resolve the number of close targets, and for the DVB-T system it has been shown that target classification may be possible. All this may also be incorporated in today's systems since the proposed algorithm is adapted to the signal processing algorithms already in place, and thus no major mathematical reformulation should be needed.

Novel contributions of the HW work includes: The design and testing of special HW for data collection. To our knowledge, such a system capable of recording high bandwidth, real sampling $80MHz$, PBR synchronized reference and surveillance channel data for longer periods, i.e. hours, has not been found/seen elsewhere.

Novel contributions in algorithm development includes: A general mathematical algorithm was developed from scratch inspired by the high range resolution radar approach, where the radar designers are allowed to avoid problems since they control the transmitter. The fundamental ideas of HRR waveforms were rewritten and adapted to the PBR case. The algorithm was implemented and tested on synthetic data as well as real life recorded FM radio and DVB-T signals, mapping its theoretical performance. Further, the algorithm was applied on real life targets of opportunity and different types for both FM radio and DVB-T, the theoretical performance were supported by results from the real life performance analysis. This work has not been seen elsewhere.

Novel contribution to the NCTR and HRR topic includes: The improved range resolution was used to resolving targets to such a degree that target class separation is possible. This work analyzed target behavior for two different targets as a function of range, time and frequency. No work on PBR target analysis with classification in mind has been seen anywhere, neither on single channel nor multi channel.

A major goal of this research has been to put the theory to test in the real world in order to fully show that the proposed algorithm works as described. This work has fully closed the circle from idea, HW design, development, and testing, theoretical algorithm development and simulations, and finally real world performance analysis as well as target analysis.

8.2 Future work

Future work may be considered in one or more of the suggested areas:

The obvious area is further fine tuning of the algorithm. The work here has been focusing on making the algorithm work, and more important, proving that it does. However, there are many parameters to be tuned once an application is decided. The Δf is an important parameter for which briefly the behavior for the two waveforms has been tabulated. Further mapping of its importance as a function of its values would be of interest. This research has chosen Δf to be a fixed value, i.e. the same frequency difference between all channels/bands. Simple tests, as well as indications in [64] suggest that the ambiguities might be reduced by choosing Δf as an irregular value across frequency for one range correlation's CPI. For the FM radio case, the fine tuning of Δf as a function of actual available bandwidth should be investigated. The results [3] suggest that the range ambiguities may be traded for range resolution and vice versa, and the trade-offs should be investigated.

In this research, all available channels/band were included in the coherent processing in order to achieve as high range resolution as possible. This might not always be the optimum case. The HRR analysis in section 7.4 showed that the target is behaving different in different bands. This has not been studied in detail for the FM radio, were the initial survey did not come up with any differences. It might be of interest to only include bands/channels closer together in order to achieve stable target performance for the coherent combination of the channels/bands. For the DVB-T waveform, target responses were varying as a function of exploited frequency bands, and this was solved by equalizing the main target scatterer across frequency bands.

This work considered FM radio, DVB-T and to some extent pseudo random noise waveforms. Due to the poor coverage of the DAB network in Norway this broadcaster of opportunity was not included in the study. However, it would be nice to see the algorithm's performance for this waveform as well.

In a future system design, more stable and better estimation of Doppler, range, phases, as well as target detections should be applied. In this work, the average value from three/four target detection channels/bands for the target's range and Doppler was applied. This will be improved once proper target tracking and detection algorithms are used, and work is being performed on this topic [38]. However, the work demonstrated the importance of proper estimation of the phase term, equation (5.27). Depending on the target behavior, it is believed that the phase term to some extent should be predictable over several CPIs, and thus some sort of averaging or phase tracking over longer periods will make the phase estimation more robust. The phase term is target dependent, but by monitoring the relative difference between the available reference channels, information which may aid the estimation should be obtained.

The proposed algorithm may serve as a recipe for coherently adding target responses from multiple geographically separated transmitters, i.e. putting multiple geometries together. The algorithm corrects for Doppler shifts of unequal magnitude, as well as in principle a random phase contribution from the target, for signals coming from the same transmitter but non-adjacent channels/bands of non-equal frequency spacing. Section 6.1 deliberately distorted the phase of the surveillance channel randomly for each of the single channels, as well as successfully corrected for it again, thus mimicking random phase contribution as will be the case across geometries. The range and Doppler term should be readily available from single channel tracking, and thus accountable for. If successful, this would enable simultaneous coherent PBR multi perspective looks on the target.

By combining non-equal geometries, an understanding of the target's RCS behavior as a function of geometry as well as frequency will be important. This applies to all waveforms and bands, being FM radio, DAB, and DVB-T to mention the major broadcasted waveforms. It was shown that the method is susceptible to target frequency variations. However, the frequency spectrum is expected to be more and more crowded, and (close to) adjacent channels are expected to be broadcasted in the future. Nevertheless, information on bistatic target behavior as a function of frequency is of high interest.

In order to properly test the claim that PBR HRR and/or ISAR is achievable, systematic testing of various targets in order to make NCTR and/or ISAR images should be performed. This includes targets of different sizes and types. The trajectories/geometries should be kept as equal as possible, and some of these should include highly maneuvering targets. Mainly due to the non-maneuvering targets of opportunity, as well as the low frequencies for FM radio and DVB-T it was not possible to produce ISAR images of the targets. However, the presented simple HRR analysis serve as positive proofs of concept for the PBR HRR, and it is the undersigned's sincere hope that this work will be extended in the future.

Appendix A

Signal Processing Fundamentals

The geometry and parameters L, R_T, and R_R can be found in figure 3.2.

A.1 Signal model

This work is using the definition of point targets of [86, pp. 432]:

> *A point target is one occupying a space much smaller than the radar resolution cell. The concept of a point target is a convenient idealization having the following properties:*
>
> 1. *The locus of phase- (wave-)fronts is a sphere with its center at the target position.*
> 2. *The amplitude of the scattered electric field is uniform over the wave front.*
> 3. *The normal to the phase-front passes through the target*
>
> *The ideal point target is non-fluctuating and does not broaden the width or the spectrum of the radar transmitted pulse*

A.1.1 Single channel case

A broadcasted signal with carrier/center frequency f_c and initial phase ϕ_c,

$$U(t) = \Re\{u(t)e^{j2\pi(f_c t+\phi_c)}\}, \tag{A.1}$$

is received directly from the transmitter (no multipath - ideal, clear air propagation) at a distance L from the transmitter. When c is the speed of propagation, the phase has changed

$$\phi_L = f_c\frac{L}{c} = f_c t_L. \tag{A.2}$$

The received signal at the receiver site, transmitted from the transmitter t_L seconds earlier, may thus be written

$$U_{ref}(t) = U(t-t_L) = \Re\{\alpha_{ref}u_{ref}(t-t_L)e^{j2\pi(f_c t - f_c t_L + \phi_c)}\}. \tag{A.3}$$

The α is a parameter taking into account the amplitude attenuation, i.e. free space with the current assumptions, during propagation from the transmitter to the receiver.

Assuming the broadcasted signal (A.1) is also reflected from a point target with the properties described above, and received at the same receiver, traveling in total a distance of $R = R_T + R_R$, which means that

$$t_T + t_R = \frac{R_T}{c} + \frac{R_R}{c} \tag{A.4}$$

later, the signal is at the receiver, and has changed its phase accordingly in two subsequent steps,

$$\phi_T = f_c t_T, \tag{A.5}$$

before being reflected off the target, and by that inducing the Doppler shift f_D. From the target to the receiver the signal now propagates with the Doppler shifted frequency $f = f_c + f_D$, and thus the phase change from target to receiver will be

$$\phi_R = (f_c + f_D)\, t_R, \tag{A.6}$$

and the received signal at the receiver is in the form

$$U_{sur}(t) = \Re\{\alpha_{sur}u_{sur}(t - t_T - t_R)e^{j2\pi((f_c+f_D)t - f_c t_T - (f_c+f_D)t_R + \phi_c)}\}, \tag{A.7}$$

where α_{sur} is the free space propagation factor accounting for the propagation (and target reflection) transmitter-target-receiver. Zero range is defined to be at the receiver, which means that $t \rightarrow t + t_L$, hence (A.3) and (A.7) can be written

$$U_{ref}(t) = \Re\{\alpha_{ref}u_{ref}(t)e^{j2\pi(f_c t + \phi_c)}\}, \tag{A.8}$$

and

$$U_{sur}(t) = \Re\{\alpha_{sur}u_{sur}(t - \nu)e^{j2\pi((f_c+f_D)t - f_c\nu - (t_R - t_L)f_D + \phi_c)}\}, \tag{A.9}$$

where $\nu = t_T + t_R - t_L$, and this corresponds to the target iso-range from receiver $R = R_T + R_R - L$, which for the bistatic case is an ellipsoid with the transmitter and receiver in its focal points.

An expression for M targets can easily be achieved by considering this to be the sum of several single point targets (A.9),

$$U_{sur}(t) = \Re\{\sum_{m=0}^{M-1} \alpha_{sur}^{m} u_{sur}^{m}(t - \nu_m)e^{j2\pi\left((f_c+f_D^m)t - f_c\nu_m - (t_R - t_L)f_D^m + \phi_c\right)}\}. \tag{A.10}$$

Real life considerations

For real life situations, one may want to take into account that the amplitudes and phases of the received signals may change continuously, meaning that α is not a real positive number, but rather a time varying complex function $\alpha(t)$. $\alpha(t)$ is accounting for the potentially time varying target reflectivity in amplitude as well as phase, and for clear air effects like multipath, gaseous absorption, diffraction, and refraction, and non-clear air effects like precipitation and clouds. Multipath reflections might also be accounted for by assigning additional targets with amplitudes, phases, Doppler shifts, and delays ($\alpha(t)$, f_D^m, and ν_m).

Stationary, volume and moving clutter might be treated in the same way as multipath targets, by assigning them a delay, amplitude and phase shifts, as well as velocity through a Doppler shift. Interference, both in- and out-of-band, might be included as target(s) where there is relatively poor match between $u_{ref}(t)$ and $u_{sur}(t)$ as well as the frequency (mis-)match induced by f_D^m. At first glance it might seem unnecessary to keep the distinction between $u_{ref}(t)$ and $u_{sur}^m(t)$ as all scaling and phase shifts from the propagation in the terms $\alpha_{ref}(t)$ and $\alpha_{sur}^m(t)$ have been accounted for. However, one might face the situation where the different propagation paths transmitter-receiver and transmitter-target-receiver will affect the signals differently, i.e. polarization changes and/or differences. Hence the notation $u_{ref}^m(t)$ and $u_{sur}^m(t)$.

In addition to this, the work has not yet in principle considered the Doppler stretch/shift of the $u_{sur}^m(t)$ due to the target induced Doppler shift, which will result in differences between $u_{ref}(t)$ and $u_{sur}^m(t)$. However, this work will disregard this effect, as small bandwidths compared to the carrier frequencies are considered. The bandwidth B of a single FM radio channel is maximum $B \leq 100kHz$, while the carrier frequency $f_c \in [88MHz, 108MHz]$. For the Norwegian DVB-T case the bandwidth is $B < 8MHz$, while $f_c \in [470MHz, 790MHz]$.

This work will also disregard the target's acceleration. In order to incorporate the acceleration effect, strategies like in [130, 131] might be applied.

By taking all this into account, it can be shown that (A.8) and (A.10) take the forms

$$U_{ref}(t) = \Re\{\alpha_{ref}(t)u_{ref}(t)e^{j2\pi(f_c t+\phi_c)}\}, \tag{A.11}$$

and

$$U_{sur}(t) = \Re\{\sum_{m=0}^{M-1} \alpha_{sur}^m(t-\nu_m)u_{sur}^m(t-\nu_m)e^{j2\pi\left((f_c+f_D^m)t - f_c\nu_m - (t_R - t_L)f_D^m + \phi_c\right)}\}. \tag{A.12}$$

Euler's formula, $e^{jx} = \cos x + j\sin x$, yields $\Re\{\exp j2\pi(f_c t + \phi_c)\} = \cos(2\pi(f_c t + \phi_c))$. Received signals are normally down modulated and/or IQ-sampled by f_x. Thus, it can be shown that

$$\cos(2\pi(f_c t + \phi_c))e^{-j2\pi f_x t} = \frac{1}{2}\left[e^{j2\pi((f_c - f_x)t+\phi_c)} + e^{-j2\pi((f_c+f_x)t+\phi_c)}\right]. \tag{A.13}$$

By filtering the high frequency component in (A.13), $f = f_c + f_x$, the following expressions for the received and down modulated signals

$$U_{ref}(t) \approx \alpha_{ref}(t)u_{ref}(t)e^{j2\pi((f_c - f_{ref})t+\phi_c)}, \tag{A.14}$$

and

$$U_{sur}(t) \approx \sum_{m=0}^{M-1} \alpha_{sur}^{m}(t-\nu_m)u_{sur}^{m}(t-\nu_m)e^{j2\pi\left((f_c+f_D^m-f_{sur})t-f_c\nu_m-(t_R-t_L)f_D^m+\phi_c\right)} \tag{A.15}$$

are achieved. Strictly speaking, this appendix treats only analogue signals, i.e. are dealing with continuous functions and not discrete time sequences. However, completely similar arguments may be achieved also for the discrete case, and as long as the sampling criteria are obeyed, as well as the condition that the two frequency components of (A.13) are not overlapping, the results above applies.

In addition to this it should be noted that no essential information is lost in equations A.14 and A.15, since the Fourier theory tells that the Fourier transform (frequency spectrum) of a Riemann integrable real function (all functions considered in this thesis will be) on $[0, 2\pi]$

$$\hat{u}_k = \frac{1}{2\pi}\int_0^{2\pi} u(t)e^{-jkt}dt, \qquad \text{for } k = 0, \pm 1, \pm 2, \ldots, \tag{A.16}$$

will obey

$$\hat{u}_k = \hat{u}^*_{-k}, \qquad \text{for } k = 0, \pm 1, \pm 2, \ldots, \tag{A.17}$$

and thus the signal can be fully recreated by knowing one side of the spectra. Correspondingly for the real discrete time sequence (sampled signal), $u(t_i)$, $i = 0, 1, \ldots, N-1$ where $t_i = i/f_s$ and f_s is the real sampling frequency. It can be shown that the discrete Fourier spectrum

$$\tilde{u}_k = \frac{1}{N}\sum_{k=-N/2}^{N/2-1} u(t_i)e^{-jkt_i}, \qquad \text{for } k = -\frac{N}{2}, -\frac{N}{2}+1, \ldots, \frac{N}{2}-1, \tag{A.18}$$

will obey

$$\tilde{u}_k = \tilde{u}^*_{-k}, \qquad \text{for } k = -\frac{N}{2}, -\frac{N}{2}+1, \ldots, \frac{N}{2}-1, \tag{A.19}$$

and thus the signal can be fully recreated by knowing one side of the spectra, if $\tilde{u}-N/2 = 0$, which normally is a very good approximation due to the asymptotic properties of most real life signals [134].

Equations (A.14) and (A.15) are on the form on which this work is going to elaborate in chapters 3 and 5.

Appendix B

FM Radio Waveform Fundamentals

This appendix will highlight aspects of the FM radio modulation, bandwidth considerations from the communication world, as well as formulate a FM SW radio demodulation algorithm. The information here is mainly adapted from [21].

B.1 FM modulation

All information in this section is adapted from [21] unless otherwise stated. The FM wave may be described by

$$x(t) = A\cos\left(\omega_c t + \theta_0 + K'' \int_{t_0}^{t} s(\lambda) d\lambda\right), \tag{B.1}$$

where $\omega_c/(2\pi)$ is the frequency, θ_0 an initial phase, K'' is a constant with units of radians per volt-second, and $s(\lambda)$ is the information carrying signal. By choosing t_0 appropriately, one can cancel θ_0, and in the following assume that t_0 is chosen in a way such that θ_0 is canceled, leaving the instantaneous phase [21]

$$\theta(t) = \omega_c t + K'' \int_{t_0}^{t} s(\lambda) d\lambda. \tag{B.2}$$

The instantaneous frequency $f(t)$ is given by

$$f(t) = \frac{\dot{\theta}(t)}{2\pi} = f_c + \frac{K''}{2\pi} s(t), \qquad f_c \overset{\text{def}}{=} \frac{\omega_c}{2\pi} \tag{B.3}$$

A pure tone modulating signal

$$s(t) = A_m \cos(\omega_m t), \tag{B.4}$$

in (B.1)

$$x_{FM}(t) = A\cos\left(\omega_c t + \frac{A_m K''}{\omega_m} \sin(\omega_m t)\right). \tag{B.5}$$

The maximum frequency deviation from the frequency of the unmodulated carrier is

$$\Delta\omega = \left| \frac{d}{dt} \left(\frac{A_m K''}{\omega_m} \sin(\omega_m t) \right) \right|_{max} = A_m K'', \tag{B.6}$$

where the quantity $\Delta\omega$ or $\Delta f = \Delta\omega / 2\pi$ is called the frequency deviation [21]. The modulation index β is defined as the maximum phase difference between the FM wave and the unmodulated carrier,

$$\beta = \frac{\Delta\omega}{\omega_m} = \frac{\Delta f}{f_m}. \tag{B.7}$$

Using the notation from (B.6) and (B.7), equation (B.5) can be written [21]

$$x(t) = A \cos(\omega_c t + \beta \sin \omega_m t). \tag{B.8}$$

The Bessel-Jacobi identity [21],

$$e^{j\beta \sin(\omega_m t)} = \sum_{n=-\infty}^{\infty} J_n(\beta)\, e^{jn\omega_m t}, \tag{B.9}$$

where $J_n(\beta)$ is the nth-order Bessel function of the first kind, together with a multiplication of both sides by $\exp(j\omega_c t)$ and equating real and imaginary parts,

$$\cos(\omega_c t + \beta \sin \omega_m t) = \sum_{n=-\infty}^{\infty} J_n(\beta) \cos(\omega_c t + n\omega_m t), \tag{B.10}$$

and

$$\sin(\omega_c t + \beta \sin \omega_m t) = \sum_{n=-\infty}^{\infty} J_n(\beta) \sin(\omega_c t + n\omega_m t). \tag{B.11}$$

[21] shows that the modulation with a sinusoid results in a line spectrum with lines at $\omega_c \pm n\omega_m$, and with the height of the lines given by $J_n(\beta)$, figure B.1. The Bessel functions exhibits many properties [21, pp. 314] one of them being $J_n(\beta) \to 0$ for $n \gg \beta$, which determines the effective bandwidth of the modulated signal. This is true particularly for large n and β, where n need not be very much larger than β for J_n to become negligibly small, figure B.1. This property has the effect of limiting the number of lines in the line spectrum to something like 2β, that is β lines on either side of the carrier. The effective bandwidth of the FM spectrum is the number of significant lines multiplied by the frequency spacing between them, nf_m, $n = \pm 1, \pm 2, \ldots$ and if the significant number of lines is approximately equal to the modulation index, $n \approx \beta$, the bandwidth being approximately equal to [21]

$$\mathrm{BW} \approx 2\beta f_m = 2\Delta f, \tag{B.12}$$

that is twice the frequency deviation. This approximation is especially good for large β, that is Δf is considerably larger than f_m, meaning the carrier is swept slowly between $f_c - \Delta f$ and $f_c + \Delta f$. As a comparison, the Norwegian FM radio broadcast system is using modulation index $\beta = 5$, and frequency deviation $\Delta f = 75kHz$.

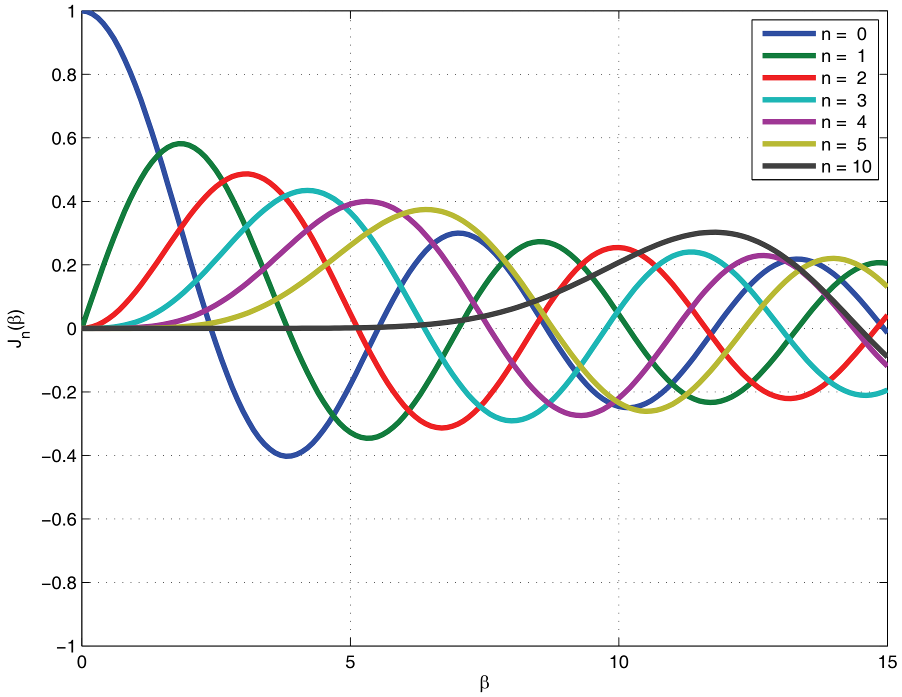

Figure B.1: Variations of $J_n(\beta)$ with β.

Consider a FM modulated signal where the modulating function consists of the summation of two sinusoidal tones [21],

$$x(t) = \cos\left(\omega_c t + \beta_1 \sin\omega_1 t + \beta_2 \sin\omega_2 t\right), \tag{B.13}$$

the resulting FM signal can be written [21]

$$\cos\left(\omega_c t + \beta_1 \sin\omega_1 t + \beta_2 \sin\omega_2 t\right) = \sum_{n=-\infty}^{\infty} \sum_{k=-\infty}^{\infty} J_n(\beta_1) J_k(\beta_2) \cos\left(\omega_c + n\omega_1 + k\omega_2\right) t. \tag{B.14}$$

When $\beta_1 = 0$, or $\beta_2 = 0$, the situation is as for a single modulating tone as described above. When $\beta_1 \neq 0$ and $\beta_2 \neq 0$, all possible frequency combinations of $\omega_c + n\omega_1 + k\omega_2$ are obtained. The new frequencies $n\omega_1 + k\omega_2$, where $n \neq 0$ and $k \neq 0$ clearly show the complexity of the FM modulation. A quick example will shed some light on the complexity. Consider the truncated version of (B.14),

$$\cos\left(\omega_c t + \beta_1 \sin\omega_1 t + \beta_2 \sin\omega_2 t\right) = \sum_{n=-N}^{N} \sum_{k=-K}^{K} J_n(\beta_1) J_k(\beta_2) \cos\left(\omega_c + n\omega_1 + k\omega_2\right) t. \tag{B.15}$$

Table B.1 lists the values parameters for (B.15), and the results are presented in figure B.2. The figure shows that when $\beta_2 = 0$ the frequency lines produced by β_1 are clustered around f_c, while the corresponding, $\beta_1 = 0$, lines from β_2 are more spread. The full two tone modulation results in the combination of the two individual spectra, as seen in figure B.2c.

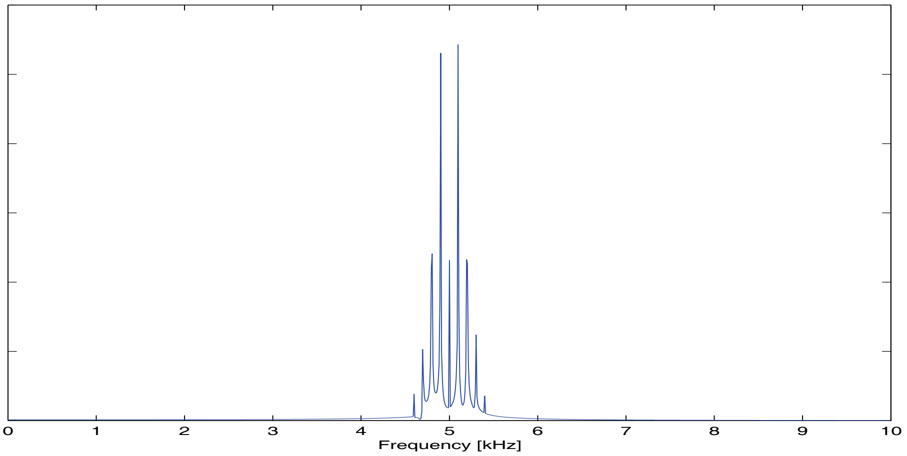

(a) $f_1 = 100Hz,\ \beta_1 = 2,\ \beta_2 = 0.$

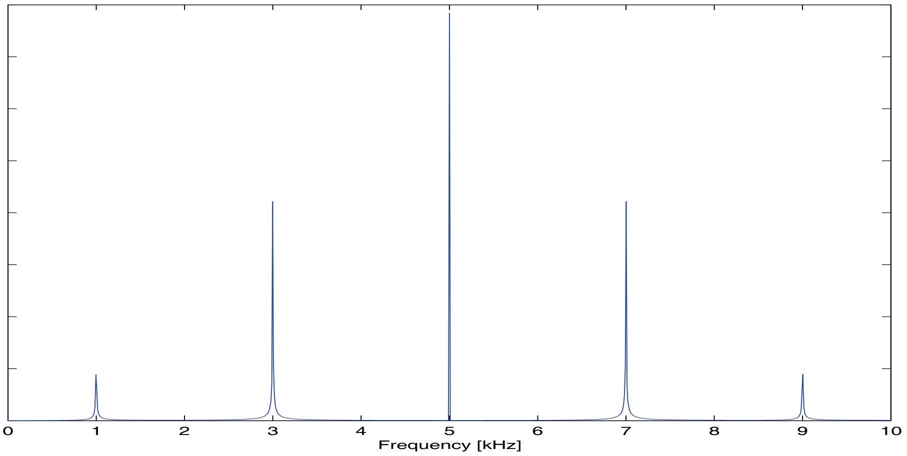

(b) $f_2 = 2000Hz,\ \beta_2 = 1,\ \beta_1 = 0.$

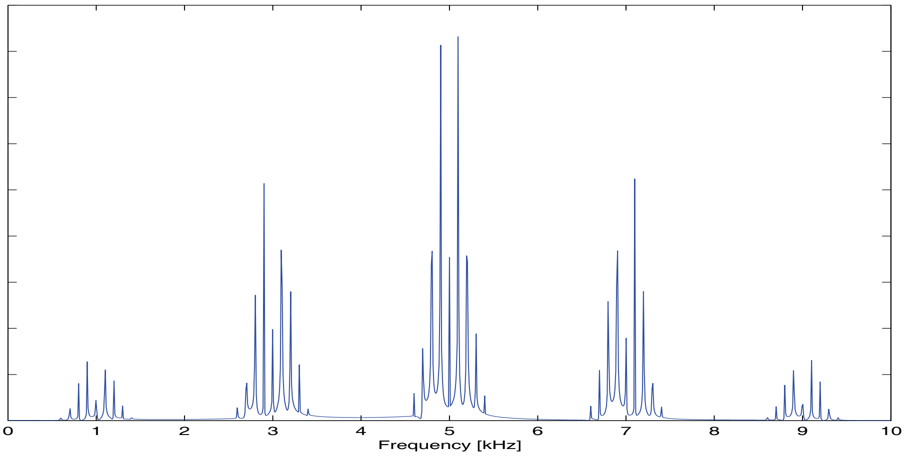

(c) $f_1 = 100Hz,\ \beta_1 = 2,\ f_2 = 2000Hz,\ \beta_2 = 1$

Figure B.2: Spectra of an FM wave generated by two modulating tones of frequency f_1 and f_2, (B.13). (a) The components due to f_1 are clustered around f_c. (b) The components due to f_2. (c) The FM wave generated by two modulating tones, parameters as in table B.1. The figure is adapted from [21].

Table B.1: Parameter values for equation (B.15).

f_c	f_1	β_1	N	f_2	β_2	K
$5000Hz$	$100Hz$	2	4	$2000Hz$	1	2

In conclusion, this section explains the $\pm 19kHz$ vertical lines in the left plots of figures 6.2a and b. All mathematics were adapted from [21].

B.2 Considerations of the FM signal bandwidth

This section will provide a short survey of the communications world's use of the word bandwidth. Carson's rule [135] gives an approximate value of the FM bandwidth of continuous modulating signals,

$$B_{CR} = 2\Delta f + 2f_m = 2f_m(1+\beta). \tag{B.16}$$

Carson's rule results in 98% of the signal energy to be within the bandwidth, i.e. $-17dB$ bandwidth in radar terms. A FM signal is considered to be Narrow Band FM (NBFM) if $\beta \ll 1$ and Wide Band FM (WBFM) otherwise, leading to the corresponding bandwidths estimates (B.16)

$$\begin{array}{lcll} B_{CR} & \backsimeq & 2f_m\beta = 2\Delta f, & \beta \gg 1 \text{ (WBFM)} \\ B_{CR} & \backsimeq & 2f_m, & \beta \ll 1 \text{ (NBFM)} \end{array} \tag{B.17}$$

For the cases when the rule $n > \beta$ equation (B.12) is not applicable another approach is needed. Carlson [136, pp. 240] suggested an approach where L is the largest integer, keeping β fixed where

$$|J_L(\beta)| \geq \epsilon, \qquad\qquad |J_{L+1}(\beta)| < \epsilon, \tag{B.18}$$

so that the significant sidebands is at least $100\epsilon\%$ of the amplitude of the unmodulated carrier. Then L depends on β and ϵ, and the required bandwidth is

$$B_\epsilon = 2L(\beta,\epsilon)f_m, \tag{B.19}$$

where numerical values of $L(\beta,\epsilon)$ can be found from tables and/or figures, i.e. [21, pp. 321]. Table B.2 gives examples of bandwidths estimated with equations (B.16) and (B.17) for various modulation frequencies and indexes and for the deviation $\Delta f = 75kHz$. $L(\beta,\epsilon)$ is estimated for the cases $\epsilon = 0.01$, and $\epsilon = 0.1$, that is the significant sidebands are 1% and 10% of the amplitude of the unmodulated carrier.

This short survey shows that the bandwidth term used in the communication world is motivated by providing sufficient spacing to adjacent signals in order to achieve high enough channel quality as well as efficiently exploit the limited frequency allocation. And thus, the bandwidth term results in very low thresholds, i.e. Carson's rule $-17dB$, for radar people, normally $-3dB$ bandwidth.

Table B.2: Bandwidths for various tones, $\Delta f = 75kHz$. The table is adapted from [21].

f_m $[Hz]$	β	$L(\beta, 0.1)$	$L(\beta, 0.01)$	$B_{0.01}$ $[kHz]$	$B_{0.1}$ $[kHz]$	B_{CR} $[kHz]$
15000	5.0	9	7	270	210	180
10000	7.5	12	9	240	180	170
3750	20.0	25	22	187	165	158
1000	75.0	82	76	164	152	152

B.3 Demodulation of the FM modulated signal

This section is a mathematical formulation of the work described in [98], in the nomenclature of section B.1.

A FM wave is described by (B.1) and the instantaneous phase in (B.2). Based on this, define the FM modulated signal

$$x_{FM}(t) = A\cos\left(\omega_c t + K'' \int_{t_0}^{t} s(\lambda)d\lambda\right) = A\frac{e^{i(\omega_c t+\theta(t))} + e^{-i(\omega_c t+\theta(t))}}{2}, \tag{B.20}$$

where

$$\theta(t) = K'' \int_{t_0}^{t} s(\lambda)d\lambda. \tag{B.21}$$

The signal in (B.20) is sampled at sample frequency f_s yielding samples at times t_j, $j = 0, 1, 2, \ldots, S-1$, where S is a finite positive integer, resulting in

$$x'_{FM}(t_j) = A\frac{e^{i(\omega_c t_j+\theta(t_j))} + e^{-i(\omega_c t_j+\theta(t_j))}}{2}, \qquad j = 0, 1, 2, \ldots, S-1. \tag{B.22}$$

In the digital domain $x'_{FM}(t_j)$ is modulated with the complex exponential $exp(-i\omega'_c t_j)$ giving

$$x''_{FM}(t_j) = \frac{A}{2}\left[e^{i((\omega_c-\omega'_c)t+\theta(t_j))} + e^{-i((\omega_c+\omega'_c)t+\theta(t_j))}\right], \qquad j = 0, 1, 2, \ldots, S-1. \tag{B.23}$$

In order to avoid aliasing it is required that $\omega_c + \omega'_c + B/2 < f_s$ where B is the bandwidth of the integrated information carrying signal $s(\lambda)$. When $\omega_c = \omega'_c$, the second term will be modulated to the frequency $2\omega_c$, which is filtered away, and thus

$$x'''_{FM}(t_j) = \frac{A}{2}e^{i\theta(t_j)} = \frac{A}{2}\exp\left(iK'' \int_{t_0}^{t_j} s(\lambda)d\lambda\right), \qquad j = 0, 1, 2, \ldots, S-1. \tag{B.24}$$

By taking two subsequent samples, multiplying and complex conjugating subsequent them,

$$x''''_{FM}(t_j) = x'''_{FM}(t_{j+1})\overline{x'''_{FM}(t_j)} = \frac{A}{2}\exp\left(iK'' \int_{t_j}^{t_{j+1}} s(\lambda)d\lambda\right), \qquad j = 0, 1, 2, \ldots, S-2, \tag{B.25}$$

where $\overline{x(t_j)}$ means the complex conjugate of $x(t_j)$. Since the bandwidth of $s(\lambda)$ is much lower than the sampling frequency, the term $K'' \int_{t_j}^{t_{j+1}} s(\lambda)d\lambda$ will be a good approximation to the instantaneous frequency. In order to recover the information carrying signal, the phase of $x''''_{FM}(t_j)$ for $j = 0, 1, 2, \ldots, S-2$ needs to be found. The phase is calculated using

$$K'' \int_{t_j}^{t_{j+1}} s(\lambda) d\lambda = \tan^{-1}\left(\frac{\text{Im}\{x''''_{FM}(t_j)\}}{\text{Re}\{x''''_{FM}(t_j)\}}\right), \qquad j = 0, 1, 2, \ldots, S-2. \tag{B.26}$$

Figure 6.1 shows a schematic diagram of the frequency content of the decoded or unmodulated FM radio signal. Although national adaptations may apply, the interesting frequency contents, the audio part, ranging from $30Hz$ to $53kHz$, is universal [16]. From $30Hz$ to $15kHz$ lies the mono audio, which consists of the sum of the left and right audio channel, followed by the attenuated $19kHz$ stereo pilot, which is used to modulate and demodulate the stereo information with correct phase. The stereo information, the difference between left and right audio channel, lies from $23kHz$ to $53kHz$ in a double sideband with suppressed carrier [16].

This is the SW digital demodulation scheme used in order to produce figure 6.2, as well as listen to the audio in the recorded signals, table 6.1.

B.4 TV channel frequencies and UHF-frequencies

The following table maps the TV UHF channel numbers (Ch No) to the corresponding UHF-frequencies in MHz.

Ch No	Center Freq [MHz]	Lower Freq [MHz]	Higher Freq [MHz]	Ch No	Center Freq [MHz]	Lower Freq [MHz]	Higher Freq [MHz]
21	474	470	478	46	674	670	678
22	482	478	486	47	682	678	686
23	490	486	494	48	690	686	694
24	498	494	502	49	698	694	702
25	506	502	510	50	706	702	710
26	514	510	518	51	714	710	718
27	522	518	526	52	722	718	726
28	530	526	534	53	730	726	734
29	538	534	542	54	738	734	742
30	546	542	550	55	746	742	750
31	554	550	558	56	754	750	758
32	562	558	566	57	762	758	766
33	570	566	574	58	770	766	774
34	578	574	582	59	778	774	782
35	586	582	590	60	786	782	790
36	594	590	598	61	794	790	798
37	602	598	606	62	802	798	806
38	610	606	614	63	810	806	814
39	618	614	622	64	818	814	822
40	626	622	630	65	826	822	830
41	634	630	638	66	834	830	838
42	642	638	646	67	842	838	846
43	650	646	654	68	850	846	854
44	658	654	662	69	858	854	862
45	666	662	670				

Bibliography

[1] K. E. Olsen and K. Woodbridge, "Performance of a Multiband Passive Bistatic Radar Processing Scheme - Part I," *IEEE AESS Systems Magazine Special Issue on PCL*, August 2011.

[2] ——, "Performance of a Multiband Passive Bistatic Radar Processing Scheme - Part II," *IEEE AESS Systems Magazine Special Issue on PCL*, August 2011.

[3] K. E. Olsen and C. J. Baker, "FM-based passive bistatic radar as a function of available bandwidth," in *Proc. of IEEE Radar Conference*, May 2008, invited paper.

[4] K. E. Olsen and K. Woodbridge, "FM based passive bistatic radar target range improvement," in *Proc. International Radar Symposium*, September 2009.

[5] K. E. Olsen, K. Woodbridge, and I. A. Andersen, "FM Based Passive Bistatic Radar Target Range Improvement - Part II," in *Proc. International Radar Symposium*, June 2010.

[6] K. E. Olsen and K. Woodbridge, "FM Based Passive Bistatic Radar Target Range Resolution Improvement - Part III," in *Proc. International Radar Symposium*, September 2011.

[7] ——, "Analysis of the Performance of a Multiband Passive Bistatic Radar Processing Scheme," in *IEEE Waveform Diversity & Design Conference*, August 2010.

[8] K. E. Olsen, "Any PCL aspects in Norway?" in *PCL Focus Day.* Franhofer FHR, November 2009.

[9] K. E. Olsen and K. Woodbridge, "Analysis of the Performance of a Multiband Passive Bistatic Radar Processing Scheme," in *PCL Focus Day.* Franhofer FHR, May 2011.

[10] (2008, March) Bandwidth (signal processing). Wikipedia. [Online]. Available: http://en.wikipedia.org/wiki/Bandwidth_(signal_processing)

[11] N. J. Willis, *Bistatic Radar.* Silver Spring, MD, USA: Technology Service Corporation, 1995.

[12] *Digital Video Broadcasting (DVB); Framing structure, channel coding and modulation for digital terrestrial television. ETSI EN 300 744 V1.5.1 (2004-11)*,

The European Telecommunications Standards Institute (ETSI) Std., 2004. [Online]. Available: http://www.etsi.org

[13] (2008, March) Passive radar. Wikipedia. [Online]. Available: http://en.wikipedia.org/wiki/Passive_radar

[14] *Propagation by diffraction - Recommendation ITU-R P.526-10*, International Telecommunication Union (ITU) Std., 2007. [Online]. Available: http://www.itu.int

[15] Software Defined and Digital Radio Technology for Sigint Comint Elint - ESM ECM EW. SAGAX Communication. [Online]. Available: http://www.sagax.hu/

[16] *Transmission standards for FM sound broadcasting at VHF - Recommendation ITU-R BS.450-3*, International Telecommunication Union (ITU) Std., 2001. [Online]. Available: http://www.itu.int

[17] (2008, March) FM broadcasting. Wikipedia. [Online]. Available: http://en.wikipedia.org/wiki/FM_broadcasting

[18] (2010, March) Boeing 737. Wikipedia. [Online]. Available: http://en.wikipedia.org/wiki/Boeing_737

[19] (2010, December) SBS-1: Real-time Virtual Radar. Kinetic Avionic Products Limited. [Online]. Available: http://www.kinetic-avionics.com/sbs-1.php

[20] (2011, April) Cessna 172. Wikipedia. [Online]. Available: http://en.wikipedia.org/wiki/Cessna_172

[21] H. Stark, F. B. Tuteur, and J. B. Anderson, Eds., *Modern Electrical Communications - Analog, Digital and Optical Systems, Second Edition.* Englewood Cliffs, New Jersey 07632: Prentice Hall, 1998.

[22] N. Willis and H. D. Griffiths, Eds., *Advances in Bistatic Radar.* Scitech Pub Inc, 2007.

[23] M. Cherniakov, Ed., *Bistatic Radar: Emerging Technology.* John Wiley & Sons Ltd, 2008.

[24] (2010, March) Silent Sentry®. Lockheed Martin. [Online]. Available: http://www.lockheedmartin.com/products/silent-sentry/index.html

[25] (2007, May) Silent Sentry®. Innovative Technology for Passive, Persistent Surveillance. Lockheed Martin. [Online]. Available: http://www.lockheedmartin.com/data/assets/10644.pdf

[26] J. Ferrier, M. Klein, and S. Allam, "Frequency and Waveform Complementarities for Passive Radar Applications," in *International Radar Symposium 2009*, September 2009.

[27] H. D. Griffiths, “From a different perspective: Principles, practice and potential of bistatic radar,” in *Proc. International Radar Conference*, September 2003.

[28] C. J. Baker and H. D. Griffiths, “Bistatic and Multistatic Radar Sensors for Homeland Security,” in *NATO Advanced Study Institute, Advances in Sensing with Security Applications*, July 2005.

[29] H. D. Griffiths and C. J. Baker, “Passive coherent location radar systems. Part 1: Performance prediction,” *IEE Proc.-Radar Sonar Navig.*, vol. 152, no. 3, pp. 153–159, June 2005.

[30] C. J. Baker, H. D. Griffiths, and I. Papoutsis, “Passive coherent location radar systems. Part 2: Waveform properties,” *IEE Proc.-Radar Sonar Navig.*, vol. 152, no. 3, pp. 160–168, June 2005.

[31] H. D. Griffiths and C. J. Baker, “The Signal and Interference Environment in Passive Bistatic Radar,” in *Information, Decision and Control, IDC’07*, February 2007.

[32] R. Saini and M. Cherniakov, “DTV signal ambiguity function analysis for radar application,” *IEE Proc.-Radar Sonar Navig.*, vol. 152, no. 3, pp. 133–142, June 2005.

[33] A. Lauri, F. Colone, R. Cardinali, C. Bongioanni, and P. Lombardo, “Analysis and Emulation of FM Radio Signals for Passive Radar,” in *Aerospace Conference, 2007 IEEE*, March 2007.

[34] T. Tsao, M. Slamani, P. Varshney, D. Weiner, H. Schwarzlander, and S. Borek, “Ambiguity function for a bistatic radar,” *IEE Trans. Aerospace and Electronic Systems*, vol. 22, no. 3, pp. 1041–1051, July 1997.

[35] F. Colone, D. W. O’Hagan, P. Lombardo, and C. J. Baker, “A multistage Processing Algorithm for Disturbance Removal and Target Detection in Passive Bistatic Radar,” *Aerospace and Electronic Systems, IEEE Transactions on*, vol. 45, no. 2, pp. 698–722, April 2009.

[36] D. O’Hagan, F. Colone, C. J. Baker, and H. Griffiths, “Passive Bistatic Radar (PBR) demonstrator,” in *Radar Systems, 2007 IET International Conference on*, October 2007, pp. 1–5.

[37] D. W. O’Hagan and C. J. Baker, “Passive Bistatic Radar (PBR) using FM radio illuminators of opportunity,” in *New Trends for Environmental Monitoring Using Passive Systems*, October 2008.

[38] C. Bongioanni, F. Colone, and P. Lombardo, “Performance Analysis of a Multi-Frequency FM Based Passive Bistatic Radar,” in *Radar Conference, 2008. RADAR 2008. IEEE*, May 2008.

[39] P. Lombardo, F. Colone, C. Bongioanni, A. Lauri, and T. Bucciarelli, “PBR activity at INFOCOM: adaptive processing techniques and experimental results,” in *Radar Conference, 2008. RADAR 2008. IEEE*, May 2008.

[40] D. Gould, R. Pollard, C. Sarno, and P. Tittensor, “Developments to a Multiband Passive Radar Demonstrator System,” in *Radar Systems, 2007 IET International Conference on*, October 2007.

[41] M. Edrich, F. Wolschendorf, and A. Schroder, “FM and DAB Experimental Passive Radar System: Concept and Measurement Results,” in *International Radar Symposium 2009*, September 2009.

[42] M. Cherniakov, Ed., *Bistatic Radar: Principles and Practice.* John Wiley & Sons Ltd, 2007.

[43] L. Ortenzi, L. Timmoneri, and D. Vigilante, “Unscented Kalman Filter (UKF) Applied to FM Based Band Passive Radar,” in *SEE Radar 2009*, October 2009.

[44] P. E. Howland, D. Maksimiuk, and G. Reitsma, “FM radio based bistatic radar,” *IEE Proc.-Radar Sonar Navig.*, vol. 152, no. 3, pp. 107–115, June 20055.

[45] P. van Dorp, R. Ebeling, and A. G. Huizing, “High Resolution Radar Imaging using Coherent MultiBand Processing Techniques,” in *Radar Conference, 2010. RADAR ’10. IEEE*, May 2010.

[46] D. R. Wehner, *High-Resolution Radar*, 2nd ed. Norwood, MA, USA: Artech House, 1995.

[47] M. Malanowski and K. Kulpa, “Analysis of Bistatic Tracking Accuracy in Passive Radar,” in *Radar Conference, 2009 IEEE*, May 2009.

[48] ——, “Experimental Analysis of Passive Radar Accuracy,” in *International Radar Symposium 2009*, September 2009.

[49] M. Tobias and A. D. Lanterman, “Probability hypothesis density-based multitarget tracking with bistatic range and Doppler observations,” *IEE Proc.-Radar Sonar Navig.*, vol. 152, no. 3, pp. 195–205, June 2005.

[50] S. Herman and P. Moulin, “A particle filtering approach to FM-band passive radar tracking and automatic target recognition,” *IEEE Aerospace Conference 2002*, vol. 4, pp. 1789–1808, 2002.

[51] M. Tobias and A. D. Lanterman, “Techniques for birth-particle placement in the probability hypothesis density particle filter applied to passive radar,” *Radar, Sonar Navigation, IET*, vol. 2, no. 5, pp. 351–365, October 2008.

[52] ——, “A probability hypothesis density-based multitarget tracker using multiple bistatic range and velocity measurements,” in *System Theory, 2004. Proceedings of the Thirty-Sixth Southeastern Symposium on*, February 2004.

[53] M. Daun and W. Koch, "Multistatic Target Tracking for Non-Cooperative Illuminating by DAB/DVB-T," in *OCEANS 2007 - Europe*, June 2007.

[54] M. Daun and C. R. Berger, "Track initialization in a multistatic DAB/DVB-T network," in *Information Fusion, 2008 11th International Conference on*, July 2008.

[55] M. Daun and W. Koch, "Multistatic target tracking for non-cooperative illumination by DAB/DVB-T," in *Radar Conference, 2008. RADAR '08. IEEE*, May 2008.

[56] A. Farina, "Tracking function in bistatic and multistatic radar systems," *Communications, Radar and Signal Processing, IEE Proceedings F*, vol. 133, no. 7, pp. 630–637, December 1986.

[57] P. E. Howland, "Target tracking using television-based bistatic radar," *IEE Proc.-Radar Sonar Navig.*, vol. 146, no. 3, pp. 166–174, June 1999.

[58] M. Malanowski and K. Kulpa, "Optimization of Confirmation Time of Bistatic Tracks in Passive Radar," *Aerospace and Electronic Systems, IEEE Transactions on*, vol. 47, no. 2, pp. 1060–1072, April 2011.

[59] M. Malanowski, K. Kulpa, and R. Suchozebrski, "Two-stage tracking algorithm for passive radar," in *Information Fusion, 2009. FUSION '09. 12th International Conference on*, July 2009.

[60] M. Skolnik, Ed., *Radar Handbook, 2nd ed.* USA: McGraw-Hill, 1990.

[61] V. S. Chernyak, *Fundamentals of Multisite Radar Systems - Multistatic Radars and Multiradar Systems.* Amsterdam: Gordon and Breach Science Publishers, 1998.

[62] H. Kuschel, M. Ummenhofer, D. O'Hagan, and J. Heckenbach, "On the resolution performance of passive radar using DVB-T illuminations," in *Radar Symposium (IRS), 2010 11th International*, June 2010.

[63] H. Kuschel, J. Heckenbach, D. O'Hagan, and M. Ummenhofer, "A Hybrid Multi-Frequency Passive Radar Concept for Medium Range Air Surveillance," in *PCL Focus Day.* Franhofer FHR, May 2011.

[64] A. S. Tasdelen and H. Köymen, "Range resolution improvement in passive coherent location radar systems using multiple FM radio channels," in *Proc. IET Forum on Radar and Sonar*, November 2006.

[65] D. Poullin, "Passive detection using digital broadcasters (DAB, DVB) with COFDM modulation," *IEE Proc.-Radar Sonar Navig.*, vol. 152, no. 3, pp. 160–168, June 2005.

[66] M. Conti, F. Berizzi, D. Petri, A. Capria, and M. Martorella, "High range resolution DVB-T Passive Radar," in *Radar Conference (EuRAD), 2010 European*, October 2010.

[67] M. Conti, D. Petri, A. Capria, F. Berizzi, and M. Martorella, "High Resolution and Artifact Cancellation in Wideband DVB-T Passive Radar," in *PCL Focus Day*. Franhofer FHR, May 2011.

[68] M. Jankiraman, *Design of Multi-Frequency CW Radars.* SciTech Publishing, Inc, 2007.

[69] O. Arikan and D. C. Munson, "A Topographic Formulation of Bistatic Synthetic Aperture Radar," *Advances in Communications and Signal Processing*, vol. 129, pp. 289–302, 1989.

[70] D. Mensa and G. Heidbreder, "Bistatic Synthetic-Aperture Radar Imaging of Rotating Objects," *Aerospace and Electronic Systems, IEEE Transactions on*, vol. AES-18, no. 4, pp. 423–431, July 1982.

[71] M. Martorella, J. Palmer, J. Homer, B. Littleton, and I. D. Longstaff, "On Bistatic Inverse Synthetic Aperture Radar," *Aerospace and Electronic Systems*, vol. 43, no. 3, pp. 1125–1134, July 2007.

[72] Z. Zhu, Y. Zhang, and Z. Tang, "Bistatic inverse synthetic aperture radar imaging," in *Radar Conference, 2005 IEEE International*, May 2005.

[73] K. Suwa, S. Nakamura, S. Morita, T. Wakayama, H. Maniwa, T. Oshima, R. Maekawa, , S. Matsuda, and T. Tachihara, "ISAR imaging of an aircraft target USING ISDB-T digital TV based passive bistatic radar," in *Geoscience and Remote Sensing Symposium (IGARSS), 2010 IEEE International*, July 2010.

[74] Y. W. A. D. Lanterman, D. C. Munson jr, "Wide-angle radar imaging using time-frequency distributions," *IEE Proc.-Radar Sonar Navig.*, vol. 150, no. 4, pp. 203–211, August 2003.

[75] Y. Wu and D. C. Munson, "Multistatic Synthetic Aperture Imaging of Aircraft using Reflected Television Signals," *Algorithms for Synthetic Aperture Radar Imagery VIII*, vol. 4382, pp. 1–12, 2001.

[76] A. D. Lanterman and D. C. Munson, "Deconvolution Techniques for Passive Radar Imaging," *Algorithms for Synthetic Aperture Radar Imagery IX*, vol. 4727, pp. 166–177, 2002.

[77] Y. Wu and D. C. Munson, "Multistatic passive radar imaging using the smoothed pseudo Wigner-Ville distribution," in *Image Processing, 2001. Proceedings. 2001 International Conference on*, 2001.

[78] ——, "Wide-angle ISAR passive imaging using smoothed pseudo Wigner-Ville distribution," in *Radar Conference, 2001. Proceedings of the 2001 IEEE*, 2001.

[79] D. Pastina, M. Sedehi, and D. Cristallini, "Passive bistatic ISAR based on geostationary satellites for coastal surveillance," in *Radar Conference, 2010 IEEE International*, May 2010.

[80] F. Daout, F. Schmitt, and G. Ginolhac, "Computation of bistatic RCS with NEC2 in a context of passive ISAR system," in *Geoscience and Remote Sensing Symposium, 2005. IGARSS '05. Proceedings. 2005 IEEE International*, July 2005.

[81] L. M. Ehrman and A. D. Lanterman, "A robust algorithm for automatic target recognition using passive radar," in *System Theory, 2004. Proceedings of the Thirty-Sixth Southeastern Symposium on*, September 2004.

[82] *IEEE Standard Definitions, IEEE Std 686-1997 (Revision of IEEE Std 686-1990)*, Institute of Electrical and Electronics Engineers (IEEE) Std., 1997. [Online]. Available: http://www.ieee.org

[83] L. V. Blake, *Radar Range Performance Analysis.* Lexington, MA, USA: Lexington Books, 1980.

[84] ——, *Radar Range Performance Analysis.* Norwood, MA, USA: Artech House, 1986.

[85] M. Skolnik, "An Analysis of Bistatic Radar," *IRE Trans. Aerospace and Navigational Electronics*, pp. 19–27, March 1961.

[86] D. K. Barton and S. A. Leonov, Ed., *Radar Technology Encyclopedia*, 1st ed. Artech House, Inc, 1997.

[87] M. C. Jackson, "The Geometry of Bistatic Radar Systems," *IEE Proc. 133(7) Pt. F*, pp. 604–612, December 1986.

[88] A. Schroeder, "Second-Generation Mobile Multiband Passive Radar Demonstrator," in *PCL Focus Day.* Franhofer FHR, May 2011.

[89] C. Coleman and H. Yardley, "Passive bistatic radar based on target illuminations by digital audio broadcasting," *Radar, Sonar Navigation, IET*, vol. 2, no. 5, pp. 366–375, October 2008.

[90] R. Zemmari and U. Nickel, "Range Performance Study of a GSM Passive Radar System," in *Radar Symposium (IRS), 2009 10th International*, September 2009.

[91] R. Zemmari, "Reference signal extraction for GSM passive coherent location," in *Radar Symposium (IRS), 2010 11th International*, June 2010.

[92] ——, "Reference Signal Extraction for GSM Passive Radar," in *PCL Focus Day.* Franhofer FHR, May 2011.

[93] H. Guo and K. Woodbridge and C. J. Baker, "Evaluation of WiFi beacon transmissions for wireless based passive radar," in *Radar Conference, 2008. RADAR '08. IEEE*, May 2008.

[94] K. Chetty and G. Smith and H. Guo and K. Woodbridge, "Target detection in high clutter using passive bistatic WiFi radar," in *Radar Conference, 2009 IEEE*, May 2009.

[95] J. M. Thomas and C. J. Baker and H. D. Griffiths, "DRM signals for HF passive bistatic radar," in *Radar Systems, 2007 IET International Conference on*, October 2007.

[96] R. Saini, M. Cherniakov, and V. Lenive, "Direct path interference suppression in bistatic system: DTV based radar," in *Radar Conference, 2003. Proceedings of the International*, September 2003.

[97] DVB Worldwide - Norway. The Digital Video Broadcasting Project (DVB). [Online]. Available: http://www.dvb.org/about_dvb/dvb_worldwide/norway/

[98] E. Blossom. (2004, September) Listening to FM Radio in Software, Step by Step. Linux Journal. [Online]. Available: http://www.linuxjournal.com/article/7505

[99] D. A. Barton, Ed., *Radar System Analysis.* Norwood, MA: Artech House, 1976.

[100] G. W. Stimson, *Airborne Radar.* Mendham, New Jersey, USA: Scitech Publishing, 1998.

[101] P. M. Woodward, *Probability and Information Theory, with Applications to Radar.* Pergamon Press, New York, 1953.

[102] J. D. Sahr and F. D. Lind, "The Manastash Ridge radar: A passive bistatic radar for upper atmospheric radio science," *Radio Science*, vol. 32, no. 6, pp. 2345–2358, 1997.

[103] (2011, May) Manastash ridge radar. University of Washington. [Online]. Available: http://rrsl.ee.washington.edu/

[104] C. Coleman, "Mitigating the effect of direct signal interference in passive bistatic radar," in *Radar Conference - Surveillance for a Safer World, 2009. RADAR. International*, October 2009.

[105] Z. Jiabing, H. Yi, and T. Liang, "Adaptive Beamforming Passive Radar Based on FM Radio Transmitter," in *Radar, 2006. CIE '06. International Conference on*, October 2006.

[106] ——, "Adaptive beamforming passive radar based on FM radio transmitter," in *Radar Systems, 2007 IET International Conference on*, October 2007.

[107] R. Tao, H. Z. Wu, and T. Shan, "Direct-path suppression by spatial filtering in digital television terrestrial broadcasting-based passive radar," *Radar, Sonar Navigation, IET*, vol. 4, no. 6, pp. 791–805, December 2010.

[108] C. Bongioanni, F. Colone, T. Martelli, R. D'Angeli, and P. Lombardo, "Exploiting polarimetric diversity to mitigate the effect of interferences in FM-based passive radar," in *Radar Symposium (IRS), 2010 11th International*, June 2010.

[109] D. W. O'Hagan, H. Kuschel, J. Heckenbach, M. Ummenhofer, and J. Schell, "Signal reconstruction as an effective means of detecting targets in a DAB-based PBR," in *Radar Symposium (IRS), 2010 11th International*, June 2010.

[110] H. Wan, S. Li, and Z. Wang, "Direct Path Interference Cancellation in FM Radio-Based Passive Radar," in *Signal Processing, 2006 8th International Conference on*, 2006.

[111] K. Kulpa and Z. Czekala, "Masking effect and its removal in PCL radar," *Radar, Sonar and Navigation, IEE Proceedings*, vol. 152, no. 3, pp. 174–178, June 2005.

[112] F. Colone, R. Cardinali, and P. Lombardo, "Cancellation of clutter and multipath in passive radar using a sequential approach," in *Radar, 2006 IEEE Conference on*, April 2006.

[113] D. W. O'Hagan, C. J. Baker, and H. D. Griffiths, "Signal and Interference Analysis: Proposed Analogue Signal Suppression Techniques for PCL Radar," in *Radar Conference, 2006. EuRAD 2006. 3rd European*, September 2006.

[114] Z. Jiabing, T. Liang, and H. Yi, "A Direct Path Interference Cancellation Approach to Passive Radar Based on FM Radio transmitter," in *Electro/information Technology, 2006 IEEE International Conference on*, May 2006.

[115] R. Cardinali, F. Colone, C. Ferretti, and P. Lombardo, "Comparison of Clutter and Multipath Cancellation Techniques for Passive Radar," in *Radar Conference, 2007 IEEE*, April 2007.

[116] K. E. Olsen, T. Johnsen, and S. Johnsrud, "Details of the signal processing, simulations and results from the Norwegian multistatic radar DiMuRa," in *Proc. IEEE Waveform Diversity and Design Conference*, February 2006.

[117] M. Wicks, E. Mokole, S. Blunt, R. Schneible, and V. Amuso, Eds., *Principles of Waveform Diversity and Design*, 1st ed. Raleigh, NC: Scitech Publishing, Inc., 2010.

[118] E. W. Weisstein, Ed., *CRC Concise Encyclopedia of Mathematics*, 2nd ed. CRC Press LLC, 2003.

[119] K. Rottmann, Ed., *Mathematische Formelsammlung*, 4th ed. B.I. Wissenschaftsverlag, 1991.

[120] E. Weisstein. (2011, September) Exponential sum formulas. Mathworld–A Wolfram Web Resource. [Online]. Available: http://mathworld.wolfram.com/ExponentialSumFormulas.html

[121] F. J. Harris, "On the Use of Windows for Harmonic Analysis with the Discrete Fourier Transform," *IEEE Proc.*, vol. 66, pp. 51–83, January 1978.

[122] K. E. Olsen, T. Johnsen, S. Johnsrud, I. Tansem, and P. Sornes, “Multistatic and/or Quasi Monostatic Radar Measurements of propeller aircrafts,” in *Radar Systems, 2007 IET International Conference on*, October 2007.

[123] K. E. Olsen, T. Johnsen, S. Johnsrud, R. Gundersen, H. B. I. Tansem, and P. Sornes, “Results from an experimental continuous wave low probability of intercept bistatic radar - the first steps toward multistatic radar,” in *Radar Conference, 2003. Proceedings of the International*, September 2003.

[124] T. Johnsen, K. E. Olsen, and R. Gundersen, “Hovering helicopter measured by bi-/multistatic CW radar,” in *Radar Conference, 2003. Proceedings of the 2003 IEEE*, May 2003.

[125] T. Johnsen, K. E. Olsen, S. Johnsrud, and R. Skjerpeng, “Simultaneous use of multiple pseudo random noise codes in multistatic CW radar,” in *Radar Conference, 2004. Proceedings of the IEEE*, April 2004.

[126] D. W. O’Hagan, “Passive Bistatic Radar Performance Characterisation Using FM Radio Illuminators of Opportunity,” Ph.D. dissertation, University College London, 2009.

[127] Triax FM Antenne 5 elm. Krogh’s elektronik. [Online]. Available: (http://www.keas.dk/store/comersus_ viewItem.asp?idproduct=138)

[128] Televes DAT75 Digital Wideband Tv Aerial. TLC Electrical Supplies direct. [Online]. Available: (http://www.tlc-direct.co.uk/Products/MXDAT75.html)

[129] Funke Digital TV FFA4522 21/69 Passive DVB-T Long range outdoor antenna. Funke digital TV. [Online]. Available: (http://www.funke.nl/site/index.php?option=com_ content&task=view&id=287&Itemid=354)

[130] M. Malanowski, K. Kulpa, and J. Misiurewicz, “Acceleration estimation for Passive Coherent Location radar,” in *Radar Conference, 2008. RADAR ’08. IEEE*, May 2008.

[131] M. Malanowski, K. Kulpa, and K. E. Olsen, “Extending the integration time in DVB-T-based passive radar,” in *Radar Conference (EuRAD), 2011 European*, October 2011.

[132] J. M. Christiansen and K. E. Olsen, “Range and Doppler walk in DVB-T based Passive Bistatic Radar,” in *Radar Conference, 2010. RADAR ’10. IEEE*, May 2010.

[133] J. M. Christiansen, “DVB-T based Passive Bistatic Radar. Simulated and experimental data analysis of range and Doppler walk,” Master’s thesis, NTNU, Norwegian University of Science and Technology, 2009.

[134] K. E. Olsen, “Anvendelse av en modifisert Fouriermetode i digital signalbehandling,” Master of Science thesis, Applied Mathematics, *In Norwegian*, University of Bergen, Norway, 1998.

[135] J. R. Carson, “Notes on the Theory of Modulation,” *Proceedings of the IRE*, vol. 10, pp. 57–64, February 1922.

[136] A. B. Carlson, *Communication Systems: An Introduction to Signals and Noise in Electrical Communications.* New York: McGraw-Hill, 1968.